
A CENSUS OF DUST IN GALAXIES ACROSS 5 BILLION
YEARS OF COSMIC TIME

by

Rosemary Alice Beeston

A THESIS SUBMITTED TO CARDIFF UNIVERSITY
FOR THE DEGREE OF DOCTOR OF PHILOSOPHY

30th SEPTEMBER 2019

Author: Rosemary Alice Beeston

Title: A census of dust in galaxies across 5 billion years of cosmic time

Date of submission: 30th September 2019

For Eve

DEDICATION

'Dear thing - tomorrow is your big day - remember to stand tall, speak loudly (as if to Archie) and remember that no other bugger knows as much as you do. BiG UP THE SELF CONFIDENCE. Huge amount of love and enjoy - relax and enjoy xx'

ANNE-MARIE SMITH

There are so many people without whom this Thesis would either not exist, or be drastically different¹. These four years have been the most demanding of my life, and I could not have made it through without the incredible and unwavering support of my fantastic supervisor, Haley Gomez, who is the most inspirational and just all-round brilliant human in existence - Haley, you are my hero, thank you.

I am so incredibly lucky to have my family, who I could not have done this without. Every single one of you is incredible and I love you so much. Mum and Dad, you made me the person I am today and I couldn't be more grateful for the love and happiness you have brought to my life every single day. Matt, I couldn't ask for a kinder, funnier, more loving brother than you, growing up with you was a privilege. I will always be thankful to my many amazing and inspiring aunties, uncles, cousins, and grandparents - you are home to me and I love you so much. This goes also for the family I have gained through George who have had an incredible (and positive!) influence on me and my life - thank you all.

¹ read: worse

Thank you to everyone in the cosmicdust group - every meeting was enlightening and interesting, and I'm so proud to have been a part of the team. A particular thanks to Steve and Loretta, without your guidance this work would be much less thorough and much less good and I am so thankful to you for every slack message and meeting.

To everyone I shared an office with at any point, I'm too lazy to list all of your names, but know that I couldn't have asked for a more supportive and lovely bunch of people to be around for four years. I will say a particular thanks to my beautiful, amazing, talented galaxies cohort Ruth, Aris, and Eleni. Even if the only thing I got out of the PhD was meeting you guys, it would be worth it. Thank you for all the dinners, coffees, heart-to-hearts, and the many many many good times. I learnt so much from you all and I feel like I've known you my whole life. Ruth, you are so talented and funny, I always look forward to visiting you in Sheffield, you make everyone feel so welcome in your presence. Eleni, you are the bravest, most passionate person I've ever known and I love you. Aris, you are always hungry, and always ready to laugh and make everyone laugh along with you. Also, Ed Fauchon-Jones, thank you for being a beautiful soul.

Thank you to Cardiff Pottery Workshops for being my happy place.

Thanks so so much to the computing support team, you guys are incredible and the department could not function without you.

Gareth, thank you for being a constant source of humour, interesting conversation, and support. To say that you were an amazing friend throughout would be to understate the role you have played and continue to play in my life.

Phil, thank you for all the jams. Alice and Josh, thank you for putting up with the racket we made looking for freedom. I don't know how I would have coped during some of the most difficult times in my life without the prospect of singing with you to look forward to (almost) every week (sometimes)... (maybe). Hopefully now we'll have time to work on our first album, which will undoubtedly go platinum overnight and make this whole PhD thing a bit pointless.

Jess, thank you for being our honorary housemate, for all the nights playing mario kart until 2am, all the runs you took my crazy dog on, the amazing hugs, the dinners, the trips to stately homes, for everything. Even Jesus doesn't love you as much as me!

To my lovely dog², Archie, thank you for making our house a home. You give the best snugs and the wettest kisses. You always know how to cheer me up when I'm down. You make me laugh, you bring me joy, you complete our little family. I can't imagine life without you and your incredible comic timing. Thank you for being an adorable little rascal.

Lastly, and most importantly, George. I love you so much. I don't know how to express how much better you make every day and how glad I am that I get to spend my life with you. I couldn't have done this without your constant support and love. You're my favourite, thank you so much for everything you have brought to my life. Here's to the next chapter.

² son

ACKNOWLEDGEMENTS

THIS work was made possible by support from the European Research Council (ERC) in the form of Consolidator Grant COSMICDUST (ERC-2014-CoG-647939, PI HL Gomez).

This work made use of the python packages Matplotlib³ (Hunter, 2007), NumPy⁴ (Oliphant, 2006), SciPy⁵, Imfit (Newville et al., 2016), emcee (Foreman-Mackey et al., 2013), corner (Foreman-Mackey, 2016), and seaborn <http://seaborn.pydata.org/index.html>. This work made use of R (R Core Team, 2016). This work made use of TOPCAT⁶ (Taylor, 2005), which was initially developed under the UK Starlink project, and has since been supported by PPARC, the VOTech project, the AstroGrid project, the AIDA project, the STFC, the GAVO project, the European Space Agency, and the GENIUS project.

GAMA is a joint European-Australasian project based around a spectroscopic campaign using the Anglo-Australian Telescope. The GAMA input catalogue is based on data taken from the Sloan Digital Sky Survey and the UKIRT Infrared Deep Sky Survey. Complementary imaging of the GAMA regions is being obtained by a number of independent survey programmes including GALEX MIS, VST KiDS, VISTA VIKING, WISE, Herschel-ATLAS, GMRT and ASKAP providing UV to radio coverage. GAMA is funded by the STFC (UK), the ARC (Australia), the AAO, and the participating institutions. The GAMA website is <http://www.gama-survey.org/>. The Herschel-ATLAS is a project with Herschel, which is an ESA space observatory with science instruments provided by European-led Principal Investigator consortia and with important participation from NASA. The *H*-ATLAS website is <http://www.H-ATLAS.org/>. This research

³ <http://matplotlib.org/>

⁴ <http://www.numpy.org/>

⁵ <http://www.scipy.org/>

⁶ <http://www.star.bris.ac.uk/~mbt/topcat/>

made use of Ned Wright's cosmology calculator <http://www.astro.ucla.edu/~wright/CosmoCalc.html> (Wright, 2006).

This work includes material reproduced under the terms of the Creative Commons Attribution ShareAlike 3.0 Unported license⁷.

⁷ <http://creativecommons.org/licenses/by-sa/3.0/deed.en>

PUBLICATIONS

1. Beeston, R. A.; Wright, A. H.; Maddox, S.; Gomez, H. L.; Dunne, L.; Driver, S. P.; Robotham, A.; Clark, C. J. R.; *et al.*, 2018, *GAMA/H-ATLAS: the local dust mass function and cosmic density as a function of galaxy type - a benchmark for models of galaxy evolution*, MNRAS, 479, p1077
2. Beeston R.A., Dunne L., *et al.*, *Evolution of the Dust Mass Function from stacking*, *in preparation*

ABSTRACT

‘Do. Or do not. There is no try.’

YODA

WE present a census of dust in galaxies out to redshifts of 0.5, the most recent five billion years of cosmic history using the wealth of data from the *Herschel Space Observatory* and the Galaxy And Mass Assembly Survey (GAMA). A key goal of this Thesis is to try and quantify the dust component in galaxies, in galaxies of different morphological types, and derive the evolution of the dust content over recent cosmic history.

We derive the dust mass function (DMF) of 15 750 galaxies with redshift $z < 0.1$, drawn from the overlapping area of the GAMA and *H-ATLAS* surveys. The DMF is derived using the density corrected V_{\max} method, where we estimate V_{\max} using: (i) the normal photometric selection limit (pV_{\max}) and (ii) a bivariate brightness distribution (BBD) technique, which accounts for two selection effects. We fit the data with a Schechter function, and find $M^* = (4.65 \pm 0.18) \times 10^7 h_{70}^2 M_{\odot}$, $\alpha = (-1.22 \pm 0.01)$, $\phi^* = (6.26 \pm 0.28) \times 10^{-3} h_{70}^3 \text{Mpc}^{-3} \text{dex}^{-1}$. The resulting dust mass density parameter integrated down to $10^4 M_{\odot}$ is $\Omega_{\text{d}} = (1.11 \pm 0.02) \times 10^{-6}$ which implies the mass fraction of baryons in dust is $f_{m_b} = (2.40 \pm 0.04) \times 10^{-5}$; cosmic variance adds an extra 7-17 per cent uncertainty to the quoted statistical errors. We investigate potential sources of bias in our derived parameters and find that they are robust to uncertainties in the flux measurements of galaxies, the shape of the dust mass function and Eddington bias, though we see a strong dependence on the derived dust mass function parameters depending on the minimum mass used in the fit.

The observed DMF does not agree with predictions from semi-analytic

models or hydrodynamical cosmological simulations. The former attributes too much dust to high stellar mass galaxies. The latter underpredicts the high mass end of the DMF potentially due to long grain growth timescales. We find that the observed dust-to-stellar mass ratio is higher for low-mass disks than currently assumed in models. Comparing the DMFs and galaxy stellar mass functions (GSMF) we find there may be an approximate linear scaling of $(8.07 \pm 0.35) \times 10^{-4}$ from the late-type galaxy (LTG) GSMF to the LTG DMF. The LTG DMF can also be approximated by scaling the disk GSMF by a factor of $(10.21 \pm 0.45) \times 10^{-4}$. We derive dust mass densities of $\Omega_d = (0.88 \pm 0.03) \times 10^{-6}$ and $\Omega_d = (0.060 \pm 0.005) \times 10^{-6}$ for LTGs and early-types respectively.

We use a stacking analysis to investigate the evolution of dust properties as a function of both luminosity and redshift. We stack the FIR *Herschel* luminosities of galaxies in the *H-ATLAS* DR1 sample in luminosity-redshift bins and then fit the resulting SEDs with one and two component modified blackbodies (MBBs). At low redshift, we find that the mass-weighted and luminosity-weighted temperatures derived for the stacked SEDs both exhibit a trend for brighter galaxies to have warmer dust. In higher redshift bins we do see an evolution in both mass-weighted and luminosity-weighted temperature, but the effect is strongest for luminosity-weighted temperature. We are not able to determine whether the evolution is due to higher dust temperatures further back in cosmic time, or because the average luminosity of galaxies also evolves strongly over this redshift range.

We derive $250 \mu\text{m}$ luminosity functions (LFs) and DMFs for the this sample of galaxies in five redshift slices with a width of 0.1 out to redshift 0.5. We find that the low redshift DMF derived in this way has a different shape to the optically selected DMF from the GAMA sample. The best-fitting SF to the low redshift DMF found for the *H-ATLAS* sample by this method has parameters $M^* = (2.55 \pm 0.09) \times 10^7 h_{70}^2 M_\odot$, $\alpha = (-1.11 \pm 0.04)$, $\phi^* = (11.58 \pm 0.53) \times 10^{-3} h_{70}^3 \text{Mpc}^{-3} \text{dex}^{-1}$. The resulting dust mass density parameter for this DMF integrated down to $10^{5.5} M_\odot$ is $\Omega_d = (1.01 \pm 0.02) \times 10^{-6}$. The uncertainty due to cosmic variance for this low-redshift sample is 14.5%. We find a strong evolution of both the luminosity ($\propto (1+z)^{6.24 \pm 0.58}$) and dust mass densities ($\propto (1+z)^{2.08 \pm 0.25}$) in our sample out to $z = 0.5$.

We note that this Thesis extends our knowledge of the dust mass content of

galaxies in the following ways (i) reducing the large uncertainty in measurements of the dust mass density from cosmic variance by using larger areas of the sky; (ii) using consistent, homogeneous measurements over these large volumes (via the GAMA and H-ATLAS surveys where photometry is derived consistently, and dust mass measurements are derived e.g. MAGPHYS for all of the sources in the same way); (iii) approaching the dust mass function from both an optically-selected and FIR-selected sample to determine if this makes a difference and finally (iv) investigating the dust content in galaxies and scaling relations with stellar mass for different morphological types (e.g. late-type/early type and bulge and disk-like galaxies).

CONTENTS

| | |
|--|--------------|
| Dedication | vii |
| Acknowledgements | xi |
| Publications | xiii |
| Abstract | xv |
| List of Tables | xxiii |
| List of Figures | xxv |
| 1 Introduction | 1 |
| 1.1 Galaxies | 3 |
| 1.2 Cosmic Dust | 5 |
| 1.2.1 The Production of Dust | 7 |
| 1.2.2 Chemical Modelling of Dust | 9 |
| 1.3 Observing Dust in Galaxies | 10 |
| 1.3.1 The <i>Herschel</i> Space Observatory | 11 |
| 1.3.2 Deriving Dust Masses for Galaxies | 13 |
| 1.3.3 <i>Herschel</i> observations of dust in galaxies | 17 |
| 1.3.4 <i>Herschel</i> observations of dust in Early Type Galaxies | 18 |
| 1.4 A Statistical View of Dust in Galaxies: The Dust Mass Function | 20 |
| 1.4.1 Evolution of the Dust Mass Function | 23 |
| 1.5 An introduction to the Datasets and Tools used in this Thesis | 25 |
| 1.5.1 Galaxy And Mass Assembly - GAMA | 25 |
| 1.5.2 The <i>Herschel</i> Astrophysical Terahertz Large Area Survey - <i>H-ATLAS</i> | 26 |

| | | |
|----------|--|-----------|
| 1.5.3 | Galaxy Photometry with LAMBDAR | 26 |
| 1.5.4 | Deriving Galaxy Properties with MAGPHYS | 29 |
| 1.6 | Thesis Outline | 31 |
| 2 | Deriving an Optically Selected Dust Mass Function from GAMA/H-ATLAS | 35 |
| 2.1 | Introduction | 35 |
| 2.2 | The sample used in Deriving the Dust Mass Function | 37 |
| 2.3 | Deriving Galaxy Properties with MAGPHYS | 38 |
| 2.3.1 | The Dust Properties of the Sample | 39 |
| 2.3.2 | The Effect of the Temperature Prior | 44 |
| 2.4 | The Dust Mass Function | 45 |
| 2.4.1 | Volume Estimators | 45 |
| 2.4.2 | Density Corrections | 48 |
| 2.4.3 | Calculating Uncertainties in the Dust Mass Function | 49 |
| 2.4.4 | The Shape of the DMF | 53 |
| 2.5 | Comparison with previous Dust Mass Functions | 57 |
| 2.6 | Conclusions | 61 |
| 3 | Biases in the Optically Selected Dust Mass Function? | 63 |
| 3.1 | Introduction | 63 |
| 3.2 | Effect of changing the bivariate dust mass function estimator to stellar mass-surface brightness | 64 |
| 3.3 | Testing the effect of low signal-to-noise photometry | 68 |
| 3.4 | Dependence on the minimum mass of the Schechter fit | 72 |
| 3.5 | A Single or Double Schechter Fit to the DMF? | 75 |
| 3.6 | Eddington Bias in the Dust Mass Function? | 76 |
| 3.7 | Conclusions | 81 |
| 4 | The Optically Selected DMF in Context | 83 |
| 4.1 | Introduction | 83 |
| 4.2 | Theoretical predictions from galaxy formation models | 84 |
| 4.3 | The DMF by morphological type | 92 |
| 4.3.1 | Little Blue Spheroids (LBS) | 98 |
| 4.4 | Comparison with the Galaxy Stellar Mass Function | 98 |

| | | |
|----------|--|------------|
| 4.5 | Investigating Evolution with redshift | 103 |
| 4.6 | Conclusions | 104 |
| 5 | Dust Properties of <i>H</i>-ATLAS Galaxies | 107 |
| 5.1 | Literature Trends for Dust Properties with Redshift, FIR luminosity, and Stellar Properties | 108 |
| 5.1.1 | Photometry | 109 |
| 5.1.2 | Optical IDs | 109 |
| 5.1.3 | Redshifts | 110 |
| 5.1.4 | Star-Galaxy Separation | 112 |
| 5.1.5 | Calculating Luminosities | 113 |
| 5.2 | Estimating Dust Properties | 113 |
| 5.2.1 | MAGPHYS estimates of Dust Properties | 113 |
| 5.2.2 | A Stacking Analysis of the <i>H</i> -ATLAS Equatorial Field Sample | 115 |
| 5.2.3 | Evolution of Dust Properties | 128 |
| 5.3 | Comparing the Dust Mass Estimates | 130 |
| 5.3.1 | Caveats | 133 |
| 5.4 | Conclusions | 137 |
| 6 | The FIR Dust Mass Function: Evolution Over the Last Five Billion Years | 139 |
| 6.1 | Introduction | 140 |
| 6.2 | Completeness Corrections | 141 |
| 6.3 | Methods of Estimating the FIR Luminosity Function | 143 |
| 6.3.1 | Recap of the V_{\max} Method | 143 |
| 6.3.2 | The Page and Carrera Method | 144 |
| 6.3.3 | The Evolution of the Luminosity Function | 148 |
| 6.4 | The Dust Mass Function | 148 |
| 6.4.1 | The Low-redshift Dust Mass Function | 150 |
| 6.5 | Evolution of the Dust Mass Function | 154 |
| 6.5.1 | Literature Comparisons | 155 |
| 6.6 | Conclusions | 159 |
| 7 | Conclusion | 161 |
| 7.1 | Dust census out to redshift 0.1 | 162 |
| 7.2 | Dust census out to redshift 0.5 | 163 |

| | |
|---------------------------|------------|
| 7.3 Future Work | 165 |
| Bibliography | 167 |

LIST OF TABLES

| | | |
|-----|--|-----|
| 2.1 | Single Schechter function (SSF) values for dust mass functions in the literature and this work. | 56 |
| 3.1 | Single schechter function fit values for dust mass functions resulting from the BBD with the second axis being stellar mass (this Chapter), and for the second axis being r -band magnitude (Chapter 2), both have surface brightness μ on the first axis. We include the density-weighted corrections from W17. | 68 |
| 3.2 | Schechter function fit values for dust mass functions resulting from the simple bootstrap (SB) and perturbed temperature bootstrap (PTB) DMF analysis. The fits include the density-weighted corrections from W17. | 71 |
| 3.3 | Schechter function values for dust mass functions in the literature and this work for single and double DMFs and different methods for deriving the BBD DMF. | 77 |
| 4.1 | Summary of the dust models used in cosmological predictions of the DMF including three models from Popping et al. (2017) and two models from McKinnon et al. (2016, 2017) | 86 |
| 4.2 | Schechter function fit parameters for the pV_{\max} DMFs for the ETG, LTG, and total populations for the low-redshift ($0.002 < z < 0.06$) subset of our sample using morphological classifications from Moffett et al. (2016a) | 97 |
| 4.3 | The ratio $M_{\text{d}}^*/M_{\text{s}}^*$ and $\rho_{\text{d}}/\rho_{\text{s}}$ values for various combinations of dust mass functions derived in this work and stellar mass functions. . . . | 104 |

| | | |
|-----|---|-----|
| 5.1 | The best-fitting SED parameters derived for the stacked galaxies in each of our $L - z$ bins. | 124 |
| 6.1 | The submm catalogue completeness correction (c_s). | 142 |
| 6.2 | The optical catalogue completeness correction (c_r). | 142 |
| 6.3 | The optical ID completeness correction (c_z) | 143 |
| 6.4 | Best fit Schechter values for H -ATLAS luminosity functions. | 150 |
| 6.5 | Comparison of the DMF Schechter functions with literature values for $z < 0.1$ | 151 |
| 6.6 | Best fit Schechter values for H -ATLAS dust mass functions. | 156 |

LIST OF FIGURES

| | | |
|------|--|----|
| 1.1 | A cartoon depicting the baryon components (including bound, unbound, and the unknown or ‘missing’ baryons in the Universe. | 2 |
| 1.2 | The structure of the Hubble tuning fork courtesy of Cappellari et al. (2011). | 4 |
| 1.3 | The structure of the Hubble comb proposed by ATLAS ^{3D} courtesy of Cappellari et al. (2011). | 4 |
| 1.4 | The 2D contours of the rest-frame $g - r$ colours vs. M_r for GAMA galaxies weighted by each galaxies accessible volume, courtesy of Bourne et al. (2012). | 6 |
| 1.5 | The average extinction curves of galaxies in the Local Group (Milky Way: MW, Small Magellanic Cloud: SMC, and Large Magellanic Cloud: LMC) courtesy of Gordon et al. (2003). | 7 |
| 1.6 | Percentage atmospheric transmission for 0.3, 0.6, and 1 mm precipitable water (PWV) for the DOME-C site (Concordiastation/Antarctica) courtesy of Schneider et al. (2009). | 10 |
| 1.7 | The measured values for $\kappa_{500\mu m}$ as a function of publication date, courtesy of Clark et al. (2019). | 16 |
| 1.8 | The dust-to-baryonic mass ratio with gas fraction for local galaxy samples. | 19 |
| 1.9 | Comparison of dust-to-stellar mass with Hubble type based on the 62 ETGs and ~ 300 late type galaxies from the <i>Herschel</i> Reference Survey (HRS, Boselli et al. 2010). | 20 |
| 1.10 | The dust mass function as published in previous works. | 22 |

| | | |
|------|--|----|
| 1.11 | A compilation of the cosmic density of different galaxy components including dark matter and baryons with look back time from Driver et al. (2018) | 24 |
| 1.12 | Multiwavelength coverage available for the GAMA survey, including the location of the three GAMA fields used in this Thesis. | 27 |
| 1.13 | The <i>Herschel</i> ATLAS GAMA fields. | 28 |
| 1.14 | An example of the LAMBDAAR deblending process courtesy of Wright et al. (2017) | 30 |
| 1.15 | An example of the LAMBDAAR sky subtraction process courtesy of Wright et al. (2017) | 31 |
| 1.16 | An example spectral energy distribution (SED) output by the MAGPHYS fitting routine. | 32 |
| 2.1 | <i>Top:</i> Distribution of redshifts for the GAMA sample. <i>Bottom:</i> Redshift distribution of the dust masses for the H-ATLAS/GAMA sample. | 40 |
| 2.2 | The normalized distribution of the cold ISM dust temperature output by MAGPHYS for the low redshift sample ($z \leq 0.1$). | 41 |
| 2.3 | The distribution of uncertainties on the dust mass estimates from MAGPHYS. | 42 |
| 2.4 | The distribution of dust mass and stellar mass in GAMA galaxies. | 43 |
| 2.5 | The bivariate brightness distribution (BBD) for our sample with surface brightness and r -band magnitude as the two "axes" | 46 |
| 2.6 | The maximum effective volumes for our galaxies at $z < 0.1$ derived using the pV_{\max} method (x -axis), and BBD method with r -band magnitude. | 47 |
| 2.7 | The running differential density as a function of redshift for the three GAMA fields taken from W17. DDP is the density defining population. | 50 |
| 2.8 | The fractional error on the volume density of the DMF with dust mass using the different methods for estimating error bars. | 53 |
| 2.9 | The dust mass functions for the GAMA/ <i>H</i> -ATLAS sources at $z < 0.1$ derived using the traditional photometric V_{\max} method (pV_{\max}) and the BBD method. | 54 |

| | | |
|------|--|----|
| 2.10 | Comparison of the DMF from this work with those from the literature. | 57 |
| 2.11 | The confidence intervals for the pV_{\max} single Schechter dust mass function fit parameters derived in this work. | 58 |
| 2.12 | Comparison of the dust mass densities Ω_d from this work with those from the literature. | 59 |
| 3.1 | The BBD for our sample with r -band magnitude and surface brightness as the two ‘axes’ | 64 |
| 3.2 | The maximum effective volumes for our galaxies at $z < 0.1$ derived using the pV_{\max} method (x -axis), and BBD method using stellar mass and surface brightness. | 65 |
| 3.3 | The DMF derived using a stellar mass and surface brightness BBD and an r -band magnitude and surface brightness BBD for the GAMA/ H -ATLAS sources at $z \leq 0.1$ | 66 |
| 3.4 | Testing for biases in cold dust temperatures | 69 |
| 3.5 | The pV_{\max} dust mass functions for the GAMA/ H -ATLAS sources, firstly showing the simple bootstrap (SB) DMF, and secondly the DMF resulting from the perturbed temperature bootstrap (PTB) method shown. | 70 |
| 3.6 | Comparison of the DMFs derived from three samples fit with MAGPHYS where the uncertainties are progressively increased to test the affect of more noise on the output. | 73 |
| 3.7 | The confidence intervals for the pV_{\max} Schechter fits (SF) to the single dust mass function derived in this work as a function of minimum mass chosen for the fit. | 74 |
| 3.8 | Comparison of the single Schechter fit (SSF) with the double Schechter fit (DSF) including the major and minor components. | 75 |
| 3.9 | Testing for Eddington Bias on the DMF | 78 |
| 3.10 | Comparison of the χ^2 confidence intervals resulting from performing the perturbed bootstrap (PB) analysis and non-perturbed bootstrap (non PB) analysis. | 79 |

| | | |
|-----|---|-----|
| 4.1 | A comparison with the predicted $z = 0$ DMFs from Popping et al. (2017) (P17) and McKinnon et al. (2017) (McK17) with the single Schechter fits (SSF) derived from the BBD and pV_{\max} methods. | 87 |
| 4.2 | Comparing the $z = 0$ stellar mass functions for the GAMA sources (Wright et al., 2017) with that derived using the SAMs of Popping et al. (2017). | 88 |
| 4.3 | The dust to stellar mass ratio for galaxies in the local Universe. | 89 |
| 4.4 | The mean dust to stellar mass ratio for galaxies in our high and low redshift samples | 94 |
| 4.5 | The pV_{\max} dust mass functions for the GAMA/ <i>H</i> -ATLAS sources at $0.002 < z < 0.06$ for ETGs and LTGs. | 95 |
| 4.6 | Testing the affect on the DMF of including little blue spheroids. | 99 |
| 4.7 | The pV_{\max} dust mass functions for the GAMA/ <i>H</i> -ATLAS sources at $0.002 < z < 0.06$ | 103 |
| 4.8 | The pV_{\max} dust mass functions for the GAMA/ <i>H</i> -ATLAS sources at $0.002 < z < 0.06$ and $0.06 < z < 0.1$ | 105 |
| 5.1 | A comparison of the redshift estimates considered in this work. | 111 |
| 5.2 | A comparison of the redshift estimates found by the KiDS team using ANNz2 and MLPQNA for the sources without a spectroscopic redshift. | 112 |
| 5.3 | The MAGPHYS dust masses as a function of the $250 \mu\text{m}$ luminosity | 116 |
| 5.4 | The fraction of galaxies with a MAGPHYS dust mass from Eales et al. (2018) as a function of redshift. | 117 |
| 5.5 | MAGPHYS cold temperatures as a function of redshift, and $250 \mu\text{m}$ luminosity. | 118 |
| 5.6 | The 1D and 2D projections of parameter probability distributions from SED fitting. | 122 |
| 5.7 | The observed $100 \mu\text{m}/160 \mu\text{m}$ and $250 \mu\text{m}/350 \mu\text{m}$ colours for the <i>H</i> -ATLAS sample stacked SEDs. | 123 |
| 5.8 | The fraction of sources with at least one PACS detection as a function of redshift. | 125 |
| 5.9 | Stacked luminosity SEDs for the $L - z$ bins in the lowest redshift slice in the sample. | 126 |

| | | |
|------|---|-----|
| 5.10 | Stacked luminosity SEDs for the higher redshift slices. | 127 |
| 5.11 | Comparison of the one and two temperature component results for stacked SEDs. | 129 |
| 5.12 | The mass-weighted temperature from the best-fitting (stacked) SEDs as a function of the 250 μm luminosity and dust mass. | 131 |
| 5.13 | The 250 μm luminosities for the <i>H</i> -ATLAS sample as a function of redshift. | 132 |
| 5.14 | The distribution of MAGPHYS based dust masses and 2C stacked dust masses at $z < 0.1$ | 133 |
| 5.15 | The difference between the MAGPHYS based dust masses and the 2C stacked dust masses as a function of 250 μm luminosity for $z < 0.1$ (top) and $z < 0.5$ (bottom). | 134 |
| 5.16 | L_{100}/L_{160} and L_{250}/L_{500} as a function of redshift for the stacked SEDs | 136 |
| 6.1 | A cartoon showing the difference between the V_{max} and PC00 methods taken from PC00. | 145 |
| 6.2 | The evolution of the 250 μm LF as a function of redshift for the <i>H</i> -ATLAS sample | 147 |
| 6.3 | The evolution of ρ_L as a function of redshift for the <i>H</i> -ATLAS sample. | 149 |
| 6.4 | The dust mass functions for the <i>H</i> -ATLAS sources at $z < 0.1$ derived using the PC00 method. | 152 |
| 6.5 | Comparison of the low-redshift dust mass densities Ω_d from the <i>H</i> -ATLAS sample with those from the literature. | 153 |
| 6.6 | The evolution of the DMF as a function of redshift for the <i>H</i> -ATLAS sample. | 157 |
| 6.7 | The evolution of Ω_d as a function of redshift for this work compared to D11. | 158 |
| 6.8 | The evolution of ρ_d as a function of redshift for this work compared to the literature. | 159 |

CHAPTER 1

INTRODUCTION

‘In the beginning the Universe was created. This has made a lot of people very angry and been widely regarded as a bad move.’

DOUGLAS ADAMS

At the most basic level, galaxies consist of the following baryonic components: supermassive black holes, stars, interstellar medium (which in turn consists of dust, metals, neutral gas and molecular gas), and the circumgalactic medium. Figure 1.1 shows a cartoon of the baryon budget from [Driver et al. \(2018\)](#), including bound and unbound baryon components. The interstellar medium (ISM) of galaxies is a blanket term for everything between stars within galaxies. Estimates of the mass of gas provide a measure of the fuel available for future star formation. The star formation rate of galaxies in the nearby Universe is approximately 20 times lower than those at redshifts of 2 (normalised by stellar mass). This suggests that there is a ‘peak’ of star formation activity at $z \sim 2$ ([Daddi et al., 2007](#); [Karim et al., 2011](#); [Madau & Dickinson, 2014](#)). The HI mass is thought to have plateaued in recent cosmic history ([Wilkins et al., 2008](#)), though the molecular gas mass (observed using CO as a tracer for H₂) is observed to be declining with time ([Walter et al., 2014](#); [Tacconi et al., 2013](#); [Combes, 2018](#)).

Cosmic dust is a significant, albeit small, component of the ISM of galaxies. Despite only making up $\sim 0.1\%$ of the baryonic mass of a galaxy ([Vlahakis et al., 2005](#); [Dunne et al., 2011](#); [Clemens et al., 2013](#); [Beeston et al., 2018](#); [Driver et al., 2018](#)), dust is responsible for obscuring the ultraviolet and optical light from stars and active galactic nuclei, and is thought to have absorbed approximately half of

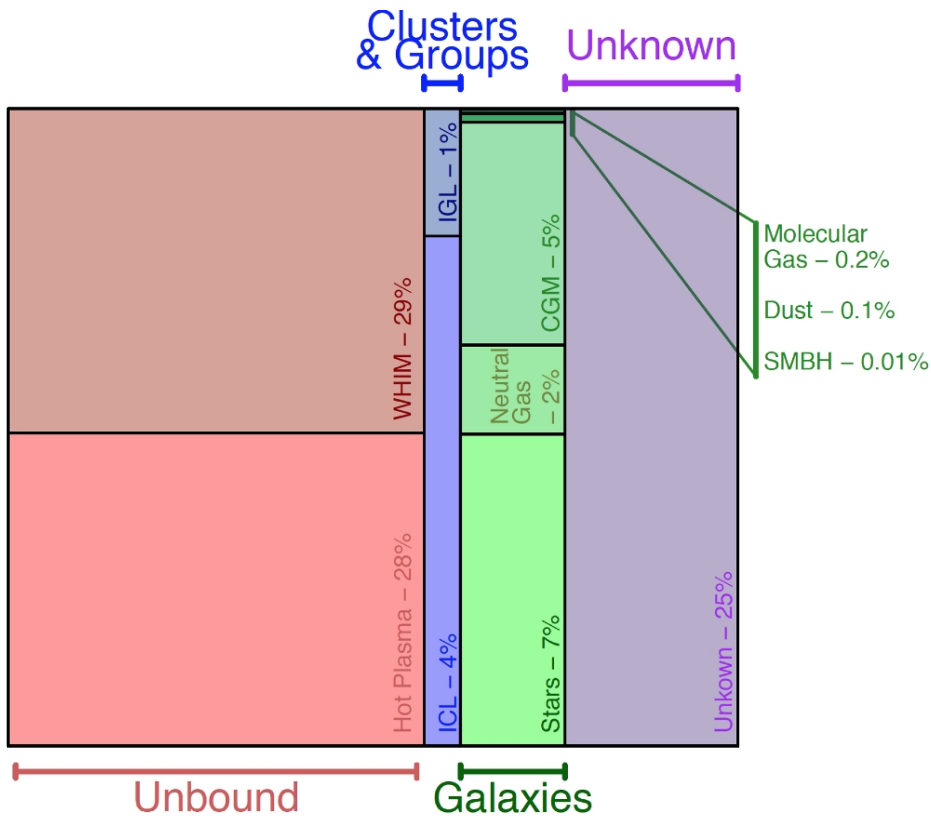


FIGURE 1.1 A cartoon depicting the baryon components (including bound and unbound and the unknown or ‘missing’ baryons, [Shull et al. 2012](#)) in the Universe, including gas, dust, metals and stars. This figure is taken from [Driver et al. \(2018\)](#). WHIM: warm ionised intergalactic medium, ICL: intracluster light. CGM: circumgalactic medium. SMBHs: supermassive black holes.

the starlight emitted since the Big Bang ([Puget et al., 1996](#); [Fixsen et al., 1998](#); [Dole et al., 2006](#); [Driver et al., 2016](#)). Measuring the dust mass in galaxies is therefore important for understanding obscured star formation ([Kennicutt, 1998](#); [Calzetti et al., 2007](#); [Marchetti et al., 2016](#)), particularly at different cosmic epochs ([Madau et al., 1998](#); [Hopkins, 2004](#); [Takeuchi et al., 2005](#)), and as a reservoir of heavy elements in galaxies. The use of dust emission to trace the interstellar medium, and thus the fuel available for star formation, has gained widespread interest in recent years, given the difficulties in observing atomic and molecular-line gas mass tracers out to high redshifts ([Tacconi et al., 2013](#); [Catinella & Cortese, 2015](#)). The advantage of using dust emission as a tracer of the ISM is that one can quickly derive gas masses for large numbers of galaxies: with far-infrared measurements available for millions of galaxies across large areas of the sky ([Eales et al., 2009](#); [Dunne et al., 2011](#); [Driver et al., 2018](#)), and with ALMA, one can detect the dust continuum in galaxies in a matter of minutes ([Scoville et al., 2016](#)). One can potentially use the dust emission to therefore probe the gas mass fraction in galaxies at more distant

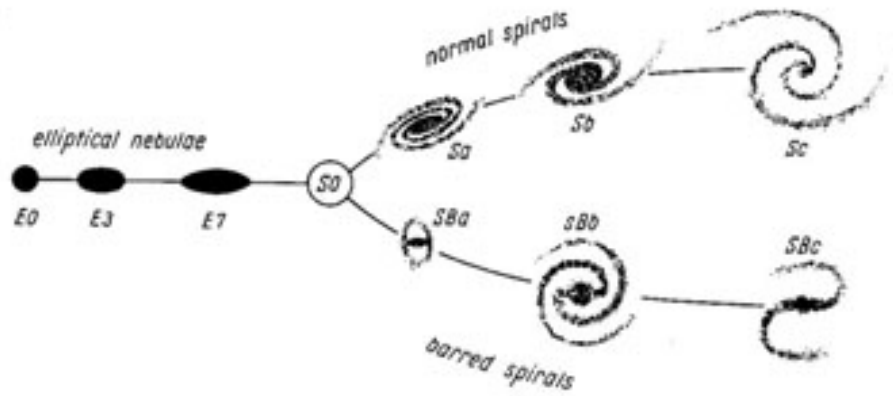
epochs such as the ‘peak of star formation’ (Hopkins, 2004), and over a larger fraction of the history of the Universe compared to direct CO or HI measurements. The cosmic dust density (Dunne et al., 2011) (which can obscure current star formation) has been shown to be declining rapidly over the past five billion years, potentially driven by a decline in the cosmic star formation history (Hopkins & Beacom, 2006; Madau & Dickinson, 2014). However, until very recently, studies measuring the dust content and evolution of the Universe have been limited due to small number statistics, or over too small an area to overcome large uncertainties due to cosmic variance (see e.g. Driver & Robotham, 2010). In this Thesis, we aim to quantify the evolution of the dust content over recent cosmic history using large area, homogeneous surveys of the Universe. In this Chapter, some of the context for this work will be reviewed.

1.1 GALAXIES

The number of bright galaxies (brighter than $7.1 \times 10^9 L_{\odot}$ in the B band) in the observable Universe is thought to be upwards of 100 billion (Gott III et al., 2005). A sample so vast calls for a classification scheme in order to probe possible causes of, or connections between, the properties they possess. It is also potentially very important for the study of galaxy evolution since all that we can draw on is essentially one timestamp of the Universe, making statistical studies the main and most important tool in extragalactic astronomy surveys.

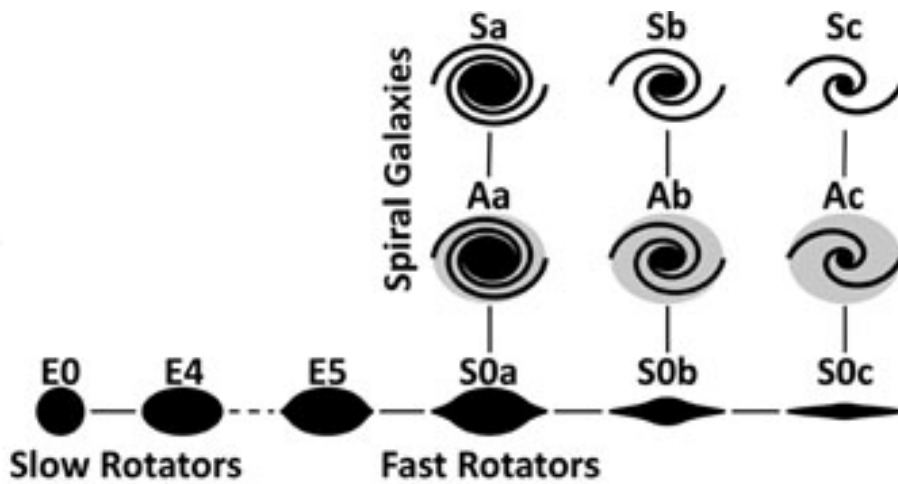
There have been many attempts to introduce universally acceptable classification schemes, but the idea of the Hubble tuning fork (Hubble, 1926) (Figure 1.2) remained largely unchallenged since its conception until the ATLAS^{3D} project (Cappellari et al., 2011). ATLAS^{3D} pioneered a new classification system called the Hubble comb (Figure 1.3), which is based on the quantifiable kinematics of a galaxy, rather than its visual appearance. The most fundamental improvement offered by the Hubble comb rather than the tuning fork is that visual classifications of galaxies are fundamentally subjective whereas the Hubble comb is entirely quantitative. ATLAS^{3D} argue that their system of splitting galaxies into fast and slow rotators is more physically meaningful than the optical-based morphological classifications into ellipticals (Es) and lenticulars (S0s).

Visual morphology is not the only galaxy property where it appears that two main classes emerge. This dichotomy is also present in the optical colour of galaxies, with late-type galaxies (LTGs) having much bluer optical colours than



Hubble (1936) tuning fork

FIGURE 1.2 The structure of the Hubble tuning fork courtesy of Cappellari et al. (2011).



The ATLAS^{3D} comb

FIGURE 1.3 The structure of the Hubble comb proposed by ATLAS^{3D} courtesy of Cappellari et al. (2011).

the typically passive early-type galaxies (ETGs). LTGs are more actively star forming than later types, and stars produce more UV radiation early in their lifetime, which accounts for the bluer colours of these galaxies. Some studies ([Driver et al., 2012](#); [Moffett et al., 2016a](#)) have identified galaxies with ETG-like spheroidal morphology, but with optically blue colours which are more typical of LTGs. These galaxies, dubbed “little blue spheroids” (LBS), could represent a population which is physically different from either ETG or LTG. It is also possible that these galaxies are actually late-types with their structure obscured by poor resolution, particularly with increasing distance.

As seen in Figure 1.4 ([Bourne et al., 2012](#)), there is a dichotomy in the $g - r$ colours of optically selected galaxies, namely red sequence and blue cloud galaxies. Between these two populations we see an underpopulated region known as the green valley, which are assumed to be the overlapping lobes of two Gaussian distributions at any given r -band magnitude. This hints towards the process of transitioning between either population to the other being very swift, with little time spent in the green phase. It is generally agreed that the blue LTGs evolve towards the red sequence of ETGs. One might expect that galaxies would gradually deplete their supply of gas and dust through star formation with no clear quenching of the star formation in a galaxy. This paradigm would give a slow decline in star formation, indicating that some other force may be at work to aid the evolution of galaxies. We also see that there are many giant ellipticals which are embedded in a large reservoir of hot gas, but which remain passive, further pointing to another driver of galaxy evolution. Mechanisms proposed to explain the rapidity of galaxy evolution include the influence of external forces, or rather the interaction of multiple galaxies. The interaction of galaxies can range from full mergers of galaxies, to galaxies passing close by one another and experiencing a gravitational disturbance. A strong correlation between environmental density and optical colours has been observed in the literature (e.g. [Butcher & Oemler, 1984](#); [Pimblet et al., 2002](#); [Goto et al., 2003](#); [Bamford et al., 2009](#)). Where there are more galaxies located near to one another, interactions and mergers become far more likely. We also see more early-types in the cluster environment, i.e. galaxies in clusters are generally more evolved than those outside clusters, where interactions are less common.

1.2 COSMIC DUST

The topic of cosmic dust is a relatively new field of study in astronomy given the difficulties of observing it (see Section 1.3), it wasn't until the 1800s that

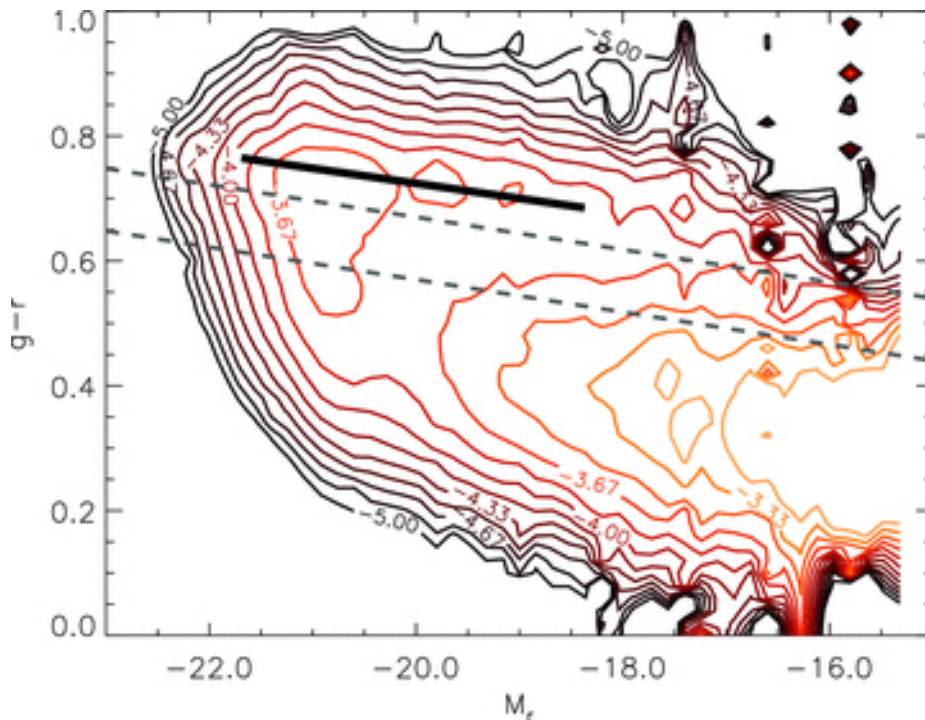


FIGURE 1.4 The 2D contours of the rest-frame $g - r$ colours vs. M_r for GAMA galaxies weighted by each galaxies accessible volume, courtesy of Bourne et al. (2012).

the idea that interstellar space may not be empty was posited (Herschel, 1811). Struve (1847) unknowingly published the first evidence for the existence of dust, observing that the number count of stars appeared to decrease with distance. We now attribute this to the obscuration of light by dust, the further light has to travel, the more dust it has to travel through, and the dimmer it will appear. At the time no explanation for why this was being observed was given, and it wasn't until the early 20th Century that the idea that stars could be being dimmed by some medium residing between stars and Earth-bound observers was really explored (e.g. Barnard 1907, 1910; Kapteyn 1909). The idea was controversial though, and did not gain traction until Trumpler (1930) showed that the inverse square law was not sufficient to explain the dimming observed in stars and open clusters, even going so far as to conclude that "fine cosmic dust particles" could be responsible.

Cosmic dust is essentially a blanket term for molecules and debris that exists between stars, and includes anything from single molecules to larger grains. Dust therefore spans a wide range of sizes anywhere from ~ 10 nm to ~ 1 μ m (Kim & Martin, 1994a,b). The composition of dust is also varied from large single molecules such as polycyclic aromatic hydrocarbons (e.g. Draine & Li, 2007, PAHS), to small soot-like grains of silicates or graphite (see e.g. Duley & Seahra 1998 and references therein). Figure 1.5 shows the average extinction curves for our galaxy,

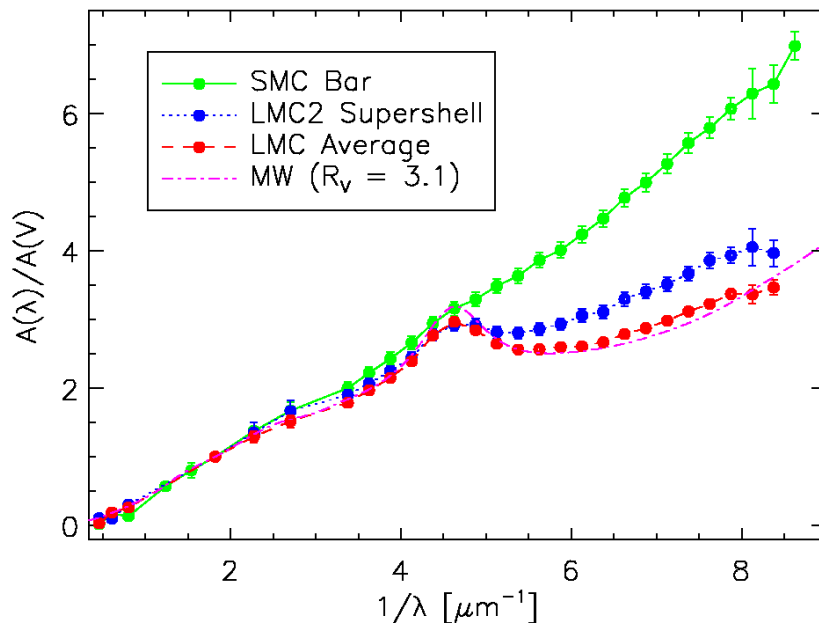


FIGURE 1.5 The average extinction curves of galaxies in the Local Group (Milky Way: MW, Small Magellanic Cloud: SMC, and Large Magellanic Cloud: LMC) courtesy of [Gordon et al. \(2003\)](#).

and the Magellanic Clouds, from which it is immediately apparent that there is a significant bump at around 2000 \AA ([Gordon et al., 2003](#)). The grains which form this bump are assumed to arise from a common formation process and be more robust to destruction mechanisms than other types of grain or molecule. Theoretical models have predicted that this feature is associated with small graphite grains that have a radius of around 20 nm ([Stecher & Donn, 1965](#); [Gilra, 1972](#)).

1.2.1 THE PRODUCTION OF DUST

A large portion of the metals in the Universe are locked up in cosmic dust. In the Early Universe only hydrogen, helium, and lithium were available, the metals required to form dust were created much later through the life cycle of stars. After a star has left the main sequence and used up the lightest elements during the triple-alpha process and CNO cycle it is forced to fuse heavier and heavier elements to continue to fuel itself. The relevance of various processes by which dust then forms is widely debated. Three main sources are generally expected to be relevant: the stellar winds of evolved low-to-intermediate-mass stars (LIMS) such as asymptotic giant branch (AGB) and red giant branch (RGB) stars, supernovae (SNe), and dust grain growth in the ISM.

The outer envelopes of evolved LIMS are thought to be an ideal environment in which to form dust, they are enriched with metals by the star, have high number-densities allowing ample opportunity for chemical reactions to form dust, and have generally low enough temperatures (~ 1000 K) for dust to survive and the grains to grow (e.g. [Carroll & Ostlie 1996](#); [Salpeter 1974](#)). Once the dust grains reach some critical size, they will be swept out into the general ISM by the stellar wind. Many studies have argued that the majority of dust is formed in stellar winds of LIMS (e.g. [Ferrarotti & Gail 2006](#); [Sargent et al. 2010](#)), particularly at higher redshifts (e.g. [Valiante et al. 2009](#); [Dwek & Cherchneff 2011](#)). Other works have reported a “Dust Budget Crisis” however, showing that it is very difficult to explain the high dust masses observed at high redshifts with dust from LIMS only ([Morgan & Edmunds, 2003](#); [Dwek et al., 2007](#); [Michałowski et al., 2010a,c](#); [Santini et al., 2010](#); [Gall et al., 2011](#); [Valiante et al., 2011](#)). It is also pointed out by e.g. [Morgan & Edmunds \(2003\)](#) that since large quantities of dust are observed in galaxies at $z > 5$, it is unclear how these stars could produce quite so much dust in a short space of time, and that a more rapid dust production mechanism for these high redshift galaxies is required ([Zafar & Watson, 2013](#)). [Valiante et al. \(2009\)](#) and [Dwek & Cherchneff \(2011\)](#) do find that AGB stars could be significant contributors to dust in the ISM after only 150-500 Myr, but the dust production rate in these scenarios is highly dependent on the initial mass function (IMF) used in the calculation.

Supernovae (SN) can provide a much more immediate dust injection than LIMS, and as such have been thought to be a dominant source of dust at higher redshifts (e.g. [Dunne et al. 2003b](#); [Morgan & Edmunds 2003](#); [Dwek et al. 2007](#); [Dunne et al. 2009](#); [Gall et al. 2011](#)). SN1987A, Cas A, and the Crab nebula have provided observations which show evidence of dust formation in the ejecta of SN. It appears that significant amounts of dust can be formed as a consequence of these incredibly explosive events, with masses up to $\sim 1 M_{\odot}$ of dust being reported (see e.g. [Dunne et al. 2003a](#); [Sugerman et al. 2006](#); [Matsuura et al. 2011](#); [Gomez et al. 2012](#); [Temim et al. 2012](#); [Matsuura et al. 2015](#); [Chawner et al. 2019](#) and references therein). That SN can and do produce large quantities of dust is widely accepted, what remains controversial, though, is whether the dust produced during the SN event can survive very long afterwards. The powerful shocks following a SN are so high energy that nearly all of the dust from the SN may in fact be quickly destroyed by these shocks ([Bianchi & Schneider, 2007](#); [Kozasa et al., 2009](#); [Jones & Nuth, 2011](#)).

The final mechanism by which the dust mass of the ISM can increase is by

grain growth in the ISM at all redshifts (see e.g. [Dwek et al. 2007](#); [Draine 2009](#); [Michałowski et al. 2010b](#); [Valiante et al. 2011](#); [Dunne et al. 2011](#); [Asano et al. 2013b](#); [Rowlands et al. 2014](#)). Dust grains grow in size and mass by acquiring an ice mantle onto which metals present in the ISM can condense, the captured metals can then adsorb onto the surface of the dust grain (e.g. [Tielens & Allamandola 1987](#); [Blain 2004](#); [Ormel et al. 2011](#)).

There are several methods by which dust can be destroyed or removed from a galaxy apart from by supernovae shocks (as discussed earlier). While collisions between particles can result in accretion onto the dust grain (i.e. the grain growth process), if the intruding particle has sufficiently high energy it can cause the dust grain to be broken down (see e.g. [Blain 2004](#)). This process is called sputtering, and is especially important in high density parts of the ISM. Dust can be carried out of galaxies by outflows in cases where it is coupled to the gas phase (see e.g. [Roth et al. 2012](#); [Heckman 2003](#) and references therein). Gravitational interactions between galaxies (either mergers or two galaxies passing close by one another) can lead to mass loss in the general ISM ([White & Rees, 1978](#); [Navarro et al., 1995](#); [Larson et al., 1980](#); [Bekki & Couch, 2011](#)).

1.2.2 CHEMICAL MODELLING OF DUST

Many attempts have been made to find a simple model for how the metals, gas, and dust in a galaxy evolve over time (e.g. [Popping et al. 2014, 2017](#); [Rowlands et al. 2014](#); [Somerville et al. 2015](#); [McKinnon et al. 2016, 2017](#); [De Vis et al. 2017b](#)). The most fundamental building blocks of chemical evolution modeling are: the IMF (see [Chabrier 2005](#) and references therein) of stars, a star formation history model (e.g. [Yin et al. 2009](#); [Lee et al. 2010](#)), and dust formation rates based on the formation and destruction mechanisms described in Section 1.2.1. The amount of dust produced and destroyed over the lifetime of a galaxy is essentially fine-tuned using a sample of galaxies across different redshifts in order to reflect the observed dust masses. Generally the metals produced by stars are tracked, and an efficiency measure for their conversion into dust grains is employed. Some models will use a “closed box” approach, where no matter is allowed to enter or leave the galaxy after the initial conditions are set (e.g. [Clark et al. 2015](#)). Most models these days do allow inflows and outflows however, since while this is computationally more expensive, it is also more realistic (e.g. [Morgan & Edmunds 2003](#); [Zhukovska & Henning 2014](#); [Rowlands et al. 2014](#); [De Vis et al. 2017b](#)). In Chapter 4 we will compare the statistical distributions of the dust masses of galaxies observed in the

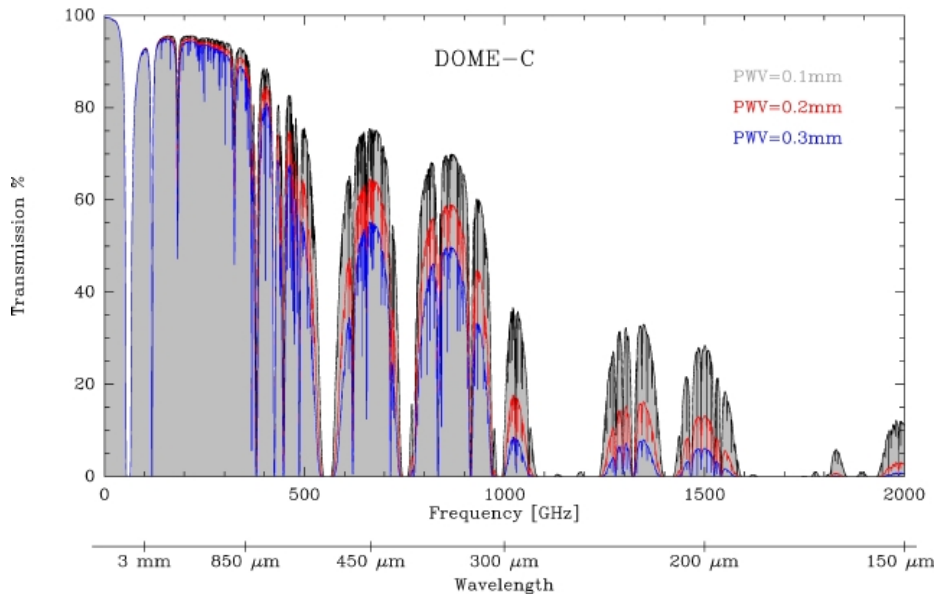


FIGURE 1.6 Percentage atmospheric transmission for 0.3, 0.6, and 1 mm precipitable water (PWV) for the DOME-C site (Concordiastation/Antarctica) courtesy of [Schneider et al. \(2009\)](#).

Universe to those found by using theoretical models.

1.3 OBSERVING DUST IN GALAXIES

Far-infrared (FIR) and submillimetre (sub-mm) astronomy is very difficult with ground-based instruments due to the interference of molecules in the atmosphere, mainly O_2 and H_2O . At certain locations at high altitude which are very dry, it is possible to observe select windows in the FIR and sub-mm regime. These windows can be seen in Figure 1.6 ([Schneider et al., 2009](#)). There are ground-based telescopes which capitalise on these windows into the FIR/sub-mm Universe, such as the Sub-millimetre Common-User Bolometer Array (SCUBA, [Holland et al. 1999](#)), and its successor SCUBA-2 ([Holland et al., 2013](#)), both situated at high-altitude on Mauna Kea.

Since observing in this regime is so limited using Earth-bound telescopes, there have been multiple space-based missions to investigate this tricky region of the light spectrum. The first of these, the Infrared Astronomical Satellite (IRAS, [Neugebauer et al. 1984](#)), was launched in 1983, and came very close to mapping the entire sky during its lifetime. IRAS took measurements at 12, 25, 60 and 100 μm for 96% of the sky, providing an unprecedented amount of knowledge about the dusty Universe, and it paved the way for future missions. One such mission was the

Spitzer Space Telescope (*Spitzer*, [Werner et al. 2004](#)) which was launched in 2003, and can observe wavelengths between 3 and 180 μm . Major advances in the study of dust came with the launch of the *Herschel Space Observatory*, which we will discuss in the next Section.

1.3.1 THE *Herschel* SPACE OBSERVATORY

The advent of the *Herschel Space Observatory* (hereafter *Herschel*, [Pilbratt et al. 2010](#)) and the *Planck* Satellite revolutionised studies of dust in galaxies, as they enabled greater statistics, better sensitivity and angular resolution in some regimes, wider wavelength coverage and the ability to observe orders of magnitude larger areas of the sky than possible before. *Herschel* was the culmination of decades of work, with the design first being proposed in 1982, and finally selected in 1993 as one of the cornerstone missions of ESA. *Herschel* had the largest mirror ever sent into space at 3.5 m, twice the collecting area of Hubble Space Telescope. A large collecting area was imperative because resolution is of the order 1000 times worse than optical wavelengths at FIR/sub-mm regime. Better angular resolution helps with confusion noise, which is a bigger problem for FIR/sub-mm than optical because of negative k-correction. Negative k-correction is the effect whereby objects at high z are just as easily visible as low z at sub-mm wavelengths because the SED shape of higher redshift sources peaks at longer wavelengths in the observed frame. While this means that it makes it harder to determine whether flux is associated with a single specific object, it also means we can more easily probe the earlier Universe than by using optical wavelengths.

Herschel launched in 2009, and used cryogenic cooling which limited its lifetime to however long the liquid Helium could be conserved for, which was until 2013, giving *Herschel* nearly four years of observing time. The majority of *Herschel* was kept at around 1.7 K, but the detectors were much cooler at 300 mK in order to keep instrumental noise to a minimum. Low temperatures are very important at long wavelengths as the temperatures of the blackbodies that are being probed are low, so the more emission from the instrument itself that can be eradicated, the better. The highest temperature part of *Herschel* was the primary mirror at around 85 K, and therefore this was the largest source of instrumental noise in *Herschel* observations.

Herschel comprised 3 instruments, a dedicated spectrometer the *Herschel*-Heterodyne Instrument for the Far-Infrared (HIFI, [de Graauw et al. 2010](#)), and two instruments with both a spectrometer and photometer on board: the Photodetector

Array Camera and Spectrometer (PACS, [Poglitsch et al. 2010](#)), and the Spectral and Photometric Imaging Receiver (SPIRE, [Griffin et al. 2010](#)). In this Thesis we only use photometric measurements from *Herschel* from both PACS and SPIRE.

1.3.1.1 SPIRE

The SPIRE photometer observed in three wavebands with central wavelengths of 250, 350, and 500 μm . The choice of these wavebands were calculated to sample the Rayleigh-Jeans slope of cold interstellar dust ($< \sim 30$ K). This meant that *Herschel* could more accurately determine cold dust temperatures than any other instrument that had come previously.

Traditionally, photometric measurements are taken by exploiting photoconductivity, whereby a captured photon is absorbed by the detector, which has a band gap of the same energy as the photon. For such low-energy photons as those in the FIR/sub-mm, though, there is no viable material with such a small band gap. Instead, SPIRE uses bolometry to measure incident light. The bolometer consists of a very low temperature element, which absorbs the light and then heats up very slightly. The small changes in temperature have a measurable effect on the resistive properties of the absorbing element, which allow the intensity of light to be measured by a well-calibrated and well-characterised bolometer.

The three SPIRE wavebands can all be measured concurrently; indeed, simultaneous measurements from both PACS and SPIRE are possible. The field of view of SPIRE is $8' \times 4'$, and sampling is performed by taking continuous observations whilst scanning across the target area. Depending on the type and size of the intended observations, there are different methods by which the mapping occurs. For individual point sources, or those which are not very extended, there was a small map mode, which covered a $5'$ patch of sky at a scanning speed of $30''\text{s}^{-1}$. For larger target areas there was a large map mode, which allowed the choice of two scanning speeds ($30''\text{s}^{-1}$ or $60''\text{s}^{-1}$) depending on the desired depth of the map. Parallel mode, during which observations are also made using PACS, allows scanning speeds of either $20''\text{s}^{-1}$ or $60''\text{s}^{-1}$. Parallel mode at the faster scanning speed of $60''\text{s}^{-1}$ was the mapping method of the *Herschel*-ATLAS survey, the largest open time survey of the FIR sky with *Herschel* ([Eales et al., 2010](#), Section 1.5.2).

1.3.1.2 PACS

PACS is the other *Herschel* instrument upon which the work in this Thesis relies. PACS is both a spectrometer and photometer, and as for SPIRE we only use photometric data. PACS covers the wavelength range 55–210 μm , and so can provide coverage for the peaks of typical cold dust emission. Like SPIRE, the PACS photometer uses bolometry to measure FIR fluxes, and covers three wavebands centred on 70, 100, and 160 μm . PACS only has two bolometer arrays however, and so cannot observe at 70 and 100 μm simultaneously. Similar to the SPIRE instrument, PACS has two scanning speeds, a standard speed of $20''\text{s}^{-1}$, or a fast mapping speed of $60''\text{s}^{-1}$. Once again, the *H-ATLAS* survey used the faster scanning speed to make their maps, and they opted only to collect data at 100 and 160 μm .

1.3.2 DERIVING DUST MASSES FOR GALAXIES

Using *Herschel*, we can study and characterise the emission of dust in the FIR and sub-mm. In order to do this we consider dust to emit as a modified blackbody.

According to Kirchhoff's law (Kirchhoff, 1860), for a body in thermal equilibrium with its surroundings, at a given frequency ν , the rate of absorption and emission of radiation for a body are equal. Therefore, we can infer that the rate of emission of energy by dust is equivalent to the rate of energy absorption by the local radiation field. The spectrum of a blackbody at temperature T as a function of frequency ν is described by the Planck function:

$$B(\nu, T) = \frac{2h\nu^3}{c^2} \frac{1}{e^{h\nu/k_{\text{B}}T} - 1}, \quad (1.1)$$

where B is the Planck function spectral radiance, h is the Planck constant, c is the speed of light, and k_{B} is the Boltzmann constant. The temperature of a blackbody can be determined using the Stefan-Boltzmann law:

$$T^4 = \frac{Uc}{4\sigma}, \quad (1.2)$$

where U is the energy density of the local radiation field, and σ is the Stefan-Boltzmann constant.

Dust is not a perfect blackbody emitter, and so we must modify the Planck function to reflect this imperfection in emission efficiency. The disparity in efficiency of the emission can be quantised as Q_{ν} , which is simply the ratio of the

emitting power of an imperfect blackbody to that of a perfect one at the same given temperature and frequency. For emission in the FIR and sub-mm, Q_ν is given by:

$$Q_\nu \propto \nu^\beta, \quad (1.3)$$

where β is the dust emissivity spectral index, and is subject to the chemical composition and size of the dust grains. Generally, β for dust in galaxies is considered to lie in the range 1-2.2. For a modified blackbody, the observed flux density S_ν (in units of Jy) is given by:

$$S_\nu \propto \nu^\beta B(\nu, T) \quad (1.4)$$

To infer properties of the dust in a galaxy, it is generally assumed that the dust exists in spherical grains with radius a in a cloud of uniform density ρ . The mass of such a cloud containing n dust grains is given by:

$$M_d = \frac{4}{3}\pi a^3 \rho n \quad (1.5)$$

where $\frac{4}{3}\pi a^3$ is the volume of the grain. Given that we assume Kirchhoff's law holds, the grains will be in radiative equilibrium, and we can therefore describe the radiative transfer of dust by:

$$I_{\text{UA}}(\nu) = (1 - e^{-\tau_\nu})B(\nu, T) \quad (1.6)$$

where $I_{\text{UA}}(\nu)$ is the spectral radiance per unit cross-sectional area of the cloud as a function of ν , and τ_ν is the optical depth at a given frequency. Dust grains are generally assumed to be much smaller the wavelengths at which they emit, allowing the assumption that the dust is optically thin, ergo the optical depth $\tau_\nu \ll 1$, and so:

$$I_{\text{UA}}(\nu) \simeq \tau_\nu B(\nu, T). \quad (1.7)$$

Optical depth can be calculated by:

$$\tau_\nu = \pi a^2 Q_\nu N = \pi a^2 Q_\nu \frac{n}{A} \quad (1.8)$$

where πa^2 is the cross-sectional area of the grains, N is the column density given by $N = n/A$, where A is the cross-sectional area of the dust cloud. Using Equations 1.7 and 1.8, we can find I_{UA} :

$$I_{\text{UA}}(\nu) = \pi a^2 N Q_\nu B(\nu, T) \quad (1.9)$$

or the spectral radiance over the whole cross-sectional area $I(\nu)$:

$$I(\nu) = \pi a^2 n Q_\nu B(\nu, T) \quad (1.10)$$

We can then find the observed flux density at frequency ν , $S(\nu)$, which falls away from the intrinsic spectral radiance as D^2 , where D is the distance from the cloud to the observer, giving:

$$S(\nu) = \frac{\pi a^2 n Q_\nu B(\nu, T)}{D^2} \quad (1.11)$$

which we can then put in terms of n and substitute into Equation 1.5 to find:

$$M_{\text{d}} = \frac{4a\rho S(\nu)D^2}{3Q_\nu B(\nu, T)} \quad (1.12)$$

Several of these terms are either very poorly constrained, or are unlikely to be well-represented by the assumptions made during the derivation of this relationship. It is not possible to measure the distribution of size and density of the dust grains in distant galaxies, nor the parameter Q_ν , which is dependent on myriad physical properties of the dust grains - the chemical composition, size, shape, etc. The assumption that all grains in a cloud are composed in the same way is also very unlikely. This introduces an uncertainty in the dust masses that are measured through observations of the IR spectrum, even when the shape of the SED of the observed dust is well-constrained. The parameters which are highly uncertain are generally grouped into one parameter: the dust mass absorption coefficient: κ_ν . κ_ν is given by:

$$\kappa_\nu = \frac{3Q_\nu}{4a\rho} \quad (1.13)$$

giving:

$$M_{\text{d}} = \frac{S(\nu)D^2}{\kappa_\nu B(\nu, T)} \quad (1.14)$$

Estimations of κ_ν vary, with measurements of κ_{500} having a range of 3.6 orders of magnitude and an overall standard deviation of 0.8 (Clark et al., 2019). To further illustrate the uncertainty in this parameter we show the literature of κ_{500} as a function of publication date in Figure 1.7 (Clark et al., 2019). Generally κ_ν is

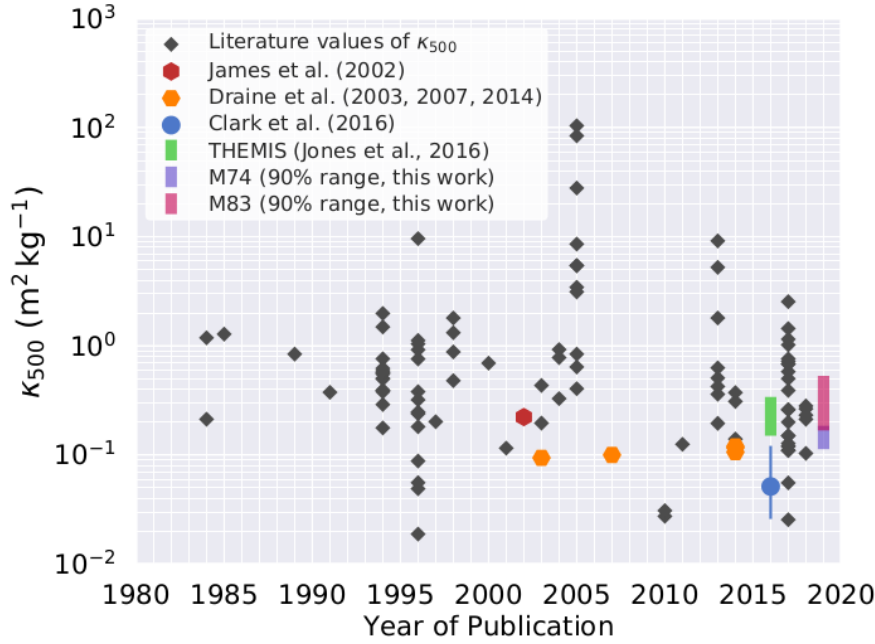


FIGURE 1.7 The measured values for $\kappa_{500 \mu m}$ as a function of publication date, courtesy of Clark et al. (2019).

extrapolated by a measurement of κ_{REF} obtained at a reference frequency ν_{REF} :

$$\kappa_\nu = \kappa_{\text{REF}} \left(\frac{\nu}{\nu_{\text{REF}}} \right)^\beta \quad (1.15)$$

In this work the James et al. (2002) value of $\kappa_{850 \mu m}$ is used ($0.077 \text{ m}^2 \text{ kg}^{-1}$). The method they use to estimate κ_d is to assume that the ratio of dust to metals (ϵ_d) in the ISM has a known and constant value for all galaxies. Using the measured ISM mass of a galaxy and the metallicity of the ISM, one can easily calculate the total mass of interstellar metals in a given galaxy. The constant ϵ_d can be used to estimate the dust mass from the metal mass, giving an estimate of dust mass which is independent of any dust emission. The combination of the observed dust emission and this independent measure of the dust mass can then be used to effectively calibrate κ_d to the dust SED. This method is only valid if we can assume that all galaxies across all types, redshifts, and environments will have the same dust-to-metal ratio. Most measurements of ϵ_d lie in the range $0.2 - 0.6$, which introduces a potential error of a factor of 3 between different galaxy types (Clark et al., 2019). This seems large, but given that the uncertainty in κ is many orders of magnitude, ϵ_d is actually far better constrained, so it is probably safe to use a single value of κ_d without introducing too much bias.

1.3.3 *Herschel* OBSERVATIONS OF DUST IN GALAXIES

In the case where FIR and sub-mm information is either not present or not strongly detected enough to draw meaningful conclusions about the dust properties of a galaxy, some studies have sought to derive dust scaling relations. Scaling relations are generally between dust mass and either stellar mass or star formation rate (e.g. [Lianou et al. 2016](#); [Genzel et al. 2015](#); [Beeston et al. 2018](#)), but scaling relations between dust and CO have also been studied (e.g. [Genzel et al. 2015](#)). Dust scaling relations can often recover dust masses fairly well, but caution must be used since dust scaling relations also seem to be dependent on factors such as galaxy type ([Lianou et al., 2016](#)) or redshift ([Genzel et al., 2015](#)).

In order to improve the reliability of dust property estimations made for galaxies with poor FIR and sub-mm constraints [Bourne et al. \(2012\)](#), hereafter B12, performed a stacking analysis to find trends in average dust properties. B12 directly stacked FIR/sub-mm images of galaxies selected in the optical and used aperture photometry to measure their flux. The bins were set up in such a way that they ought to contain galaxies with similar dust properties. As discussed in Section 1.1, galaxies can be split into red, green, and blue. In each of these galaxy types, B12 split the galaxies into bins of redshift and r -band magnitude in order to probe the evolution of the dust properties with these two variables. Bin edges were chosen such that all bins contained roughly the same number of galaxies to ensure a strong signal-to-noise ratio (SNR). B12 found that the different galaxy types followed different evolutionary trends with both redshift and r -band magnitude.

[Clark et al. \(2015\)](#) demonstrated using a blind survey selected at $250\ \mu\text{m}$ that around a third of the dust mass in the local Universe is contained within galaxies that are low stellar mass, gas-rich and have very blue optical colours. These galaxies were shown to have colder dust populations on average ($12 < T_d < 16\ \text{K}$, where T_d is the cold-component dust temperature) compared to other *Herschel* studies of nearby galaxies, e.g. the *Herschel* Reference Survey ([Boselli et al., 2010](#)), the Dwarf Galaxy Survey ([Madden et al., 2013](#); [Rémy-Ruyer et al., 2013](#), see also [De Vis et al. 2017a](#)) and higher stellar mass *H*-ATLAS galaxies ([Smith et al., 2012a](#)). Later [De Vis et al. \(2017b\)](#) modeled the local *Herschel* galaxy samples but added an additional set of galaxies found by selecting on atomic gas instead of optical or FIR brightness. In their sample, they found more gas-rich but dust-poor galaxies than previously seen in the blind or targeted *Herschel* surveys (the *H*-ATLAS and HRS respectively). These sources were shown to be offset in terms of the simple evolutionary scenario put forward in [Clark et al. \(2015\)](#) where they proposed that the

dust content of galaxies first rises steeply as galaxies convert their gas into stars, then levels off and reaches its peak at roughly a gas fraction¹ of a half, and finally declines. The galaxies in De Vis et al. (2017b) instead had dust masses significantly below this prediction, and well below the M_d/M_* and M_d/M_{gas} scaling relations seen in earlier works.

To summarise the results from some local galaxy samples using *Herschel*, Figure 1.8 compares the dust-to-baryonic mass ratio with gas fraction for local galaxy samples including the blind *Herschel* local sample of Clark et al. (2015) (HAPLESS), the HI-detected sample (HIGH, De Vis et al. 2017b), the *Herschel* Dwarf Galaxy Sample (DGS, Madden et al. 2013) with a range of dust evolution models from Clark et al. (2015) and De Vis et al. (2017b). To explain the observed dust-poor at high gas fraction sources, models with radically lower rates of dust injection from massive stars (supernovae) is needed, though it is not yet clear why. Thus the picture of dust evolution, and its relationship to stellar mass and gas mass may be more complex than realised, and the current trend in using the dust mass to trace the gas mass in galaxies (e.g. Scoville et al. (2014)) may produce unreliable results based on some of the dust-poor galaxies observed in the local Universe. The properties of dust and its scaling relationships with stellar and gas mass for local galaxies, where one can study sources in detail, are important as they provide a benchmark to surveys that are interested in statistical properties of a population of galaxies (as we are in this Thesis).

1.3.4 *Herschel* OBSERVATIONS OF DUST IN EARLY TYPE GALAXIES

ETGs are among the most massive galaxies today and yet their formation routes are not yet constrained. They are often thought of as red and dead systems with little interstellar medium. Observing dust in ETGs allows us to search for the presence of the ISM and probe the past history of these systems since it traces the interstellar content. We can also observe disks and structures in the dust emission that could trace whether mergers or interactions may have occurred in the past. The improved resolution, sensitivity and wavelength coverage of *Herschel* has made the first studies of dust at all temperatures, in greater detail and in large samples of ETGs possible. To date, there have been a handful of studies with *Herschel* to look at the dust and gas properties of ETGs.

¹ the gas fraction is defined as $f_{\text{gas}} = \frac{M_{\text{gas}}}{M_{\text{gas}} + M_*}$ though in Figure 1.8, the gas fraction is made up of atomic hydrogen data only.

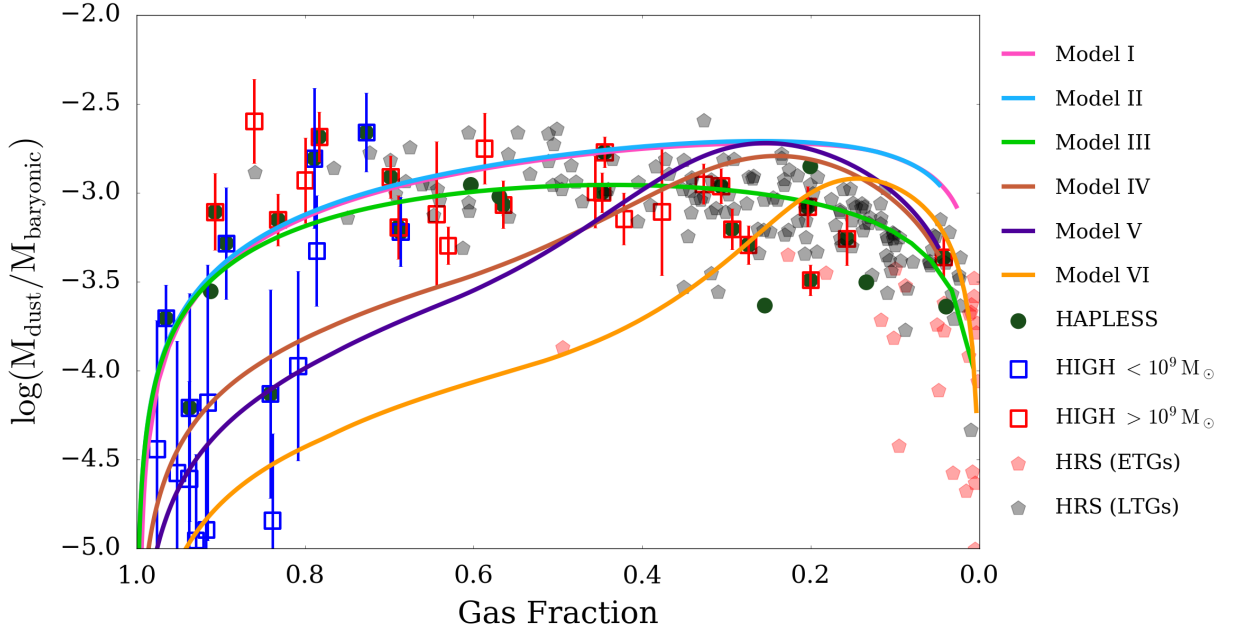


FIGURE 1.8 A compilation of the dust-to-baryonic mass ratio with gas fraction for local galaxy samples including the blind *Herschel* local sample of Clark et al. (2015) (HAPLESS), the HI-detected sample (HIGH, De Vis et al. 2017b), the *Herschel* Dwarf Galaxy Sample (DGS, Madden et al. 2013) and the HRS (Smith et al., 2012c; Cortese et al., 2012a) with a range of dust evolution models from Clark et al. (2015) and De Vis et al. (2017b) (solid lines). The dust models assume galaxies with the same initial gas mass, but different combinations of star formation histories, gas inflows and outflows and dust sources (see Table 2 in De Vis et al. 2017b, note that models I and II overlap in this parameter space). This image is adapted from De Vis et al. (2017b).

The *Herschel* Reference Survey (HRS, Boselli et al., 2010) is a quasi volume-limited sample ($15\text{Mpc} < d < 25\text{Mpc}$) consisting of 323 galaxies, 62 of which were classified as ETGs. This subsample is further split into 39 galaxies classified as lenticular, and 23 classified as elliptical (Boselli et al., 2010). This made it the largest FIR survey of elliptical galaxies with *Herschel* (Smith et al., 2012c; Cortese et al., 2012a) at the time. They found that a large number of ETGs that lie on the traditional optical red sequence are still detected by *Herschel* (with detection rates of 62 per cent for S0 and 24 per cent for E galaxies), demonstrating that optically red-and-dead galaxies can still have significant reservoirs of interstellar material, and that the dust emission may be the most sensitive method to detect the interstellar medium in early types. The *Herschel* Reference Survey (HRS, Boselli et al., 2010) also showed that the mass of dust increases along the Hubble sequence (Figure 1.9), with dust to stellar mass ratios increasing by approximately an order of magnitude for each step taken along the tuning fork with $\log(M_d/M_*) = -5.83 \pm 0.11$ observed in the E sample, increasing to the S0 and

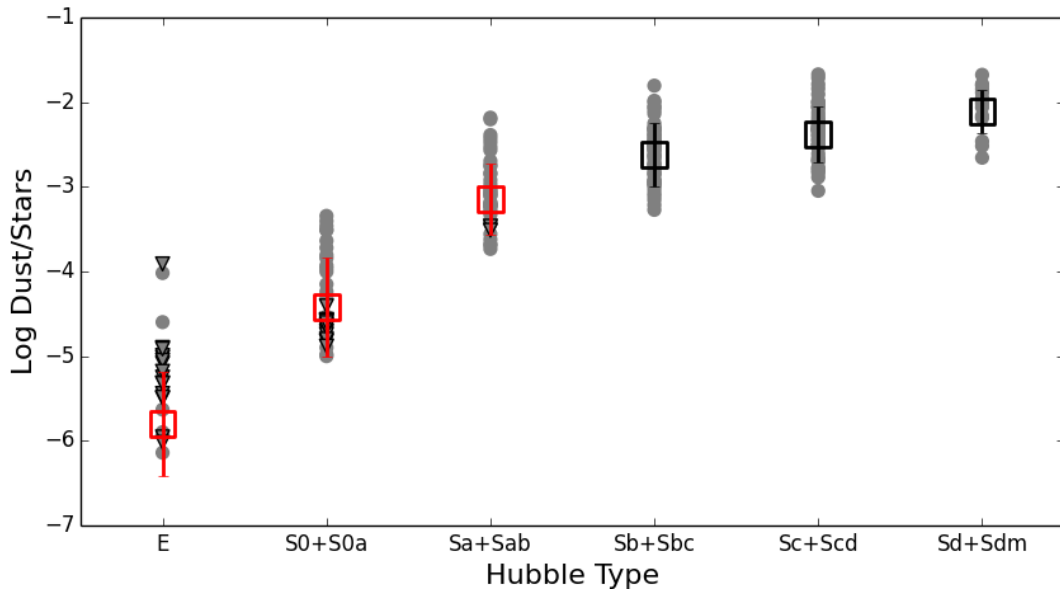


FIGURE 1.9 Comparison of dust-to-stellar mass with Hubble type based on the 62 ETGs and ~ 300 late type galaxies from the *Herschel* Reference Survey (HRS, [Boselli et al. 2010](#)). Grey points show the measurements for individual galaxies where upper limits are denoted with triangles. The mean value in each morphological class is indicated by the box, with standard error shown by the error bars. ETGs are coloured red as the upper limit values are included in the mean. This image is adapted from [Smith et al. \(2012c\)](#).

spirals ([Smith et al., 2012c](#); [Cortese et al., 2012a](#)). [Cortese et al. \(2012a\)](#) also compared the dust-to-atomic gas ratio for the HRS, finding that this ratio is flat across the range of Hubble types, but the environment that a galaxy resides is important. Galaxies in high density environments, e.g. cluster or groups, contain less dust and gas compared to field galaxies.

1.4 A STATISTICAL VIEW OF DUST IN GALAXIES: THE DUST MASS FUNCTION

In the previous Section, dust masses for individual galaxies were discussed. Here we take a more statistical approach to discussing the dust content of galaxies by introducing the dust mass function (DMF): the space density of dust in galaxies. The DMF is a fundamental measurement of the dust content of the Universe, providing crucial information on the reservoir of metals that are locked up in dust grains ([Issa et al., 1990](#); [Edmunds, 2001](#); [Dunne et al., 2003a](#)). Pinning down the space density of dusty galaxies is becoming even more relevant given the widespread use of dust emission as a tracer for the gas in recent years ([Eales](#)

et al. 2010, 2012; Magdis et al. 2012; Scoville et al. 2014, 2017; see also the comprehensive review of Casey et al. 2014). This is of particular interest given difficulties in observing atomic and molecular-line gas mass tracers out to higher redshifts (Tacconi et al., 2013; Catinella & Cortese, 2015; Genzel et al., 2015).

Ground-based studies including observations at 450 and 850 μm with the Submillimetre Common User Bolometer Array (SCUBA) on the James Clerk Maxwell Telescope, led to the first measurements of the DMF over the mass range $\sim 10^7 M_\odot < M_d < \text{few} \times 10^8 M_\odot$ (Dunne et al., 2000; Dunne & Eales, 2001; Vlahakis et al., 2005), where M_d is dust mass. Unfortunately the state-of-the-art at that time meant fewer than 200 nearby galaxies were observed with small fields of view and selected at optical or infrared (60 μm) wavelengths. At higher redshifts, the Balloon-borne Large Aperture Submillimeter Telescope (BLAST, observing at 250-500 μm) enabled a DMF to be derived out to $z = 1$ (Eales et al., 2009) and a valiant effort to measure at even higher redshifts ($z = 2.5$) using SCUBA surveys was attempted by Dunne et al. (2003a). These studies were hampered by small number statistics and difficulties with observing from the ground.

The advent of *Herschel* (Pilbratt et al., 2010) and the *Planck* Satellite revolutionised studies of dust in galaxies, as they enabled greater statistics, better sensitivity and angular resolution in some regimes, wider wavelength coverage and the ability to observe orders of magnitude larger areas of the sky than possible before. The largest dust mass function of galaxies using *Herschel* was presented in Dunne et al. (2011) (Figure 1.10, top) consisting of 1867 sources out to redshift $z = 0.5$. They estimated a dust mass density parameter of $\Omega_d = \rho_d / \rho_{\text{crit}} = (0.7 - 2) \times 10^{-6}$ where ρ_d is the dust density and ρ_c is the critical density of the Universe (assuming a cosmology of $\Omega_m = 0.3$, $\Omega_\Lambda = 0.7$ and $H_0 = 70 \text{ km s}^{-1} \text{ Mpc}^{-1}$). Subsequently, Negrello et al. (2013); Clemens et al. (2013) published the DMF of 234 local star-forming galaxies from the all sky *Planck* catalogue. Clark et al. (2015) then derived a local DMF from H-ATLAS (a 250- μm selected sample consisting of 42 sources - the HAPLESS sample) finding galaxies with colder dust than seen in the previous DMF samples.

Interestingly, although the dust mass density measured is broadly consistent across most of these surveys, the shape of the dust mass function differs (bottom panel of Figure 1.10, see Chapter 2 for more details). The functional form of the curves in Figure 1.10) are simply a fit to the data using a single Schechter function (SSF, Schechter 1976), which takes the form in $\log M$ space of:

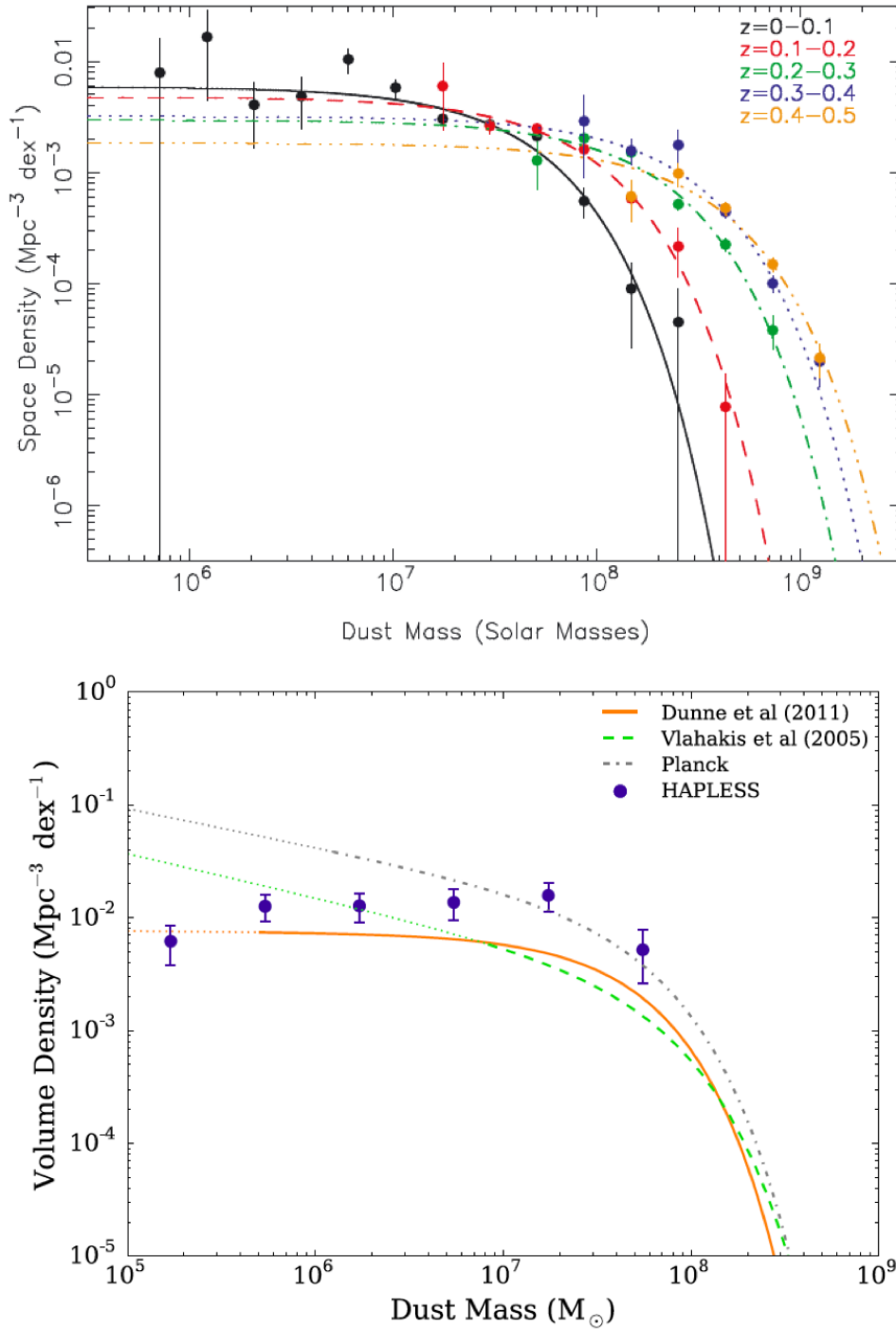


FIGURE 1.10 The dust mass function as published in previous works. *Top*: Evolution of the dust mass function from $z = 0$ to $z = 0.5$ for a sample of ~ 1900 galaxies in a small area of the sky. This image is taken from Dunne et al. (2011). Solid lines show the Schechter fits to each data set (Equation 1.16). *Bottom*: A comparison of local, $z = 0$ dust mass functions from Clark et al. (2015), where the HAPLESS sample is the $250\text{-}\mu\text{m}$ detected sample from the H-ATLAS and Planck refers to the sample from Clemens et al. (2013). Galaxies at the same $250\text{-}\mu\text{m}$ luminosity as Dunne et al. (2011) tended to have colder dust temperatures. Note that the Schechter fits in this panel are shown as solid for the regime that each survey sampled, with the extrapolated best-fit α parameters from their Schechter fits highlighted with dotted lines. This highlights the lack of information on the space density of galaxies at dust masses below $10^6 M_{\odot}$, and therefore the resulting uncertainty on the total dust mass density derived by these studies. This image is taken from Clark et al. (2015).

$$S(M; \alpha, M^*, \phi^*) = \phi^* e^{-10^{\log M - \log M^*}} \times \left(10^{\log M - \log M^*}\right)^{\alpha+1} d \log M, \quad (1.16)$$

and α , M^* and ϕ^* are the power law index of the low-mass slope, the characteristic mass (location of the function's 'knee'), and the number volume density at the characteristic mass respectively. Here we have explicitly included the factor $\ln 10$ in the definition of ϕ^* , such that ϕ^* is in units of $\text{Mpc}^{-3} \text{dex}^{-1}$. The DMFs in Figure 1.10 (bottom) diverge significantly at the low dust mass regime.

1.4.1 EVOLUTION OF THE DUST MASS FUNCTION

Previous studies have shown that the dust luminosity of galaxies appears to evolve rapidly with redshift (Dye et al., 2010). The driving force behind dust luminosity evolution in this paradigm has been attributed to the increased heating of the dust due to the higher star formation rates in the past (Magdis et al., 2012; Rowan-Robinson, 2012; Symeonidis et al., 2013; Berta et al., 2013; Casey et al., 2014). However, the gas content of the Universe has been decreasing with time, and typically a galaxy's gas mass is strongly linked to its dust content. Interestingly, there is contention in the literature as to the cause of the evolution of the dust luminosity. Dunne et al. (2011) determined that there was no evidence for the evolution of dust temperature with either redshift or luminosity, based on the H-ATLAS Science Demonstration Phase sample of ~ 1800 selected in the FIR. Instead, they proposed that the dust mass of the Universe evolved dramatically out to $z = 0.5$, with the dust mass decreasing by a factor of five over the past five billion years of cosmic history (the Schechter fits in the top panel of Figure 1.10 show evolution in different redshift slices). They found a relationship for dust density ρ_d where $\rho_d \propto (1+z)^{4.5}$ to $z = 0.5$. Similarly, the sub-mm selected samples from Eales et al. (2009) and Dunne et al. (2003a) found that the DMF evolved significantly between $z = 0$ and $z = 2$. However, as noted earlier, these samples were hampered by small number statistics, and covering small areas of the sky, or based on ground-based studies.

Recently (whilst the work in this Thesis was being carried out), Driver et al. (2018) produced a dust mass function and measure of the dust mass density out to a redshift of $0 < z < 5$ based on an optically-selected sample of hundreds of thousands of galaxies. Their measurement of ρ_d at $z = 0$ is consistent with

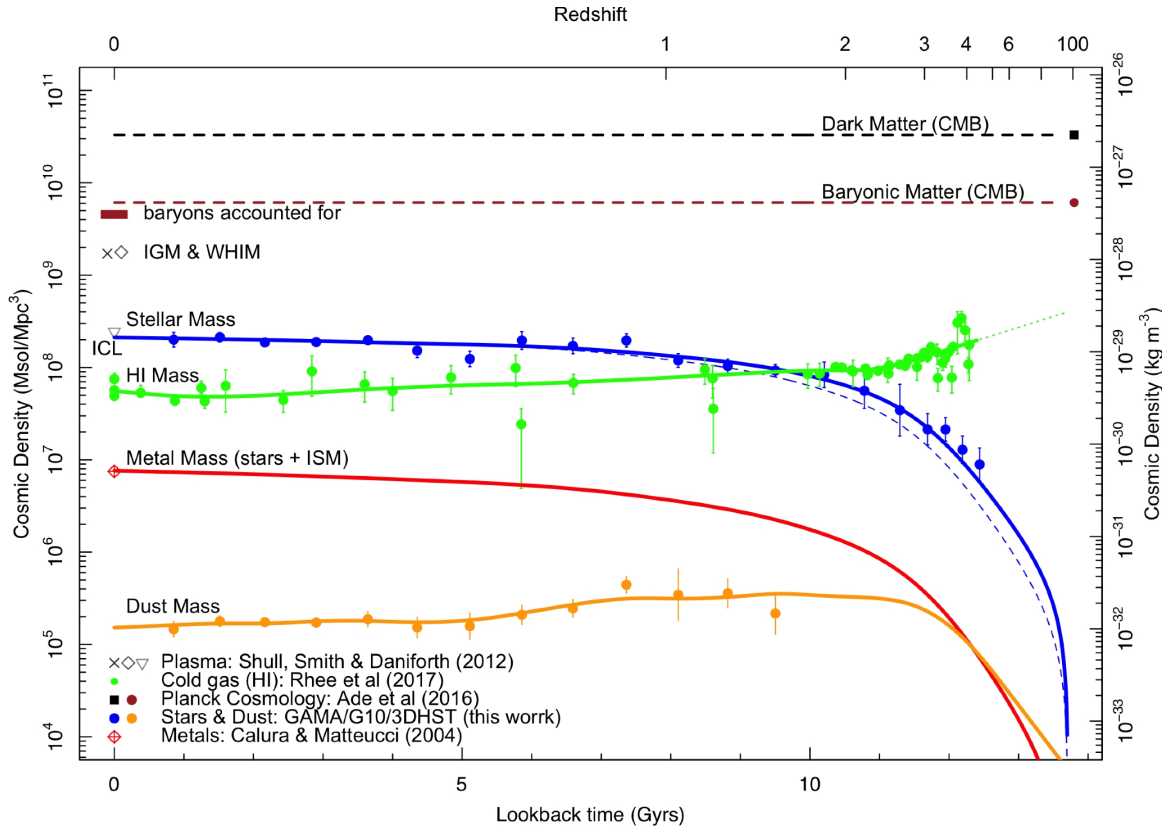


FIGURE 1.11 A compilation of the cosmic density of different galaxy components including dark matter and baryons: stars, gas, metals and dust with lookback time and redshift from [Driver et al. \(2018\)](#). WHIM: warm ionised intergalactic medium, ICL: intracluster light. This work was carried out concurrently with this Thesis, the low redshift bin for dust mass density agrees with the results from Chapter 2.

the earlier [Vlahakis et al. \(2005\)](#) and [Dunne et al. \(2011\)](#) observations. At high redshifts, the [Driver et al. \(2018\)](#) dust mass density peaks at $z \sim 1$ (~ 8 billion years ago) potentially coinciding with the so-called peak epoch of star formation. However, they found no evidence that the dust content of galaxies was evolving in recent cosmic history ($0 < z < 0.5$), finding a relatively flat dust mass density in contrast to [Dunne et al. \(2011\)](#).

Although they differ, both of the evolutionary trends seen in [Dunne et al. \(2011\)](#) at $z < 0.5$ and [Driver et al. \(2018\)](#) at higher redshifts, are attributed to a declining dust mass with time due to dust destruction processes. [Driver et al. \(2018\)](#) compared the dust mass density measured with that predicted from simple dust models whereby dust is formed in winds of evolved stars, core-collapse supernovae and grown in the ISM (eg [Popping et al. \(2017\)](#)) at $z = 0$ and proposed that 90 to 95% of all the dust mass formed in galaxies is destroyed. [Dunne et al. \(2011\)](#) also found that (i) dust destruction needed to be highly efficient and (ii) that 90%

of the dust mass in galaxies is formed via grain growth in the interstellar medium in order to explain their observed decline in cosmic dust density. The dust mass function therefore enables one to test predictions from dust models and investigate potential dust sources and sinks. We will return to this in Chapter 5.

1.5 AN INTRODUCTION TO THE DATASETS AND TOOLS USED IN THIS THESIS

1.5.1 GALAXY AND MASS ASSEMBLY - GAMA

The GAMA² survey is a panchromatic compilation of galaxies built upon a highly complete magnitude limited spectroscopic survey of around 286 square degrees of sky (with limiting magnitude $r_{\text{petro}} \leq 19.8$ mag as measured by the Sloan Digital Sky Survey (SDSS) DR7, Abazajian et al., 2009). Around 238,000 objects have been successfully observed with the AAOmega Spectrograph on the Anglo-Australian Telescope as part of the GAMA survey. As well as spectrographic observations, GAMA has collated broad-band photometric measurements in up to 21 filters for each source from ultraviolet (UV) to FIR/sub-mm (Driver et al., 2016; Wright et al., 2017). The imaging data required to derive photometric measurements come from the compilation of many other surveys: GALEX Medium Imaging Survey (Bianchi & GALEX Team, 1999); the SDSS DR7 (Abazajian et al., 2009), the VST Kilo-degree Survey (VST KiDS, de Jong et al., 2013); the VISTA Kilo-degree INfrared Galaxy survey (VIKING, de Jong et al., 2013); the Wide-field Infrared Survey Explorer (WISE, Wright et al., 2010); and the *Herschel*-ATLAS (Eales et al., 2010). Figure 1.12 (top) illustrates the multiwavelength coverage available in GAMA from UV to sub-mm wavelengths (Driver et al., 2016). The motivation and science case for GAMA is detailed in Driver et al. (2009). The GAMA input catalogue definition is described in Baldry et al. (2010), and the tiling algorithm in Robotham et al. (2010). The data reduction and spectroscopic analysis can be found in Hopkins et al. (2013). An overview and the survey procedures for the first data release (DR1) are presented in Driver et al. (2011). The second data release (DR2) was nearly twice the size of the first and is described in Liske et al. (2015). Information on data release 3 (DR3) can now be found in Baldry et al. (2018). There is now a vast wealth of data products available for the GAMA survey, making it an

² <http://www.gama-survey.org/>

incredibly powerful database for all kinds of extragalactic astronomy and cosmology. In this Thesis, we will use galaxies in the three equatorial fields of the GAMA survey, which cover ~ 180 square degrees of sky between them. (Chapter 2). The equatorial fields GAMA09, GAMA12 and GAMA15 (hereafter G09, G12 and G15) are located on the celestial equator at roughly 9 h, 12 h, and 15 h, respectively (Figure 1.12, bottom).

1.5.2 THE *Herschel* ASTROPHYSICAL TERAHERTZ LARGE AREA SURVEY - *H-ATLAS*

The FIR and sub-mm imaging data, which are necessary to derive dust masses, are provided via *H-ATLAS*³ (Eales et al., 2010), the largest extragalactic Open Time survey using *Herschel* (see Figure 1.13). This survey spans ~ 660 square degrees of sky and consists of over 600 hours of observations in parallel mode across five bands (100 and 160 μm with PACS - Poglitsch et al. 2010, and 250, 350, and 500 μm with SPIRE - Griffin et al. 2010). *H-ATLAS* was specifically designed to overlap with other large area surveys such as SDSS and GAMA. The GAMA/*H-ATLAS* overlap covers around 145 sq. degrees over the three equatorial GAMA fields, G09, G12, and G15 (Figure 1.13 bottom). Photometry in the five bands for the *H-ATLAS* DR1 is provided in Valiante et al. (2016) based on sources selected initially at 250 μm using MADX (Maddox et al. *in prep.*) and having $S/N > 4$ in any of the three SPIRE bands. Bourne et al. (2016) present optical counterparts to the *H-ATLAS* sources, identified from the GAMA catalogue using a likelihood ratio technique (Smith et al., 2011). In this Thesis, we use the aperture-matched photometry from *Herschel* based on the GAMA *r*-band aperture definitions using the LAMBDAR package (Wright et al., 2016), this method is described in Section 1.5.3.

1.5.3 GALAXY PHOTOMETRY WITH LAMBDAR

The Lambda Adaptive Multi-band Deblending Algorithm in R (LAMBDAR)⁴ is an aperture photometry package developed by Wright et al. (2016), which performs photometry based on an input catalogue of sources. Aperture-matched photometry can be implemented on any number of bands and for each band the apertures are convolved by the PSF of the instrument. LAMBDAR also deblends sources occupying the same on-sky area, this is achieved by sharing the flux in each pixel

³ <http://www.h-atlas.org/>

⁴ LAMBDAR is available from <https://github.com/AngusWright/LAMBDAR>

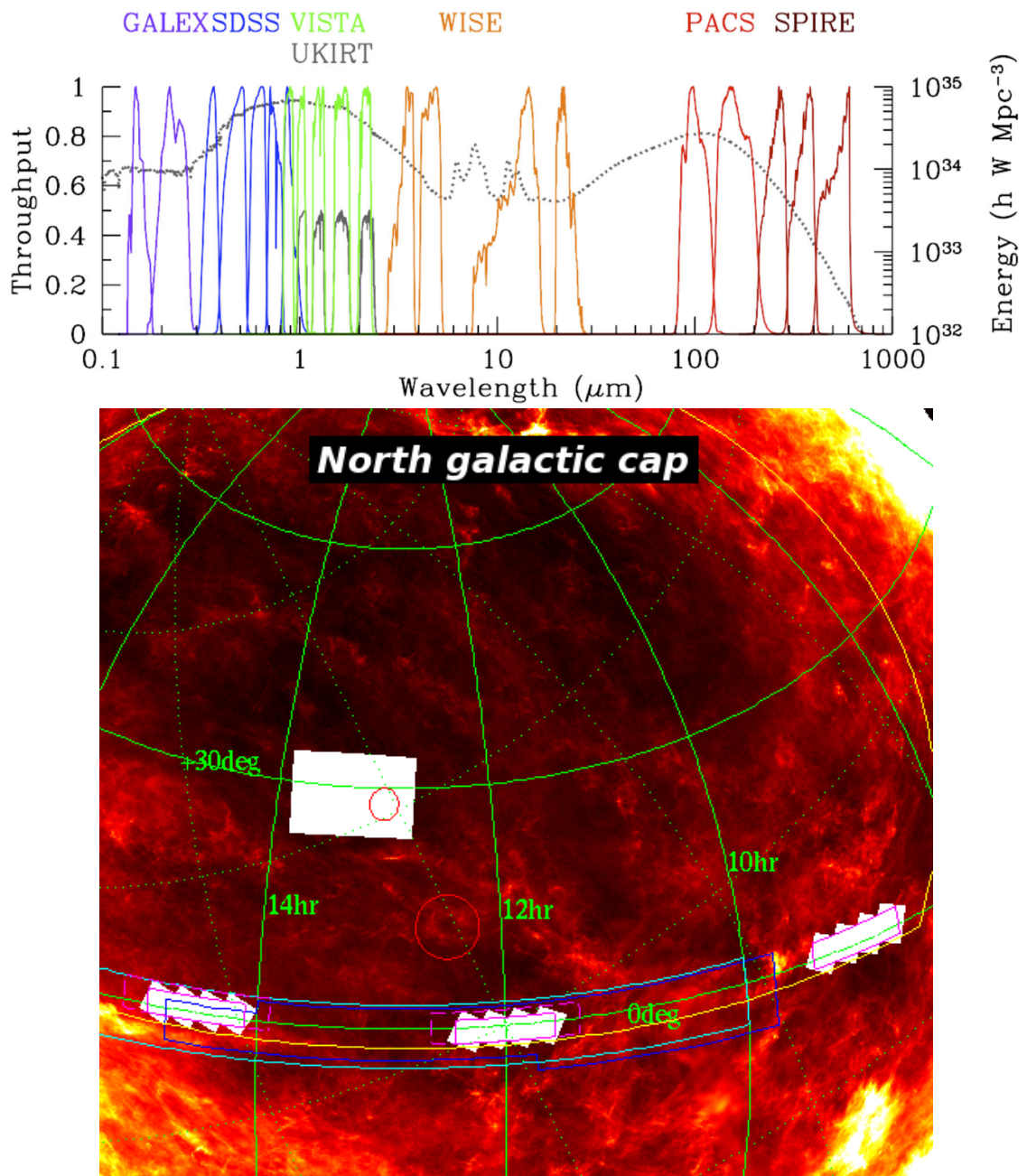


FIGURE 1.12 *Top:* A schematic of the coverage of the spectral energy distribution from multiple telescopes over multiple wavelengths available from the GAMA survey. This image is taken from [Driver et al. \(2016\)](#). *Bottom:* The location of the *Herschel* ATLAS fields superimposed on the InfraRed Astronomical Satellite $100\mu\text{m}$ map of the Galactic dust in the north Galactic plane. The GAMA equatorial fields are the white blocks located along the equatorial plane at 0 degrees; these are the fields that will be used in this Thesis. This image is taken from [Eales et al. 2010](#).



FIGURE 1.13 Three colour *Herschel* SPIRE images of the *Herschel* ATLAS GAMA fields. *Top*: GAMA 09 *Middle*: GAMA 12 and *Bottom*: GAMA 15. Images from <https://www.h-atlas.org/> and from Nathan Bourne https://www.roe.ac.uk/~bourne/docs/HATLAS_Overview_Lisbon2016.pdf.

between all overlapping apertures. The fractional splitting is done iteratively and, depending on user preference, can be based on the mean surface brightness of a source, central pixel flux, or a user-defined weighting system. Each source is considered in a postage stamp of the input image focused on the source, the size of which depends upon the size of the aperture itself. All known sources within the postage stamp are deblended, including an optional list of known contaminants specified by the user (Figure 1.14). For this Thesis this includes *H*-ATLAS detected sources from Valiante et al. (2016) which do not have a reliable optical counterpart. These are assumed to be higher redshift background sources.

The sky estimate for each source is calculated by randomly placing blank apertures with dimensions equal to the object aperture on the postage stamp, using the number of masked pixels in each blank aperture to weight its contribution to the background estimate (Figure 1.15). Furthermore, during flux iteration, if any component of a blend is assigned a negative flux then it is rejected for all subsequent iterations (and any negative measurement is set to zero). There are a very small number of sources which end up with negative fluxes at the final iteration and, for consistency, the LAMBDAAR pipeline sets these to zero also. For further details on the LAMBDAAR software and data release see Wright et al. (2016).

1.5.4 DERIVING GALAXY PROPERTIES WITH MAGPHYS

In this Thesis, we use the spectral energy distribution fitting software MAGPHYS⁵ package (da Cunha et al., 2008) to fit model SEDs to the 21-band LAMBDAAR photometry of each galaxy in the three GAMA fields (Chapter 2). MAGPHYS uses libraries containing 50 000 model SEDs covering both the UV-NIR (Bruzual & Charlot, 2003) and MIR/FIR (Charlot & Fall, 2000) components of a galaxy's SED along with a χ -squared minimisation technique to determine physical properties of a galaxy, including stellar mass, dust mass and dust temperature. MAGPHYS imposes energy balance between these components, so that the power absorbed from the UV-NIR matches the power re-radiated in the MIR/FIR. In the FIR-sub-mm regime, two major dust components are included in the libraries: a warm component (30 to 60 K) associated with stellar birth clouds; and a cold dust component (15 K to 25 K) associated with the diffuse ISM. A dust mass absorption coefficient of $\kappa_{850} = 0.077 \text{ m}^2\text{kg}^{-1}$ is assumed, with an emissivity index of $\beta = 1.5$ for the warm dust, and $\beta = 2$ for cold dust, where $\kappa_\lambda \propto \lambda^{-\beta}$. For each galaxy MAGPHYS uses all of the LAMBDAAR measurements to find the best-fitting combination

⁵ MAGPHYS is available from <http://www.iap.fr/magphys/>

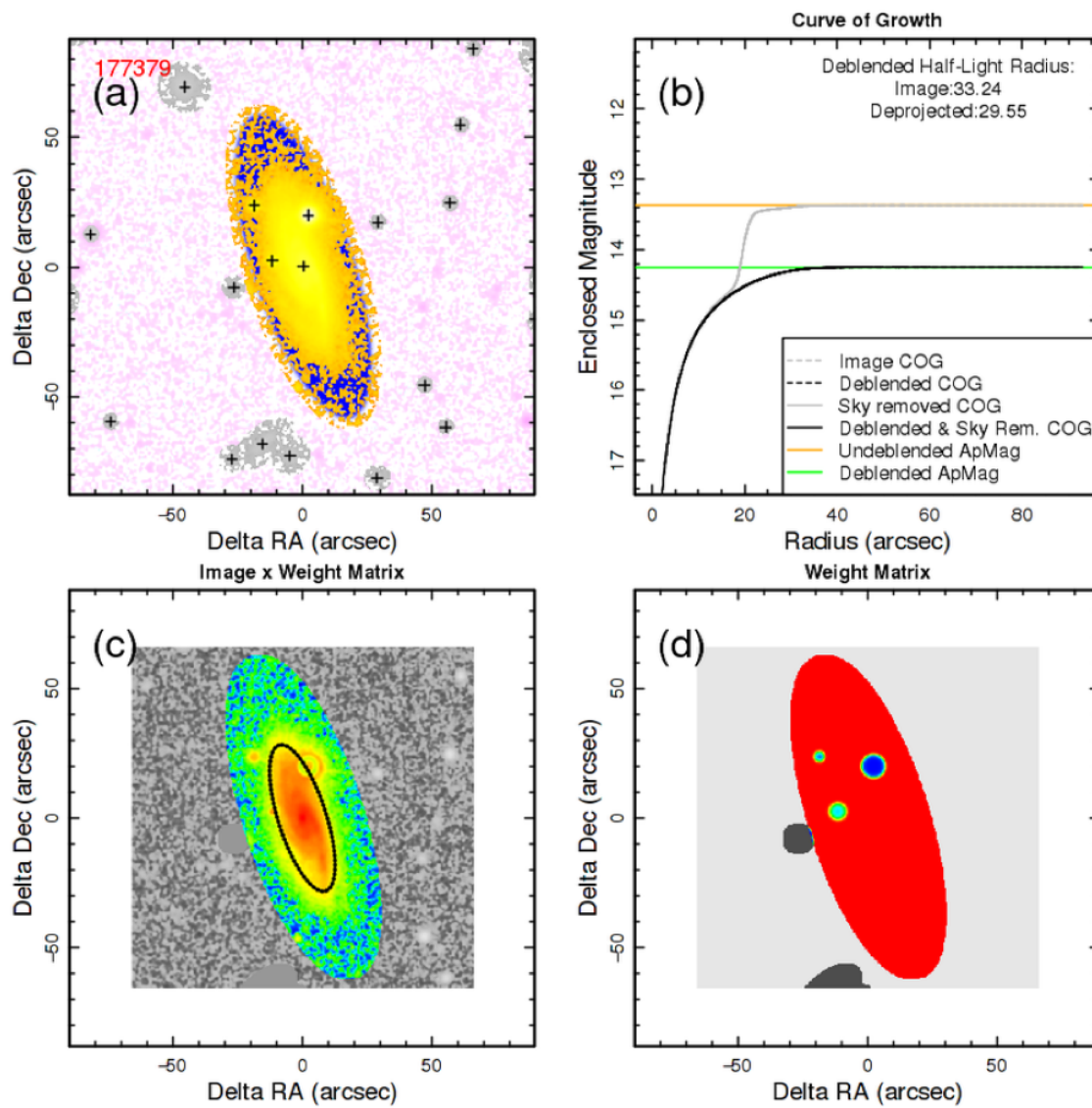


FIGURE 1.14 An example of the LAMBDA-R debblending process courtesy of [Wright et al. \(2017\)](#)

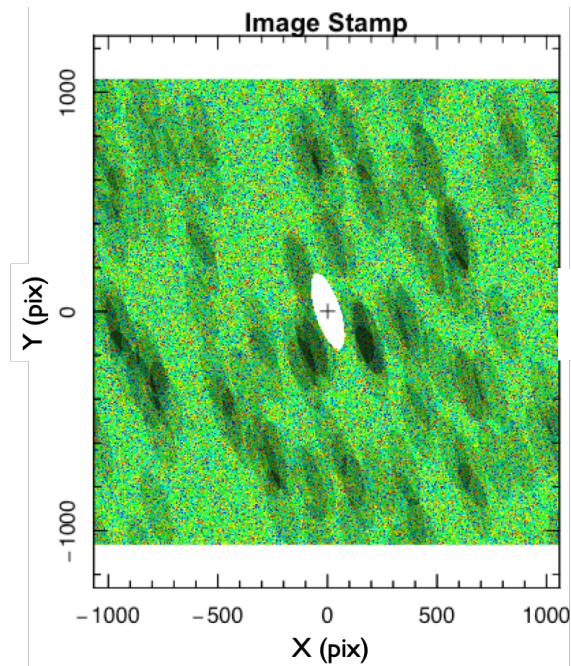


FIGURE 1.15 An example of the LAMBDAAR sky subtraction process courtesy of [Wright et al. \(2017\)](#)

of optical and FIR model SEDs, and outputs the physical parameters for this combined SED. MAGPHYS also generates a ‘probability distribution function’ (PDF) for each parameter by summing $e^{-\chi^2/2}$ over all models. The PDF for each parameter is used to determine the acceptable range of the physical quantity, expressed as percentiles of the probability distribution of model values. An example output file from MAGPHYS is provided in Figure 1.16.

1.6 THESIS OUTLINE

A key goal of this Thesis is to try and quantify the dust component in galaxies, in galaxies of different morphological types, and derive the evolution of the dust content over recent cosmic history. We therefore measure the dust content of galaxies both locally and in the past five billion years. We directly measure the dust mass function out to redshifts $z = 0.1$ and employ stacking techniques to measure the content in 29 235 galaxies from $0 < z < 0.5$. The previous measurements of the local dust mass function is based on only 3% of the entire areal coverage of the H-ATLAS ([Dunne et al., 2011](#)) or only a handful of close sources (42, [Clark et al. 2015](#)). We also investigate the dust properties of late type and early type galaxies out to $z = 0.1$. We note that this Thesis extends our knowledge of the dust mass

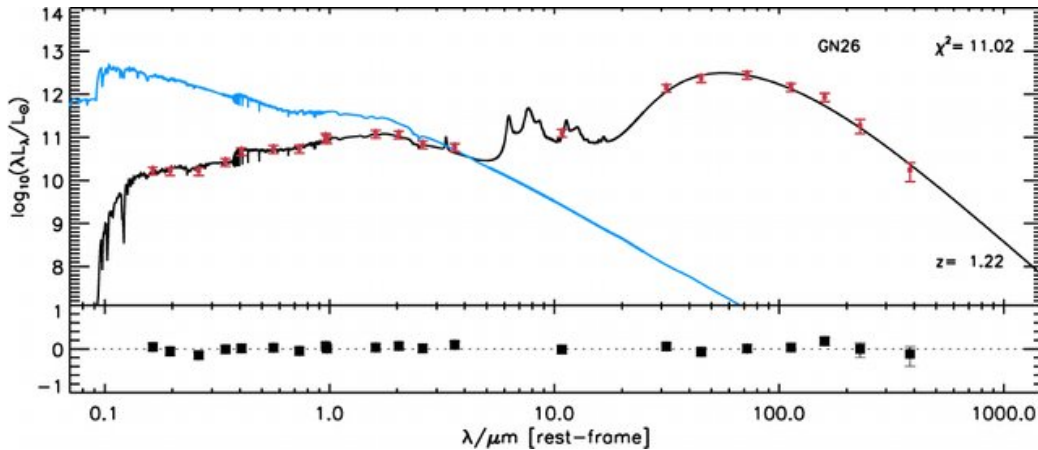


FIGURE 1.16 An example spectral energy distribution (SED) output by the MAGPHYS fitting routine (from Rowlands et al. 2014). This SED is for the high-redshift submillimetre galaxy GN21. The observed multiband photometry from the rest-frame UV to the submillimetre is shown by the red data points, with the black line showing the best-fit model SED (determined via χ^2). The blue line is the recovered unattenuated optical emission for the galaxy (ie if the dust was not present). The residuals between the MAGPHYS returned best-fit model photometry and the observed data are shown in the bottom panel. For this example, the redshift z and χ^2 value are also shown in the panel.

content of galaxies in the following ways (i) by reducing the large uncertainty in measurements of the dust mass density from cosmic variance by using larger areas of the sky; (ii) using consistent, homogeneous measurements over these large volumes (via the GAMA and H-ATLAS surveys where photometry is derived consistently, and dust mass measurements are derived e.g. MAGPHYS for all of the sources in the same way); (iii) approaching the dust mass function from both an optically-selected *and* FIR-selected sample via stacking and finally (iv) by investigating the dust content in galaxies and scaling relations with stellar mass for different morphological types (e.g. late-type/early type, slow-fast rotators, and bulge and disk-like galaxies).

A brief breakdown of the Thesis content is listed below.

- In Chapter 2, the dust mass function is measured for an optically selected sample of $\sim 16,000$ galaxies from an area containing both the GAMA/H-ATLAS surveys. The process of producing the dust mass function, details of the sample, the method used to derive the dust masses using the energy balance technique MAGPHYS and a measurement of the cosmic dust mass density at $0 < z < 0.1$ is presented.
- In Chapter 3, the potential biases that may exist in our measure of the dust

mass function e.g. due to the SED fitting performed by MAGPHYS, the selection affects of our data, or the form of the fit to the data are investigated.

- In Chapter 4 the optically selected dust mass function is placed in context with the literature both in terms of observations as well as simulations. The dust mass function is also split by galaxy morphology and compared to the galaxy stellar mass functions from the same sample in order to investigate if one can derive scaling relations between stellar mass and dust mass.
- In Chapter 5 we derive dust properties for a FIR selected sample of $\sim 30\,000$ galaxies from the *H*-ATLAS equatorial fields out to $z = 0.5$. This is achieved through two methods, firstly using MAGPHYS and secondly through a stacking analysis similar to [Bourne et al. \(2012\)](#).
- In Chapter 6 we derive the FIR selected dust mass function in five redshift slices. We compare the lowest redshift slice dust mass function to the one found in Chapter 4, and also investigate whether the dust mass function has been evolving over cosmic time.
- In Chapter 7 we summarise our findings in the preceding Chapters.

Throughout this Thesis we use a cosmology of $\Omega_m = 0.3$, $\Omega_\Lambda = 0.7$ and $H_0 = 70 \text{ km s}^{-1} \text{ Mpc}^{-1}$.

CHAPTER 2

THE LOCAL DUST MASS FUNCTION

‘Let us not take ourselves too seriously. None of us has a monopoly on wisdom.’

HER MAJESTY THE QUEEN, ELIZABETH II

In this Chapter we derive the low redshift, ‘local’ Dust Mass Function (DMF) for the largest sample of galaxies to date, using data from the Galaxy And Mass Assembly (GAMA) and H-ATLAS. Properties of the full GAMA sample are discussed in detail in [Driver et al. \(2018\)](#) and the accompanying stellar mass function of the same sample is published in [Wright et al. \(2017\)](#), hereafter W17. The work in this Chapter has been published in [Beeston et al. \(2018\)](#).

2.1 INTRODUCTION

The dust mass function (DMF) is one of the most fundamental measurements of the dust content of galaxies, providing crucial information on the reservoir of metals that are locked up in dust grains ([Issa et al., 1990](#); [Edmunds, 2001](#); [Dunne et al., 2003a](#)). Ground-based studies with SCUBA led to the first measurements of the DMF over the mass range $\sim 10^7 M_{\odot} < M_d < \text{few} \times 10^8 M_{\odot}$ ([Dunne et al., 2000](#); [Dunne & Eales, 2001](#); [Vlahakis et al., 2005](#)), where M_d is dust mass. Unfortunately the state-of-the-art at that time meant fewer than 200 nearby galaxies were observed with small fields of view and selected at optical or infrared ($60 \mu\text{m}$) wavelengths. At higher redshifts, the Balloon-borne Large Aperture Submillimeter Telescope (BLAST, observing at $250\text{-}500 \mu\text{m}$) enabled a DMF to be derived out

to $z = 1$ (Eales et al., 2009) and SCUBA measured the DMF at redshift ($z = 2.5$) (Dunne et al., 2003a).

Dunne et al. (2011) used 1867 sources observed with *Herschel* out to redshifts $z = 0.5$, selected from the Science Demonstration Phase (SDP) of the *Herschel* Astrophysical Terahertz Large Area Survey (*H-ATLAS*) blind 250- μm fields (Eales et al., 2010, 16 sq. degrees). Their DMF extended down to a mass of $5 \times 10^5 M_\odot$ and they derived a redshift dependent dust mass density parameter of $\Omega_d = \rho_d / \rho_{\text{crit}} = (0.7 - 2) \times 10^{-6}$ where ρ_{crit} is the critical density (the matter density of a spatially flat Universe). Subsequently, Negrello et al. (2013) and Clemens et al. (2013) published the DMF of 234 local star-forming galaxies from the all sky *Planck* catalogue. Clark et al. (2015) then derived a local DMF from a 250- μm selected sample consisting of 42 sources in the very nearby Universe $D < 42$ Mpc. These DMFs covered a dust mass range from $10^6 M_\odot < M_d < \text{few} \times 10^8 M_\odot$ and $2 \times 10^5 M_\odot < M_d < 10^8 M_\odot$ respectively. These measurements were found to be consistent with the $z = 0$ estimate from Dunne et al. (2011), once scaled to the same dust properties¹, as well as those derived from optical obscuration studies using the Millenium Galaxy Catalogue (Driver et al., 2007).

Interestingly, although the dust mass density is broadly consistent across most surveys, the shape of the dust mass function differs between all of these different estimates. Clark et al. (2015) demonstrated using a blind survey selected at 250- μm , around a third of the dust mass in the local universe is contained within galaxies that are low stellar mass, gas-rich and have very blue optical colours. These galaxies were shown to have colder dust populations on average ($12 < T_d < 16$ K, where T_d is the cold-component dust temperature) compared to other *Herschel* studies of nearby galaxies, e.g. the *Herschel* Reference Survey (Boselli et al., 2010), the Dwarf Galaxy Survey (Madden et al., 2013; Rémy-Ruyer et al., 2013, see also De Vis et al. 2017a) and higher stellar mass *H-ATLAS* galaxies Smith et al. (2012a). This led to higher numbers of galaxies in the low dust mass regime than predicted from extrapolating the Dunne et al. (2011) DMF down to the equivalent mass bins (Clark et al., 2015).

In comparison, the Clemens et al. (2013) and Vlahakis et al. (2005) DMFs are in reasonable agreement and both suggest a low-mass slope that is much steeper than the Dunne et al. (2011) function. Overall, comparing between these different measures is complex due to different selection effects; furthermore they are limited due to (i) small number statistics, and/or (ii) lack of sky coverage or volume, inflating uncertainties due to cosmic variance. (Note, we will show later that fitting the

¹ scaled to the same dust absorption coefficient, κ

same dataset over different mass ranges can have an effect on the resulting best-fit parameters, since we probe further down the low-mass end than any literature study, this could therefore have a significant impact.)

Here we further the study of the DMF by deriving the ‘local’ ($z < 0.1$) dust mass function for the largest sample of galaxies to date. The sample is taken from the Galaxy and Mass Assembly Catalogue (GAMA, [Driver et al. 2011, 2018](#)). The large size of this sample reduces the statistical uncertainties and the effect of cosmic variance compared to previous literature studies of the DMF. We also employ statistical techniques to address selection effects in our sample, which allows us to probe further down the dust mass function by at least an order of magnitude compared to previous works. The observations and sample selection are presented in Section 2.2 and the method used to derive the dust masses for the GAMA sources is detailed in Section 2.3. The dust mass function is presented in Section 6.4 and is compared to the earlier studies in Section 2.5. Biases and effects on our measurements due to data sample selection, signal-to-noise issues and fitting techniques are investigated in Chapter 3.

2.2 THE SAMPLE USED IN DERIVING THE DUST MASS FUNCTION

For this analysis of the dust content of the local Universe, we use the wealth of data available from the GAMA survey (Section 1.5.1) in the three equatorial fields G09, G12 and G15. K-corrections (which account for the difference in observed and rest-frame fluxes) for GAMA sources are available from [Loveday et al. \(2012\)](#) using `K-CORRECT v4_2` ([Blanton & Roweis, 2007](#)). Redshifts derived using `AUTOZ` are available from [Baldry et al. \(2014\)](#). GAMA has a redshift completeness of > 98 per cent at $r_{\text{petro}} \leq 19.8$ mag ([Liske et al., 2015](#)) in the three equatorial fields. GAMA distances were calculated using spectroscopic redshifts and corrected ([Baldry et al., 2012](#)) to account for bulk deviations from the Hubble flow ([Tonry et al., 2000](#)). Here we use the following GAMA catalogues: `LambdaCatv01`, `SersicCatSDSSv09`, `VisualMorphologyv03`, `DistancesFramesv14`, and `TilingCatv46` and the `MAGPHYS` results presented in [Driver et al. \(2018\)](#). We also removed one galaxy from our sample, GAMA CATAID 49167, due to an error in the GAMA r -band aperture chosen to derive the photometry of this source. We select only galaxies within the redshift range $0.002 \leq z \leq 0.1$, with the upper limit matching the low z bin from the earlier DMF study of [Dunne et al. \(2011\)](#); this redshift

range contains 20,387 galaxies (with spectroscopic redshift quality set at $n_{\text{Qual}} \geq 3$). These GAMA galaxies have been further split into Early Types (ETGs), Late Types (LTGs) and little blue spheroids (LBSs) based on classifications using *giH*-band images from SDSS (York et al., 2000), VIKING (Sutherland et al., 2015) or UKIDSS-LAS (see Kelvin et al. 2014a; Moffett et al. 2016a for more details on the classification). We will return to this in Chapter 4.

As we require *Herschel* data for the FIR photometry required to derive dust masses, we need to select sources that are covered in both the *H*-ATLAS and GAMA fields (Sections 1.5.1 and 1.5.2). The final sample for this work therefore consists of 15,951 galaxies, this number includes a selection on $r_{\text{petro}} \leq 19.8$ and the fact that due to the different shapes of the *H*-ATLAS and GAMA fields, some of the GAMA sources were not covered by *Herschel*. The Lambda Adaptive Multi-band Deblending Algorithm in R (LAMBДАР) is used to derive aperture photometry (this package was developed by Wright et al. (2016) and performs photometry based on an input catalogue of sources, see Section 1.5.3).

Finally, the LAMBДАР fluxes for 11,210 (70.3 per cent) sources are not above the 3σ level at $250\ \mu\text{m}$. However, even galaxies which fall below 3σ do have a valid measurement and error estimate in five *Herschel* bands and thus we will argue they do provide useful information for deriving dust masses. We discuss potential biases this might introduce in our estimation of the dust mass function and dust mass density in later Sections of this Chapter and in Chapter 3. We note that the DMF in this Chapter is fundamentally an optically selected DMF, unlike that of the FIR/submillimetre selected samples from Dunne et al. (2011); Clemens et al. (2013) and Clark et al. (2015).

2.3 DERIVING GALAXY PROPERTIES WITH MAGPHYS

For each galaxy we take the dust and stellar properties from Driver et al. (2018), who used MAGPHYS to derive galaxy properties for the entire GAMA fields (Section 1.5.4). The version of MAGPHYS used by GAMA (and therefore used in this Thesis) is slightly modified compared to the default distribution available online. It includes the most up-to-date estimates of the *Herschel* band-pass profiles for both the PACS and SPIRE instruments and the model photometry for each of the *Herschel* pass bands is calibrated to the nominal central wavelength of each band, as described in the SPIRE Handbook² (Griffin et al., 2010, 2013), rather than

² The SPIRE Observer’s Manual is available at http://herschel.esac.esa.int/Docs/SPIRE/spire_handbook.pdf

the effective wavelength, which is the case for other photometry. Running the code with and without these changes does not highlight any systematic error in the FIR-based MAGPHYS output; however, it does change individual measurements by up to a few percent (Driver et al., 2018). For our analysis we use the median value output by MAGPHYS for each parameter we use in this work, since this is more robust than the estimate from the best fit model combination. Where uncertainties are required, we use the 16th and 84th percentiles output by MAGPHYS for the parameters, which correspond to a 1σ uncertainty for a Gaussian error distribution.

The assumed dust model used in MAGPHYS is effectively consistent with dust mass absorption coefficient κ as empirically measured in nearby galaxies (James et al., 2002; Clark et al., 2016, see also Dunne et al., 2000) and ~ 2.4 times higher than the oft-used Draine (2003) theoretical values (based on their κ scaled to $850\ \mu\text{m}$ with $\beta = 2$). We note that we have not considered the effects of changes in the dust mass absorption coefficient κ in this study. As we are not able to test this using this dataset, we elect to keep κ constant. Different grain properties could plausibly lead to an uncertainty of a factor of a few in κ (and therefore dust mass which scales with κ , see for example the discussion in Rowlands et al., 2014). Using the latest values for κ observed in the diffuse ISM of the Milky Way from Planck Collaboration XXIX (2016) would give dust masses 1.6 times higher than quoted here.

As noted earlier, a large fraction of the GAMA sources in our sample have measurements with signal-to-noise ratio below 3σ in the FIR bands: for the $z < 0.1$ sample that we use here 32 per cent have fluxes $> 3\sigma$. Given that LAMBDA assigns a zero flux for each blend component that returns a negative flux at any iteration (Section 1.5.3), the error distribution of faint sources becomes one-sided. If we assume that the errors are Gaussian and consider sources which have a true flux much less than σ , then the bias introduced in the SED fitting as a result of poor signal-to-noise is the mean value of the positive half of a Gaussian i.e. $\sigma/\sqrt{2\pi} \approx 0.4\sigma$. Sources with more positive fluxes will have a smaller bias.

2.3.1 THE DUST PROPERTIES OF THE SAMPLE

The distribution of redshifts and the dust mass-redshift distribution from MAGPHYS for the final sample used in this Thesis are shown in Figure 2.1. Note that for GAMA, all the redshifts are spectroscopically obtained.

The normalized distribution of dust temperatures output by MAGPHYS for LAMBDA sources with fluxes above 3σ in one, two or three *Herschel*-SPIRE bands

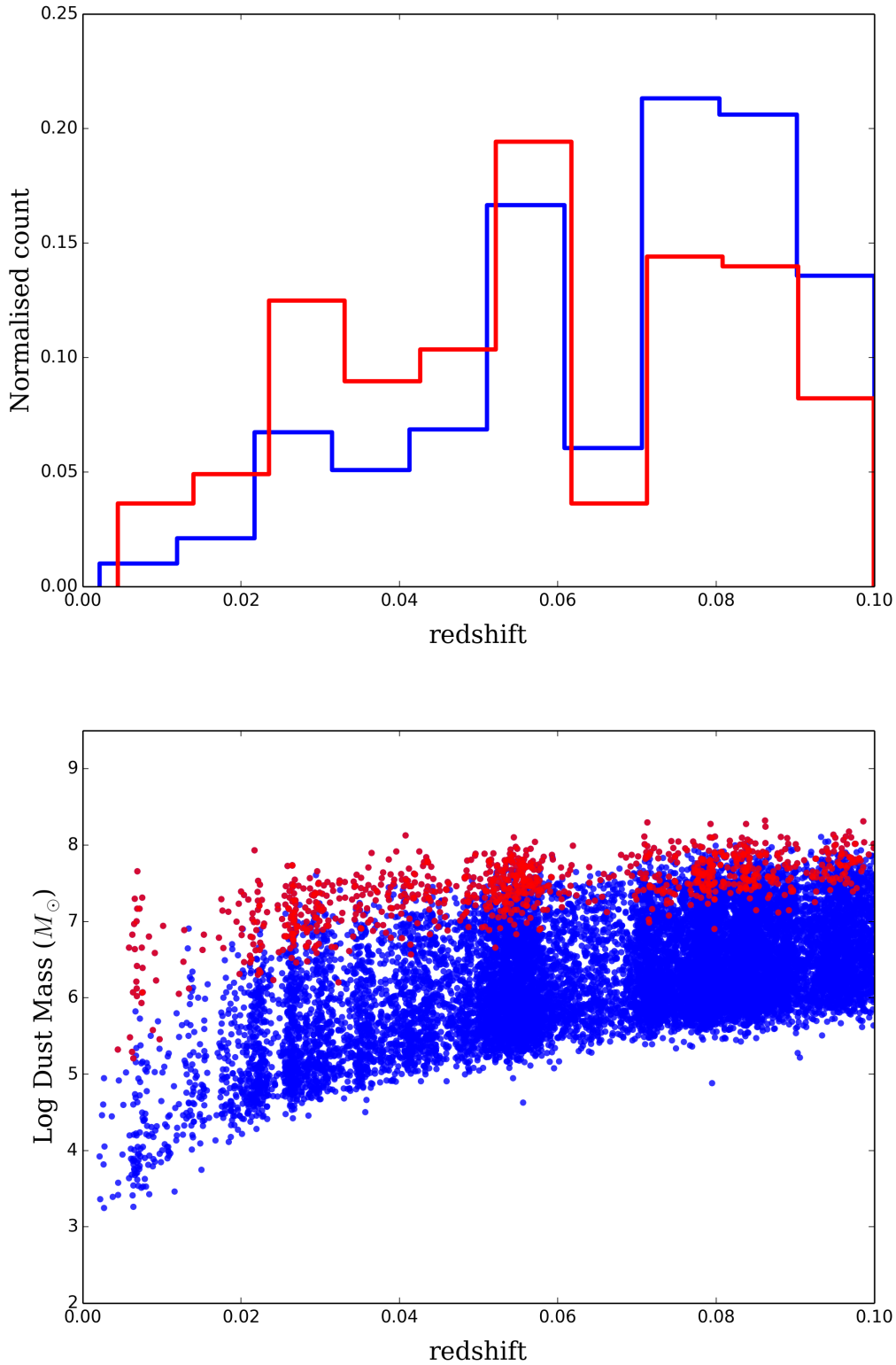


FIGURE 2.1 *Top*: Distribution of redshifts for the GAMA sample at $0.002 < z < 0.1$ used in this Thesis. *Bottom*: Redshift distribution of the dust masses for the H-ATLAS/GAMA sample. Blue data points are the whole sample, red data points shows sources with fluxes above 3σ in the three *Herschel*-SPIRE bands.

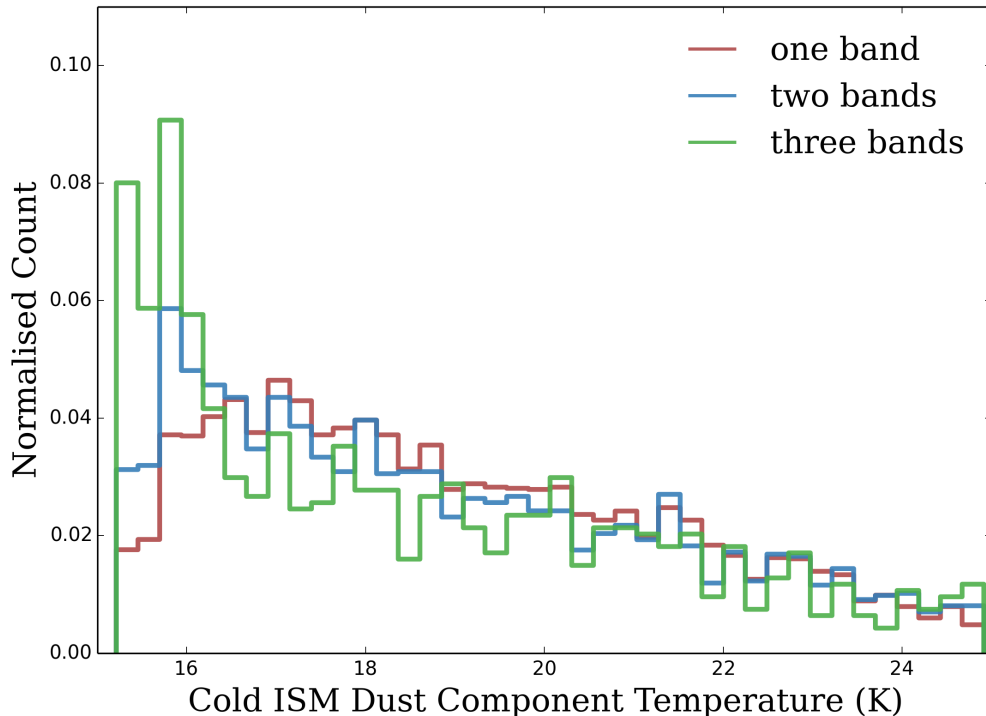


FIGURE 2.2 The normalized distribution of the cold ISM dust temperature output by MAGPHYS for the low redshift sample ($z \leq 0.1$). The red, blue and green histograms show galaxies with $> 3\sigma$ fluxes in one, two or three SPIRE bands respectively. Each histogram is normalized to a total count of one: the fraction of sources in each histogram is 32, 17 and 6 per cent respectively.

is shown in Figure 2.2. Where we have sources with *Herschel* fluxes $> 3\sigma$ in one or more bands, the temperature is well constrained ($\pm \sim 1$ K), and has a tendency to be fairly cold, ~ 18 K. There is also a tendency for the galaxies with *Herschel* fluxes $> 3\sigma$ in all three bands to be colder than those with only one or two bands; this is not unexpected given that the combination of the shape of the SED of a modified blackbody, and the more sensitive bluer SPIRE bands. The temperature histogram for these sources appears to continue to rise at temperatures below 17 K, with a peak at 16 K. This potentially suggests that a colder dust prior than the 15 – 25 K used in the MAGPHYS version for this work might be needed for a small fraction of galaxies (e.g. De Vis et al. 2017a; Viaene et al. 2014; Smith et al. 2012a). We will return to this in Chapter 3.

For the galaxies that have fluxes below 3σ in all of the *Herschel* SPIRE bands we have poor constraints on the cold dust temperature. For these galaxies, the

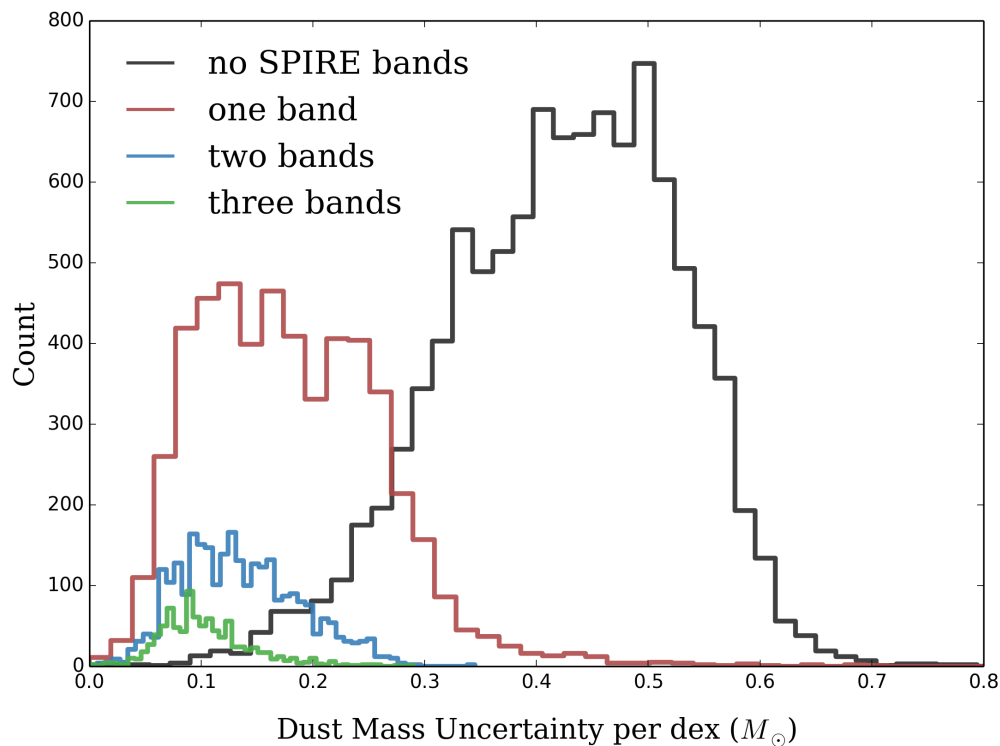


FIGURE 2.3 The distribution of uncertainties on the dust mass estimates. The uncertainties are calculated as half the difference between the 84th and 16th percentiles of the PDF; if the uncertainties are Gaussian, they correspond to one sigma. The black, red, blue and green histograms show galaxies with $> 3\sigma$ flux measurements in zero, one, two or three SPIRE bands respectively.

temperature PDF follows the underlying *flat* temperature prior used in the MAGPHYS code with limits from 15-25 K. Since the temperature estimate is the median of the PDF, this tends towards the median of the prior as the constraints become weaker. Despite this, the combination of UV and optical photometry and *the FIR measurements* do provide useful information on the dust masses for those galaxies with FIR fluxes $< 3\sigma$ in all Herschel bands. This can be seen in Figure 2.3, which shows the distribution of estimated dust mass uncertainties for galaxies with $> 3\sigma$ in zero, one, two or three SPIRE bands. For the subsets in one, two or three bands the corresponding uncertainties in mass are 0.18, 0.14 and 0.1 dex. Galaxies with $< 3\sigma$ in any SPIRE band typically have dust mass uncertainties of 0.4 dex on average. As a further, though indirect, check that the estimated uncertainties are reasonable we look at the distribution of dust mass and stellar mass of the GAMA $z \leq 0.1$ sample, as shown in Figure 2.4. The sources with fluxes $> 3\sigma$ in at least one band are shown in green (as expected, these are the more dusty galaxies), with the

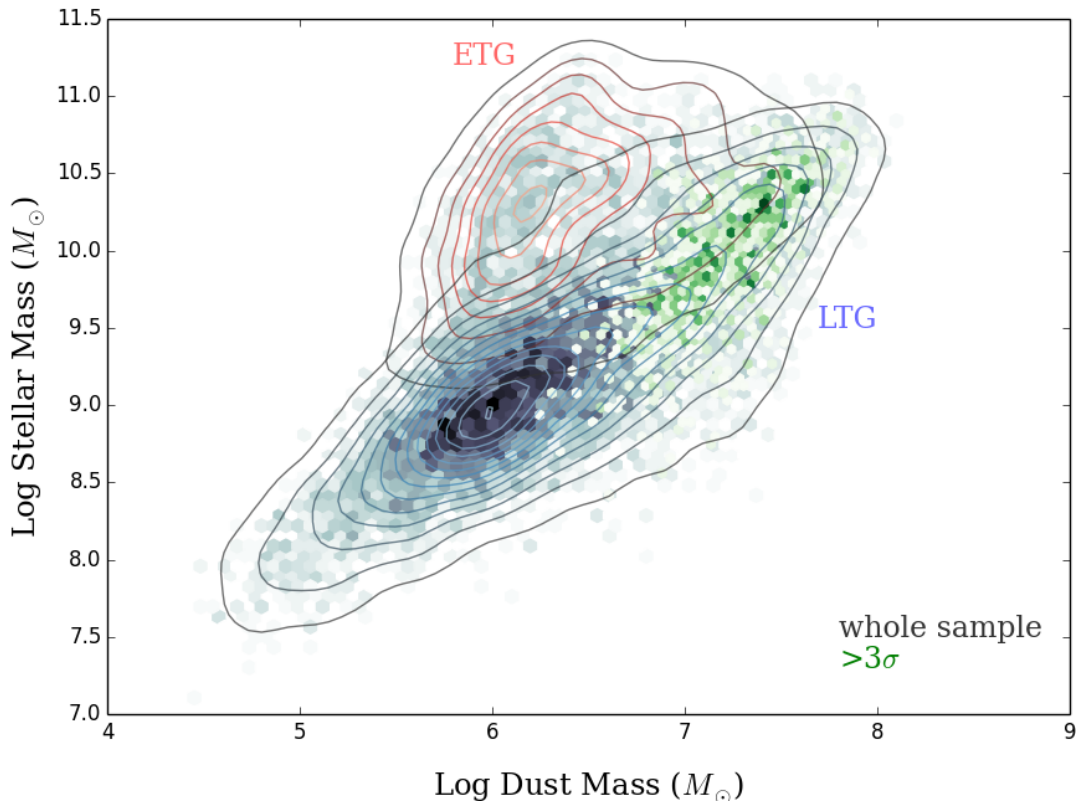


FIGURE 2.4 The distribution of dust mass and stellar mass in GAMA galaxies. The black underlying points show the whole low redshift ($z \leq 0.1$) sample. The green points show galaxies with $> 3\sigma$ fluxes in one or more SPIRE bands. Contours show the demarcation into ETGs (black/red contours) and LTGs (black/blue contours) - see text for details.

entire sample shown by the grey bins. We see that the distribution shows a marked bimodality in this plane, clearly visible even for sources without fluxes $> 3\sigma$ in any of the FIR bands. To investigate this further, Figure 2.4 highlights the morphological classifications of the galaxies split into ETGs and LTGs (Moffett et al., 2016a) (we will return to galaxy morphology in Chapter 4). The ETGs have many fewer $> 3\sigma$ sources than the LTGs, even for bright optical sources, and this is as expected given that ETGs contain an order of magnitude less dust than late-type galaxies of the same stellar mass (see e.g. Bregman et al., 1998; Clemens et al., 2010; Skibba et al., 2011; Rowlands et al., 2012; Smith et al., 2012c; Agius et al., 2013, 2015). If the true uncertainties in M_d were larger than 0.5 dex, the bimodal structure in Figure 2.4 would be smeared out, suggesting the errors in MAGPHYS do reasonably represent the uncertainties.

In summary, we find that while the dust-mass error decreases as we move from detecting galaxies in zero to three FIR filters (from ~ 0.5 dex to 0.1 dex), there

is no evidence of an obvious systematic bias in our dust measurements due to this uncertainty.

2.3.2 THE EFFECT OF THE TEMPERATURE PRIOR

The cold dust temperature prior is clearly going to impose some limits on the dust mass uncertainty from the fits. However, we argue that the prior temperature range from MAGPHYS used in this work is appropriate for a number of reasons. (i) A range of cold dust temperatures between 15-25 K is in fact a good description of the range of cold dust temperatures observed in galaxies (Dunne & Eales, 2001; Skibba et al., 2011; Smith et al., 2012c; Clemens et al., 2013; Clark et al., 2015). (ii) Smith et al. (2012a, their Appendix A) investigated whether a broader temperature prior should be used in MAGPHYS fitting. They found that changing the prior range suggested that only 6 per cent of their *Herschel* detected sources were actually colder than 15 K. They also demonstrated that adopting a wider temperature prior is not always appropriate given the non-linear increase in dust mass when the temperature falls below 15 K (where the SPIRE bands are no longer all on the Rayleigh-Jeans tail). At $T < 15$ K, symmetric errors in the fitted temperature produce a very skewed PDF for the dust mass and result in a population bias to higher dust masses for a distribution of Gaussian errors in cold temperature. Furthermore, in relation to SED fitting, a very cold dust component contributes very little to the luminosity in the FIR per unit mass, so it can be included by a fitting routine with very little penalty in χ^2 when the photometry in the FIR and sub-mm is of low SNR. Indeed Smith et al. (2012a) use simulated photometry to show that galaxy dust masses can be overestimated by (in excess of) 0.5 dex when widening the prior to below 15 K; they therefore strongly caution in using wider temperature priors for sources with weak sub-mm constraints (as is the case here). (iii) Though some galaxies have been shown to require colder dust temperatures than 15 K (Viaene et al., 2014; Clark et al., 2015; De Vis et al., 2017a; Dunne et al., 2018), the fraction of our sample with $> 3\sigma$ in at least one band that have dust temperatures < 16 K is < 9 per cent, ie they are not common in our sample.

As an example to illustrate the potential size of the effect, consider the case that 6 per cent of our galaxies had a true dust temperature of 12 K but instead we fit a temperature of 15 K due to the limited prior. We would underestimate the dust mass for this population by a factor of ~ 2.6 (ie 0.4 dex). However, 94% of galaxies have true temperatures in the range 15–25 K and since most of them do not have $> 3\sigma$ FIR fluxes they will have errors on the fitted temperature of order

± 5 K. Widening the prior to extend to 12 K would mean that 16 per cent of sources would be erroneously returned a temperature which was below 15 K resulting in a large positive bias to their dust masses.

Chapter 3 will provide a more thorough investigation of the effects on the DMF that result from poorly constrained photometry and cold dust temperatures for galaxies with low signal to noise in the FIR.

2.4 THE DUST MASS FUNCTION

2.4.1 VOLUME ESTIMATORS

To estimate the dust mass function, we use the V_{\max} method (Schmidt, 1968) with a correction to account for density fluctuations as suggested by Cole (2011).

$$\phi(M_i) = \sum_{n=1}^{N_i} \left(\frac{1}{V'_{\max,n}} \right) = \sum_{n=1}^{N_i} \left(\frac{1}{V_{\text{eff},n}} \frac{\langle \delta_f \rangle}{\delta_n} \right), \quad (2.1)$$

where $V_{\text{eff},n}$ is the effective volume accessible to a galaxy within the redshift range chosen, and the sum extends over all N_i galaxies in the bin M_i of the mass function; V'_{\max} is the density-corrected accessible volume; δ_n is the local density near galaxy n and $\langle \delta_f \rangle$ is a fiducial density for each field, both of these parameters are defined fully in the next section.

We use two methods to estimate the accessible volume for each galaxy. First we derive V_{\max} for each galaxy by estimating the maximum redshift at which that source would still be visible given the limiting magnitude of the survey. This requires taking into account both the optical brightness of each galaxy and the K -correction required as the galaxy SED is redshifted. The maximum redshift is not allowed to exceed the user-imposed redshift range of the sample (here we use $z < 0.1$). Using this maximum redshift and the area of the survey, an accessible comoving volume can be calculated. These maximum volumes are the same as used in W17 where the stellar mass function of galaxies in the GAMA sample is derived. Hereafter we refer to this method as pV_{\max} , since it is based on the simple photometric selection of the survey.

The second method we use to estimate the V_{\max} for each galaxy is based on a bivariate brightness distribution (BBD, see W17 for full details). This involves binning the data in terms of the two most prominent selection criteria for a given sample, eg optical brightness and mass, and aims to account for the selection effects that they introduce. Since our sample is optically selected, we choose the

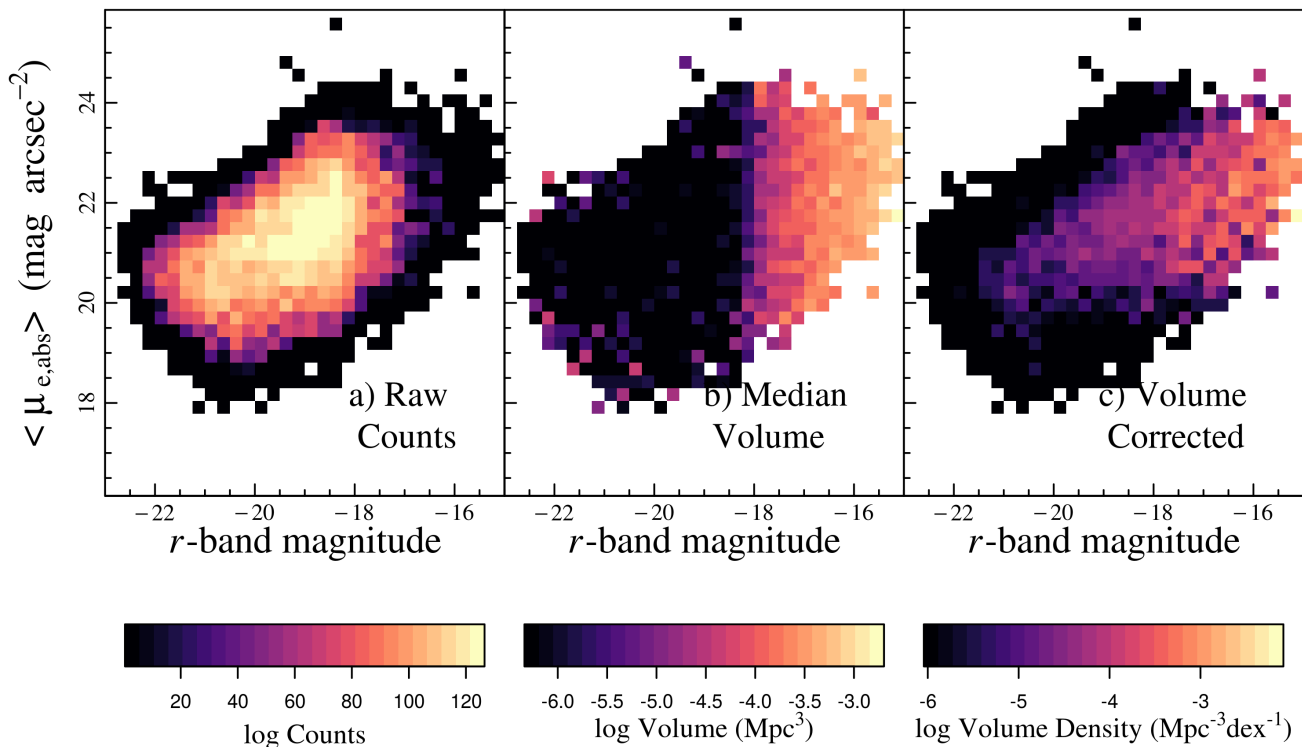


FIGURE 2.5 The bivariate brightness distribution (BBD) for our sample with surface brightness and r -band magnitude as the two “axes” (W17) with a) Raw counts in surface brightness/ r -band magnitude bins, b) Median volume in surface brightness/ r -band magnitude bins, c) Weighted counts, i.e. volume density in the surface brightness/ r -band bins. Each of the panels represents the BBD resulting from the median of 1000 Monte Carlo simulations where we perturb the r -band magnitude and surface brightness within their associated uncertainties.

absolute r -band magnitude, and for the second axis we choose surface brightness μ in the r -band (Loveday et al., 2012, 2015). We have estimated fluxes in all other bands for all galaxies, even if they are not significantly detected, so we do not directly apply any further selection criteria.

This method follows closely the format of the Galaxy Stellar Mass Function (GSMF) produced by W17 for the same sample; see also Figure 2.5, which is a diagrammatic representation of the BBD method. For each 2D r -band magnitude/surface brightness bin (Figure 2.5a), the volume enclosed by the median luminosity distance of the galaxies in the bin and the on-sky area of GAMA is calculated (Figure 2.5b) and doubled in order to find an ‘accessible volume’ for all of the galaxies in that bin (Figure 2.5c). Using twice the median value will provide an effective V_{\max} that, at some level, corrects for the incompleteness at large distances whatever the cause of the incompleteness. Thus the BBD method has

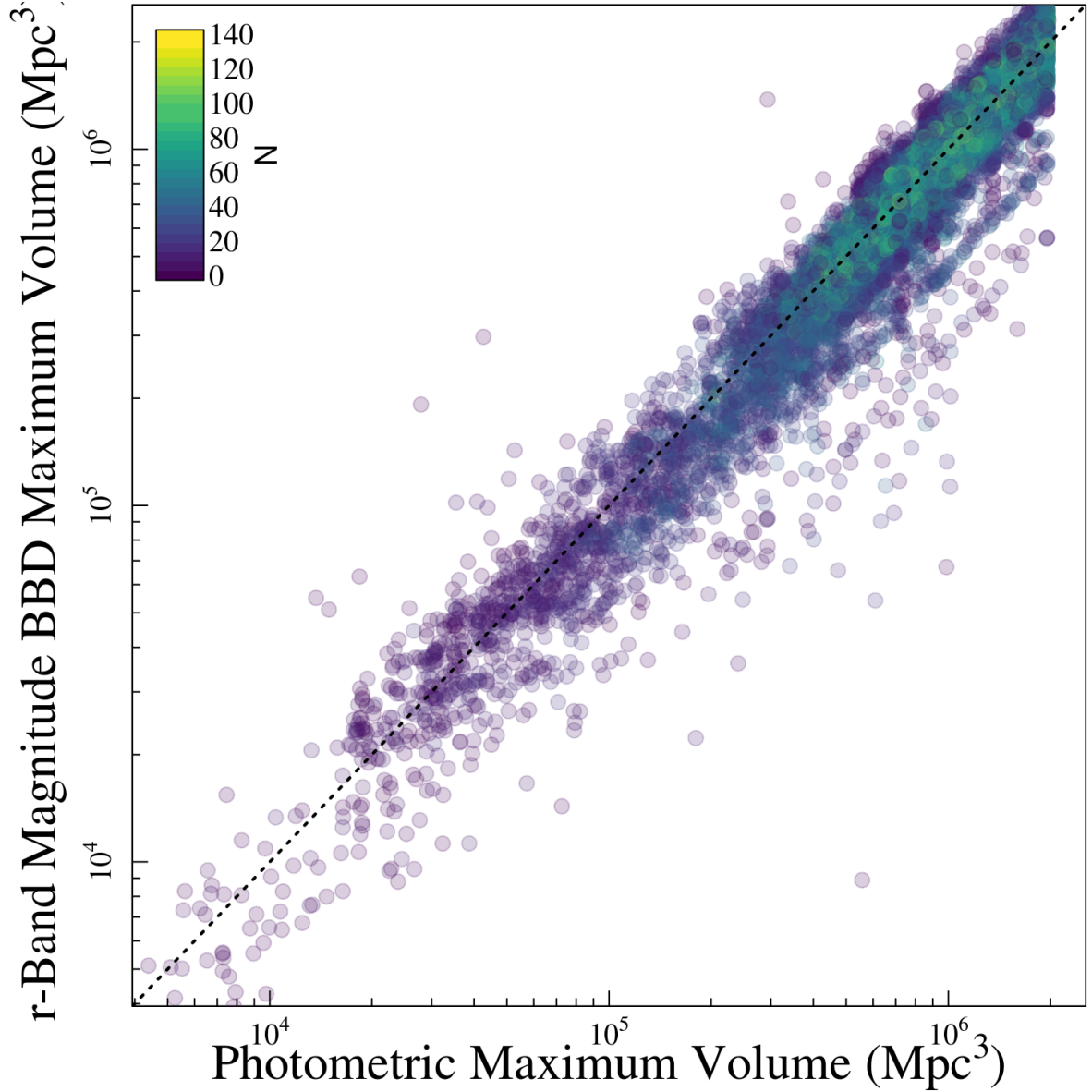


FIGURE 2.6 The maximum effective volumes for our galaxies at $z < 0.1$ derived using the pV_{max} method (x-axis), and BBD method using r -band magnitude and surface brightness as the two selection features (y-axis). The colour of the points is determined by the number of galaxies in the BBD bin that each galaxy resides in (Fig 2.5), as shown by the colour bar in the top left corner. We note that the number of galaxies per bin is the median resulting from 1000 Monte Carlo simulations, where we perturb the r -band magnitude and surface brightness within their associated uncertainties.

the benefit that it can correct for selection effects in two parameters at once. Using the median volume to determine the effective V_{\max} has the advantage that it is more statistically robust than the actual maximum volume observed in a given bin. However, this estimator is only strictly valid when the underlying galaxy distribution in any given bin is randomly and evenly distributed in space, so the average $V/V_{\max} = 0.5$. Given the large density fluctuations seen in the galaxy distribution, we cannot state that it is always the case, particularly for local, low-mass galaxies, which are hampered by small-number statistics and strongly affected by cosmic variance. It is more likely to be the case that $\langle V/V'_{\max} \rangle = 0.5$, i.e. the maximum volume weighted by density. To allow for these density fluctuations, we find a median weighted by the inverse of the density correction factors $\delta_n/\langle\delta_f\rangle$, defined in the next Section. Galaxies in over-dense regions are given less weight in the median compared to galaxies in under-dense regions, so any bias in the median volume from density fluctuations should be minimised. We note that in order to reduce noise introduced into the DMF from BBD bins with poor statistics we perform a Monte Carlo (MC) simulation whereby we perturb the quantities used for the two ‘axes’ of our BBD within their associated uncertainties and recalculate the BBD 1000 times and find the median BBD V_{\max} associated with each bin. In essence, this smooths the BBD by the estimated errors, and reduces the uncertainty in the BBD V_{\max} .

A direct comparison of the maximum volumes derived from both the pV_{\max} and BBD methods is shown in Figure 2.6 with the points coloured by the average number of galaxies in the BBD bin containing that galaxy across all the MC simulations. The largest deviation from the 1:1 line is seen for galaxies that lie in bins with a small number of galaxies contributing to the median volume. These volumes are generally low, meaning they are also strongly affected by cosmic variance. The pV_{\max} values are systematically higher by 0.8% on average than those derived from the BBD method, which translates to an average offset of 1% in the binned DMF values when determined by the median weighted by the error on the measurement.

2.4.2 DENSITY CORRECTIONS

Natural fluctuations in the density of the Universe can affect our measurement of the DMF e.g. G09 is known to be relatively under-dense and this can have a pronounced effect on the DMF [Driver et al. \(2011\)](#); [Dunne et al. \(2011\)](#); [Clark et al. \(2015\)](#). We therefore apply density corrections calculated by W17 to account for the

over- or under-densities present in each of the equatorial fields (see e.g. [Loveday et al. 2015](#)). These multiplicative corrections were derived as a function of redshift by determining the local density of the survey at the redshift of the galaxy in question. This is achieved by simply finding the running density as a function of redshift, and convolving this function with a kernel of width 60 Mpc. These were compared to the fiducial density $\langle\delta_f\rangle$, taken from a portion of the GAMA equatorial fields with stellar masses above $10^{10} M_\odot$ and over the redshift range $0.07 < z < 0.19$. This subset was chosen by W17 because of its high completeness level, uniform density distribution, and low uncertainty due to cosmic variance ($< 10\%$). To correct the effective volume for galaxy n , $V_{\text{eff},n}$, we simply multiply by a factor of $\delta_n/\langle\delta_f\rangle$ to obtain V'_{max} . The running densities are presented as a function of redshift for each GAMA field in [Figure 2.7](#).

To remove any spuriously low V'_{max} values introduced either by the density correction factor or by uncertainties in the calculated V'_{max} , we employ a clipping technique. We split the galaxies into 100 stellar mass bins and remove 5% of the most spurious V'_{max} values, and up-weight the remaining galaxies accordingly giving a final sample size of 15,750. For consistency with W17, the 5% clipping is performed on the total sample, i.e. before the imposition of the requirement of *H-ATLAS* coverage, translating to the removal of ~ 200 galaxies from the sample requiring *H-ATLAS* coverage that we use for this work. W17 perform a one-sided clipping, since higher V'_{max} values tend to be more stable than lower ones since brighter galaxies tend to have better constraints. Galaxies with high V'_{max} values also contribute less volume density and therefore tend to add less noise to their given bin than faint galaxies. Once removed, the weights of the remaining galaxies are scaled by the fraction of removed galaxies; this has the effect of smoothing the low-mass end of the DMF.

2.4.3 CALCULATING UNCERTAINTIES IN THE DUST MASS FUNCTION

We estimate uncertainties on the dust mass function using four techniques. First we use two estimates of the bootstrap error by (i) performing 1000 bootstrap resamplings on the sample of dust masses output by MAGPHYS (so-called simple bootstrap, hereafter SB), and (ii) by perturbing the dust masses for each realisation using the 16-84 percentile uncertainties in dust masses for each galaxy output by MAGPHYS (the perturbed bootstrap, hereafter PB, this will be investigated in the next Chapter). We also estimate uncertainties using a jackknife method in two

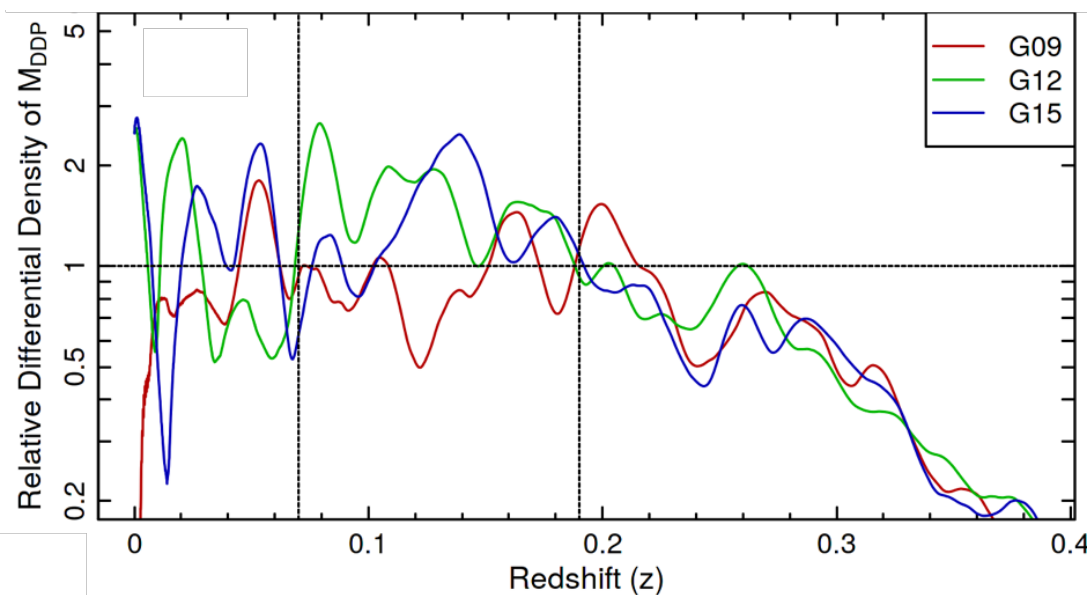


FIGURE 2.7 The running differential density as a function of redshift for the three GAMA fields taken from W17. DDP is the density defining population.

ways: (i) taking random subsamples of the data, and (ii) by splitting the sample by their location on the sky (hereafter on-sky jackknife).

2.4.3.1 BOOTSTRAP

A bootstrap analysis involves resampling with replacement. For each bootstrap realisation, a random sample of datapoints is drawn from the underlying dataset of the same length as that dataset. So for example, the first element of the dataset could be chosen five times and the next element could be omitted entirely. We perform two bootstrap analyses, one where we simply perform this resampling on the dust masses for the sample of galaxies, and another where we resample in the same way, but for every galaxy included in the realisation we *also* perturb the dust mass of that galaxy by using the 16th and 84th percentile outputs from MAGPHYS for each individual galaxy. This sets up a probability distribution from which to randomly draw a new dust mass. Once the resampling has been performed, the uncertainty estimate $\Delta\hat{\theta}_{\text{bootstrap}}$ can be computed using:

$$\Delta\hat{\theta}_{\text{bootstrap}} = \sqrt{\frac{1}{b} \times \sum_{i=1}^b (\hat{\theta}_i - \hat{\theta}_{(\cdot)})^2} \quad (2.2)$$

where b is the number of bootstrap realisations.

2.4.3.2 JACKKNIFE

The jackknife method is a method of resampling without replacement (Que-
nouille, 1949; Tukey, 1958). In order to perform a delete-1 jackknife analysis on a
given sample, one would remove each datapoint in turn to produce n jackknife
realisations, each of length $n - 1$, where n is the number of points in the sample. If
the sample is defined as

$$X = \{X_1, X_2, \dots, X_{n-1}, X_n\} \quad (2.3)$$

Each realisation, $X_{[i]}$, is therefore defined as $\{X_1, \dots, X_{i-1}, X_{i+1}, \dots, X_n\}$.

There is another form of the jackknife method, the delete- d jackknife in
which the dataset is split into d groups, all with as equal a size as possible, and
these groups are each removed in turn. We use this method here since it gives
a robust estimate of uncertainty with fewer resamplings, and therefore requires
less computational power. It essentially works in the same way as the delete-1
jackknife, except that each X_i is a dataset which contains n/d datapoints. The un-
certainty estimate, $\Delta\hat{\theta}_{\text{jackknife}}$, is then given by

$$\Delta\hat{\theta}_{\text{jackknife}} = \sqrt{\frac{d-1}{d} \times \sum_{i=1}^d (\hat{\theta}_i - \hat{\theta}_{(\cdot)})^2} \quad (2.4)$$

where $\hat{\theta}_i$ is the statistic of interest for realisation i , $\hat{\theta}_{(\cdot)}$ is the empirical average of
the statistic for all the jackknife realisations.

As well as producing estimates of uncertainty, the delete- d jackknife method
gives an interesting opportunity to test the effect of cosmic variance on our sample.
The use of density-corrected pV_{max} values should mitigate the impact of cosmic
variance on our DMFs; however, by setting up our jackknife regions in two dif-
ferent ways, we can test the efficiency of the density corrections. Firstly, we split
the sample up into d on-sky regions, and secondly, we split the sample into d ran-
dom groups. By removing a small section of the data for each jackknife realisation
we introduce a small bias into the DMF. Since the maximum accessible volumes
are calculated under the assumption that the full area of the GAMA/H-ATLAS
overlap is present, they will be slightly overestimated, resulting in a consistent un-
derestimation of the volume density ϕ across the DMF. The correction for this is
very simple, we scale the pV_{max} values by the ratio of the area used in the jackknife
realisation and the total area of the overlap, for the random jackknife we simply
assume that the area is equal for each subset. Since we use 108 jackknife subsets in

this analysis, the correction is very small, of the order $\sim 1\%$.

2.4.3.3 COMPARING THE UNCERTAINTIES

The jackknife and simple bootstrap methods for deriving uncertainties on the dust volume densities are compared with Poisson statistics in Figure 2.8. Unsurprisingly, uncertainties derived using simple Poisson statistics agree with all these error techniques at the high mass end ($M_d > 10^{7.8} M_\odot$), but underestimate the uncertainty in the mid and low dust mass bins ($M_d < 10^6 M_\odot$). The random jackknife and SB error estimates agree very well (within 0.5%), whereas the on-sky jackknife uncertainty is around 5% higher. This is not unexpected since this method will include a component of uncertainty from any cosmic variance that remains within the survey volume even after the correction for density fluctuations. The larger uncertainty for the on-sky jackknife suggests an error due to cosmic variance of at least 7 per cent, assuming that the difference is due only to cosmic variance. The cosmic variance estimator from Driver & Robotham (2010)³ gives an estimate of the cosmic variance of a survey given $N = 3$ independent volumes, an aspect ratio of $X = 4$ for the survey fields and a sampling volume of each independent field in the survey V :

$$\eta_{cv} = (1.00 - 0.03\sqrt{X-1}) \times \frac{219.7 - 52.4 \log_{10}(V) + 3.21 (\log_{10}(V))^2}{\sqrt{N}} \quad (2.5)$$

Equation 2.5 suggests an error in volume densities of 16.5 per cent given the entire sample survey volume. This is significantly higher than the effective cosmic variance that we measure in the jack-knife method, because we have already corrected the data for the density variations within the survey volume (Section 2.4.2). For the rest of this Thesis, we use the simple bootstrap method without perturbation of the dust mass (SB) for the data points for our DMF. The error bars on each data point is derived using the bootstrap with additional perturbation from the MAGPHYS uncertainties in individual galaxy dust masses (PB) since this takes into account both the variation within the sample and the uncertainty in the dust mass estimations themselves. As will be discussed in Chapter 3, the PB method is likely to give biased estimates when we fit functional forms to the DMF, but since it includes our mass uncertainties, it provides a better estimate of the uncertainties.

³ cosmocalc.icrar.org

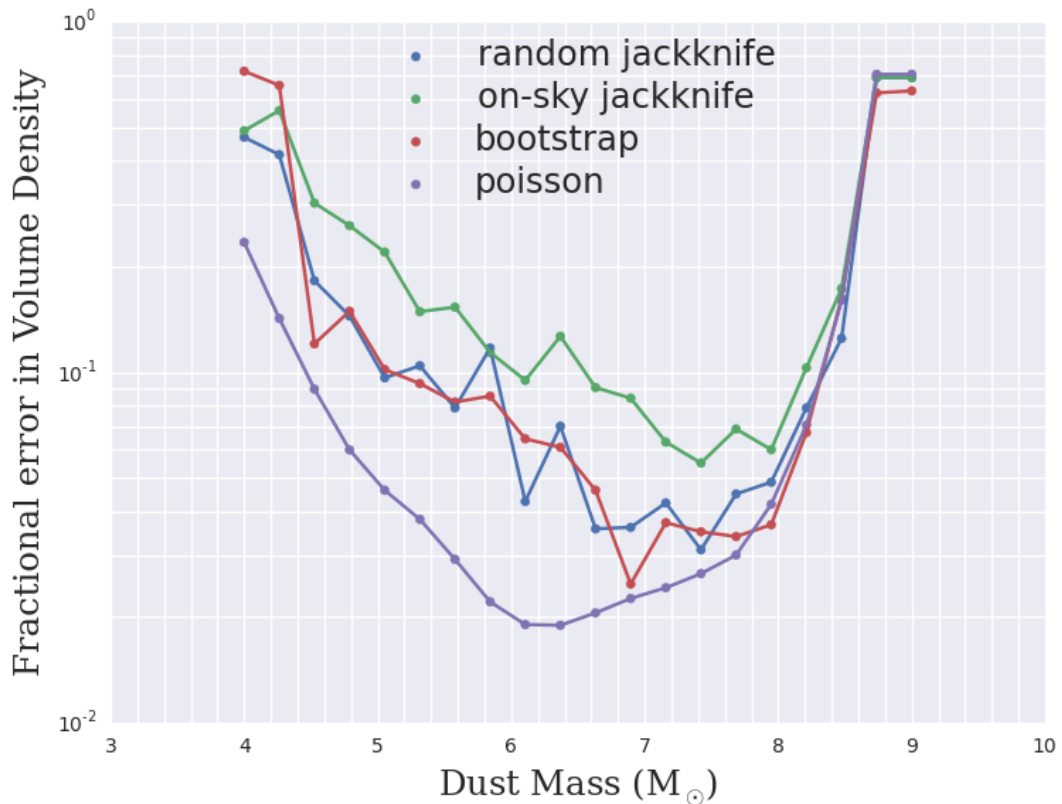


FIGURE 2.8 The fractional error on the volume density of the DMF with dust mass using the different methods for estimating error bars. With random jackknife analysis shown in blue, on-sky jackknife shown in green, the simple bootstrap shown in red, and a simple Poisson noise estimate in purple.

2.4.4 THE SHAPE OF THE DMF

The DMF (see Section 1.4), derived for the largest sample of galaxies to date, based on the optically selected GAMA sample, is shown in Figure 2.9 using the two methods described in Section 2.4.1 to calculate volume densities (the BBD and pV_{\max}). The offset seen in the dust mass volume densities at the low-mass end seen between the two methods can be attributed to the differences shown in Figure 2.6: the sources with the lowest dust mass tend to be those which are nearby and faint, and so most likely to be affected by small number statistics when calculating the BBD V_{\max} values. We have extended the function well below the low dust mass limit of all previous studies; indeed we extend to dust masses $\sim 10^4 M_{\odot}$ whilst dust masses above $10^{4.5} M_{\odot}$ are well constrained. We have therefore extended the observed range of the DMF by ~ 2 dex in dust mass compared to e.g. Dunne et al. (2011) and significantly reduced the statistical uncertainty compared to previous

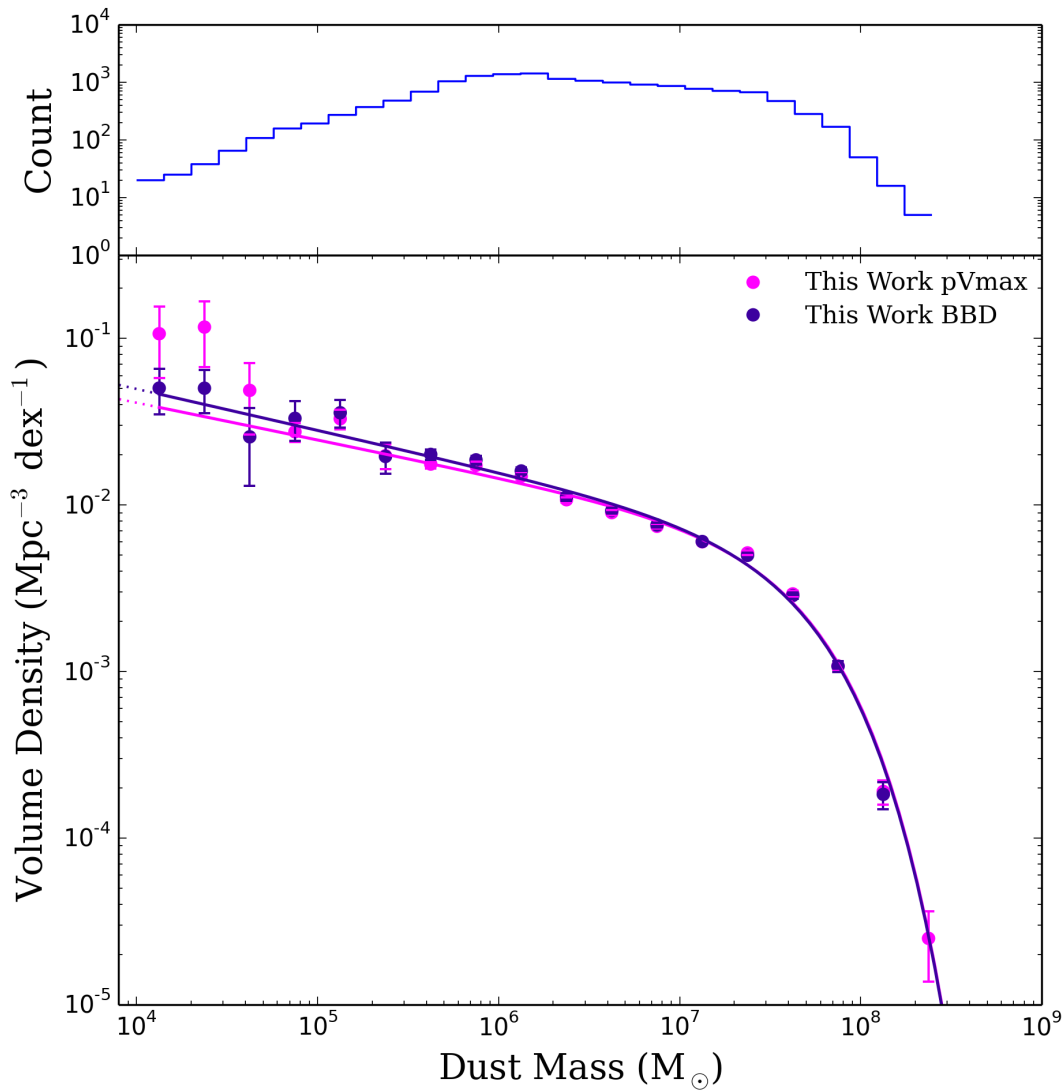


FIGURE 2.9 The dust mass functions for the GAMA/H-ATLAS sources at $z < 0.1$ derived using the traditional photometric V_{\max} method (pV_{\max} , purple) and the BBD method (blue) - see Section 2.4.1. The data points show the observed values corrected for over and under densities in the GAMA fields (see W17 and Section 2.4.2). The solid lines are the best fitting (minimum χ^2) single Schechter functions from our simple bootstrap (SB) measurements. Error bars on the data points are derived from our perturbed bootstrap (PB) measurements. The total number of sources in each bin is shown in the top panel.

measurements (with $\sim 70\times$ the sample size, see Section 2.5 for more details).

Following Dunne et al. (2011), we fit a single Schechter function (SSF) (Schechter, 1976) (Eq 2.6, see also Section 1.4) to the observed DMF, using χ^2 minimisation to derive the best-fit values for α , M^* and ϕ^* which are the power law index of the low-mass slope, the characteristic mass (location of the function’s ‘knee’), and the number volume density at the characteristic mass respectively. This takes the form (in $\log M$ space):

$$S(M; \alpha, M^*, \phi^*) = \phi^* e^{-10^{\log M - \log M^*}} \times \left(10^{\log M - \log M^*}\right)^{\alpha+1} d \log M, \quad (2.6)$$

where we have explicitly included the factor $\ln 10$ in the definition of ϕ^* , such that ϕ^* is in units of $\text{Mpc}^{-3} \text{dex}^{-1}$.

We fit a Schechter function to each of our bootstrap realisations, and use the median of the resulting values as the best fit value for each parameter. We use the standard deviation between the values to estimate uncertainty on the parameters. The parameters for both the pV_{max} and BBD fits are quoted in Table 2.1 with the fits shown in Figure 2.9. Note that cosmic variance will introduce further uncertainty in our measurements. This will mostly be seen as an increased uncertainty on ϕ^* , though both M^* and α will also have slightly larger errors.

The integrated dust mass density parameter Ω_d at $z \leq 0.1$ is derived by using the incomplete gamma function to integrate down to $M_d = 10^4 M_\odot$ (our lower limit on measurement of the form of the DMF). This gives $(1.11 \pm 0.02) \times 10^{-6}$ for both the pV_{max} and BBD methods. For comparison, our Ω_d values calculated without imposing this limit are $(1.11 \pm 0.02) \times 10^{-6}$ and $(1.06 \pm 0.01) \times 10^{-6}$ for the pV_{max} and BBD methods respectively, so the difference is very small. The value $\Omega_d = 1.11 \pm 0.02 \times 10^{-6}$ corresponds to an overall fraction of baryons (by mass) stored in dust $f_{m_b}(\text{dust}) = (2.40 \pm 0.04) \times 10^{-5}$, assuming the Planck $\Omega_b = 45.51 \times 10^{-3} h_{70}^{-2}$ (Planck Collaboration XIII, 2016). In comparison the mass fraction of baryons in stars from the GAMA sample of W17 is $f_{m_b}(\text{stars}) = (3.66_{-0.51}^{+0.53}) \times 10^{-2}$ (corrected to the same cosmology)⁴.

⁴ Note that Wright et al. (2017) used the incorrect value of Ω_b as they had assumed that the h quoted in Table 4 of Planck Collaboration XIII (2016) was $h_{67.7}$ (ie mistakenly assumed this was h_{planck} rather than h_{100}).

| Survey | M^* ($10^7 h_0^2 M_\odot$) | α | ϕ^* ($10^{-3} h_0^3 \text{Mpc}^{-3} \text{dex}^{-1}$) | Ω_d (10^{-6}) |
|------------------------------------|-----------------------------------|-------------------------|---|-----------------------------|
| C13 | 5.27 ± 1.56 | -1.34 ± 0.4 | 4.78 ± 1.81 | 1.1 ± 0.22 |
| D11 | $3.9^{+0.74}_{-0.63}$ | $-1.01^{+0.17}_{-0.14}$ | $8.09^{+1.9}_{-1.72}$ | 1.01 ± 0.15 |
| V05 | $6.0^{+0.45}_{-0.55}$ | $-1.39^{+0.03}_{-0.02}$ | $3.33^{+0.74}_{-0.5}$ | 0.94 ± 0.44 |
| This work single pV_{max} | 4.65 ± 0.18 | -1.22 ± 0.01 | 6.26 ± 0.28 | 1.11 ± 0.02 |
| This work single BBD | 4.67 ± 0.15 | -1.27 ± 0.01 | 5.65 ± 0.23 | 1.11 ± 0.02 |

TABLE 2.1 Single Schechter function (SSF) values for dust mass functions in the literature and this work. The other literature studies include: C13 - [Clemens et al., 2013](#), D11 - [Dunne et al., 2011](#), V05 - [Vlahakis et al., 2005](#). All have been scaled to the same dust mass absorption coefficient used here. The [Dunne et al. \(2011\)](#) DMF includes a correction of 1.42 for the density of the GAMA09 field ([Driver et al., 2011](#)) and the fits in this work include the density-weighted corrections from W17.

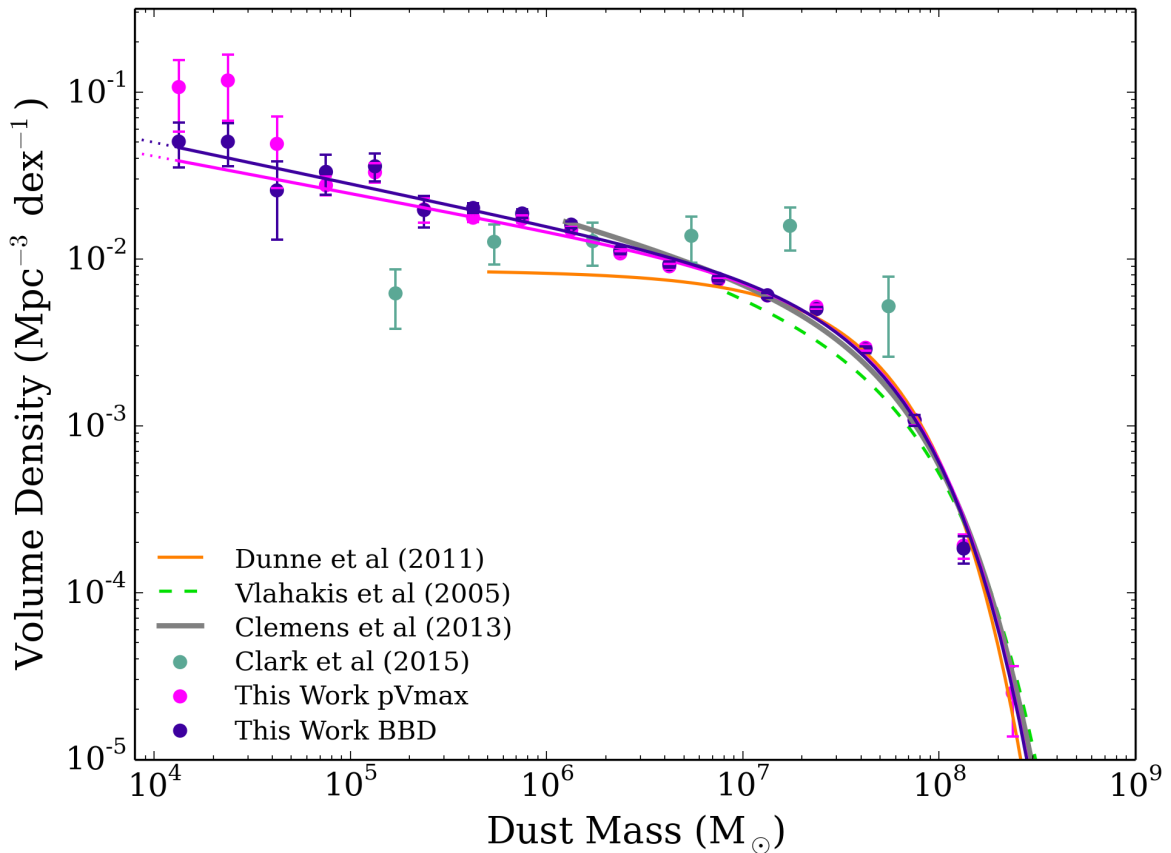


FIGURE 2.10 Comparison of the DMF from this work with those from the literature. We compare with (i) the blind, local $z < 0.01$ galaxy sample from [Clark et al. \(2015\)](#) (ii) the all-sky local star-forming galaxies from the bright *Planck* catalogue from [Clemens et al. \(2013\)](#) (iii) the ground-based submm measurements of local optical galaxies from [Vlahakis et al. \(2005\)](#) and (iv) the 222 galaxies out to $z < 0.1$ from the *H-ATLAS* survey ([Dunne et al., 2011](#)). Schechter fit parameters for this work and the literature studies are listed in [Table 2.1](#). The [Dunne et al. \(2011\)](#) DMF includes the correction factor of 1.42 for the density of the GAMA09 field ([Driver et al., 2011](#)) whilst our data points have been weighted by density correction factors from W17.

2.5 COMPARISON WITH PREVIOUS DUST MASS FUNCTIONS

We compare the single Schechter function fits (SSF) parameters derived here with those from the literature ([Figure 2.10](#) and [Table 2.1](#)). We also compare the confidence intervals for our derived parameters in [Figure 2.11](#) with previous work. For the first time we are able to directly measure the functional form at masses below $5 \times 10^5 M_{\odot}$ and determine the low mass slope of the DMF, α . We see that there is a good overall match at the high mass end with the [Dunne et al. \(2011\)](#) DMF,

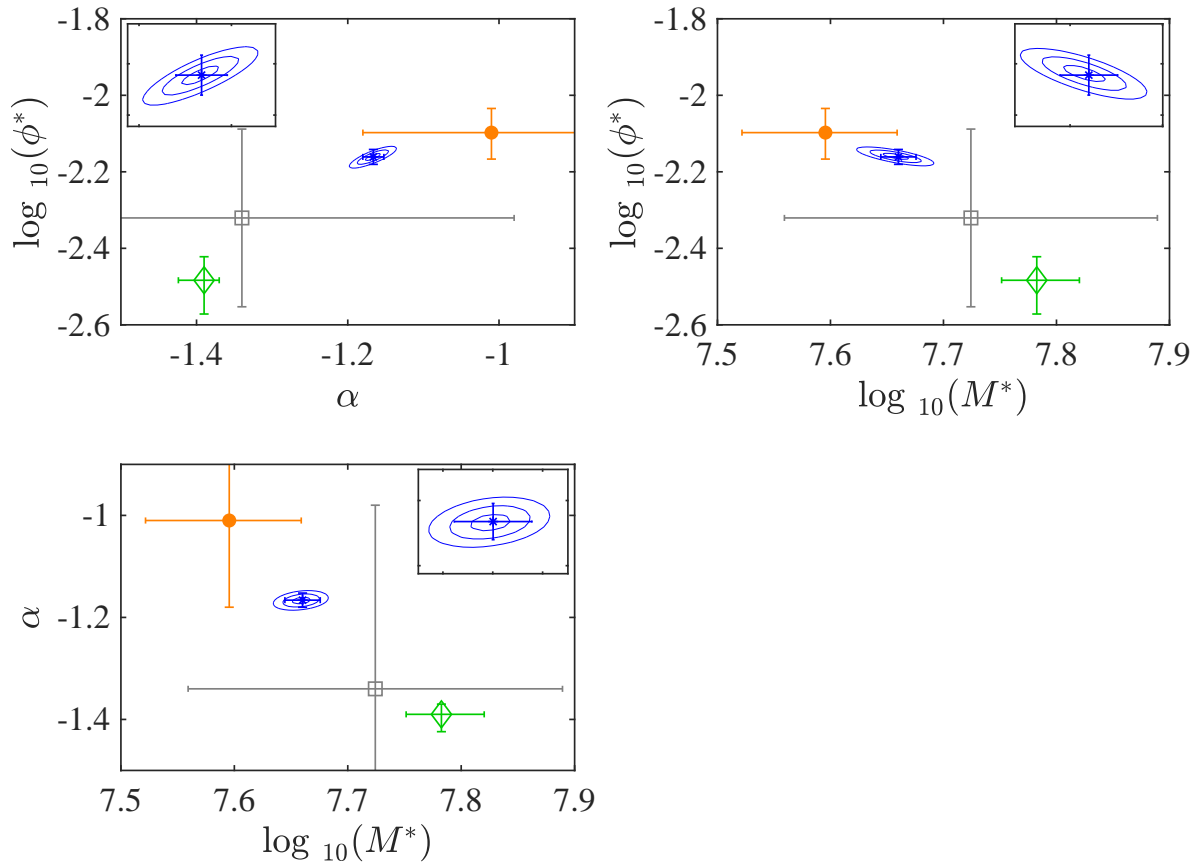


FIGURE 2.11 The confidence intervals for the pV_{\max} single Schechter dust mass function fit parameters derived in this work (blue ellipses) showing the correlation between the fit parameters (insets) and comparison with previous literature values (denoted by coloured data points). Note that ϕ^* is in units of $\text{Mpc}^{-3}\text{dex}^{-1}$. For simplicity, we simply show error bars on our fit parameters from the $\Delta\chi^2 = 1$ for each parameter (these are consistent with errors derived from the bootstrap process described in Section 6.4). The contours are therefore the 1, 2, 3 σ values of $\Delta\chi^2$ for the parameter slice centred on the best fit for the non-plotted 3rd parameter. Green denotes Vlahakis et al. (2005), orange represents Dunne et al. (2011), and grey shows Clemens et al. (2013). We note that the error bars on the Vlahakis et al. (2005) values were derived using Poisson statistics, and so may be an underestimate of the true error in their measurements.

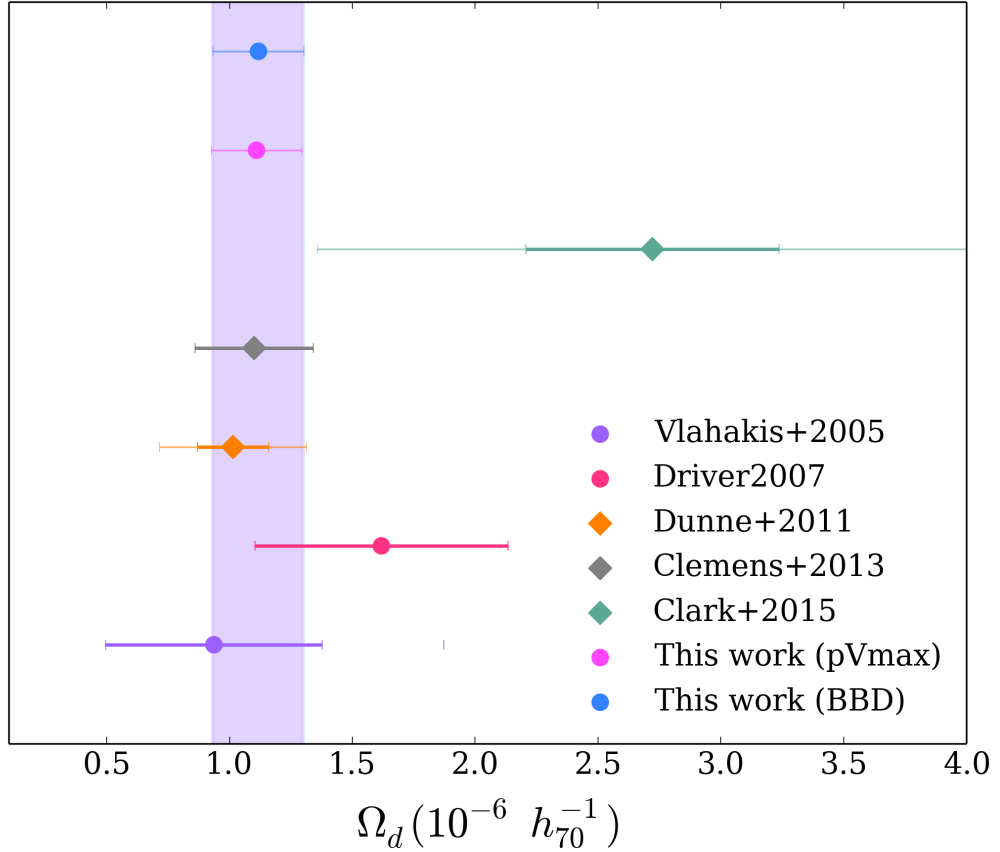


FIGURE 2.12 Comparison of the dust mass densities Ω_d from this work with those from the literature. We compare with (i) the blind, local $z < 0.01$ galaxy sample from [Clark et al. \(2015\)](#) (ii) the all-sky local star-forming galaxies from the bright *Planck* catalogue from [Clemens et al. \(2013\)](#) (iii) the ground-based submm measurements of local optical galaxies from [Vlahakis et al. \(2005\)](#) and (iv) the 222 galaxies out to $z < 0.1$ from the *H-ATLAS* survey ([Dunne et al., 2011](#)). The dust density parameter (Ω_d) measurements are scaled to the same cosmology, with diamonds representing dust-selected measurements and circles representing optically-selected samples (including this work). We show both the results from the pV_{\max} and BBD for the single Schechter fit (SSF) DMFs. The solid error bars on Ω_d indicate the published uncertainty derived from the error in the fit whilst the transparent error bars indicate the total uncertainty derived by combining the published uncertainty and the cosmic variance uncertainty estimate for that sample (where known). We note that the solid error bars indicating the uncertainty from our bootstrap analysis lie within the point itself for both our BBD and pV_{\max} values. The [Dunne et al. \(2011\)](#) DMF includes the correction factor of 1.42 for the density of the GAMA09 field ([Driver et al., 2011](#)) whilst our data points have been weighted by density correction factors from W17. The shaded vertical region emphasises the range of Ω_d derived from our SSF fits to the DMFs with width showing the error from cosmic variance.

but at the faint end, the DMF is steeper than predicted from the [Dunne et al. \(2011\)](#) function suggesting larger numbers of cold or faint galaxies than expected. We note that the [Dunne et al. \(2011\)](#) sample is different to our DMF in two ways (i) it is a dust-selected (or rather 250- μm -selected) sample rather than optically selected and (ii) was drawn from the *H*-ATLAS science demonstration phase data, which is only 16 sq deg of the GAMA09 field at $z < 0.1$ and is known to be under-dense compared to the other GAMA fields ([Driver et al., 2011](#)). Our DMF is also similar to the optically-selected PSCz-extrapolated DMF from [Vlahakis et al. \(2005\)](#) (where they assume a 20 K cold dust component for their sources) at the highest masses, though we find a higher space density of galaxies around the ‘knee’ of the function potentially due to the higher redshift limit probed in this study and improvement in statistics in this work. In general, the 2-d parameter comparisons in [Figure 2.11](#) show that the DMF in this work has intermediate values of α , M^* and ϕ^* in comparison to the [Clemens et al. \(2013\)](#), [Vlahakis et al. \(2005\)](#), and [Dunne et al. \(2011\)](#) parameters but here we have tighter constraints due to the larger sample of sources. Differences could also arise because of the variation of best-fit parameters with the minimum mass limit of the fit since all the surveys have different mass ranges (we will return to this in [Chapter 3](#)). Note that the fit parameters quoted in this work for [Clemens et al. \(2013\)](#) are different to those that appear in their paper and in [Clark et al. \(2015\)](#). The reason for this is that [Clemens et al. \(2013\)](#) did not include the $\ln 10$ factor when calculating their integrated dust densities, and [Clark et al. \(2015\)](#) erroneously attributed this error to a missing per dex factor in ϕ^* . In fact the error in [Clemens et al. \(2013\)](#) was only in converting from ϕ^* to ρ_{d} . We discuss the implications of changing the minimum mass limit of our fits in [Chapter 3](#).

Previous measurements of Ω_{d} are shown in [Figure 2.12](#) (all scaled to same cosmology and κ). Our measurement is consistent with [Dunne et al. \(2011\)](#), [Vlahakis et al. \(2005\)](#), [Clemens et al. \(2013\)](#) and with the lower range of [Driver et al. \(2007\)](#) but significantly smaller than the [Clark et al. \(2015\)](#) value. However, the latter measurement is subject to a large uncertainty due to cosmic variance (46.6 per cent, [Driver et al., 2007](#)) in comparison to the 7-17 per cent for this work. We note that the cosmic variance in the [Dunne et al. \(2011\)](#) study is 25.7 per cent for $z < 0.1$ ([Driver et al., 2011](#)).

2.6 CONCLUSIONS

We measure the DMF for galaxies at $0.002 \leq z \leq 0.1$ using a modified V_{\max} method for 15,750 sources. This represents the largest study of its kind both in terms of numbers of galaxies and the volume probed at this redshift range. Our main findings are:

- Despite the sources that have measurements below 3σ in one or more *Herschel* SPIRE bands, we show that the MAGPHYS derived errors of 0.4, 0.18, 0.14 and 0.1 dex for galaxies with flux $> 3\sigma$ in zero, one, two and three SPIRE bands do reasonably represent the uncertainty in dust mass.
- We use a single Schechter function fit (SSF) to our data to compare with previous observations and we extend the DMF down to lower dust masses than probed before, constraining the faint end slope below $10^5 M_{\odot}$.
- We compare the dust mass function derived using the traditional pV_{\max} method and the BBD method which allows us to incorporate selection effects using the surface-brightness and r -band magnitude plane, and find both ultimately produce similar results. The best fitting single Schechter function for the $z \leq 0.1$ DMF has $\alpha = -1.22 \pm 0.01$, $M^* = (4.65 \pm 0.18) \times 10^7 h_{70}^2 M_{\odot}$, $\phi_* = (6.26 \pm 0.28) \times 10^{-3} h_{70}^3 \text{Mpc}^{-3} \text{dex}^{-1}$, and $\Omega_d = (1.11 \pm 0.02) \times 10^{-6}$. The overall fraction of baryons (by mass) stored in dust is $f_{m_b}(\text{dust}) = (2.40 \pm 0.04) \times 10^{-5}$, roughly 1000 times less than the fraction of baryons in stars. There is an additional uncertainty from cosmic variance of 7-17%, with the lower limit representing our measured effective error due to cosmic variance, and the latter a more pessimistic uncertainty derived using the [Robotham et al. \(2010\)](#) estimator.

CHAPTER 3

INVESTIGATING BIAS IN THE DMF

‘It’s probably quite difficult to organise trillions of particles separated by light years to improve their concerted efforts.’

GEORGE SMITH

In Chapter 2, the optically selected dust mass function (DMF) at redshift $z \leq 0.1$ was determined, probing lower dust masses than before, and constraining the faint end slope below $M_d = 10^5 M_\odot$ for the first time. In this Chapter we attempt to investigate potential biases in that measurement. The work in this Chapter has been published in [Beeston et al. \(2018\)](#).

3.1 INTRODUCTION

Although the GAMA sample is highly complete (97%), there are still multiple ways in which our sample could be biased. For example, since our DMF is built from an optically-selected sample (i.e. not selected for its dust properties) there are a large fraction of galaxies which are not detected in any of the FIR *Herschel* bands. Indeed we saw in Chapter 2 that around 30% of our galaxies have a combined signal to noise ratio of less than one across all five *Herschel* bands. This makes the measurements we have for the dust properties of individual sources uncertain. Another concern is that we may be biased due to the dependence of MAGPHYS on its priors or indeed in our choice of fitting parameters (the Schechter function). Here we test multiple potential sources of bias or errors: in Section 3.2, we investigate the affect of changing the axes chosen for the Bivariate Brightness

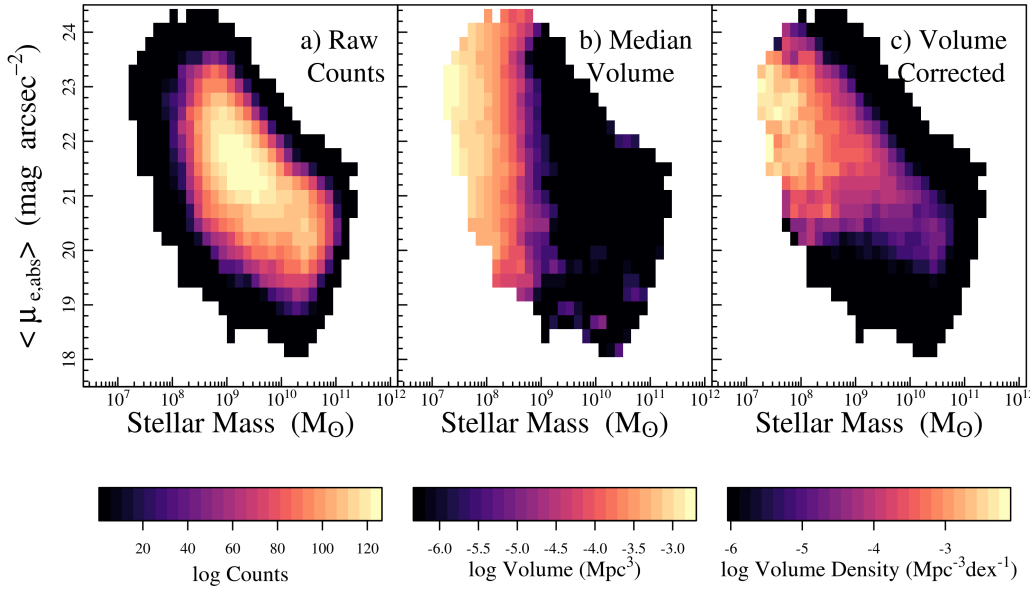


FIGURE 3.1 The BBD for our sample with r -band magnitude and surface brightness as the two ‘axes’ (W17) a) Raw counts in stellar mass/surface brightness bins, b) Median volume in the stellar mass/surface brightness bins, c) Weighted counts, i.e. volume density in the stellar mass/surface brightness bins. Each of the panels represents the BBD resulting from the average of 1000 Monte Carlo simulations where we perturb the stellar mass and surface brightness within their associated uncertainties.

Distribution (BBD) method. Section 3.3 tests the affect of poor signal to noise on our individual galaxy flux measurements in both the galaxy properties output by MAGPHYS, and in the resulting DMF. We test for potential sources of bias from the parameters chosen to fit the dust mass function in Sections 3.4-3.5. Finally we test for Eddington bias in the DMF due to scatter in the mass error potentially moving galaxies into neighbouring dust mass bins (Section 3.6).

3.2 EFFECT OF CHANGING THE BIVARIATE DUST MASS FUNCTION ESTIMATOR TO STELLAR MASS-SURFACE BRIGHTNESS

We also performed the BBD analysis described in Section 2.4.1 with stellar mass and surface brightness as the two ‘axes’ in order to compare to W17 who used these two quantities as their BBD axes when deriving the galaxy stellar mass function (GSMF) of the same volume and sample. We show the raw counts of galaxies in $M_s/\mu_{e,abs}$ bins in Figure 3.1a, the median volume in Figure 3.1b, and

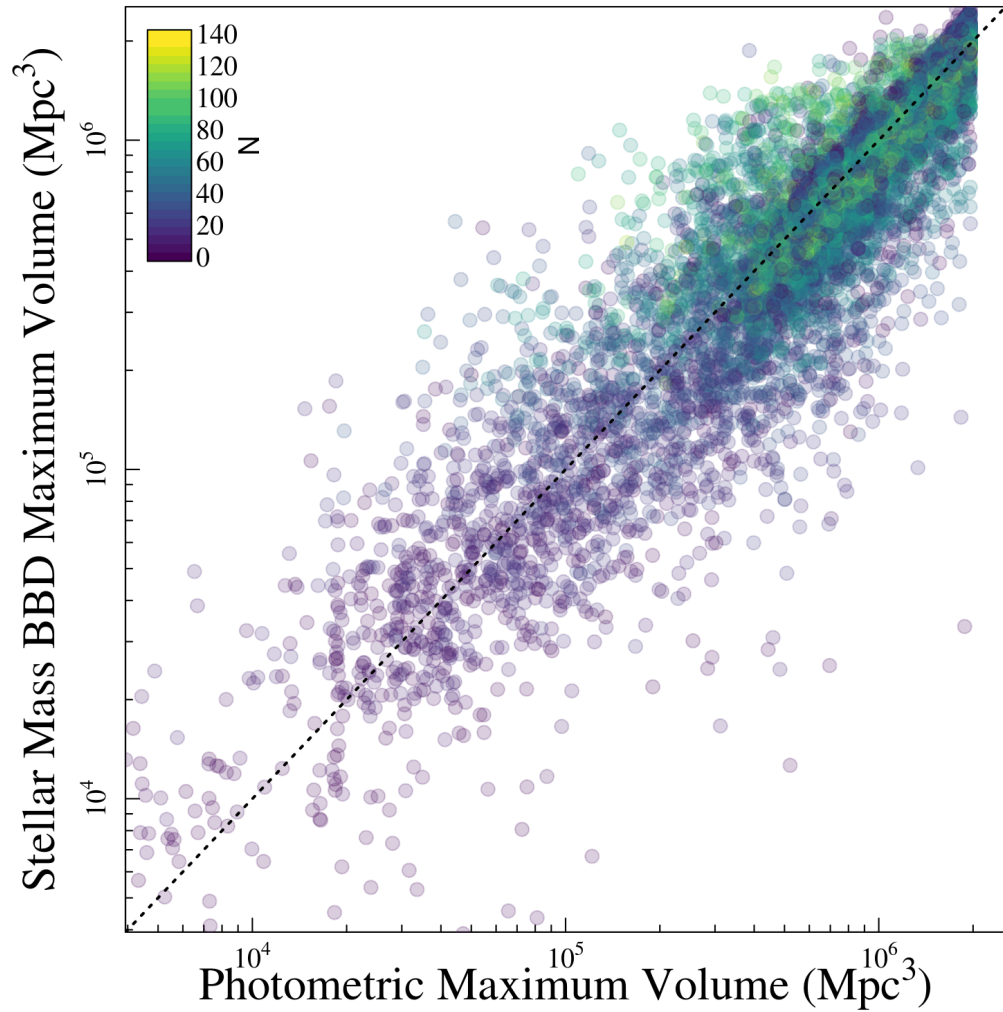


FIGURE 3.2 The maximum effective volumes for our galaxies at $z < 0.1$ derived using the pV_{\max} method (x-axis), and BBD method using stellar mass and surface brightness as the two selection features (y-axis). The colour of the points is determined by the number of galaxies in the BBD bin that each galaxy resides in (Fig 3.1), as shown by the colour bar in the top left corner.

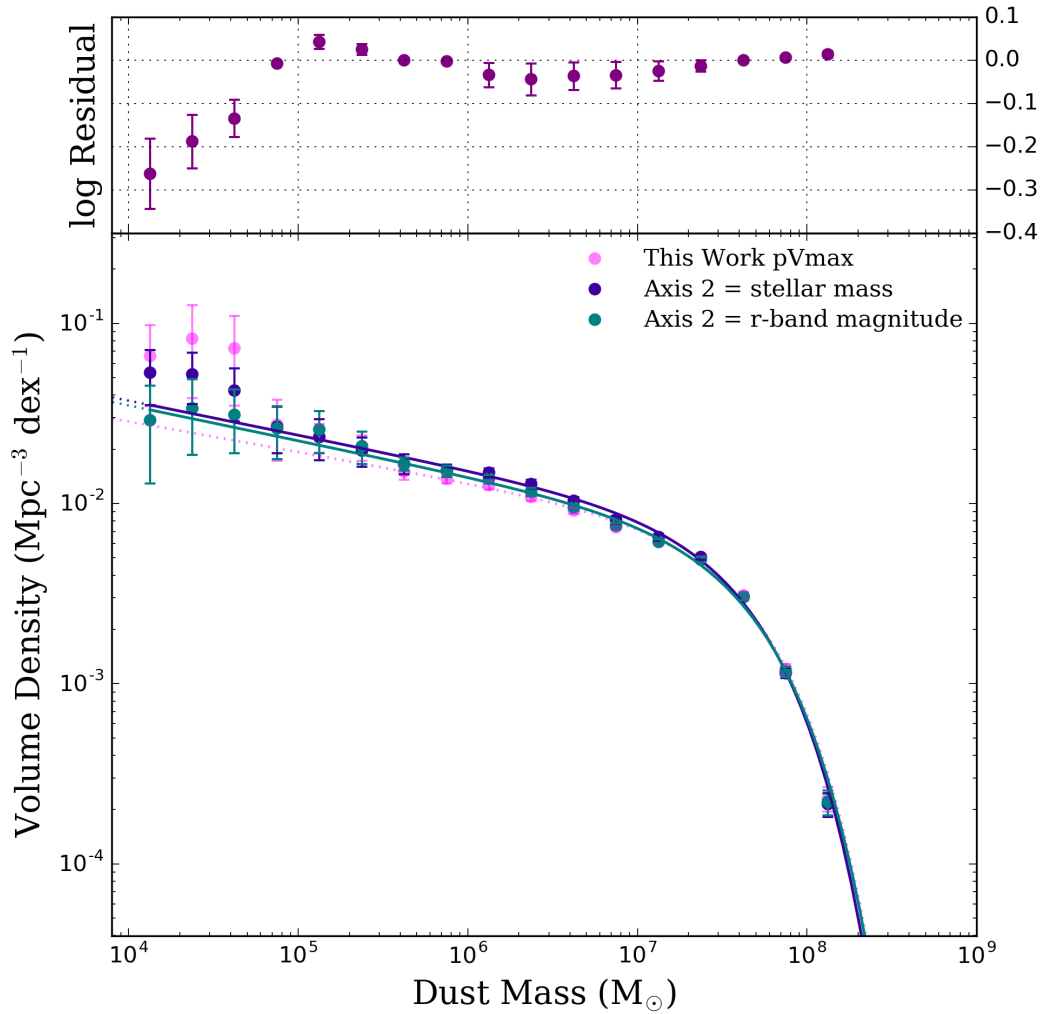


FIGURE 3.3 The DMF derived using a stellar mass and surface brightness BBD (blue - this Chapter) and an r -band magnitude and surface brightness BBD (green - Chapter 2) for the GAMA/ H -ATLAS sources at $z \leq 0.1$. Also shown are the pV_{\max} values for comparison in magenta. The data points show the observed values and the solid lines are the best-fitting (χ^2) single Schechter functions to the data. Error bars are derived from a bootstrap analysis and the data points have been corrected due to over and under densities in the GAMA fields (see W17). The residual between the two BBD DMFs is shown in the top panel, as points with error bars in purple.

the weighted counts (volume density) in Figure 3.1c. In comparison to Figure 2.5, we can see that the shapes and trends of the BBDs with r -band/ $\mu_{e,abs}$ or $M_s/\mu_{e,abs}$ as the second axis are very similar. The main difference between the two is that the shape of the latter reflects a slightly stronger evolution of stellar mass compared to r -band magnitude with surface brightness.

Figure 3.2 reproduces Figure 2.6 but now with stellar mass as the second ‘axis’ of the BBD. The pV_{max} and $M_s/\mu_{e,abs}$ are coloured by the number of galaxies in the BBD bin containing that galaxy. The largest deviations from the 1:1 line are seen when the galaxy lies in a more sparsely populated bin, generally these volumes are low and are therefore subject to large cosmic variance. The pV_{max} values are systematically higher by 1.2% on average than those derived from the $M_s/\mu_{e,abs}$ BBD method, which gives an average offset of 6% in the binned DMF values. This is because the largest differences in the binned DMF values come from the low dust mass end where BBD bins are more likely to be below the required 4 galaxies per bin. The scatter about the 1:1 line is large compared to Figure 2.6 since a galaxy’s r -band magnitude has more reason to impact the sample selection than its stellar mass, and so ultimately the r -band magnitude BBD from Chapter 2 is likely to be a more important selection criteria than the stellar mass tested here.

Finally, Figure 3.3 compares the resulting DMFs from using r -band magnitude or stellar mass as the second ‘axis’ of the BBD, where the surface brightness is used for the remaining axis. The Schechter fit parameters are compared in Table 3.1, and the residuals between the datapoints resulting from the both the $M_s/\mu_{e,abs}$ and r -band magnitude/ $\mu_{e,abs}$ BBD are shown in Figure 3.3. The Schechter fit parameters for both sets of BBD DMFs agree within uncertainties; however, the r -band magnitude BBD is closer to the pV_{max} fit parameters. The pV_{max} DMF points are offset from the stellar mass BBD by ~ 6 per cent, and the r -band magnitude BBD by ~ 3 per cent on average.

We also tried using dust mass and stellar mass as the two axes for the BBD since there is a dichotomy seen in the dust properties for ETGs and LTGs (as well as for sources with and without a 3σ measurement in any SPIRE band, Section 2.3.2). We found no significant departure from either the r -band magnitude or the stellar mass BBD and so we cannot say that either split strongly affects the resulting BBD V_{max} since it is not possible to deconvolve the effects that each split may have on the accessible volumes.

| | Axis 2 | |
|--|------------------|---------------------|
| | Stellar Mass | r -band Magnitude |
| α | -1.24 ± 0.02 | -1.27 ± 0.01 |
| M^* ($10^7 M_\odot$) | 4.32 ± 0.17 | 4.67 ± 0.15 |
| ϕ^* ($10^{-3} h_{70}^3 \text{Mpc}^{-3} \text{dex}^{-1}$) | 6.94 ± 0.36 | 5.65 ± 0.23 |
| Ω_d (10^{-6}) | 1.11 ± 0.02 | 1.11 ± 0.02 |

TABLE 3.1 Single schechter function fit values for dust mass functions resulting from the BBD with the second axis being stellar mass (this Chapter), and for the second axis being r -band magnitude (Chapter 2), both have surface brightness μ on the first axis. We include the density-weighted corrections from W17.

3.3 TESTING THE EFFECT OF LOW SIGNAL-TO-NOISE PHOTOMETRY

In Section 2.3.2, we found that when a galaxy has poor FIR constraints, the cold dust temperature PDF from MAGPHYS simply reflects the prior temperature distribution. Since the FIR data provide the only constraints on the cold temperature, this is the correct result that MAGPHYS should output. However, taking the median of the PDF in these cases may lead to a systematic bias in the temperature, which would in turn lead to a bias the dust mass. Roughly one third of our sample has a combined FIR signal to noise, i.e. the sum of SNRs of all *Herschel* fluxes for each source, of less than 1, so potentially, it is a significant effect. Here we attempt to quantify how this effect propagates into in our estimates of the DMF. In panel (a) of Figure 3.4 we show the median cold dust temperature output by MAGPHYS as a function of total FIR signal to noise. As the total FIR signal to noise decreases there is a clear trend for galaxies to be assigned a cold dust temperature nearer to 20 K, the median of the MAGPHYS temperature prior. Panel (b) shows the distribution of cold dust temperatures for sources with a total FIR signal to noise of at least 7σ (in black), where the constraints on the dust temperature are very good. Assuming the underlying temperature distribution is independent of observed signal to noise, we can use this as a new prior (blue) for the temperatures of sources which have poor FIR constraints.

We next perform another form of perturbed bootstrap (PB, Chapter 2),

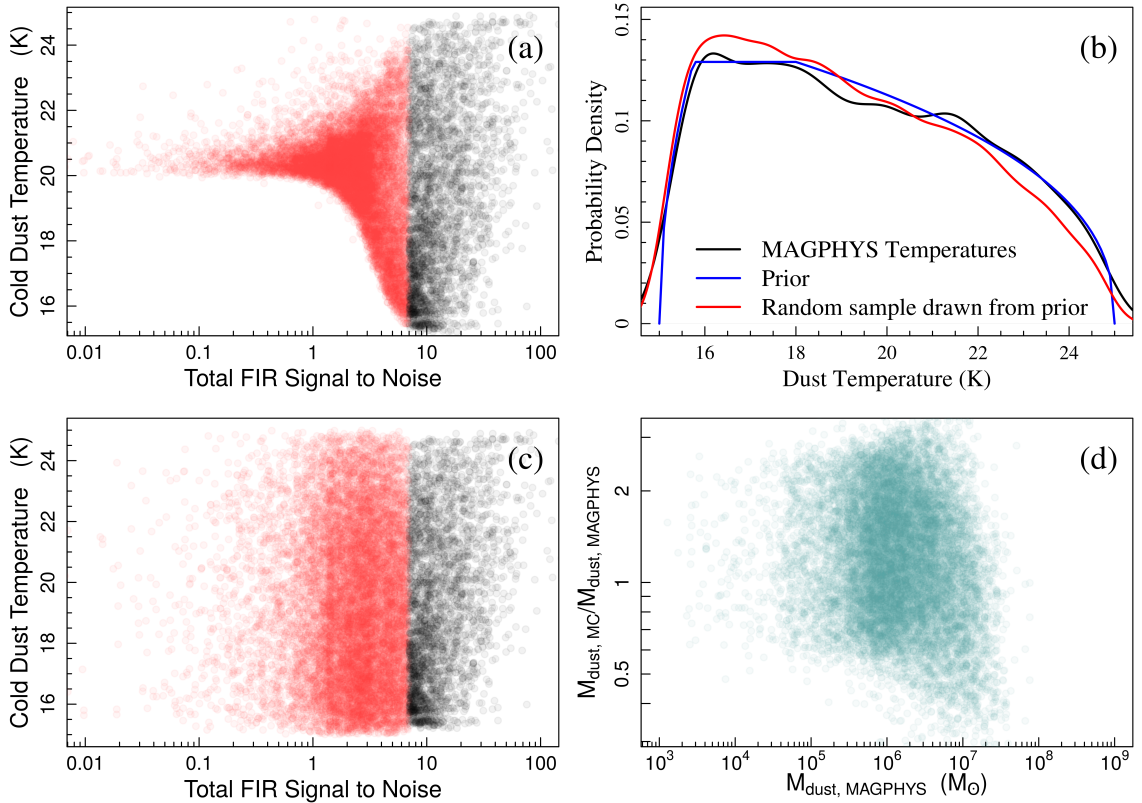


FIGURE 3.4 (a) The cold dust temperature from MAGPHYS as a function of total FIR signal to noise, in red all those sources below 7σ , in black all those sources with 7σ or greater total FIR flux. (b) In black the probability density function (PDF) of temperatures from MAGPHYS for those galaxies with a total FIR signal to noise greater than 7 using kernel density estimation (KDE), in blue the prior we use to describe this PDF, in red a KDE of one example of a random draw of temperatures from this prior. (c) In red we show one Monte Carlo simulation of new cold dust temperatures for sources below 7σ total FIR flux, in black the MAGPHYS cold dust temperatures for sources with 7σ or greater total FIR flux. (d) One MC realisation of the ratio of dust masses adjusted for their MC temperature as a function of their dust mass as assigned by MAGPHYS.

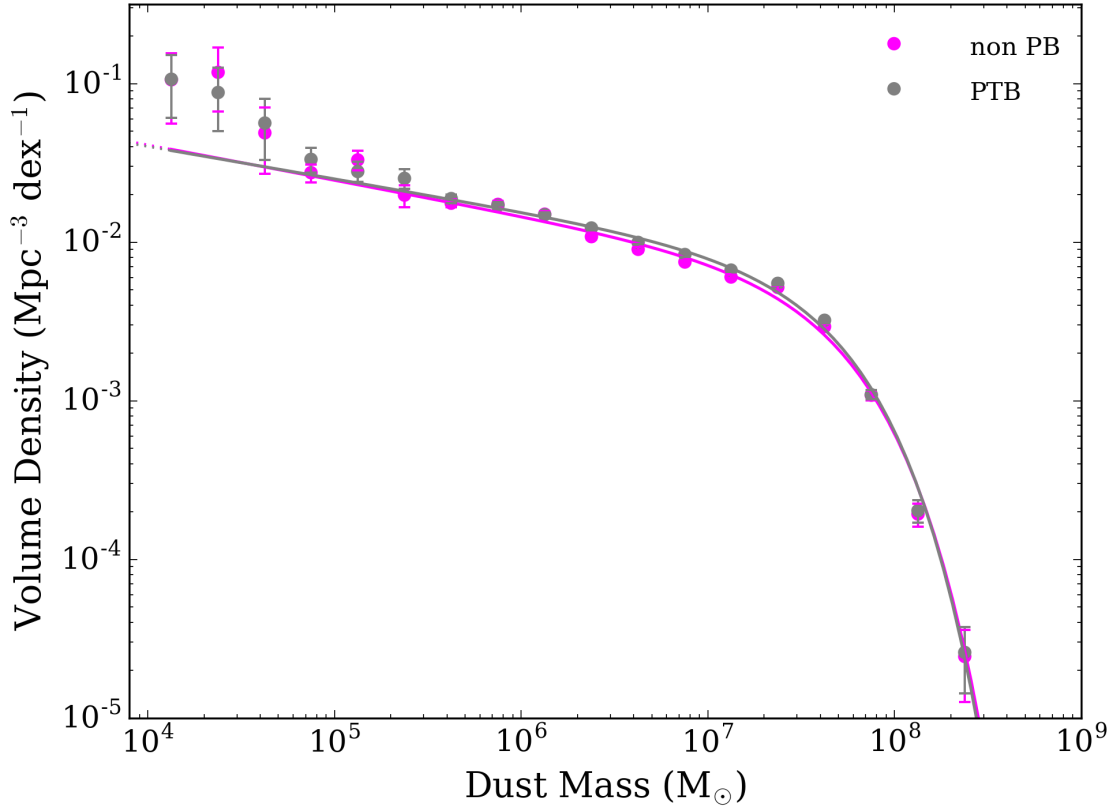


FIGURE 3.5 The pV_{\max} dust mass functions for the GAMA/*H*-ATLAS sources, firstly showing the simple bootstrap (SB) DMF as seen in Section 6.4 in magenta (here labeled non PB), and secondly the DMF resulting from the perturbed temperature bootstrap (PTB) method shown in grey. The data points show the observed values and the solid lines are the best fitting (χ^2) single Schechter functions to the data for their respective fitted regions, beyond this we show extrapolations down to $10^4 M_{\odot}$ as dashed lines. Error bars are derived from a bootstrap analysis and the data points have been corrected for over and under densities in the GAMA fields (see W17).

whereby instead of perturbing the masses based on the 16 and 84 percentiles output by MAGPHYS, we now perturb their cold dust temperatures to match the new prior temperature distribution. As in the PB method we first resample from the underlying dataset to give each bootstrap realisation. We keep the temperatures of the high signal to noise sources the same, but for all other galaxies we assign new temperatures using the prior from the high signal to noise sample. This means that the resulting temperature distribution for all sources matches the prior. This is shown for one realisation in panel (c) of Figure 3.4. Finally we adjust the galaxy dust masses in proportion to the change in black body luminosity at $250 \mu\text{m}$ given

| | SB | PTB |
|--|------------------|------------------|
| α | -1.22 ± 0.01 | -1.21 ± 0.01 |
| M^* ($10^7 M_\odot$) | 4.65 ± 0.18 | 4.47 ± 0.16 |
| ϕ^* ($10^{-3} h_{70}^3 \text{Mpc}^{-3} \text{dex}^{-1}$) | 6.26 ± 0.28 | 6.97 ± 0.30 |
| Ω_d (10^{-6}) | 1.11 ± 0.02 | 1.17 ± 0.02 |

TABLE 3.2 Schechter function fit values for dust mass functions resulting from the simple bootstrap (SB) and perturbed temperature bootstrap (PTB) DMF analysis. The fits include the density-weighted corrections from W17.

the original and re-assigned temperatures. We refer to this method as the perturbed temperature bootstrap (PTB). The ratio of the PTB and MAGPHYS temperatures as a function of dust mass from MAGPHYS for one realisation can be seen in panel (d) of Figure 3.4. The figure shows that the dust mass can increase or decrease as a result of the temperature MC, but generally the dust masses increase as a result of the new temperature.

Figure 3.5 and Table 3.2 show the resulting DMF and best fit Schechter function parameters along with our simple bootstrap (SB) results. The differences are very small, showing that the poorly constrained temperatures do not introduce a significant bias in our DMF estimates, even though they make up a significant fraction of our sample. The derived α and M^* values both agree within uncertainties. The value of ϕ_* is 2σ or $\sim 16\%$ higher for the PTB DMF. Overall the revised temperatures lead to a difference in the cosmic dust density of only $\sim 6\%$. Thus we are confident that any bias from poor mass constraints for the lower signal to noise sources in our sample is at the level of a few percent.

In order to test the effectiveness of the perturbed temperature bootstrap (PTB) method described above, we generated two new samples by taking exactly the same flux measurements for each galaxy but multiplying the FIR flux uncertainties firstly by a factor of 2 (named S2) and then by a factor of 3 (named S3). MAGPHYS SED fitting was performed on the two samples (carried out by Simon Driver), and again on the original sample with no change to the uncertainties provided to MAGPHYS (named S1) to check that the results were consistent with the initial run.

The resulting DMFs from these three samples are shown in Figure 3.6. The top panel shows the DMF as calculated using the simple bootstrap method, and

the bottom panel showing the DMF calculated using the perturbed temperature bootstrap method. The effect on the DMF is also an artefact of the test that we did, in that the biggest changes will occur where we do have good constraints on the FIR properties of a galaxy and have degraded those constraints by multiplying the errors by a factor of 2 and 3. This introduces the effect shown in the top panel of Figure 3.6, where the ‘knee’ of the DMF (M_*) appears to be shifted to lower dust mass for the two samples with increased FIR uncertainties. This is because the largest effect of increasing the noise will be on the cold dust temperature output by MAGPHYS. Increasing the uncertainty for galaxies which already have a poor constraint on the peak of the FIR SED will simply return the prior as before, and so the increase in noise here will have little effect on the resulting dust mass. For galaxies that previously did have good constraints that are being degraded artificially here though, there will be a larger effect on the temperature, and therefore the resulting mass.

Therefore we conclude that this test is not entirely a fair representation on its own of the effect galaxies with poor FIR constraints may have on the DMF. Instead, by performing the perturbed temperature bootstrap (PTB) method on these two samples, we have an opportunity to attempt to reproduce the DMF without artificially increasing the noise far more accurately, suggesting this is the better test on the validity of the DMF based on our sample and its uncertainties in the measurement of dust mass. As can be seen in the bottom panel of Figure 3.6, the PTB DMF for each of the two samples S2 and S3 is closer to S1 (the original sample) than when the simple bootstrap is used. The PTB method appears to provide a better picture of the uncertainties in underlying DMF than the simple bootstrap alone. In summary, we find in this Section that the bias introduced to the DMF due to including sources with poor FIR constraints is very small, and therefore suggests that the DMF measurements presented in Chapter 2 are robust.

3.4 DEPENDENCE ON THE MINIMUM MASS OF THE SCHECHTER FIT

When testing for various biases in the DMF fit, it became clear that the resulting parameters could be sensitive to the minimum mass chosen for the fit. Figure 3.7 compares the resulting single Schechter function fit parameters derived using different low mass limits ranging from 10^4 to $10^{5.5} M_\odot$. We see a convergence of the derived α , M^* and ϕ^* when using the single fit with $M_{\min} < 10^{4.5} M_\odot$.

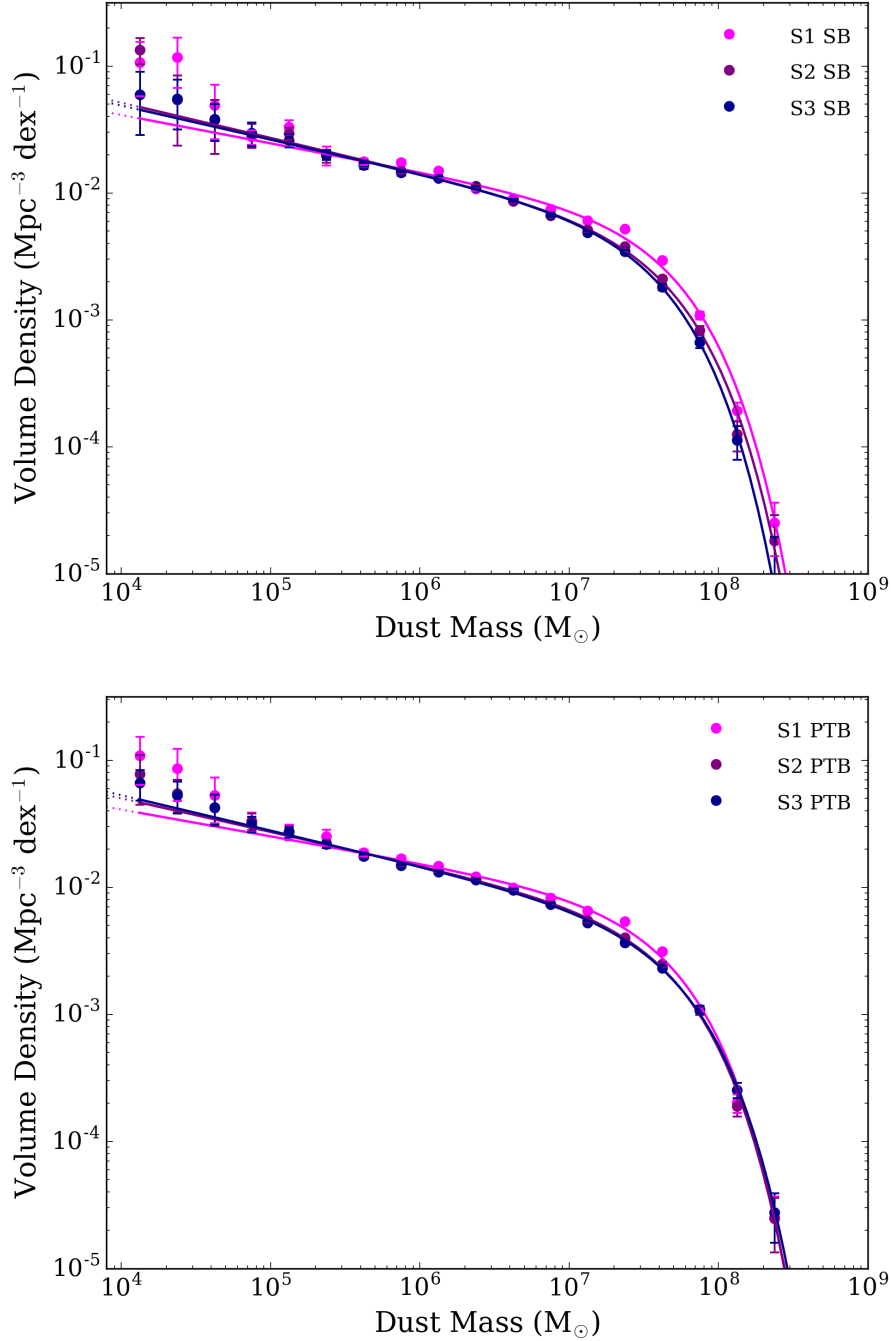


FIGURE 3.6 Comparison of the three samples, S1, S2 and S3, based on Simon Driver's re-run of MAGPHYS where S1, S2, and S3 are where the sample's original uncertainties are multiplied by 1, 2, and 3 respectively. We compare the simple bootstrap (SB) method (i.e. no perturbation either to mass or temperature) from Chapter 2 (*top*) and also using the perturbed temperature bootstrap (PTB) method (*bottom*). The data points show the volume densities in each mass bin. Error bars are derived from a bootstrap analysis and the data points have been corrected for over and under densities in the GAMA fields (see W17). Schechter fits to the data are also shown.

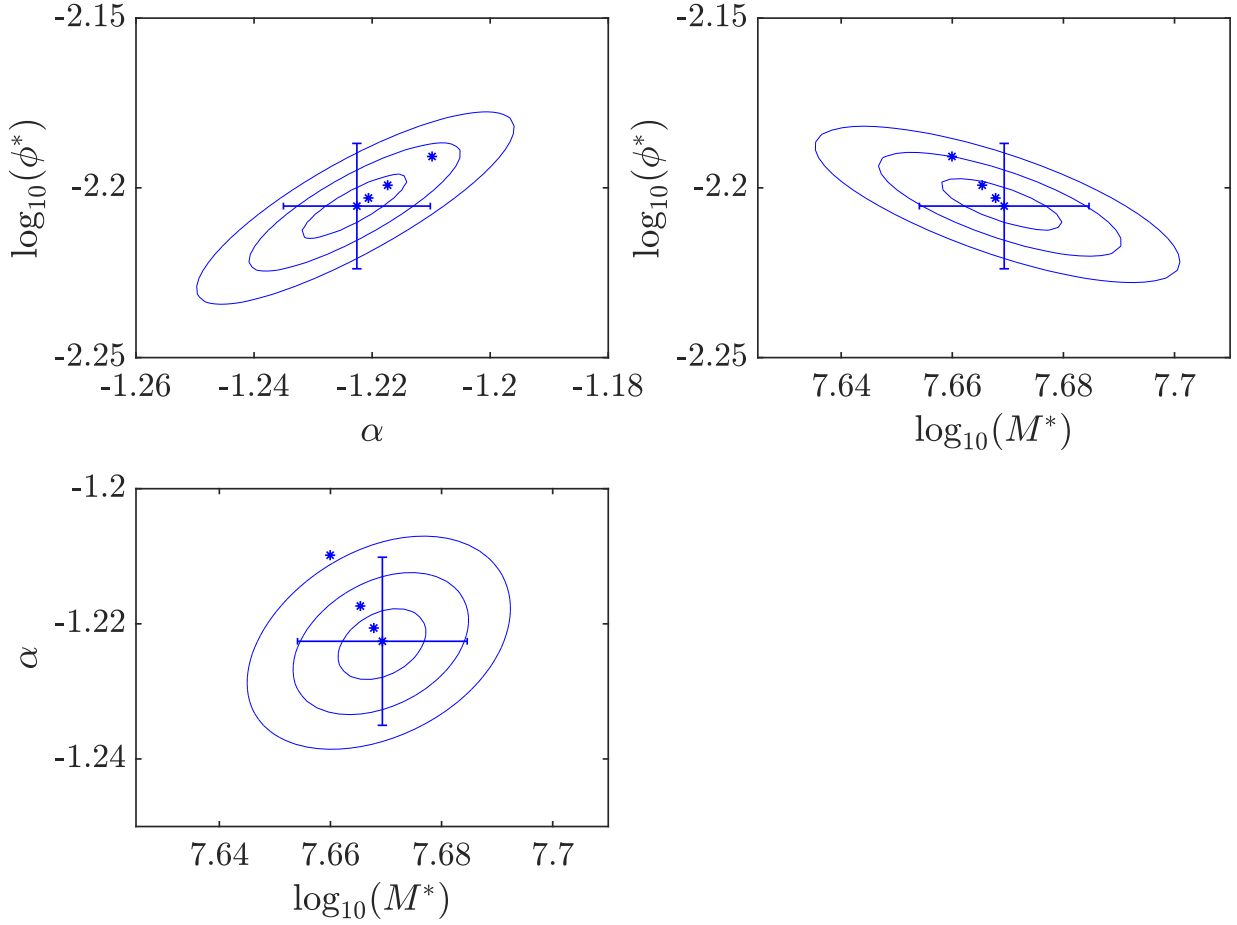


FIGURE 3.7 The confidence intervals for the pV_{\max} Schechter fits (SF) to the single dust mass function derived in this work (blue ellipses) as a function of minimum mass chosen for the fit (blue asterisks) for $\log_{10}(M_{\min}/M_{\odot}) = 4, 4.5, 5$ and 5.5 . The contours and error bars are centred on the fit with $\log_{10}(M_{\min}/M_{\odot}) = 4$. Error bars on the fit parameters are taken from the $\Delta\chi^2 = 1$ for each parameter. Note that ϕ^* is in units of $\text{Mpc}^{-3} \text{dex}^{-1}$.

Beyond this point we see that there is a strong dependence on the derived best-fitting parameters for the Schechter function with varying M_{\min} . This difference could explain in part the offset of our DMF from the [Vlahakis et al. \(2005\)](#) and D11 parameters (Figure 2.10); however, this offset is within the error bounds of the different surveys. We note also that the difference in the DMF resulting from changing the minimum mass increases the differences between our measured parameters and the previous observations.

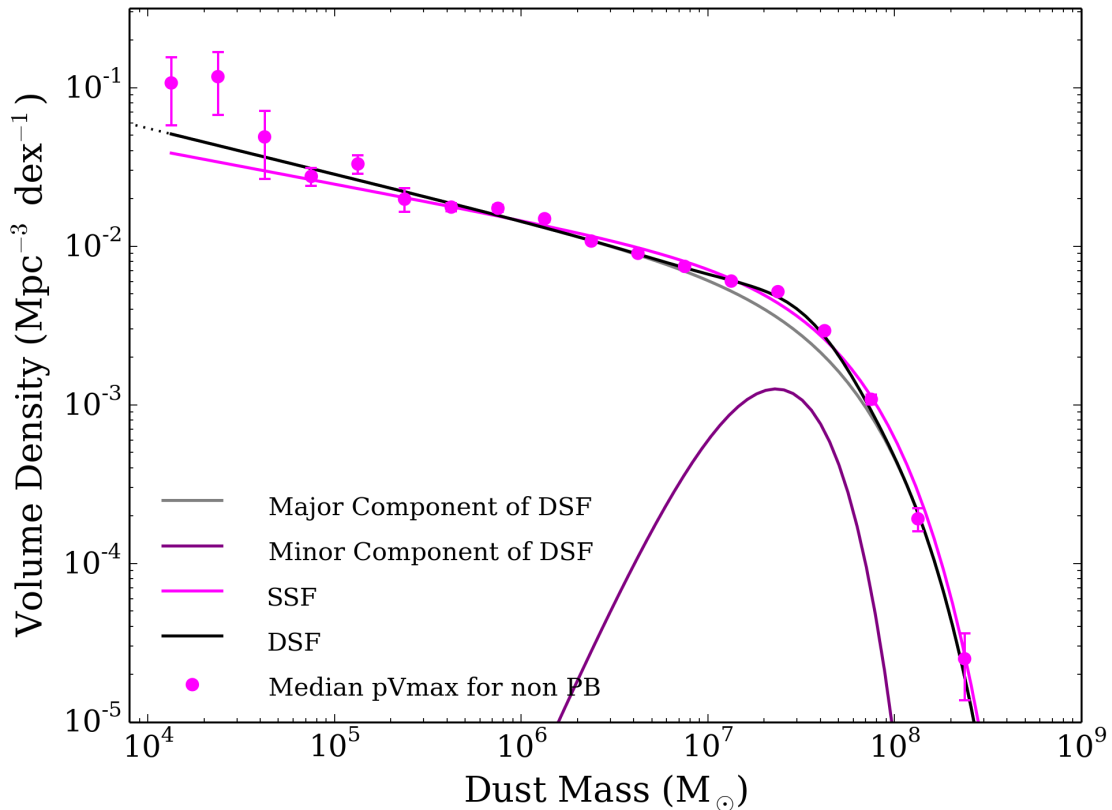


FIGURE 3.8 Comparison of the single Schechter fit (SSF) with the double Schechter fit (DSF) including the major and minor components. The data points show the volume densities in each mass bin, derived using the pV_{\max} volume estimator. The major and minor components are shown in grey and purple respectively, the overall DSF is shown in magenta. Error bars are derived from a bootstrap analysis and the data points have been corrected for over and under densities in the GAMA fields (see W17).

3.5 A SINGLE OR DOUBLE SCHECHTER FIT TO THE DMF?

The dependence of the single Schechter function (SSF) fit parameters with the chosen lower mass limit of the fit in Section 3.4 suggests that the observed DMF may not be adequately represented by the SSF used so far. W17 also found that a SSF fit was not sufficient to fit their stellar mass function of the same sample, instead they required a double Schechter function (DSF) fit with the same characteristic M^* , but with different faint-end slopes. We therefore follow W17 and fit a DSF to the DMF but unlike W17, we do not couple the two M^* values, since there is no reason to believe that multiple populations in the dust mass functions would have the same characteristic dust mass. The DSF is therefore just defined as the

sum of two single functions of the form:

$$D(M; M_1^*, M_2^*, \alpha_1, \alpha_2, \phi^*, f_{\text{mix}}) = S(M; M_1^*, \alpha_1, \phi^*) \times f_{\text{mix}} + S(M; M_2^*, \alpha_2, \phi^*) \times (1 - f_{\text{mix}}) \quad (3.1)$$

where f_{mix} is the fractional contribution of one of the components. Figure 3.8 compares the DSF with the SSF. The major component of the DSF is similar to the SSF, but the former provides a better fit to the ‘shoulder’ in the data at $M \sim 10^7 M_\odot$ and results in a reduced $\chi^2 \sim 3 \times$ lower than the SSF fit. Although the DSF significantly reduces the χ^2 of the best fit, the variation of mass errors as a function of mass could introduce this kind of shape in the DMF. We therefore cannot be sure that the DSF represents a fundamentally better model of the data even if it is formally a better fit. We therefore keep the SSF as our standard fit. For completeness, the best-fit parameters for the DSF are listed in Table 3.3.

The dust density for the pV_{max} DSF fit is $1.11 \pm 0.02 \times 10^{-6}$, corresponding to an overall fraction of baryons (by mass) stored in dust $f_{m_b} = (2.51 \pm 0.04) \times 10^{-5}$, assuming the Planck $\Omega_b = 45.51 \times 10^{-3} h_{70}^{-2}$ (Planck Collaboration XIII, 2016). The DSF therefore returns the same value for dust density as using the simpler SSF. We also note that the improvement in χ^2 from SSF to DSF becomes insignificant when the uncertainty due to cosmic variance is included in the fitting process.

It is tempting to link the two Schechter components of the double fit to the DMF to physical properties of galaxies e.g. dust poor and dust rich early and late-type galaxies respectively, but the parameters of the minor component of the DSF do not match those of the early-types, as we will see in Chapter 4. This suggests that the two components of the DSF do not represent physically distinct populations, and again does not support the idea that the DSF is a better representation of the data than the single fit from Chapter 2.

3.6 EDDINGTON BIAS IN THE DUST MASS FUNCTION?

Finally we perform an additional check on whether an additional bias is introduced to the DMF parameters due to the dust mass errors from MAGPHYS. Since the scatter due to the mass error could move galaxies into neighbouring bins in either direction, and as the volume density is not uniform, this could have the effect of introducing an Eddington bias (Eddington, 1913) into the DMF. Loveday et al. (1992) showed that this bias effectively convolves the underlying DMF with a

| Method | M^* ($10^7 h_{70}^2 M_{\odot}$) | α | ϕ^* ($10^{-3} h_{70}^3 \text{Mpc}^{-3} \text{dex}^{-1}$) | f_{mix} | Ω_{d} (10^{-6}) |
|--------------------|--|-------------------------------------|--|------------------|--------------------------------------|
| Single fits | | | | | |
| pV_{max} | 4.65 ± 0.18 | -1.22 ± 0.01 | 6.26 ± 0.28 | - | 1.11 ± 0.02 |
| BBD | 4.67 ± 0.15 | -1.27 ± 0.01 | 5.65 ± 0.23 | - | 1.11 ± 0.02 |
| DpV_{max} | 4.39 ± 0.17 | -1.22 ± 0.01 | 6.49 ± 0.30 | - | 1.08 ± 0.02 |
| DBBD | 4.40 ± 0.15 | -1.27 ± 0.01 | 5.85 ± 0.24 | - | 1.08 ± 0.02 |
| Double | (1), (2) | (1), (2) | (1), (2) | (1), (2) | |
| pV_{max} | $(4.65 \pm 0.55), (0.89 \pm 0.44)$ | $(-1.29 \pm 0.08), (1.85 \pm 1.69)$ | 6.15 ± 2.72 | 0.80 ± 0.17 | 1.11 ± 0.02 |
| BBD | $(4.59 \pm 0.73), (0.75 \pm 0.43)$ | $(-1.33 \pm 0.15), (2.07 \pm 1.69)$ | 5.47 ± 5.80 | 0.81 ± 0.17 | 1.11 ± 0.02 |
| DpV_{max} | $(4.16 \pm 0.95), (0.78 \pm 0.45)$ | $(-1.29 \pm 0.13), (2.32 \pm 1.68)$ | 6.04 ± 5.28 | 0.85 ± 0.18 | 1.11 ± 0.02 |
| DBBD | $(4.05 \pm 1.20), (0.71 \pm 0.54)$ | $(-1.33 \pm 0.17), (2.42 \pm 1.86)$ | 5.61 ± 8.97 | 0.85 ± 0.18 | 1.11 ± 0.02 |

TABLE 3.3 Schechter function values for dust mass functions in the literature and this work. The other literature studies include: C13 - Clemens et al., 2013, D11 - Dunne et al., 2011, V05 - Vlahakis et al., 2005. All have been scaled to the same dust mass absorption coefficient used here. The Dunne et al. (2011) DMF includes a correction of 1.42 for the density of the GAMA09 field (Driver et al., 2011) and the fits in this work include the density-weighted corrections from W17. For comparison we include the deconvolved Schechter function fit parameters in the final section of the table (see Section 3.6) listed as DBBD and DpV_{max} , these are very similar to the ordinary Schechter function fit parameters.

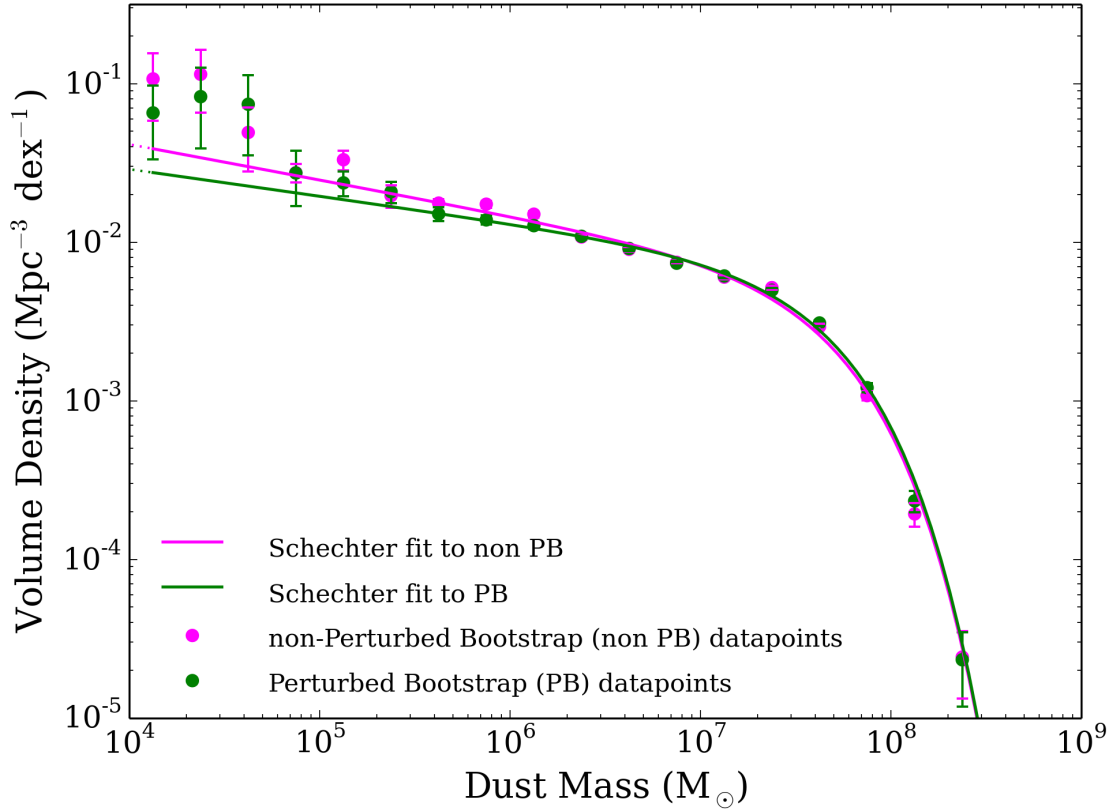


FIGURE 3.9 The pV_{\max} DMF (purple) from the SB measurements compared to the DMF derived using the bootstrap perturbed (PB) by the uncertainties in the dust mass estimates from MAGPHYS (the PB DMF, green). The data points show the volume densities in each mass bin and the solid lines are the best fitting (χ^2) single Schechter functions, SSF, to the data.

Gaussian with width equal to the size of the scatter in the variable of interest (here dust mass) to give the observed DMF. This is valid assuming that the parameter uncertainties, and hence resulting errors, have a Gaussian distribution. Here we test whether we can correct for the Eddington bias in the DMF by deconvolving our observed DMF and attempt to extract the underlying ‘true’ DMF. We expect that any bias in the overall cosmic dust density will be small since galaxies with at least one measurement over 3σ in one of the *Herschel* SPIRE bands contribute around four times as much to the dust density of the Universe than those without a 3σ measurement in the FIR regime.

We first fit the single Schechter fit (SSF) from Chapter 2 convolved with a Gaussian, where we estimate the width of the Gaussian using two methods. We derive the width of the convolved function by calculating the mean dust mass error from MAGPHYS as a function of mass (the varying error method). Second, we take

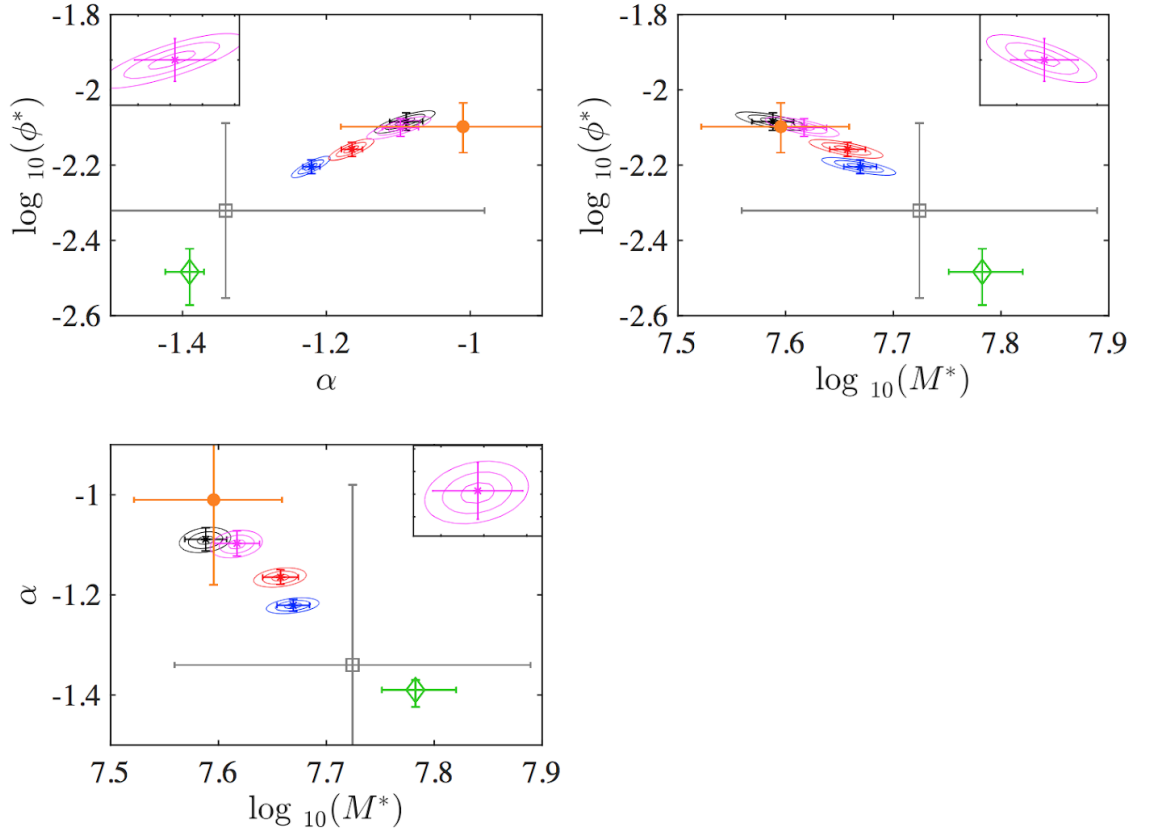


FIGURE 3.10 Comparison of the χ^2 confidence intervals resulting from performing the perturbed bootstrap (PB) analysis (red and magenta ellipses) and non-perturbed bootstrap (non PB) analysis (blue and black ellipses). The blue contours are non PB with $\log_{10}M_{\min}/M_{\odot} = 4.25$, the black are non PB with $\log_{10}M_{\min}/M_{\odot} = 6.2$, the red are PB with $\log_{10}M_{\min}/M_{\odot} = 4.25$, and finally the magenta are PB with $\log_{10}M_{\min}/M_{\odot} = 6.2$. Green denotes Vlahakis et al. (2005), orange represents Dunne et al. (2011), and grey shows Clemens et al. (2013). We note that the error bars on the Vlahakis et al. (2005) values were derived using Poisson statistics, and so may be an underestimate of the error in the measurements.

the mean value of the error in dust mass around the knee of the single Schechter function where the convolution will have the strongest effect (here the mean error is 0.11 dex, we will call this the constant error method). Both produce very similar deconvolved Schechter function fit parameters that are in agreement with the traditional Schechter function method within a few per cent. The deconvolved fit parameters derived with constant error are listed in Table 3.3; this produces a dust mass density of $(1.08 \pm 0.02) \times 10^{-6}$ for both the pV_{\max} and BBD DMFs. We find that the traditional single Schechter function is formally a better fit ($\Delta\chi^2 \sim 0.75$) than the deconvolved constant error function, and the varying error method produces a comparable goodness of fit to the traditional SSF without deconvolution. The reason that the best fit is insensitive to the mass errors is that the mass errors are a strong function of mass: for low mass galaxies, the errors are large (~ 0.5 dex); while for higher masses ($\sim M^*$), the errors are small (<0.1 dex). At low masses the DMF is a power law, the slope of which is unchanged when convolved by a Gaussian. At higher masses, near the exponential cut-off, the errors are small, and so the effect on the knee is negligible. We therefore conclude that there is no strong argument for choosing to use the deconvolved SSF fits instead of the original single Schechter functions, therefore we include the results here for completeness but continue using the original SSF fits throughout the Thesis.

As an aside, the difference between the DMFs simple bootstrap method (the SB) and the bootstrap method where we perturbed the data by the underlying uncertainties in dust mass from MAGPHYS (the PB, see Section 2.4.3.1) provides us another method to test whether the DMF is Eddington-biased and could provide a way to correct for this. Figure 3.9 compares the SB and PB DMFs with the latter producing larger errors for the fit parameters, as one would expect. This Figure shows that the uncertainties in MAGPHYS dust mass measurements appears to bias the DMF low at low dust masses and high at high dust masses. However the largest differences in the DMF are seen at the noisier low dust mass end, and are generally only at the few percent level, suggesting the biases from this error source are indeed small. We also find that the derived value of M^* for the PB DMF is lower which is not expected if the PB (with the dust mass uncertainties added) is effectively the Eddington bias in the sample. However, we attribute this to the fit dependence on minimum mass (Section 3.4). With higher M_{\min} cut, the PB M^* is significantly higher than the non PB M^* . With the lower M_{\min} cut the PB M^* is lower than the non PB M^* (Figure 3.10). The errors in the final fit parameters alpha, M^* and ϕ^* increase by a small fraction using the perturbed fits compared to previous non perturbed errors.

In summary, the largest differences in the DMF due to Eddington bias are seen at the noisier low mass end, and for all other mass bins, the error is small due to the low observed errors around the knee of the DMF. We do not use the perturbed bootstrap to derive Schechter fit quantities as perturbing the fit to the DMF with the uncertainties from MAGPHYS is effectively doubling the Eddington bias.

3.7 CONCLUSIONS

In Chapter 2, we used a single Schechter function fit to our data to derive a dust mass function, and we extended this to lower dust masses than probed before, constraining the faint end slope below $10^5 M_{\odot}$. Here we test the robustness of the DMF to potential biases in the methods and datasets. Our main findings are:

- We test for biases in the dust mass function due to low signal to noise FIR photometry and find that any bias from poor mass constraints from these sources is at the level of a few percent.
- We show that the derived values for the Schechter fit to the BBD-derived dust mass function are robust to changing the selection ‘axes’ from surface brightness/*r*band magnitude, *r*–band magnitude/stellar mass, and M_d /stellar mass.
- We find the single Schechter fit results is dependent on the minimum stellar mass of the fit, and this can explain part of the differences between the DMF in this work and those published previously.
- The perturbed temperature bootstrap (PTB) appears to recover the underlying DMF from the sample with artificially higher uncertainties.
- We find that a double Schechter function is marginally formally a better fit to the observed DMF, though the minor and major components do not seem to relate to physical properties of the sample. Given the sources of errors in the DMF, we do not have confidence that the double Schechter function represents a better description of the DMF than the single fit used in Chapter 2.
- We test for Eddington bias in the DMF by deconvolving the Schechter fits and by comparing the DMF derived by bootstrapping on the dust masses (SB method) with the DMF derived by also bootstrapping the masses with

the individual errors in dust mass for each galaxy (the PB method). We find that this error is likely at the level of a few percent and is dominated by the fact that the uncertainties in the mass around the knee of the function (where the Eddington bias would have a strong affect) are small.

CHAPTER 4

THE OPTICALLY SELECTED DMF IN CONTEXT

*‘There’s no plan, there’s no hand on the rein
As Mack explained, there will be darkness again’*

HOZIER

In this Chapter, we compare the observed dust mass function at redshift $z = 0$ from Chapter 2 to predictions based on theoretical models including semi-analytical and hydrodynamical galaxy formation models. The results from this Chapter have been published in [Beeston et al. \(2018\)](#).

4.1 INTRODUCTION

A goal of this thesis is to measure the dust content and dust mass density of galaxies using data across a large area of the sky and using datasets that have been ‘homogeneously treated’. An important step is then to compare the observed dust mass function from Chapter 2 with theoretical predictions. Simulations of dust mass functions exist in the literature for $z = 0$, including the semi-analytic dust model of [Popping et al. \(2017\)](#) and hydrodynamical simulations from [McKinnon et al. \(2017\)](#). These theoretical predictions are in turn based on chemical evolution models that trace the build up, and destruction of, dust and metals in galaxies (eg [Dwek, 1998](#); [Edmunds, 2001](#); [Morgan & Edmunds, 2003](#); [Dunne et al., 2011](#); [Asano et al., 2013a](#)) as stars form out of the gas. We can also test the standard prejudice that spiral galaxies are full of dust, and ellipticals have very little dust by using

our DMF to quantify the difference in dust content of early-type galaxies (ETGs) and late-type galaxies (LTGs). Scaling relations between dust and stellar mass can reveal the relation between internal galaxy properties and the dust content and whether there is a simple prescription that can tell us how much dust exists in galaxies given a unit of stellar mass (e.g. [Driver et al. 2018](#)). With our dataset we can test whether there is a simple scaling relation between dust and stellar mass by simply comparing the dust and stellar mass functions. Finally, whether or not the dust mass function does evolve with redshift in recent cosmic history is debated in the literature with evidence for in [Dunne et al. \(2011\)](#) and evidence against in [Driver et al. \(2018\)](#). Here we attempt to investigate if there is evolution of the dust density of galaxies in our (albeit narrow) redshift range of $z \leq 0.1$. Section 4.2 compares the observed DMF with predictions from theoretical models. We take the observed dust mass function and split by morphological type in Section 4.3 and derive the dust mass density in early- and late-types as well as in disk and bulge-like galaxies. We compare our DMF with the stellar mass functions of galaxies in Section 4.4, providing scaling relations between stellar and dust mass for late and early type galaxies. We split the sample by redshift in an attempt to investigate evolution of the dust mass density within the redshift range $0 < z < 0.1$ (Section 4.5).

4.2 THEORETICAL PREDICTIONS FROM GALAXY FORMATION MODELS

Here we compare the dust mass function from Chapter 2 with theoretical predictions for $z = 0$ from the dust models of [Popping et al. \(2017\)](#) and [McKinnon et al. \(2017\)](#). [Popping et al. \(2017\)](#) derive DMFs from semi-analytic models (SAMs) of galaxy formation based on cosmological merger trees from [Somerville et al. \(2015\)](#) and [Popping et al. \(2014\)](#) and include prescriptions for metal and dust formation based on chemical evolution models. They predict DMFs at different redshifts using dust models with dust sources from stars in stellar winds and supernovae (SNe), grain growth in the interstellar medium, and dust destruction by SN shocks and hot halo gas (see also [Dwek 1998](#); [Morgan & Edmunds 2003](#); [Michałowski et al. 2010b](#); [Dunne et al. 2011](#); [Asano et al. 2013a](#); [Rowlands et al. 2014](#); [Feldmann 2015](#); [De Vis et al. 2017b](#)). Note that for consistency, we have scaled the Popping DMFs down by a factor of 2.39 in dust mass since their $z = 0$ models were calibrated on dust masses for local galaxy samples from the *Herschel Reference*

Survey (Boselli et al., 2010; Smith et al., 2012c; Ciesla et al., 2012) and KINGFISH (Skibba et al., 2011) where Draine (2003) dust absorption coefficients are assumed. After this scaling, their DMF (based on their SAMs) is consistent with a Schechter function with characteristic mass $M^* \sim 10^{7.9} M_{\odot}$. In Figure 4.1 we compare three of their $z = 0$ DMF models as defined in Table 4.1: the so-called fiducial, high-cond and no-acc models. Their fiducial model assumes 20 per cent of metals from stellar winds of low-intermediate mass stars (LIMS) and SNe are condensed into dust grains, with interstellar grain growth also allowed. The high-cond assumes that almost all metals available to form dust that are ejected by stars and SNe are condensed into dust grains, with additional interstellar grain growth. The no-acc model assumes 100 per cent of all metals available to form dust that are ejected by stars and SNe are condensed into dust grains, with no grain growth in the ISM.

The fiducial and high-cond models overpredict the number density of galaxies in the high dust mass regime, $> 10^{7.5} M_{\odot}$. The no-acc model is the closest model to the observed high mass regime of the DMF, though underestimates the volume density around M^* compared to our DMF (dotted lines in Figure 4.1). Both the no-acc and high-cond models are better matches at low masses ($< 10^7 M_{\odot}$), while the fiducial model underpredicts the volume density in this regime. This likely suggests that LIMS and SNe have to be more efficient than the fiducial model at producing dust in low dust-mass systems i.e. the dust condensation efficiencies in both stellar sources need to be larger than 0.3, or that the dust destruction and dust grain growth timescales in the fiducial model need to be increased and decreased respectively. At high masses, the fiducial and high-cond models appear to be forming too much dust. This implies that dust production and destruction are not realistically balanced in these models. This is likely due to the model introducing too much interstellar gas and metals, which allow for very high levels of grain growth in the ISM.

We note that the no-acc P17 model (without grain growth in the ISM) is likely not a valid model as it assumes 100 per cent efficiency for the available metals condensing into dust in LIMS and SNe which is unphysically high, see e.g. Morgan & Edmunds (2003); Rowlands et al. (2014). Hereafter we no longer discuss this model even though by eye (Figure 4.1) it appears to be an adequate fit to the observed DMF at masses below $10^7 M_{\odot}$.

To investigate the discrepancy between the observed DMF in this work and the predicted SAM DMF from Popping et al. (2017), we first check that the stellar mass function from the SAMs of P17 is consistent with the observed galaxy stellar mass function (GSMF) for the GAMA sample in Wright et al. (2017) (Figure 4.2).

| Model Name | Efficiency dust LIMS | | Efficiency dust Type I/II SNe | | grain growth ^a | dust destruction ^b | |
|------------|-----------------------|-------------------------------|-------------------------------|-------------------------------|---|-------------------------------|------|
| | Carbon (not in CO) | other Z (Mg,Si,S,Ca,Ti,Fe) | Carbon (not in CO) | other Z (Mg,Si,S,Ca,Ti,Fe) | | SNe | halo |
| Popping | | | | | | | |
| fiducial | 0.2 | 0.2 | 0.15 | 0.15 | $Y, t_{\text{acc},0} = 15 \text{ Myr}$ | Y | Y |
| high-cond | 1.0 | 0.8 | 1.0 | 0.8 | $Y, t_{\text{acc},0} = 15 \text{ Myr}$ | Y | Y |
| no-acc | 1.0 | 1.0 | 1.0 | 1.0 | N | Y | Y |
| Mckinnon | | | | | | | |
| Mck16 | 1.0 | 0.8 | 0.5 | 0.8 | $Y, \text{fixed } t_{\text{acc}} = 200 \text{ Myr}$ | Y | N |
| Mck17 | 1.0 | 0.8 | 0.5 | 0.8 | $Y, t_{\text{acc},0} = 40 \text{ Myr}$ | Y | Y |

TABLE 4.1 The dust models used in cosmological predictions of the DMF including three models from Popping et al. (2017) and two models from Mckinnon et al. (2016, 2017). All of the models presume dust formation in LIMS (low-intermediate stars) in their stellar wind AGB phase and in Type Ia and II supernovae. ^a - the timescale for interstellar grain growth in Milky Way molecular clouds such that the grain growth timescale of the system t_{acc} is either fixed or derived from $t_{\text{acc}} \propto t_{\text{acc},0} n_{\text{mol}}^{-1} Z^{-1}$ where Z is the metallicity and n_{mol} is the molecular number density. ^b - destruction of dust by either SN shocks in the warm diffuse ISM or via thermal sputtering in the hot halo gas. In Popping et al. (2017) $600 M_{\odot}$ and $980 M_{\odot}$ of carbon and silicate dust are assumed to be cleared by each SN event respectively. In Mckinnon et al. (2017) dust destruction is derived in each cell of the simulation, with each SN releasing 10^{51} ergs; this is effectively consistent with SN shocks clearing out $6800 M_{\odot}$ of gas, so for a gas-to-dust ratio of 100, this would imply $680 M_{\odot}$ of dust cleared out by each SN event.

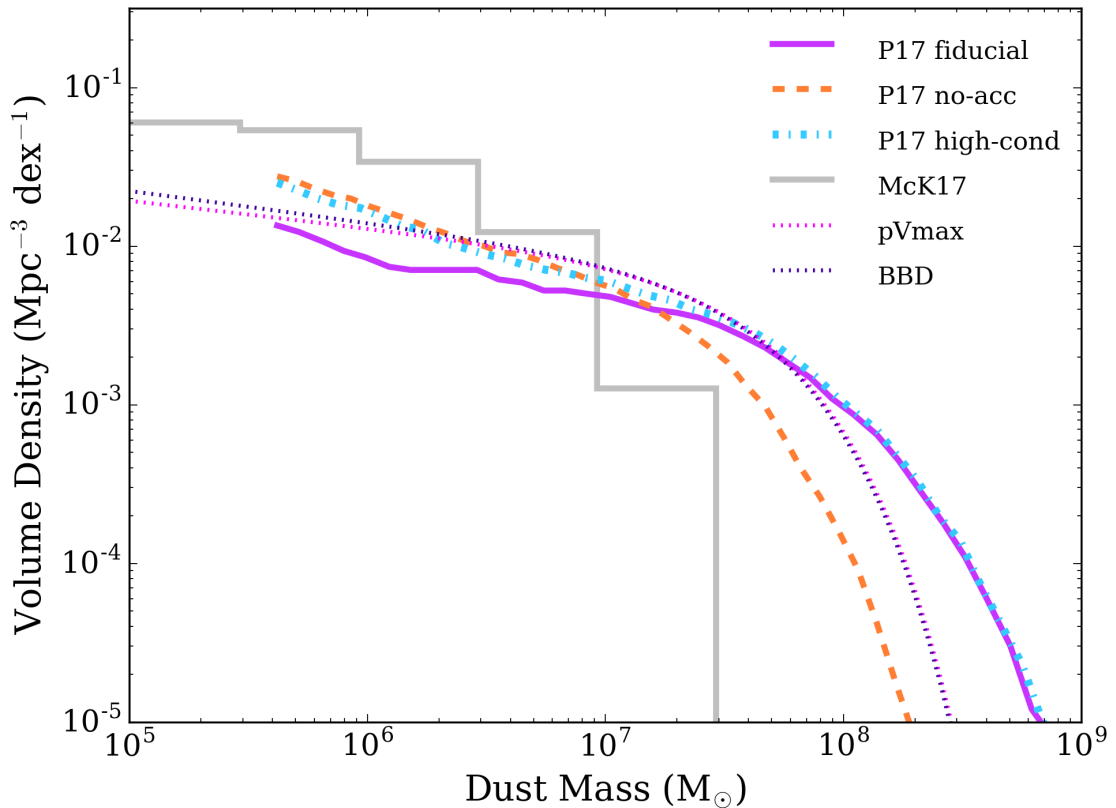


FIGURE 4.1 A comparison with the predicted $z = 0$ DMFs from Popping et al. (2017) (P17) and McKinnon et al. (2017) (McK17) with the single Schechter fits (SSF) derived from the BBD and pV_{\max} methods, Chapter 2, see also Table 4.1. We include three models from P17: the fiducial, no-acc and high-cond models which consist of varying dust condensation efficiencies in stellar winds, supernovae and grain growth in the interstellar medium respectively. The McK17 histogram is their L25n512 simulation at $z = 0$ (their Figure 2).

The SMFs at the high mass end are in agreement though the model SMF has a slight overdensity of galaxies in the range $10^8 < M_s (M_\odot) < 10^{9.4}$, where M_s is stellar mass. If this overdensity of sources were responsible for the discrepancy between the predicted and observed DMFs in the high M_d regime, those intermediate stellar mass sources would have to have dust-to-stellar mass ratios of ~ 0.5 which is again unphysical. We can see this is not the case when comparing the dust-to-stellar mass ratios of the Popping et al. (2017) fiducial $z = 0$ model in Figure 4.3 (as mentioned earlier, this is based on *Herschel* observations of local samples of galaxies).

In Figure 4.3 we compare the observed dust and stellar masses from the compilation of local galaxy samples collated in De Vis et al. (2017a,b) with the simulations from P17 and our sample of $\sim 15,000$ sources. The local galaxy samples include the stellar-mass selected *Herschel* Reference Survey (HRS, Boselli et al., 2010), the dust-selected sample of Clark et al. (2015), the HI-selected sample from

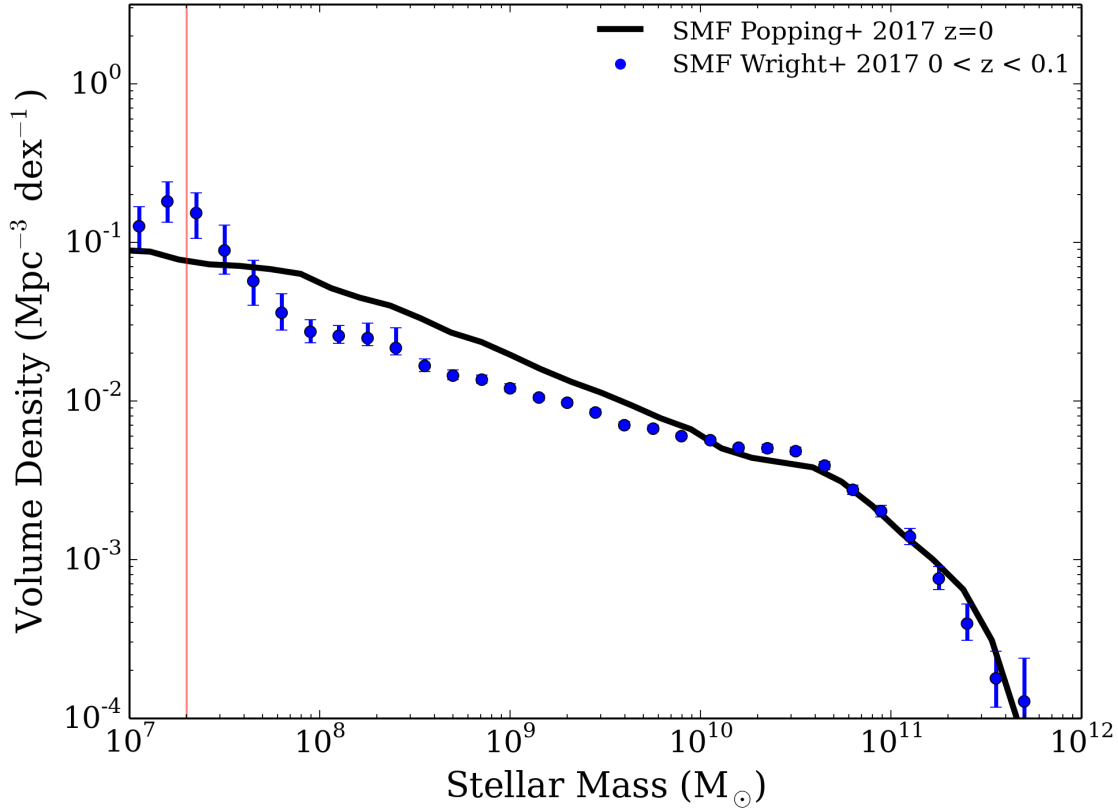


FIGURE 4.2 Comparing the $z = 0$ stellar mass functions for the GAMA sources (Wright et al. 2017, in blue) with that derived using the SAMs of Popping et al. (2017) (in black). The data from Wright et al. (2017) is based on the same optical sample from which our DMF is derived. The vertical line shows the boundary at which Wright et al. (2017) fit their data with a Schechter function.

De Vis et al. (2017a) and the dwarf galaxy survey (DGS) from Rémy-Ruyer et al. (2013), these samples have all been scaled to the same value of κ and apart from the Dwarf Galaxy Survey all galaxy parameters have been derived using the same fitting techniques. Here we can clearly see the cause for the discrepancy between the observed DMF from this work and the model: *the model overpredicts the amount of dust in high stellar mass sources, well above any dust-to-stellar ratios observed locally.* Although the observations show a flattening of dust mass at the highest stellar mass (M_s) regime (where early type galaxies are dominating), this is not the case in the SAM of P17, which continues to rise even beyond $M_s = 10^{10} M_{\odot}$. In general the SAM prediction assumes a constant dust-to-stars ratio of ~ 0.001 across all mass ranges. The observations however suggest that there is a roughly linear relationship between the dust and stellar mass until $M_s > 10^{10} M_{\odot}$, after which the slope flattens, with $M_d/M_s < 0.001$.

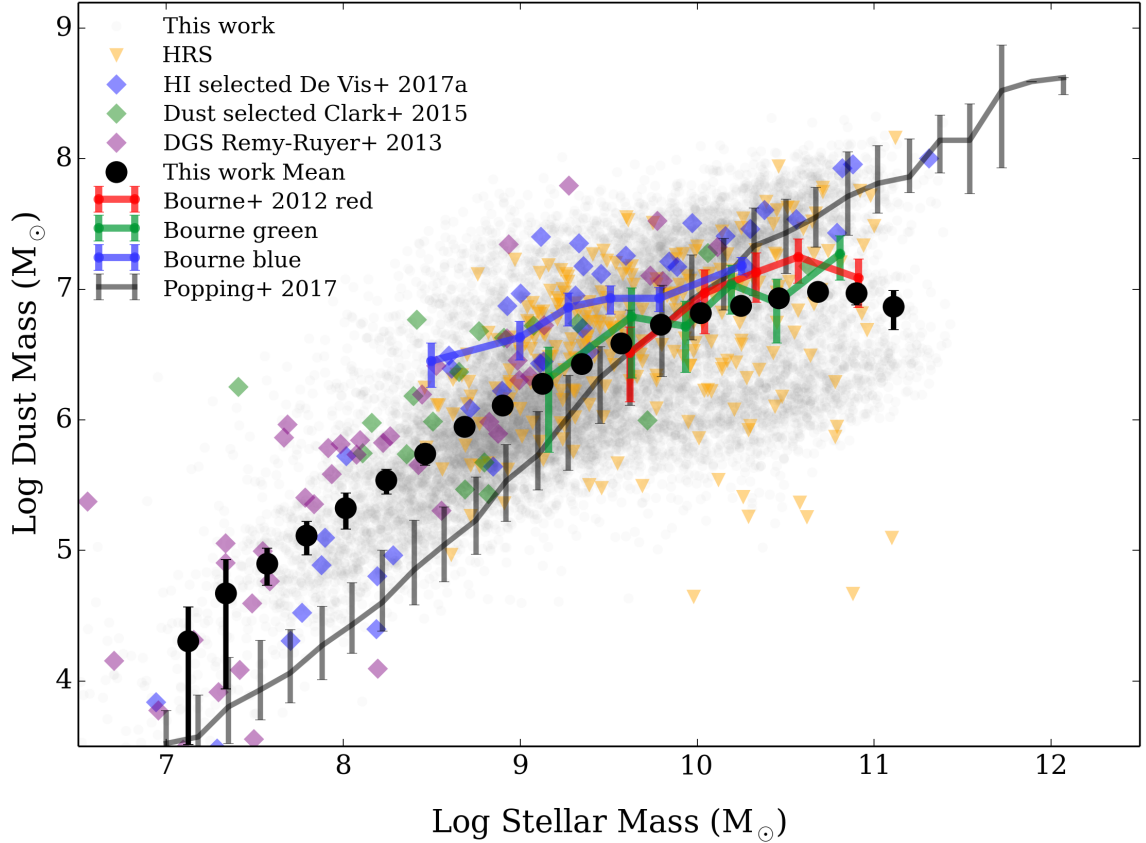


FIGURE 4.3 The dust to stellar mass ratio for galaxies in the local Universe. The data from this work is shown in the underlying grey points with mean dust masses (\pm standard error) in each stellar mass bin (black). We include a compilation of *Herschel* results for local galaxies including the stellar-mass selected HRS (Boselli et al., 2010), the dust-selected sample of Clark et al. (2015), the HI-selected sample from De Vis et al. (2017a) and the dwarf galaxy survey from Rémy-Ruyer et al. (2013). Overlaid are the local universe relationships ($z < 0.12$) based on stacking on *Herschel* maps for 80,000 galaxies from Bourne et al. (2012) in three different $g - r$ colour bins (their Figure 16). All of these samples have been scaled to the same the κ value with parameters derived using MAGPHYS (see De Vis et al. 2017a) or modified blackbody fitting but scaled to the same κ (DGS and stacked samples). The median dust and stellar masses from Popping et al. (2017) are shown by the grey line with 16 and 84 percentile errorbars (scaled by a factor of $1/2.39$ in dust mass).

Figure 4.3 also suggests that the observed M_d/M_s in our sample increases well above the P17 model prediction, rising to ~ 0.025 in low stellar mass galaxies (in agreement with previous work on smaller *Herschel* galaxy samples including Santini et al. 2014; Clark et al. 2015; De Vis et al. 2017a). This is further supported by the stacking analysis carried out in Bourne et al. (2012) whose dust-to-stellar mass trends in different bins of optical colour are added to Figure 4.3. These were derived by stacking on $\sim 80,000$ galaxies in the *Herschel* maps, revealing that low stellar mass galaxies had higher dust-to-stellar mass ratios, consistent with these sources having the highest specific star formation rates. Our binned data (black points) are in agreement with local galaxy surveys and the Bourne et al. (2012) trends: we see that the slope of dust-to-stellar mass flattens at high masses, and that there exists a population of dusty low-stellar-mass sources that the SAM does not predict.

Alternative predictions for a local DMF are provided by McKinnon et al. (2016, 2017, hereafter McK16, McK17). In these models, dust is tracked in a hydrodynamical cosmological simulation with limited volume. The McK16 dust model is similar to the P17 high-cond model (including interstellar grain growth and dust contributed by both low mass stellar winds and SNe) but has no thermal sputtering component. The updated model from McK17 reduces the efficiency of interstellar grain growth and includes thermal sputtering (see Table 4.1). The DMF from McK17 (their L25n512 simulation at $z = 0$) is shown in Figure 4.1. Their values have been scaled to the same cosmology as used here (they use the same κ and Chabrier IMF as this work). We can see that McK17 predicts fewer massively dusty galaxies than P17 and our observed DMFs. Although their DMF fails to produce enough galaxies in the highest mass bins in Figure 4.1, the simulated DMF becomes more strongly affected by Poissonion statistics in this regime due to the small volume of the simulation.

Possible explanations for the difference between the predicted (P17, McK17) and observed DMFs at large dust masses are (i) the efficiency of thermal sputtering due to hot gas in the halo has been under or overestimated in these highest stellar mass sources; (ii) the fiducial and high-cond dust models of P17 allow too much interstellar grain growth in highest stellar mass galaxies due to the assumed timescales or efficiencies of grain growth being too high; (iii) the predicted highest stellar mass galaxies have too little (McK17) or too much (P17) gas reservoir potentially due to feedback prescriptions being too strong/not strong enough, respectively. If the gas reservoir is too large, interstellar metals can continue to accrete onto dust grains and increase the dust mass. Conversely if it is too low, then the

contribution to the dust mass via grain growth will be reduced. We will address each of these possibilities in turn.

1. We can test if the amount of dust destruction by thermal sputtering in hot (X-ray emitting) gas could explain the differences in the predicted and observed DMF at the high mass end as McK16 and McK17 already compared the results using dust models without and with thermal sputtering respectively. They find that including thermal sputtering only makes small changes to the shape of DMF since this affects dust in the halo rather the interstellar medium, this is therefore not likely to be responsible for the discrepancy.
2. Comparing the dust models in P17, McK16 and McK17 allow us to test the effect of changing the grain growth parameters. The timescale for grain growth is shortest in P17 and McK16 and both those models produce too much dust in the high dust mass regime of the DMF. McK17 has a longer grain growth timescale ($t_{\text{acc},0} = 40 \text{ Myr}$, Table 4.1) than both P17 and McK16 and this change indeed reduces the volume density of the highest dust mass sources. McK17 also compares the DMFs from the same simulation methods with different dust models and they find that a significantly reduced DMF at the high mass end can be attributed to the longer grain growth timescales in McK16.
3. Earlier we showed that the galaxies that are responsible for the highest dust mass bins in the P17 DMF have too much dust for their stellar mass (Figure 4.3). To test whether they have too much dust due to the gas reservoir of the SAM massive galaxies being too high (hence leading to more interstellar grain growth) we refer to the predicted and observed gas mass function comparison carried out in Popping et al. (2014). There they showed that the predicted and observed gas mass functions for the same redshift range are not as discrepant as we see here with the modeled and observed dust mass functions, and therefore this is likely not responsible for the discrepancy in the DMF.

We therefore conclude that it is likely that the interstellar grain growth in these massive galaxies is simply too efficient/fast in the P17 and McK16 dust models. In this scenario, the few largest stellar mass galaxies are allowed to form too much dust in the interstellar medium at a rate that is not observed in real galaxies. However, the growth timescale may also be too slow in the McK17 model for high stellar mass sources, since this model still does not produce a good fit to the observed DMF. All of the P17 high-cond, McK16 and McK17 dust models

assume very high dust condensation efficiencies in AGB stars and Type Ia and II SNe. We propose therefore that the most realistic dust model must lie somewhere in between these and the fiducial P17 model, with stardust condensation efficiencies larger than 0.3 but lower than 0.8 and a similar dust grain growth timescale as assumed in P17.

Neither the P17 fiducial, nor the McK16 and McK17 dust models provide reasonable matches to the low dust mass regime ($\sim 10^{7.5} M_{\odot}$) of the DMF. McK16 and McK17 overpredicts the dust masses in the low mass regime and P17 fiducial model underpredicts the DMF suggesting again that stardust condensation efficiencies may be intermediate between the three models with a grain growth timescale similar to P17. Only the P17 high-cond model provides an adequate match to this regime (since we have previously ruled out the P17 no-acc model). However, the underlying dust-to-stellar mass properties for the models from P17 do not provide an adequate match to the observed galaxy properties at the low and high stellar mass regimes. The observed DMF therefore can provide some constraints on model predictions though the degeneracy/uncertainties between dust sources, dust destruction and the timescales for grain growth in the interstellar medium are too complex to disentangle fully with the DMF alone. In combination with stellar mass and interstellar gas mass functions and exploration of a wider range of model parameter space, it might be possible to revisit this in future.

4.3 THE DMF BY MORPHOLOGICAL TYPE

We saw in Section 4.2 that the dust mass function and the dust-to-stellar mass of galaxies in our sample can provide some constraints on the dust sources and sinks in galaxies for low and high stellar mass sources which are observed to have high and low dust mass per unit stellar mass respectively - Figure 4.3). An interesting question then is whether the dust content of late type and early type (LTGs and ETGs respectively) could partly explain this, i.e. can we test using our larger statistical sample whether ETGs are really as dust poor as observed in local *Herschel* surveys (Gomez et al., 2010; Smith et al., 2012c; Cortese et al., 2012a; Amblard et al., 2014), though we note that there are more dust-rich examples of ETGs in the samples of Rowlands et al. (2012); Agius et al. (2013, 2015). In this Chapter, we create ETG and LTG subsets for our sample of galaxies based on classifications carried out by GAMA in Driver et al. (2012) and Moffett et al. (2016a). For both studies visual classifications were based on three colour images built from H

(VIKING), i , and g (SDSS) bands. Classifications were based on three pairs of classifiers in which there was an initial classifier and a classification reviewer. [Driver et al. \(2012\)](#) classified the entire sample out to $z \leq 0.1$ and split the sample only into ‘Elliptical’ and ‘Not Elliptical’ galaxies, which we hereafter refer to as ETGs and LTGs (defined here as *later* type galaxies). The classifications from [Moffett et al. \(2016a\)](#) were carried out on the same sample as [Driver et al. \(2012\)](#), but limited to $z \leq 0.06$. In [Moffett et al. \(2016a\)](#) they attempted to produce an updated set of morphological classifications using classification trees with a finer binning system than the earlier [Driver et al. \(2012\)](#). However, for consistency with the [Driver et al. \(2012\)](#) classifications (and because here we do not want to split the DMF into finer morphological classes), we include the [Moffett et al. \(2016a\)](#) Ellipticals in the ETG class, and we group all remaining galaxy types apart from little blue spheroids (LBSs) into the LTG category (following [Moffett et al. 2016a](#), see Section 4.3.1).

We next use these morphologies in order to investigate the shape and dust mass density of ETGs and LTGs. We choose to limit our redshift range to $z \leq 0.06$ for two reasons (i) the finer, updated classifications of [Driver et al. \(2012\)](#) provided in [Moffett et al. \(2016a\)](#) is limited to this range and beyond this range visual classifications become more uncertain (ii) with increasing redshift, the sample will suffer more from incompleteness at lower masses. This is demonstrated in Figure 4.4 where we compare the individual measurements of dust and stellar masses of the ETGs and LTGs and the binned values using the classifications from [Driver et al. \(2012\)](#) at $z \leq 0.06$ and $0.06 < z \leq 0.1$. We see a dearth of galaxies below $M_d \sim 10^{5.5}$ and stellar masses below $M_s \sim 10^{7.5}$ in the higher redshift bin compared to the lower redshift bin, therefore we believe there is incompleteness in the morphologically classified sample at $0.06 < z \leq 0.1$.

Our $z < 0.06$ sample of morphologically classified galaxies consist of a total of 5736 sources classified by [Driver et al. \(2012\)](#), 588 of which were ETGs, 4837 as LTGs, and 474 as LBS. In the same redshift range, [Moffett et al. \(2016a\)](#) classified 5765 galaxies with 639 ETGs, 4599 LTGs, and 690 LBSs. There are 773 disagreements between the two sets of classifications (13% of the overall sample). The resulting DMFs from the two classification methods are displayed in Figure 4.5 using single Schechter fits (SSF) to the data (Chapters 2 and 3). The red and blue points are ETG and LTG respectively, and translucent and solid represent the DMFs for the early and late populations as defined by [Driver et al. \(2012\)](#) and [Moffett et al. \(2016a\)](#) respectively. The DMFs agree well out to $z \leq 0.06$ showing that although the individual classifications are not an exact match, the shapes of the DMFs of the

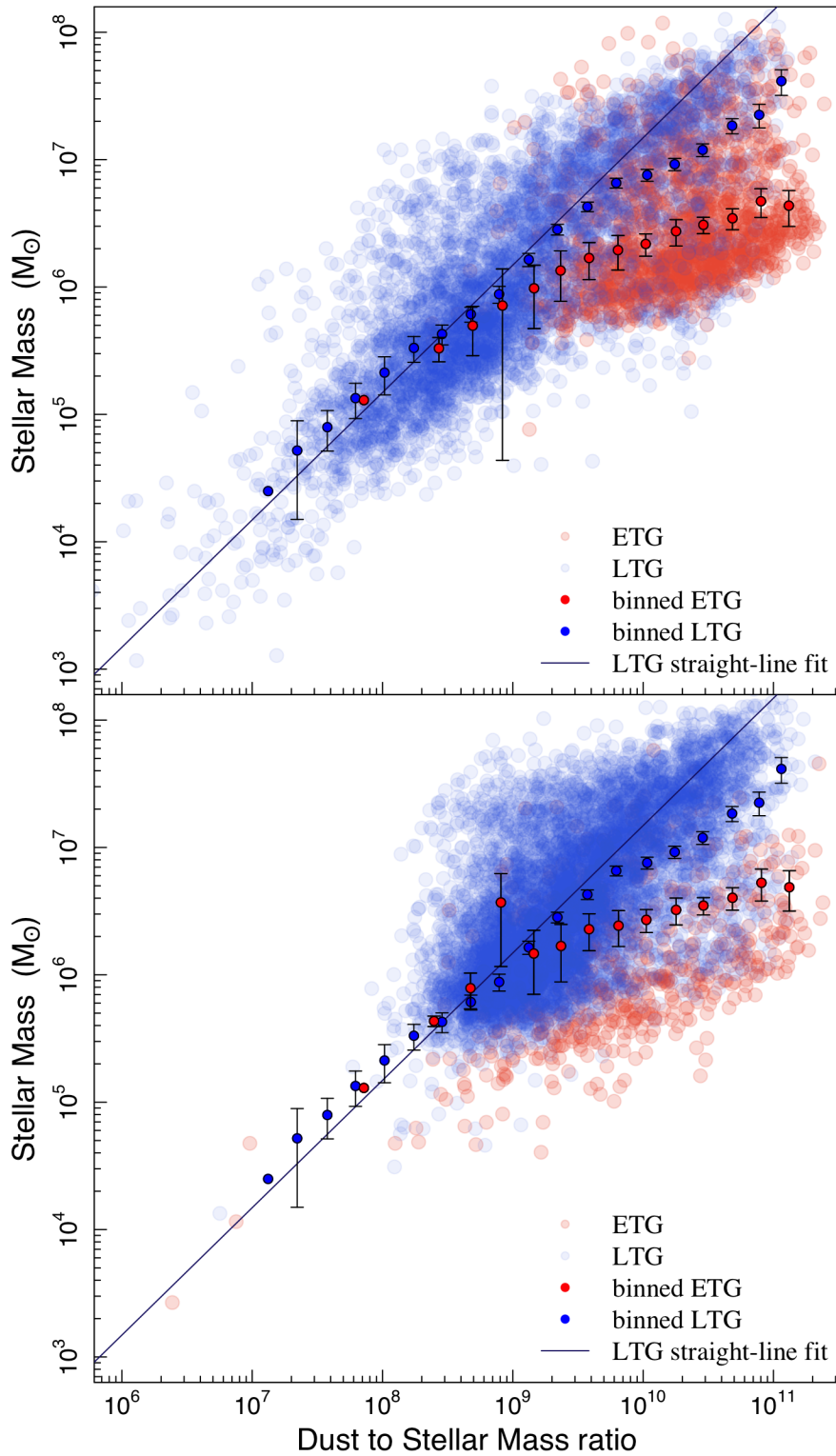


FIGURE 4.4 The mean dust to stellar mass ratio for galaxies in our high and low redshift samples (*Top*: $0.002 \leq z \leq 0.06$, *Bottom*: $0.06 \leq z \leq 0.1$) in bins of galaxy stellar mass for ETGs (red), LTGs (blue) using the morphological classifications of [Driver et al. \(2012\)](#). This illustrates the incompleteness in the [Driver et al. \(2012\)](#) sample of ETGs and LTGs in the higher redshift bin at low stellar masses. We also show in blue a straight-line fit to the LTG data to illustrate the approximate linear scaling of the LTG dust-to-stellar mass ratio at low masses.

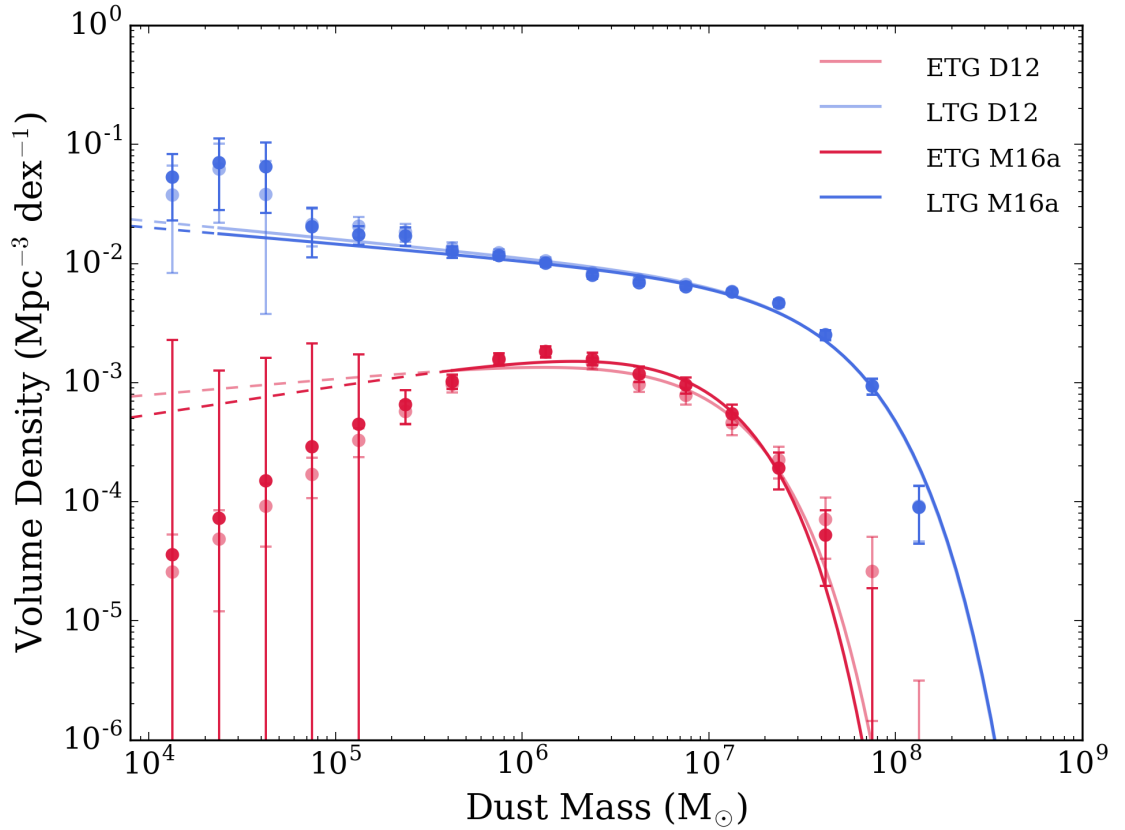


FIGURE 4.5 The pV_{\max} dust mass functions for the GAMA/*H*-ATLAS sources at $0.002 < z < 0.06$. Here the opaque lines show the sample for the fitted range split into ETGs and LTGs by Moffett et al. (2016a) (M16a), and the translucent lines show the sample for the fitted range as split into ETG and LTG by Driver et al. (2012) (D12). Red denotes ETGs and blue the LTGs. The data points show the observed values and the solid lines are the best fitting (χ^2) single Schechter functions to the data for their respective fitted regions, beyond this we show extrapolations down to $10^4 M_{\odot}$ as dashed lines. Error bars are derived from a bootstrap analysis and the data points have been corrected for over and under densities in the GAMA fields (see Wright et al. 2017).

ETG and LTG populations appear to be consistent between the two different classification methods. The Schechter function fit parameters and dust mass densities for ETGs and LTGs are listed in Table 4.2. (From now on we choose to discuss only the Schechter fit parameters arising from the Moffett et al. (2016a) classifications as these are the most recent).

Unsurprisingly we see there is an order of magnitude more dust mass contained within LTGs than ETGs at $z \leq 0.06$, with dust mass density parameters of $\Omega_d = (0.88 \pm 0.03) \times 10^{-6}$ and $\Omega_d = (0.060 \pm 0.005) \times 10^{-6}$ respectively. Therefore we confirm that LTGs contain most of the dust content of the Universe (in galaxies at least). However, Figure 4.5 demonstrates that the ETG DMF is not well described by a Schechter function, indeed there is a significant downturn in the volume density of ETGs below dust masses of $10^6 M_\odot$. We believe this is a real effect since we have no reason to believe that incompleteness may be biasing our measurements at this redshift range. The downturn is also in line with the shape of the elliptical galaxy stellar mass function (GSMF) as measured by Moffett et al. (2016b) (see Section 4.4). Since the DMF for the ETGs clearly does not match a Schechter function, the dust mass density in Table 4.2 may be overestimated. We therefore also calculate the dust mass density for these galaxies using an alternative approach: we simply sum the contribution from each galaxy. We derive a dust density parameter of $\Omega_d = (0.060 \pm 0.005) \times 10^{-6}$. This revised measurement is consistent with the results from the integrated Schechter function since although the Schechter fit over-predicts the total dust mass density in low dust mass sources, it also underpredicts the dust mass density at the high mass end, i.e. the ‘two wrongs’ average out to give a similar answer. Comparing our ETG and LTG Schechter fits with the double component Schechter fit to the total sample from Section 3.5, we find that the major component of the double fit matches the high mass end but slightly overshoots the volume densities derived for the LTGs at intermediate masses $10^5 < M_d(M_\odot) < 10^7$ whereas the second component has a peak volume density at higher dust masses than the ETGs. This suggests that the ETGs and LTG populations cannot be mapped onto the minor and major components of the double Schechter function for the DMF obtained in Chapter 3. However, this may be affected by potential misclassification of galaxy types or due to the degeneracy in what the fitting routine assigns to each component at the faint end, where error bars on the space density of dust galaxies can be large.

| | Population | M^* ($10^7 h_{70}^2 M_\odot$) | α | ϕ^* ($10^{-3} h_{70}^3 \text{Mpc}^{-3} \text{dex}^{-1}$) | Ω_d (10^{-6}) | Number of Galaxies |
|------------------|------------|--------------------------------------|--------------|--|-----------------------------|-----------------------|
| 0.002 < z < 0.06 | ETG | 0.98 ± 0.23 | -1.01 ± 0.08 | 2.05 ± 0.41 | 0.060 ± 0.005 | 639 |
| | LTG | 4.17 ± 0.25 | -1.18 ± 0.03 | 5.75 ± 0.48 | 0.88 ± 0.03 | 4599 |
| | total | 3.72 ± 0.15 | -1.24 ± 0.02 | 6.36 ± 0.45 | 0.92 ± 0.02 | 5937 |

TABLE 4.2 Schechter function fit parameters for the pV_{max} DMFs for the ETG, LTG, and total populations for the low-redshift ($0.002 < z < 0.06$) subset of our sample using morphological classifications from [Moffett et al. \(2016a\)](#).

4.3.1 LITTLE BLUE SPHEROIDS (LBS)

The little blue spheroid class of galaxies in the GAMA sample are, as their name suggests, spheroidal, optically blue, compact and faint (Kelvin et al., 2014b). As such it is difficult to know which class of galaxies these LBS sources belong to: although part of their name suggests they belong with other spheroidal galaxies (ellipticals and S0s), the other part suggests they are blue and have similar colours therefore to the disk-dominated spirals and Irregular classes (LTGs). Kelvin et al. (2014b) showed that including the LBS population in with the ETG class produces a significant upturn in their galaxy stellar mass function at the low mass end, but argue that it is not clear whether this adding LBSs to ellipticals and S0s is physically appropriate. Recent work by Moffet et al. (*in preparation*) provides further evidence that the GAMA LBSs have structural properties that are similar to ETGs, but star forming properties similar to low mass late type galaxies. Although we follow Moffett et al. (2016a) in keeping the little blue spheroids (LBSs) sources in GAMA at $z \leq 0.06$ separate to our ETG and LTG morphological samples (we do not attempt to investigate that morphological class in this work), here we briefly test whether including these sources leads to any difference in the derived dust mass density or the shape of the DMF split by morphological type. We note that the sample size of the LBS is comparable to the ETG sample so one would expect a larger affect on the ETG DMF if LBS galaxies are included in that category compared to the LTG subset.

Figure 4.6 compares the DMFs derived with and without the LBS galaxies, and we see ultimately the DMFs are very similar, with differences in the derived dust mass density and Schechter fit parameters at the level of 2%. The change in the ETG DMF is significant, with the SF parameters changing by around 50%. We therefore feel that the LBS galaxies are probably more similar to LTGs than ETGs.

4.4 COMPARISON WITH THE GALAXY STELLAR MASS FUNCTION

Scaling relations between dust and stellar mass can reveal the relation between internal galaxy properties and the dust content and whether there is a simple prescription that can tell us how much dust exists in galaxies given a unit of stellar mass (e.g. Driver et al. 2018). Cortese et al. (2012b) and Smith et al. (2012c) investigated $M_d - M_s$ scaling relations in local galaxies using the HRS, finding that

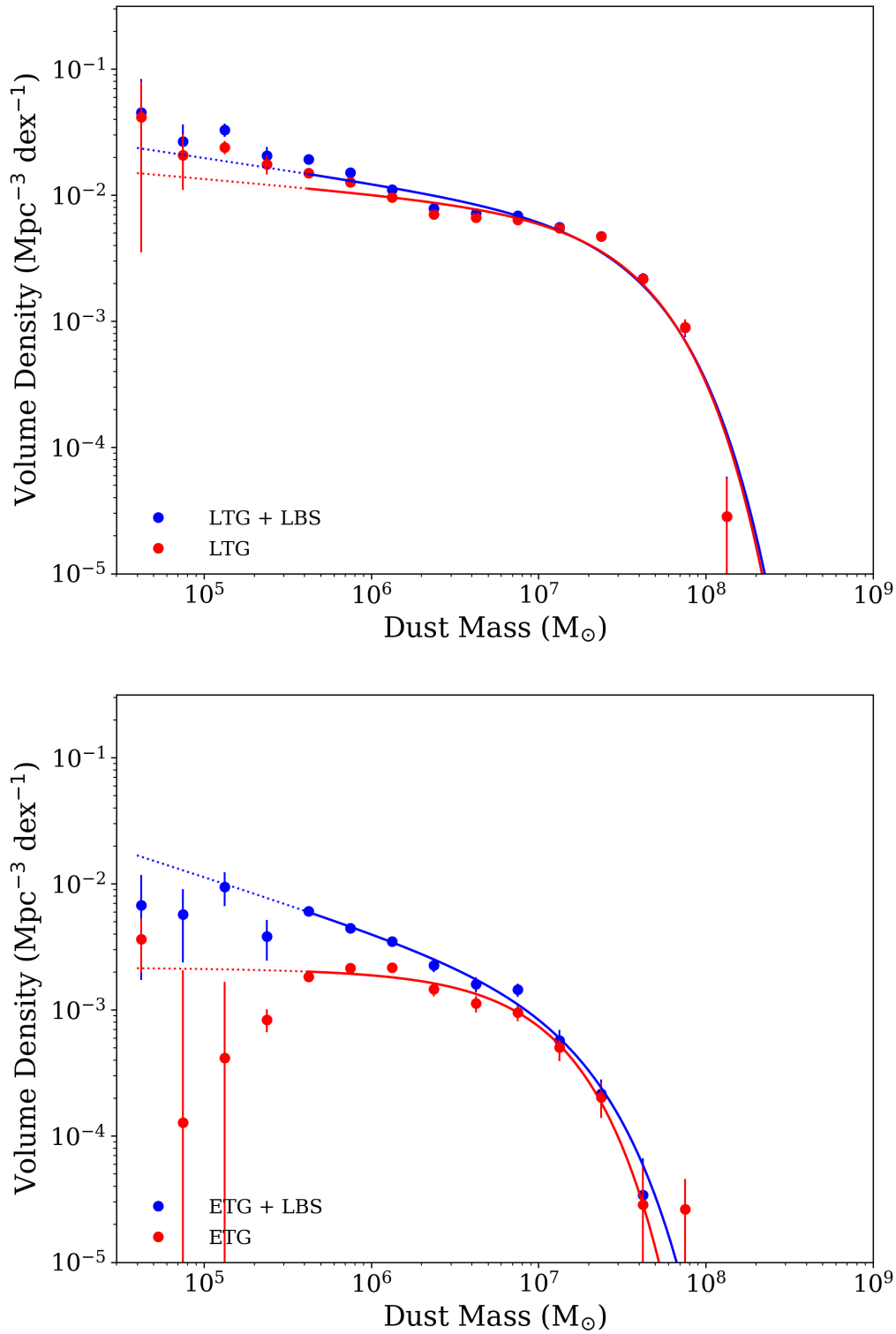


FIGURE 4.6 The DMF in the redshift range $0.002 < z < 0.06$ for *Top*: LTGs with and without including the little blue spheroid (LBS) galaxies classified by [Moffett et al. \(2016a\)](#) and *bottom* for ETGs with and without LBS galaxies.

larger stellar mass galaxies have lower dust-to-stellar mass ratios (see also [Santini et al. 2014](#)). This was further confirmed in the larger statistical study of [Bourne et al. \(2012\)](#) from H-ATLAS (Figure 4.3). As we saw in Section 4.2, the [Popping et al. \(2017\)](#) SAMs produce a trend in $M_d - M_s$ which does not agree with the scatter seen in the observations of local galaxies (due to colour, morphological type, environment etc.) and their models produce too much dust in the highest stellar mass galaxies and not enough dust in the low stellar mass sources. Further modelling of dust and stellar mass scaling relations carried out in [Bekki \(2013\)](#) using chemodynamical simulations approximately reproduces the $M_d - M_s$ trend of local galaxies (with massive disk galaxies more likely to have smaller dust-to-stellar mass ratios), but could not reproduce the $M_d - M_s$ at stellar masses $> 10^{10} M_\odot$. Returning to Figure 4.4, where we show the mean dust mass as a function of mean stellar mass, we see that the low-mass end of the LTG dust versus stellar mass is actually fairly well-represented by a linear relationship, but diverges at higher masses. The change in slope at high M_s is largely caused by LTGs with M_d similar to ETGs at similar M_s ; it is difficult to disentangle whether this effect is entirely physical (ie due to dust-poor LTGs) or due to the misclassification of ETGs as later-type galaxies. However, we can conclude from Figure 4.4 that ETGs do not follow a linear trend of increasing dust mass with increasing stellar mass.

With our dataset we can test whether there is a simple scaling relation between dust and stellar mass by simply comparing the dust and stellar mass functions. Since the Galaxy Stellar Mass Function (GSMF) in [Wright et al. \(2017\)](#) is fit by a coupled double Schechter function (DSF) with shared characteristic mass M^* , it is not equivalent to our DSF in Chapter 3. Instead we compare the single Schechter fit (SSF) with the GSMFs from [Moffett et al. \(2016a\)](#) who present fits for ellipticals and for later morphological types including Sab-Scd, SBab-SBcd, Sd-Irr and S0-Sa. We also compare with [Moffett et al. \(2016b\)](#) who have further decomposed the sample into bulges, spheroids and disk components. This decomposition of galaxies into bulge and disk was performed by fitting a double-Sérsic profile to those galaxies which were morphologically classified as double-component galaxies to obtain bulge-to-total luminosity ratios. From these ratios, the $g - i$ colour and i -band absolute magnitudes for both bulge and disk were derived and used, along with the stellar mass relation of [Taylor et al. \(2011\)](#), to calculate bulge and disk component stellar masses. We have already seen that the DMF is dominated by the LTGs in the previous Section, we now test whether most of the dust will be associated with the disk component of galaxies and whether we can scale from stellar mass to dust mass for different galaxy subsamples. In

Table 4.3 we compare the ratio of the knee of the Schechter function fit parameters (M_d^*/M_s^*) for the GSMF and DMF and the integrated mass densities (ρ_d/ρ_s) between different galaxy populations including LTG, ETGs and disks.

First we compare the GSMFs to their equivalent DMFs for ETGs and LTGs. We produce a composite Schechter function from the later-type GSMFs from Moffett et al. (2016a) containing the same sample of galaxies as our LTG DMF. We show a version of the LTG GSMF composite Schechter function as scaled by the ratio ρ_d/ρ_s in Figure 4.7. The scaled LTG GSMF fits the high-mass end of the LTG DMF; however, it diverges from the datapoints around $10^7 M_\odot$ where a more pronounced shoulder is seen in the GSMF than we observe in the DMF. Otherwise the composite LTG GSMF is in good agreement with our data, and therefore an estimate of the LTG DMF could be made by scaling the LTG GSMF by a factor of $(8.07 \pm 0.35) \times 10^{-4}$.

Moffett et al. (2016a) includes an Elliptical GSMF (equivalent to what we have defined here as ETG), and we scale this function by the ρ_d/ρ_s in order to compare with the ETG DMF. As seen in Figure 4.7, the scaled Elliptical GSMF is not a good match to the ETG DMF data or Schechter function. Compared to the data, the scaled GSMF is too high for $M_d > 10^7$ and $M_d < 10^{5.5}$, and too low for $10^{5.5} < M_d < 10^{6.5}$. Indeed, the Elliptical GSMF is also not well-fitted by a Schechter function, and displays the same downturn that we see in the DMF. Whilst the low-mass slope derived by Moffett et al. (2016a) does show a drop-off, it is not as severe as actually observed in either the dust mass or stellar mass function data. Also, we note that the dust mass as a function of stellar mass for ETGs as seen in Figure 4.4 is not consistent with a simple linear relationship. We therefore caution against using a scaling law between stars and dust that relies upon a Schechter function fit to ETGs. We also note that the ratio M_d^*/M_s^* for this sample is $(0.94_{-0.24}^{+0.25}) \times 10^{-4}$, which is of order 17-25 times higher than the average dust-to-stellar mass ratios of ellipticals observed in recent *Herschel* studies of ETGs in the local volume ($D < 40$ Mpc, Smith et al., 2012c; Amblard et al., 2014). This may suggest some contamination in our E category from S0s, though we note that the targeted *Herschel* studies were potentially biased to older redder sources (Rowlands et al., 2012; Clark et al., 2015) and high density environments (Smith et al., 2012c; Agius et al., 2013).

Next we attempt to explore the relationship between stellar mass of the disk component and the dust mass of a galaxy. Moffett et al. (2016b) found that the disk GSMF is well fit by a Schechter function with $\alpha_{\text{disk}} = -1.20 \pm 0.02$, which is consistent with our alpha values both for the LTG DMF and the total DMF for

the $z < 0.06$ sample. (We have corrected for the fact that the ϕ^* values for the stellar mass functions listed in [Moffett et al. \(2016b\)](#) are in units of Mpc^{-3} and not $\text{Mpc}^{-3} \text{dex}^{-1}$.) Based on the compatibility of the α values, there may be a simple scaling from the disk GSMF to either the total or LTG population DMFs. The scaled function is a good but imperfect fit, and we see a moderate overshoot of the high mass data points by this scaled function, reflecting the fact that the dust-to-stellar mass ratio is not constant. We therefore conclude most of the dust in galaxies is associated with their disk components, and that it is possible to obtain a reasonable representation of the DMF by scaling the disk GSMF by the ratio $\rho_d/\rho_s = (10.21 \pm 0.45) \times 10^{-4}$. We can see that the ratios M_d^*/M_s^* and ρ_d/ρ_s for the disk GSMF and both the total and LTG DMFs shown in [Table 4.3](#) are discrepant by more than 1σ . This provides further evidence that the scaling from the disk GSMF to the DMF of either population cannot be exactly linear. We also infer from this that the dust-to-stellar mass ratio is higher for lower-mass disks. We refer the reader to [De Vis et al. \(2017b\)](#) whose work hints that the observed dust-to-stellar mass properties of local galaxies may require the contribution of dust sources from stars and interstellar grain growth to be different for low and high mass galaxies.

Given that the observed dust-to-stellar masses of galaxies are not linear across the whole stellar mass range ([Figure 4.3](#) and [4.4](#)), it is somewhat surprising that we can simply scale the GSMFs of LTGs and disks and obtain DMFs close to that observed in this work. Although the binned dust masses in [Figure 4.4](#) at stellar masses greater than $10^{9.5} M_\odot$ depart from a linear scaling relation, on average we can assume the slopes are close to linear (especially around the knee of the SF) and therefore this simple scaling appears to work. Surprisingly, this simple scaling from stellar mass to dust mass for LTGs at $z = 0$ ([Figure 4.7](#)) may suggest that all the different dust processes (dust condensation in stellar atmospheres and SNe, grain-growth, dust destruction) are correlated to the growth of stellar mass in galaxies. The dispersion in this scale (e.g. [Figure 4.3](#) and [4.4](#)) could potential place limits on the way dust is formed and how it evolves.

We note that the uncertainties on the datapoints in the GSMFs quoted in [Moffett et al. \(2016a\)](#) and [Moffett et al. \(2016b\)](#) are based on an on-sky jackknife analysis. As we described in [Section 6.4.1](#), this estimate will include a cosmic variance uncertainty component. Since we cannot disentangle the inherent cosmic variance from their values we choose instead to use the same percentage uncertainty in the integrated stellar mass density as our percentage uncertainty in the integrated dust mass density. Since the errors in dust mass are larger than for stellar mass for our dataset, the uncertainty in the integrated stellar mass density

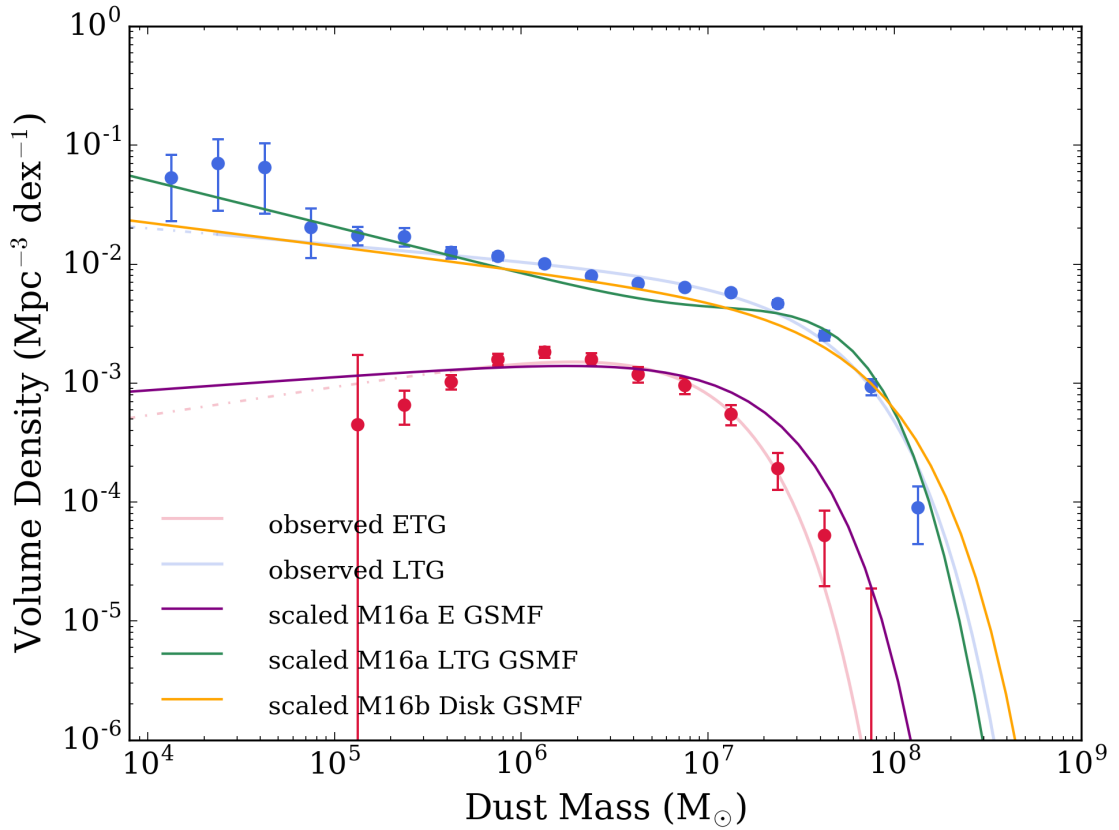


FIGURE 4.7 The pV_{\max} dust mass functions for the GAMA/*H*-ATLAS sources at $0.002 < z < 0.06$. The Schechter fits for the ETGs and LTGs are shown by the solid red and blue lines for the fitted range, beyond this we show extrapolations down to $10^4 M_{\odot}$ as dashed lines. We also compare the GAMA galaxy stellar mass functions from Moffett et al. (2016a) (M16a) and Moffett et al. (2016b) (M16b) scaled by ρ_d/ρ_s . This includes the Moffett et al. (2016a) Elliptical and Late types GSMFs scaled by $\rho_{d,ETG}/\rho_{s,Elliptical}$ and $\rho_{d,LTG}/\rho_{s,(Sab-Scd+Irr+S0-Sa)}$ (purple and green respectively) and the Moffett et al. (2016b) disk GSMF scaled by $\rho_{d,LTG}/\rho_{s,disk}$ (yellow).

should not be larger than for our integrated dust mass density for the same sample; as such this estimate of the error is a conservative one.

4.5 INVESTIGATING EVOLUTION WITH REDSHIFT

We attempted to split the sample into two redshift bins ($0.002 < z < 0.06$ and $0.06 < z < 0.1$) in Figure 4.8. We see very little difference in the resulting DMFs. The evolution in this low redshift bin is not strong enough to make a definitive conclusion about whether the DMF evolves with redshift. The decline of *Herschel* detections with redshift makes trying to establish an estimate of the DMF at higher redshifts with this sample unreliable. A large portion of the low-redshift

| DMF Population | Stellar Mass Population | M_d^*/M_s^* (10^{-4}) | ρ_d/ρ_s (10^{-4}) |
|----------------|-------------------------|--------------------------------|----------------------------------|
| ETG | Elliptical | $0.94^{+0.25}_{-0.24}$ | 1.00 ± 0.11 |
| LTG | All Disks | $7.77^{+0.76}_{-0.73}$ | 10.21 ± 0.45 |
| LTG | LTG | - | 8.07 ± 0.35 |
| Total | All Disks | $6.93^{+0.61}_{-0.58}$ | 10.66 ± 0.38 |

TABLE 4.3 The ratio M_d^*/M_s^* and ρ_d/ρ_s values for various combinations of dust mass functions derived in this work and stellar mass functions for different populations from this work and from [Moffett et al. \(2016a,b\)](#). The LTG category in the stellar mass column from [Moffett et al. \(2016a\)](#) is defined as the combination of sources classified as Sab-Scd+Irr+S0-Sa. We have corrected for the fact that the ϕ^* values for the stellar mass functions listed in [Moffett et al. \(2016b\)](#) are in units of Mpc^{-3} and not $\text{Mpc}^{-3} \text{dex}^{-1}$.

galaxies already do not have any constraints on the FIR and submm and therefore rely heavily on the MAGPHYS priors. For an investigation of this sort we would require a much larger sample of galaxies with far better *Herschel* constraints at higher redshifts. Further investigation into the evolution of the DMF in terms of redshift will be explored later in the Thesis.

4.6 CONCLUSIONS

In this Chapter we compare the observed DMF from Chapter 2 with theoretical models, and split the sample into populations in order to investigate scaling models between stars and dust, early and late type galaxies and evolution in redshift. We find:

- We find that there is a discrepancy between the observed and predicted dust mass functions derived from the semi-analytic models of [Popping et al. \(2017\)](#). This is largest at the high-stellar mass end, with the model predictions of M^* higher by 0.5 dex compared to our observed, Schechter functions. The likely cause for the discrepancy is that the Popping model uses a relationship between dust and stellar mass which is inconsistent with properties observed in local galaxies samples such as the *Herschel*-ATLAS, the HRS and the DGS, and also with our sample of GAMA sources: the models produce high stellar mass galaxies with dust masses far higher than is observed. This discrepancy is alleviated somewhat when we compare with the predicted DMF

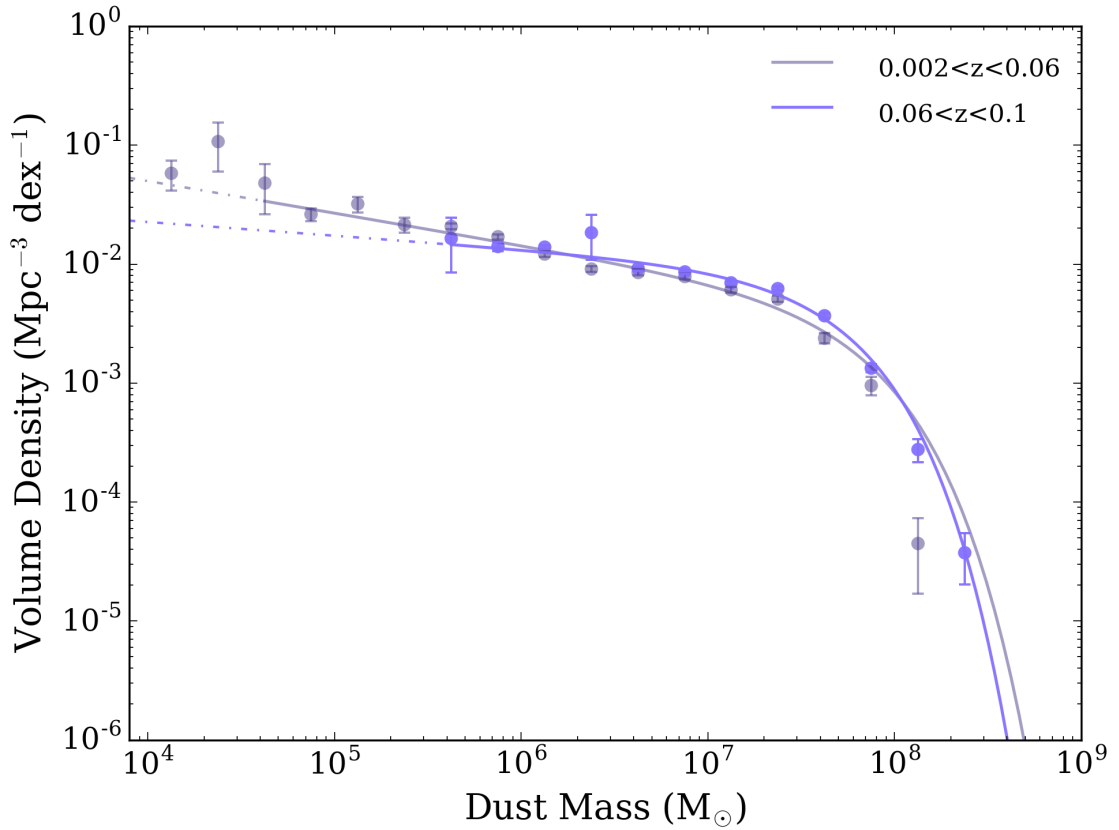


FIGURE 4.8 The pV_{\max} dust mass functions for the GAMA/H-ATLAS sources at $0.002 < z < 0.06$ (grey) and $0.06 < z < 0.1$ (blue). The data points show the observed values and the solid lines are the best fitting (χ^2) single Schechter functions to the data for their respective fitted regions, beyond this we show extrapolations down to $10^4 M_{\odot}$ as dashed lines. Error bars are derived from a bootstrap analysis and the data points have been corrected for over and under densities in the GAMA fields (see [Wright et al. 2017](#)).

from cosmological hydrodynamical simulations ([McKinnon et al., 2017](#)) who use longer grain growth timescales. This reduces the amount of dust formed in high mass galaxies; however, [McKinnon et al. \(2017\)](#) under-predict the number of high dust mass galaxies compared to our observations, although the limited volume of their simulation does not allow a proper comparison. Both sets of theoretical predictions also fail to match the observed volume density of low dust mass galaxies. Our dataset thus provides a useful benchmark for models.

- Splitting our sample into early and late-type on the basis of morphology and colour (to a redshift limit of $z \leq 0.06$), results in DMFs with very different shapes. The late-type DMF is well represented by a Schechter function, whereas the ETG DMF is not. The LTG DMF has far higher space density at a

given dust mass. We derive dust mass densities of $\Omega_d = (0.88 \pm 0.03) \times 10^{-6}$ and $\Omega_d = (0.060 \pm 0.005) \times 10^{-6}$ for late types and early types respectively. In total there is ~ 10 times more dust mass density in late-type galaxies compared to early-types at $0.002 < z \leq 0.06$. There is not as large a difference (factor of ~ 50) as seen in the sample from the local *Herschel* Reference Survey (Boselli et al., 2010; Smith et al., 2012c; Cortese et al., 2012a), though Agius et al. (2015) suggests that the difference in dust mass in ETGs and LTGs in that sample may be due to oversampling dust poor galaxies in high density environments.

- In comparing our DMF to the galaxy stellar mass functions (GSMFs) from Wright et al. (2017) and Moffett et al. (2016a,b), it is possible to scale from the LTG galaxy stellar mass function (GSMF) to the LTG DMF using a ratio of $\rho_d/\rho_s = (8.07 \pm 0.35) \times 10^{-4}$. Similarly, we show that one can scale from the disk GSMF to the LTG DMF using the ratio $\rho_d/\rho_s = (10.21 \pm 0.45) \times 10^{-4}$. We caution that using Schechter values derived from Schechter function fits to the ETG DMF and Elliptical GSMF may be inadvisable since neither are well-fitted by a Schechter function, although scaling from the Elliptical GSMF to the ETG DMF by multiplying by $\rho_d/\rho_s = (1.00 \pm 0.11) \times 10^{-4}$ returns a reasonable representation of the ETG DMF around the knee.
- We do not see a large difference in the DMFs split into the redshift bins $0.002 < z < 0.06$ and $0.06 < z < 0.1$ though here we are looking at a narrow range in redshift. We will return to the redshift evolution in a later Chapter.

CHAPTER 5

DERIVING DUST PROPERTIES FOR THE FIR-SELECTED GALAXIES OF THE *H-ATLAS* EQUATORIAL FIELDS

‘He’d have been happier if there’d been a demon or some sort of magic. Something simple and understandable. He didn’t like the idea of meddling in science’

TERRY PRATCHETT

In this Chapter, we derive dust properties for the FIR-selected *H-ATLAS* equatorial regions. A comprehensive review of the first data release (DR1) of *H-ATLAS* including photometry, and optical ID matching can be found in [Valiante et al. \(2016\)](#) and [Bourne et al. \(2016\)](#). We use two methods to find dust masses for the galaxies in the sample, firstly the method outlined in [Dunne et al. \(2011\)](#), hereafter D11 which relies upon MAGPHYS fits to a subsection of the sample. Secondly, we perform a stacking analysis similar to [Bourne et al. \(2012\)](#), where we stack the *Herschel* luminosities of galaxies we assume to have similar FIR SEDs in order to find trends with redshift and luminosity of dust properties. We use both estimations to test trends between dust properties, 250 μm luminosity, and redshift. In previous Chapters we have presented the dust properties of the equatorial fields using a sample comprised of optically selected galaxies. Here we study the same patch of sky but through a catalogue formed of galaxies selected on their FIR and sub-mm emission.

5.1 LITERATURE TRENDS FOR DUST PROPERTIES WITH REDSHIFT, FIR LUMINOSITY, AND STELLAR PROPERTIES

[Bourne et al. \(2012\)](#) performed a stacking analysis on the overlap between the equatorial regions of *H*-ATLAS and GAMA in order to probe trends of dust properties for galaxies of different types, optical brightness, optical colour, stellar mass, and redshift. This study was based on stacking directly into SPIRE maps from *H*-ATLAS at the location of sources from the GAMA survey, which selected galaxies with a petrosian *r*-band magnitude limit of 19.8. They found that the dust properties for optically red, green, and blue galaxies are markedly different, and that the evolution of dust properties with redshift, stellar mass, and *r*-band magnitude is dependent on galaxy type. They found that the dust temperature of blue galaxies in particular strongly increased with increasing stellar mass and *r*-band magnitude. Similarly [Hwang et al. \(2010\)](#) used PACS Extragalactic Probe (PEP), *Herschel* Multi-tiered Extragalactic Survey (HerMES, [Oliver et al. 2012](#)), and SDSS to form a sample of 190 local galaxies to show that there was a strong increase in dust temperature with IR luminosity. [Smith et al. \(2011\)](#) however, found no correlation between temperature and luminosity for a sample of 2423 local galaxies from the *H*-ATLAS SDP with matched counterparts in SDSS.

The fantastic sensitivity achieved by *Herschel* combined with the beneficial effects of negative *K*-correction means that a large high-redshift contingent is present in the *H*-ATLAS sample. Negative *K*-correction is the effect whereby a modified blackbody emitting at FIR/sub-mm wavelengths has a steep SED above the selection wavelength. Any reduction in brightness due to redshifting is made up for by the *K*-correction since the SED is proportionally brighter at shorter wavelengths. The effect of introducing more high redshift sources into the catalogue is beneficial in that it allows for studies further back in cosmic time; however, it also means that there is much more confusion in FIR/sub-mm maps than in optical ones.

In Chapters 2-4 we studied the overlap between *H*-ATLAS and GAMA from the optically selected point of view, and now in this Chapter we will approach the overlap on the basis of FIR selection. We are therefore uniquely able to probe the differences in the dust properties of samples selected based on their stellar and dust populations for a very large number of galaxies. In this Chapter we derive dust properties for the galaxies in the FIR selected *H*-ATLAS DR1 sample.

5.1.1 PHOTOMETRY

The FIR/sub-mm fluxes used in this work come from [Valiante et al. \(2016\)](#), which contains 29 235 galaxies below $z = 0.5$. MADX ([Maddox et al., in prep.](#)) was used to extract sources from the *Herschel* maps and estimate their point source fluxes. MADX first removed the diffuse Galactic dust emission, and then convolved the $250\ \mu\text{m}$ maps with a matched-filter. The signal to noise ratio (SNR) limit for the extraction of sources was set at 2.5σ . After initial extraction, a more accurate point source flux measurement was estimated for each of the three SPIRE bands for all source positions, after which point any source with a $\text{SNR} > 4$ in any band made it into the final catalogue. In the case of an extended source, the flux was measured using aperture photometry. In theory the selection could depend on any of the three SPIRE bands, but in practice this selection is determined by the $250\ \mu\text{m}$ flux.

5.1.2 OPTICAL IDS

[Bourne et al. \(2016\)](#) used a likelihood ratio technique to match *H-ATLAS* sources to optical counterparts in SDSS. For each *H-ATLAS* source they searched a 10 arcsecond radius around the source for potential optical counterparts and assigned each source in that area a reliability R , which is simply the probability that the optical source is the true counterpart to the *H-ATLAS* source. The likelihood ratio is the ratio between the probability of identifying the correct counterpart, and of identifying another source not associated to the FIR source in question. The likelihood of a source being the true counterpart is given by:

$$L = \frac{q(m)f(r)}{n(m)} \quad (5.1)$$

where $q(m)$ is the r -band magnitude probability distribution of true counterparts, $f(r)$ is the radial probability distribution of the offsets between the on-sky positions of the FIR and optical sources, and $n(m)$ is the r -band magnitude probability distribution of the full r -band catalogue. The likelihood ratio R is then computed as the ratio of the likelihood that a given optical source is the true counterpart divided by the sum of the likelihoods of all other possible optical counterparts. Here we use the advised reliability cut of $R > 0.8$, which gives a good balance between contamination rate of incorrect optical IDs, and the introduction of incompleteness to the catalogue ([Smith et al., 2011](#)).

5.1.3 REDSHIFTS

Where available spectroscopic redshifts are used during this analysis, preferentially taken from GAMA (Baldry et al., 2014) where there is overlap between the two catalogues. GAMA compiled a catalogue of supplementary spectroscopic redshifts from SDSS DR7 and DR10 (Ahn & et al., 2013), WiggleZ (Drinkwater et al., 2010), 2SLAQ LRG and QSO samples (Cannon et al., 2006; Croom et al., 2009), 6dF (Jones et al., 2009), MGS (Driver et al., 2005), 2QZ (Croom et al., 2004), 2dF (Colless et al., 2001), and UZC (Falco et al., 1999). Further spectroscopic redshifts were provided for this work by the HELP team (Matt Smith, private communication) that were not available at the time of the DR1 release. *H*-ATLAS did produce their own photometric redshifts using ANNz, an artificial neural network (Collister & Lahav, 2004); however, these were shown to be biased past a redshift of ~ 0.3 by D11, where a strong deviation from the spectroscopic redshifts is observed, as seen in Figure 5.1. For those galaxies with no spectroscopic redshift, we use photometric redshifts from the Kilo Degree Survey (KiDS) catalogue (de Jong et al., 2017). There are two different estimates for the redshift available from KiDS, firstly using an artificial neural network ANNz2 (the successor to ANNz, (Sadeh et al., 2016)), and secondly the Multi Layer Perceptron with Quasi Newton Algorithm (MLPQNA; Bilicki et al. 2018). A comparison of the redshift estimates from the available sources can be seen in Figure 5.1. The recommendation from de Jong et al. (2017) is to use MLPQNA for relatively bright, nearby sources ($r < 20.5$; $z < 0.5$), which covers more than half (55%) of the galaxies in this sample which do not have spectroscopic redshifts. This is because the dataset used to train MLPQNA lay mostly within these ranges, and so are most reliable for this kind of source. MLPQNA has the tighter correlation with the GAMA spectroscopic redshifts, but since it is trained on relatively bright and nearby sources this is unsurprising. A comparison of the redshifts from MLPQNA and ANNz2 for galaxies without a spectroscopic redshift are shown in Figure 5.2, which shows that they are very consistent within our sample. Generally the photometric redshifts from ANNz calculated by *H*-ATLAS are in good agreement with both sets of redshifts from KiDS with a small tendency for *H*-ATLAS to under-estimate compared to the KiDS estimates at higher redshifts. A problem that was pointed out by D11 was that photometric redshift estimates for the SDP field tended to underestimate z compared to spectroscopic redshifts above $z \sim 0.5$. This still seems to be the case, and could introduce some bias into our results. We choose to use the MLPQNA photometric redshifts for galaxies without a spectroscopic redshift in this work.

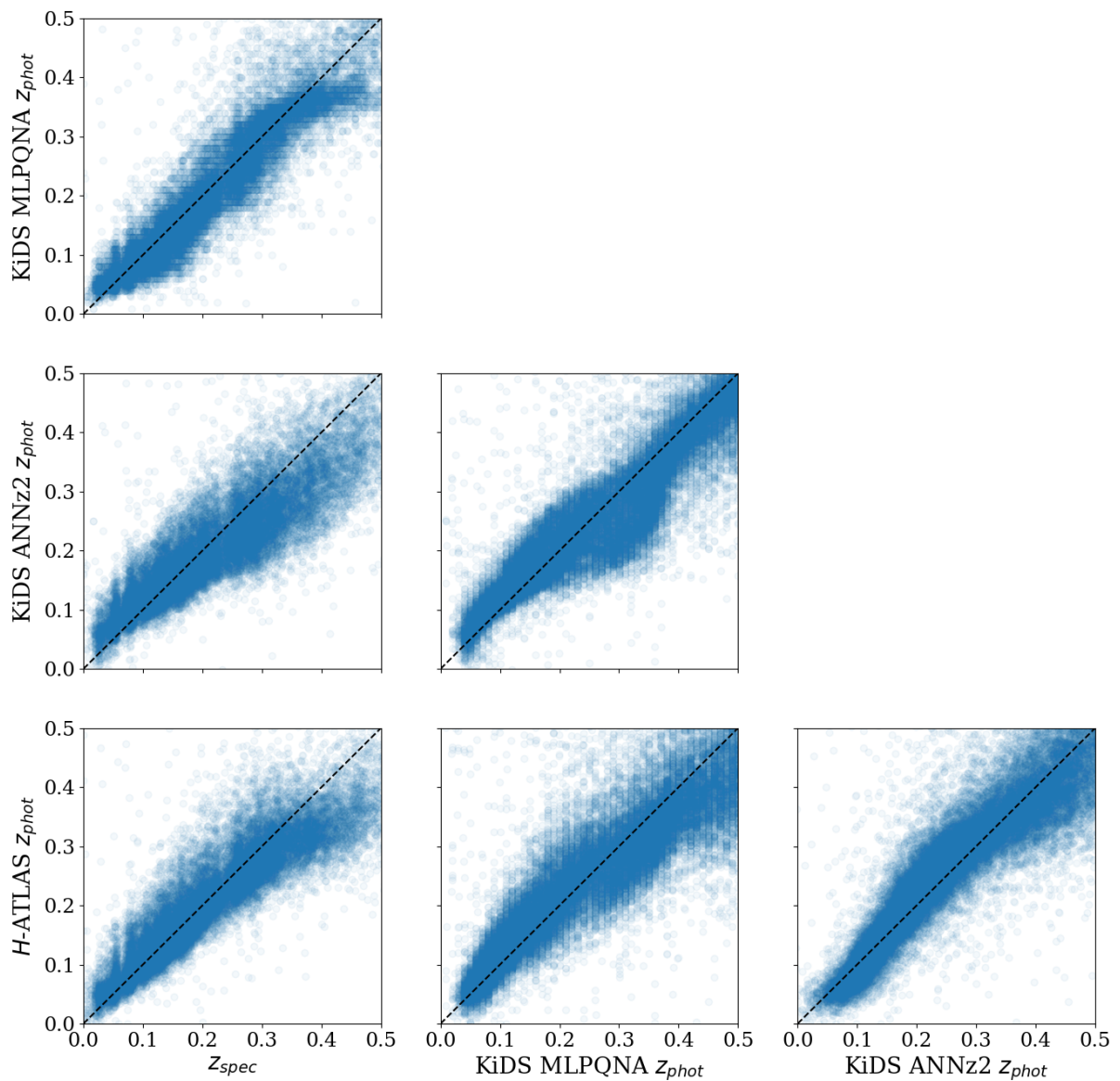


FIGURE 5.1 A comparison of the redshift estimates considered in this work. Spectroscopic redshifts were collected from GAMA, SDSS DR7 and DR8, 2SLAQ LRG and QSO samples, 2dF, and 6dF. Three estimates of photometric redshifts are also shown, those found by the *H-ATLAS* team using the ANNz software, and two estimates found by the KiDS team using ANNz2 and MLPQNA.

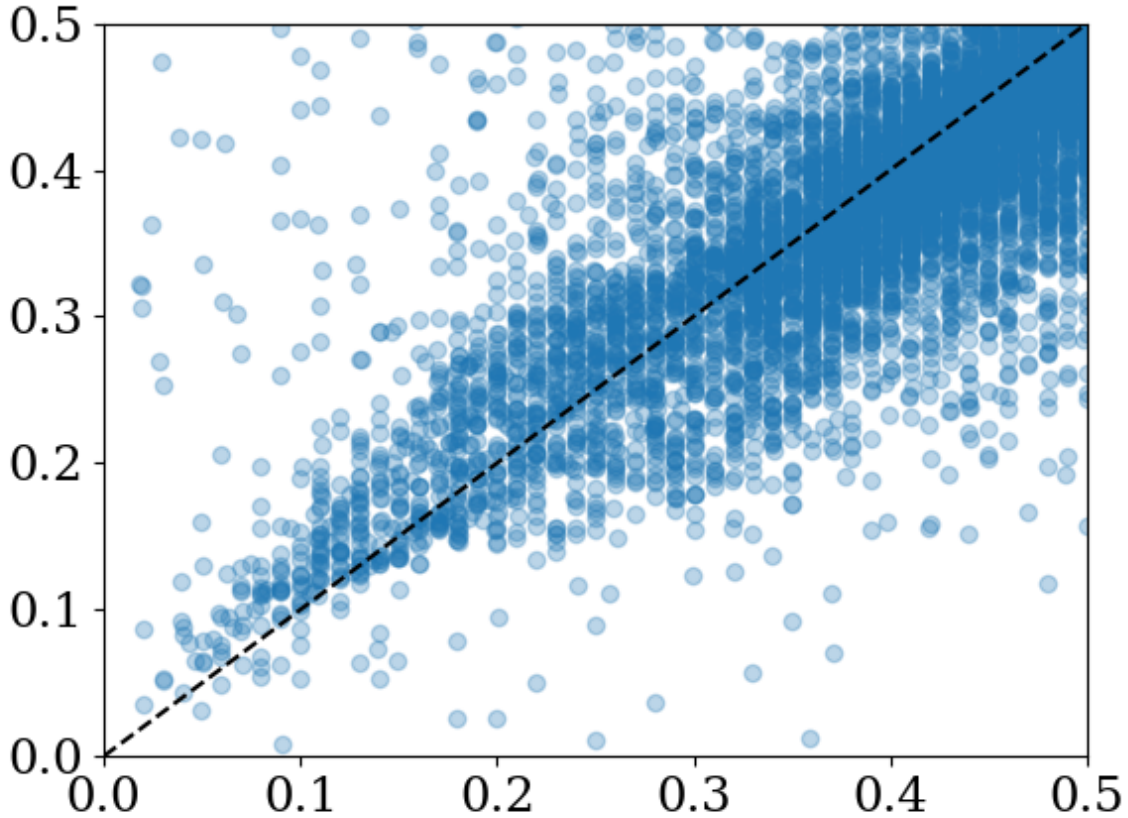


FIGURE 5.2 A comparison of the redshift estimates found by the KiDS team using ANNz2 and MLPQNA for the sources without a spectroscopic redshift.

5.1.4 STAR-GALAXY SEPARATION

SDSS sources are matched to the UKIDSS (DR8) catalogue, which provides values for J and K magnitudes. Sources in the *H*-ATLAS catalogue can therefore be separated into stars and galaxies, either because they are extended sources (using the r -band point spread function (PSF) and model magnitudes), or because they have colours which are not consistent with those of a star (Bourne et al. 2016, B16). Any source which was classed as a star with a redshift > 0.001 was reclassified as either a quasar or a quasar candidate depending on whether it had a good-quality spectroscopic redshift, or a photometric redshift respectively.

5.1.5 CALCULATING LUMINOSITIES

Monochromatic rest-frame luminosities are calculated using the *Herschel* fluxes derived by *H-ATLAS*, and the equation:

$$L_\nu = \frac{4\pi D_L^2 S_\nu K}{(1+z)} \quad (5.2)$$

where L_ν , and S_ν are the luminosity, and flux respectively at frequency ν in W Hz^{-1} and $\text{W Hz}^{-1} \text{m}^2$, D_L is the luminosity distance, z is the redshift of the source, and K is the K -correction, given by:

$$K = \left(\frac{\nu_{\text{rest}}}{\nu_{\text{obs}}} \right)^{3+\beta} \frac{e^{h\nu_{\text{obs}}/k_B T_d} - 1}{e^{h\nu_{\text{rest}}/k_B T_d} - 1} \quad (5.3)$$

where ν_{obs} , and ν_{rest} are the observed, and rest-frame frequency respectively, k_B is the Boltzmann constant, β is the emissivity index, and T_d is the temperature corresponding to the SED shape. Here the T_d is initially assumed to be 26 K.

5.2 ESTIMATING DUST PROPERTIES

We perform two methods of finding dust properties for the galaxies in *H-ATLAS* DR1 fields, firstly, we use *MAGPHYS* to find estimates of dust masses and temperatures for individual galaxies with spectroscopic redshifts in our sample. Using the masses for these galaxies, we derive a simple relationship between $250 \mu\text{m}$ luminosity and dust mass. For the remaining galaxies without a *MAGPHYS* fit, we use this relationship and their $250 \mu\text{m}$ luminosity to calculate an estimate of their dust mass. Secondly, we group galaxies in $250 \mu\text{m}$ luminosity and redshift bins and perform a stacking analysis on their *Herschel* luminosities in order to find a more reliable global SED shape and use this to find dust mass estimates for the galaxies in that bin.

5.2.1 MAGPHYS ESTIMATES OF DUST PROPERTIES

A *MAGPHYS* analysis was performed by [Eales et al. \(2018\)](#) for the subsection of galaxies with a spectroscopic redshift < 0.4 using the method outlined in ([Smith et al., 2012b](#)). The *MAGPHYS* results provide dust masses for 21 083 galaxies in the *H-ATLAS* DR1 fields, which leaves 8152 galaxies without a dust mass estimate. In this Section we attempt to find a simple relationship between $250 \mu\text{m}$ luminosity and dust mass using the available *MAGPHYS* dust masses as a "training set"

for galaxies without MAGPHYS fits. Using this relation we will find a dust mass estimate for the galaxies in the remainder of the sample. Unfortunately this may introduce bias into our results since the galaxies used to derive the relationship will be those that are optically bright enough to have a spectroscopic redshift, but we expect this bias to be small.

MAGPHYS was discussed in detail in Section 2.3, but we provide a brief recap here. MAGPHYS fits model SEDs to galaxy spectra using χ^2 minimisation and vast libraries of optical and FIR models. MAGPHYS requires energy balancing, which means that all of the energy absorbed in the optical regime must be re-radiated in the FIR regime. MAGPHYS returns many different stellar and dust properties, presenting both a ‘best fit’ for each parameter as well as percentile values corresponding to the median, and the 1, 2, and 3σ confidence intervals. The MAGPHYS results from Eales et al. (2018) were found using a slightly different version of MAGPHYS to the one used by GAMA, and did not include the most up-to-date versions of the *Herschel* band-pass profiles¹. We note that the B18 analysis used the median values for all dust properties. In this analysis however, we are forced to use the best-fitting masses since the version of MAGPHYS used by Eales et al. (2018) contained an error which affected the calculation of the percentile values.

5.2.1.1 DERIVING A RELATIONSHIP BETWEEN 250 μm LUMINOSITY AND DUST MASS

D11 used dust masses obtained via MAGPHYS SED fitting for 1120 galaxies in the SDP field of *H*-ATLAS (14.4 sq deg) to derive a relationship between the observed 250 μm luminosities (L_{250}), and dust mass. They then applied this relationship to the L_{250} of a further 747 sources, which had no available MAGPHYS fits in order to estimate their dust mass. They found that a simple linear relationship between $\log(M_d)$ and $\log(L_{250})$ was a good descriptor of this trend, given by:

$$\log(M_d) = \log(L_{250}) - C \quad (5.4)$$

The value for C found by D11 ($C = 16.47$) is equivalent to a one component modified blackbody (MBB) with dust temperature ~ 20 K. We carry out the same analysis here using the MAGPHYS dust masses available for 21 083 sources in the *H*-ATLAS DR1 fields with a spectroscopic redshift < 0.4 . We find $C = 16.46$,

¹ There was a GAMA MAGPHYS run before the band-pass profiles were updated, and the difference between the resulting dust properties of the two catalogues was very small.

i.e. we obtain the same trend as the smaller D11 sample, even over two orders of magnitude wider range of luminosities in the DR1 sample from this work. This relationship is shown in Figure 5.3 alongside the very similar trend found by D11. Using this relationship is in effect the same as applying a one component MBB with $T_d = 20$ K to the remaining sources. As such, the resulting dust masses may be over or underestimated depending on the "true" dust temperature for each source. Many studies of nearby galaxies have found that 20 K is a good approximation of the dust temperature for most galaxies (e.g. Dunne & Eales 2001; Draine & Li 2007; Bendo et al. 2010; Boselli et al. 2010, D11). We do note however that Clark et al. (2015) found that for a sample of local FIR selected galaxies, the average dust temperature was 14.6 K. Bendo et al. (2015) showed that low-luminosity cold components often exist, and can account for most of the dust mass of a galaxy but are much harder to detect.

The relationship derived here may not be valid for all redshift ranges. As seen in Figure 5.4, the fraction of galaxies with an individual dust mass measurement decreases rapidly after a redshift of 0.3 meaning that we are increasingly reliant on the $L_{250} - M_d$ relationship beyond this point. It is important to know whether the trend holds since this relationship will be important in determining the evolution of dust properties with redshift, particularly for the highest redshift slice. We tested splitting the dataset into five redshift slices and re-fitting the $L_{250} - M_d$ relationship and found negligible change (<0.01) in C . This implies that the average dust temperature as a function of redshift is stable. In Figure 5.5 we show the evolution of cold dust temperature from MAGPHYS with redshift (top) and L_{250} (bottom) for those galaxies which have either a 4σ detection in either a PACS band, or at $350\mu\text{m}$ as well as a 4σ detection in L_{250} . We do not see any evolution of cold dust temperature in these plots with either redshift or $250\mu\text{m}$ luminosity.

5.2.2 A STACKING ANALYSIS OF THE *H*-ATLAS EQUATORIAL FIELD SAMPLE

A high portion of galaxies in our sample (74%) have only one *Herschel* band with a $> 4\sigma$ measurement. Fitting a modified blackbody to these individual SEDs would therefore be unreliable in most cases. For this reason we sought a better way to quantify the dust properties of galaxies, and so in this Section, we perform a stacking analysis on the *Herschel* luminosities to derive dust properties in different $250\mu\text{m}$ luminosity and redshift ($L - z$) bins.

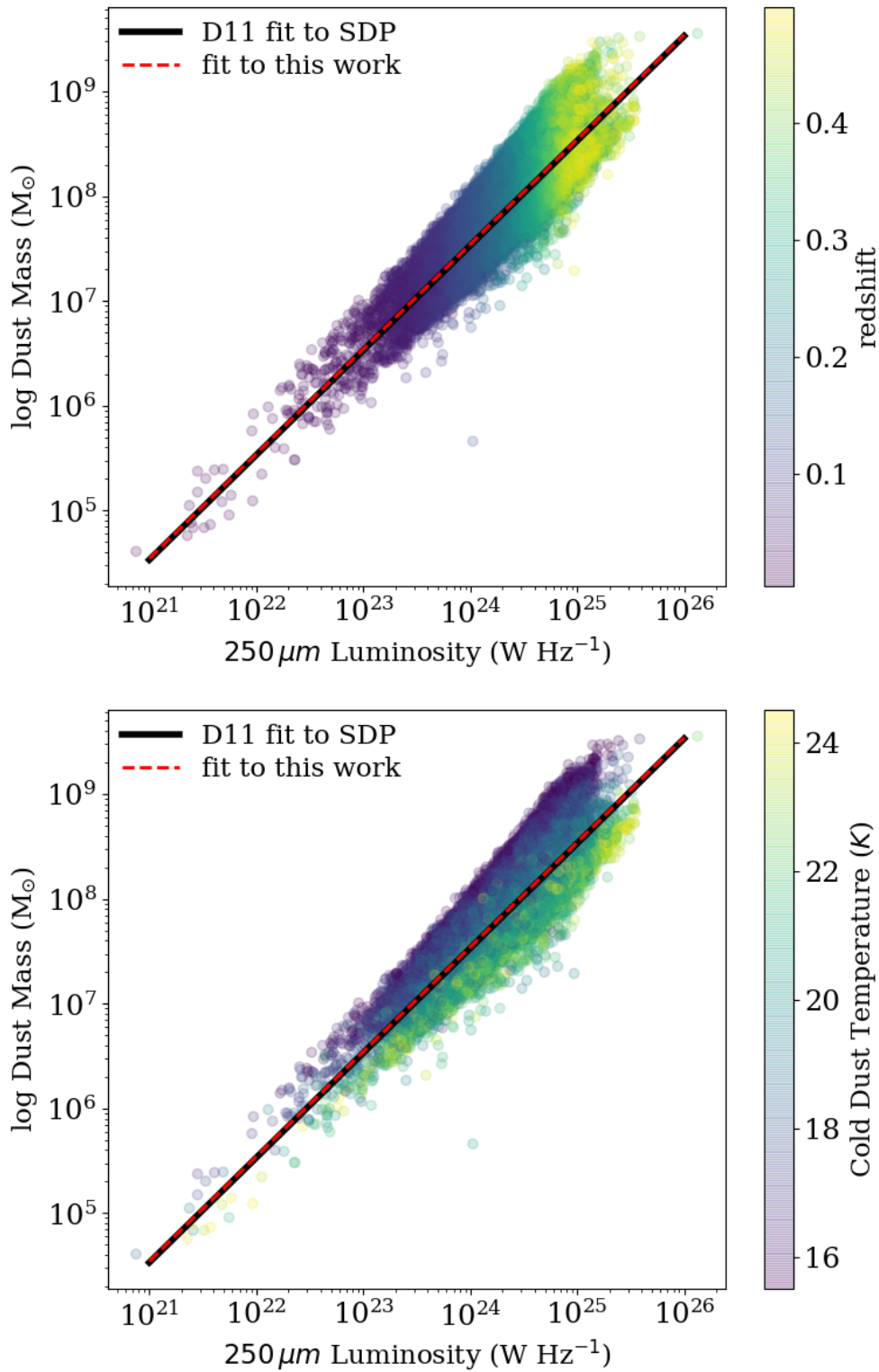


FIGURE 5.3 The MAGPHYS dust masses found by Eales et al. (2018) as a function of the 250 μm luminosity with the relationship found by D11 to the *H*-ATLAS SDP field shown in black and the linear relationship fitted to the points shown as a red dashed line with the data coloured by *Top*: redshift, and *Bottom*: cold dust temperature.

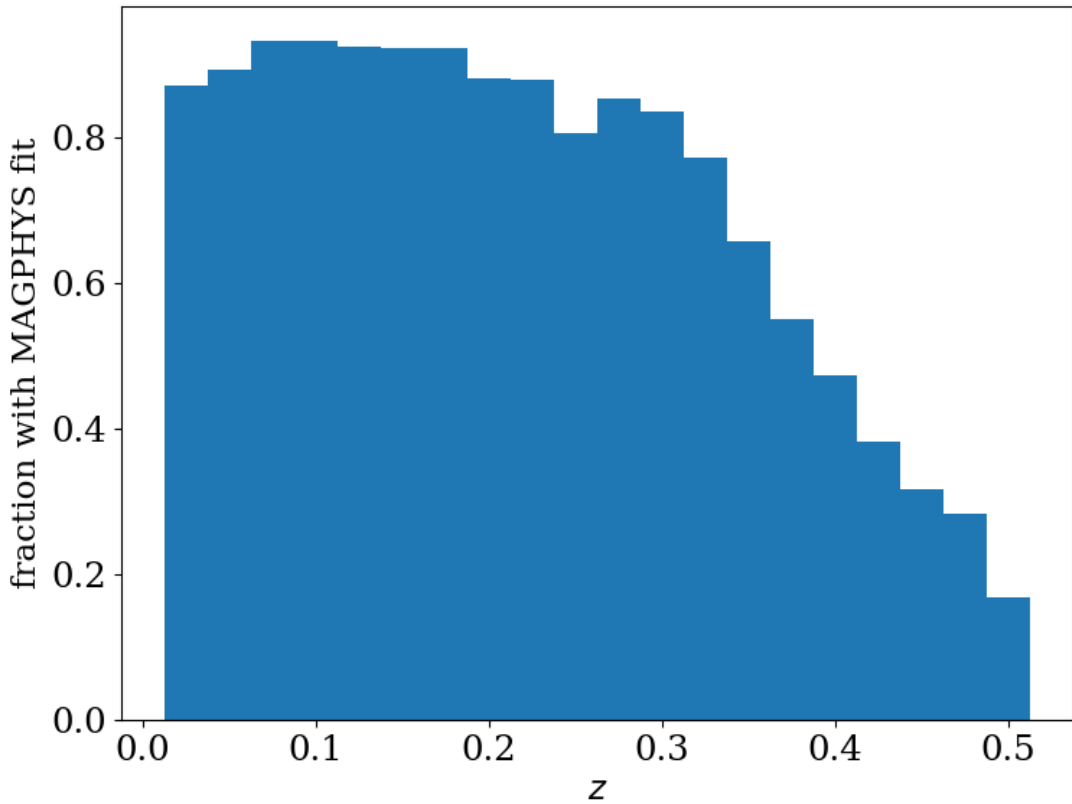


FIGURE 5.4 The fraction of galaxies with a MAGPHYS dust mass from [Eales et al. \(2018\)](#) as a function of redshift.

5.2.2.1 CALCULATING STACKED LUMINOSITIES

We initially calculate $250\ \mu\text{m}$ luminosities for each galaxy assuming a general modified blackbody SED shape with $\beta = 2$ and $T_d = 20\ \text{K}$. We then split the galaxies into 5 equal redshift bins in increments of 0.1. From there we split the lowest redshift bin into 5 equal size $\log(L)$ bins. To ensure that there are sufficient number statistics in any given bin, if any $\log(L)$ bin has fewer than 20 galaxies it is aggregated into the next closest $\log(L)$ bin. For the remaining redshift bins we put all of the galaxies into one $\log(L)$ bin. Binning in this way gives 9 $L - z$ bins. We initially used two even $\log(L)$ bins for these redshift slices as well; however, we found that this resulted in having one very densely populated bin and one very sparsely populated one. Grouping the most extreme galaxies in each redshift slice meant that the masses and temperatures derived for these galaxies were very noisy. We choose to split into $L - z$ bins in this way since there have been studies showing that dust temperatures may evolve with either luminosity or redshift (e.g. [Hwang et al. 2010](#); [Bourne et al. 2012](#); [Symeonidis et al. 2013](#)). We can therefore use

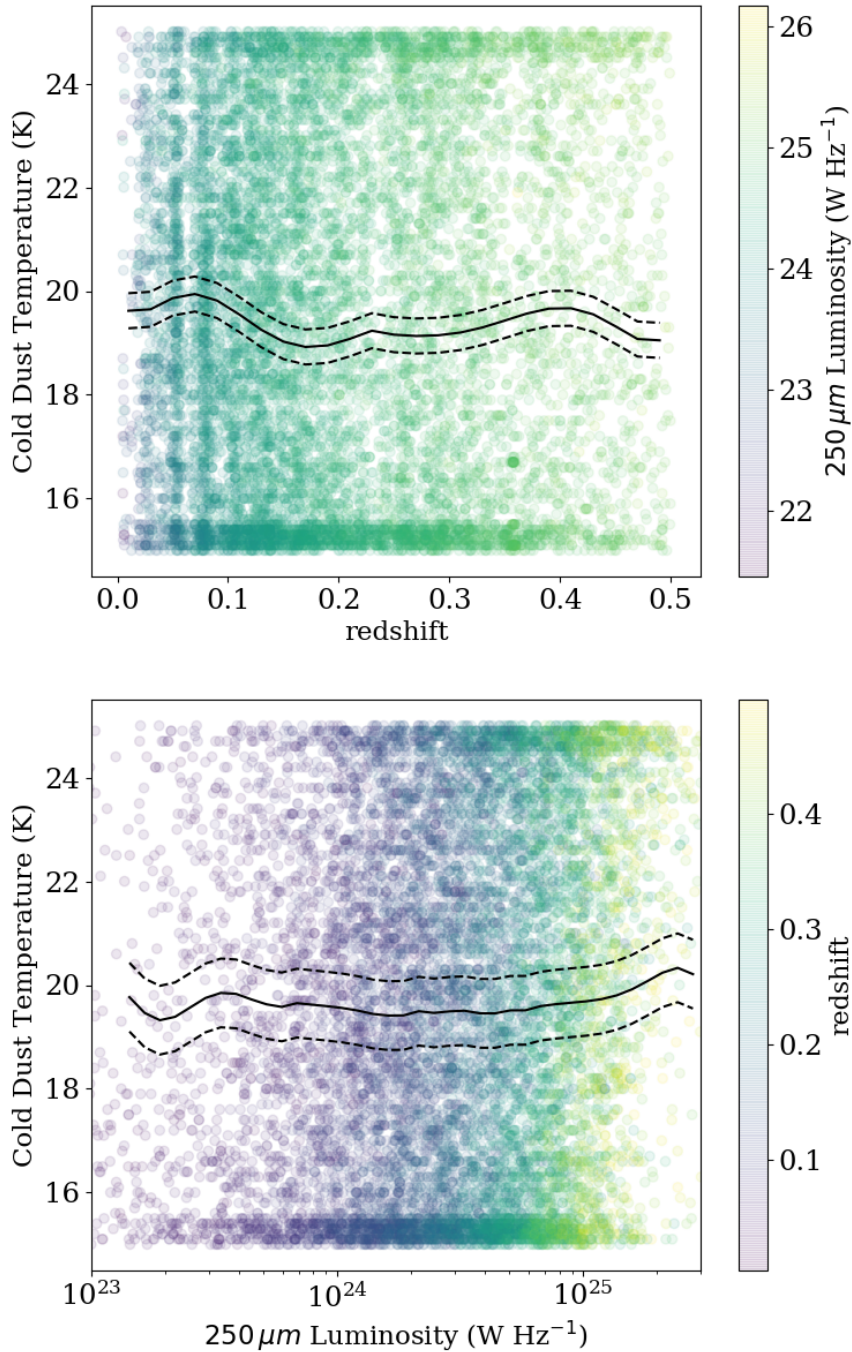


FIGURE 5.5 *Top*: The MAGPHYS cold temperatures as a function of redshift, coloured by their 250 μm luminosity. The mean dust temperature as a function of z is shown as a black line with dashed lines to indicate the 1σ error on the mean. *Bottom*: The 250 μm luminosities as a function of MAGPHYS cold dust temperatures, coloured by their redshift. The mean dust temperature as a function of L_{250} is shown as a black line with dashed lines to indicate the 1σ error on the mean. Here we only show those galaxies which have a detection in one of the PACS bands or at 350 μm as well as the 250 μm detection.

this analysis to probe any trends whilst ensuring that the SED shapes of the galaxies in any bin are likely to be similar. This will mean that the stacked SED ought to be representative of most of the galaxies in the $L - z$ bin.

Traditionally for this kind of analysis, the inverse variance weighted average (IVWA, [Hartung et al. 2011](#)) would be used to find the stacked luminosities in each bin since it gives the lowest variance estimate of the average. The inverse variance weighted average (\hat{y}) of a quantity y is given by:

$$\hat{y} = \frac{\sum_N y_i / \sigma_i^2}{\sum_N 1 / \sigma_i^2} \quad (5.5)$$

where N is the number of independent observations, and y_i and σ_i are the value and variance of the i^{th} measurement. The variance ($D^2(\hat{y})$) associated with the IVWA is given by:

$$D^2(\hat{y}) = \frac{1}{\sum_N 1 / \sigma_i^2} \quad (5.6)$$

Comparing to the median and mean estimates of the average, it was apparent that whilst the IVWA may give the answer with the least variance, this estimate is biased when used for values with a large (orders of magnitude) range of values. Since the weighting is not the SNR, but the SNR divided by the individual absolute uncertainties, in the case where a constant uncertainty is assumed galaxies with a lower signal, and therefore lower absolute noise, will be erroneously up-weighted using this technique. We therefore opt to use the median, which is not biased in this way.

At this step, in order to minimise the effect of using a poor representation of the SED shape to find the k -correction, we simply apply the correction to shift the SED of the stacked bin to the median redshift in each bin rather than to $z = 0$, which is a much smaller correction and so will introduce less bias. We account for this redshift by adjusting the temperatures by a factor of $(1 + z)$ within the modified blackbody fitting stage. Once the SED has been fitted with a two-component modified blackbody, we re-calculate the luminosities of each $L - z$ bin assuming that the shape is well-represented by the best-fitting modified blackbody.

The statistical uncertainty estimates for the stacked luminosities come from the [Gott et al. \(2001\)](#) method for those bins with more than 500 galaxies, since this method is only valid for large samples. In brief, given N measurements M_i in order of value, then the probability that the median of the underlying population from which the sample is drawn lies between M_i and M_{i+1} is

$$P = \frac{2^N N!}{i!(N-i)!} \quad (5.7)$$

We then define $r = i/N$, and $M(r) = M_i$. The expectation value of r is simply 0.5, and the standard deviation is given by $1/(4N)^{0.5}$, the 1σ confidence interval one simply takes values at indexes $i \pm (4N)^{-0.5}$. For bins with fewer galaxies we perform a simple bootstrapping analysis where we resample with replacement and use the bootstrap error as described in a previous Chapter. To this statistical uncertainty, we add the calibration errors for PACS and SPIRE in quadrature, which are 7% and 5.5%, respectively.

5.2.2.2 FITTING MODIFIED BLACKBODIES TO THE STACKED SEDS

To find dust properties for the galaxies in each $L - z$ bin we attempt to fit both one and two component modified blackbodies to the stacked SEDs. To find the best-fitting SED shapes we use the python package ‘Imfit’, specifically its implementation of the Monte Carlo Markov Chain (MCMC) python package ‘emcee’ (Newville et al., 2016; Foreman-Mackey et al., 2013). The posterior distributions are sampled by emcee, and the user sets up a log-posterior probability, essentially calculating the probability that the combination of parameters at the current step is the represents the ‘true’ values, given the observed data. Plots of one and two dimensional projections of the probability distributions can be presented using the corner package (Foreman-Mackey, 2016), an example of which can be seen in Figure 5.6. We use the median of the probability distributions for each parameter as the best-fitting value, and the 16th and 84th percentiles for the 1σ uncertainty estimates. The equations describing the modified blackbody (MBB) functions are:

$$L_\nu = 4\pi\kappa_\nu(\beta)M_d B(\nu, T_d) \quad (5.8)$$

for a single component MBB, where the dust emissivity spectral index (β), dust mass (M_d) and dust temperature (T_d) are allowed to vary, and:

$$L_\nu = 4\pi\kappa_\nu(\beta) [M_{d,w}B(\nu, T_{d,w}) + M_{d,c}B(\nu, T_{d,c})] \quad (5.9)$$

for a two component MBB, where $T_{d,w}$ and $T_{d,c}$ are the warm and cold temperatures respectively, and $M_{d,w}$ and $M_{d,c}$ are the warm and cold mass components respectively. We choose to limit our cold and warm temperatures to the ranges 15 – 25 K, and 20 – 60 K, respectively. Our main concern is not how much mass is assigned to each component but rather the total mass, we therefore instead

choose to fit the total mass and the fraction of mass in the cold component by sampling the total mass in the MCMC rather than the warm and cold masses. We also marginalise over the warm temperature by finding the optimum mass-weighted temperature ($T_{d,MW}$). This is defined as the average of the cold and warm components as weighted by their individual masses, and is given by:

$$T_{d,MW} = \frac{M_{d,c}T_{d,c} + M_{d,w}T_{d,w}}{M_{d,c} + M_{d,w}} = T_{d,c} + \frac{T_{d,w} - T_{d,c}}{1 + \frac{M_{d,c}}{M_{d,w}}} \quad (5.10)$$

And the total mass is simply the addition of the warm and cold masses. Marginalising the parameters in this way gives two advantages: firstly, the warm component properties will always be much noisier than the cold component. This is because the constraints on the warm component are necessarily weaker than the cold since it will peak at higher frequencies where we have less coverage. Secondly, the total mass and mass-weighted temperature are far better indicators of the overall dust properties corresponding to a two component MBB than individual warm and cold components.

We allow β to vary for the one component MBB since it can improve the fit to the SED shape; however, there is not sufficient data to constrain β for the two component MBB. We therefore choose to use a fixed β of 2 for the two temperature MBB fitting. Hereafter we will refer to the one and two temperature MBB fits as 1C and 2C respectively. Figure 5.7 shows two sets of simulated grids of *Herschel* FIR colours ($250 \mu\text{m}/350 \mu\text{m}$ and $100 \mu\text{m}/160 \mu\text{m}$) derived assuming a fixed $\beta = 1.8$ and $\beta = 2$, a fixed $T_{d,w} = 40 \text{ K}$ and varying $T_{d,c}$ between 12 and 30 K, and varying cold to warm mass ratio between 0 and 1. The observed colour ratios of the stacked $250 \mu\text{m}/350 \mu\text{m}$ and $100 \mu\text{m}/160 \mu\text{m}$ corrected to the bin centre are also shown for comparison. Here we show the grids as they would appear if redshifted to 0.5; we choose to redshift the grid rather than show rest-frame colours since this does not rely on K -corrections based on SED fits. In order to inform our choice of β , we note that the grid using $\beta = 2$ better covers the parameter space sampled by the stacked observations, and so we choose to use this value for β for this analysis in the 2C fits.

The warm component temperature can only be constrained when PACS data are present; however, most galaxies are not detected by PACS in our sample, particularly at higher redshifts, as seen in Figure 5.8. This makes the stacking analysis even more necessary to probe the evolutionary trends in our data since so few galaxies at higher redshifts will have a sufficient signal-to-noise in either of the PACS bands to constrain the warm component through fitting the SEDs of

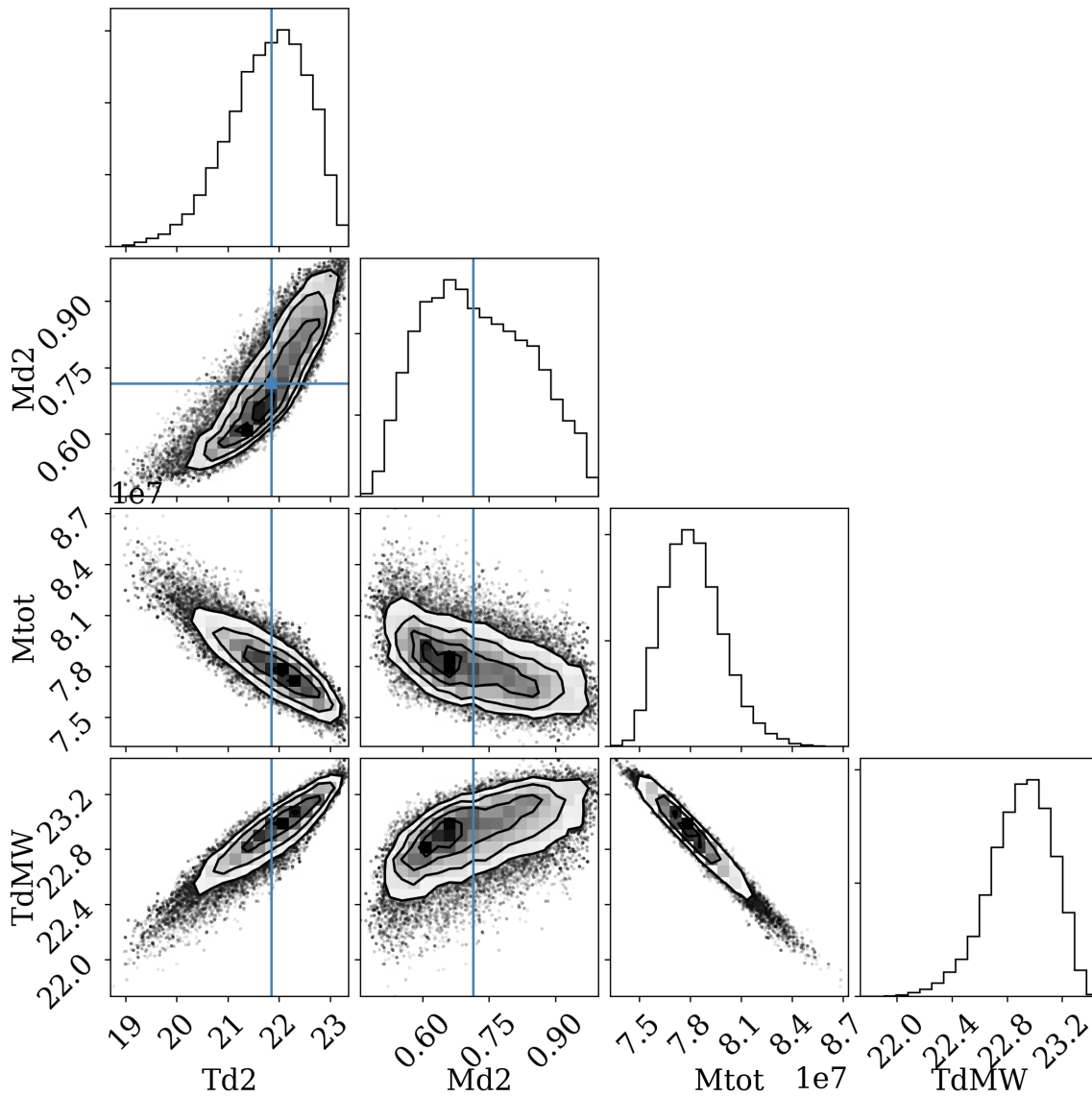


FIGURE 5.6 The one and two dimensional projections of the probability distributions from fitting two component MBB using MCMC sampling of the posterior for the highest $L - z$ luminosity bin in the lowest redshift slice. $Td2$ is the cold dust temperature in K. $Md2$ is the fraction of dust mass in the cold component, i.e. $M_{d,c}/M_{tot}$. M_{tot} is the total dust mass $M_{d,tot}$. Td_{MW} is the mass-weighted temperature $T_{d,MW}$.

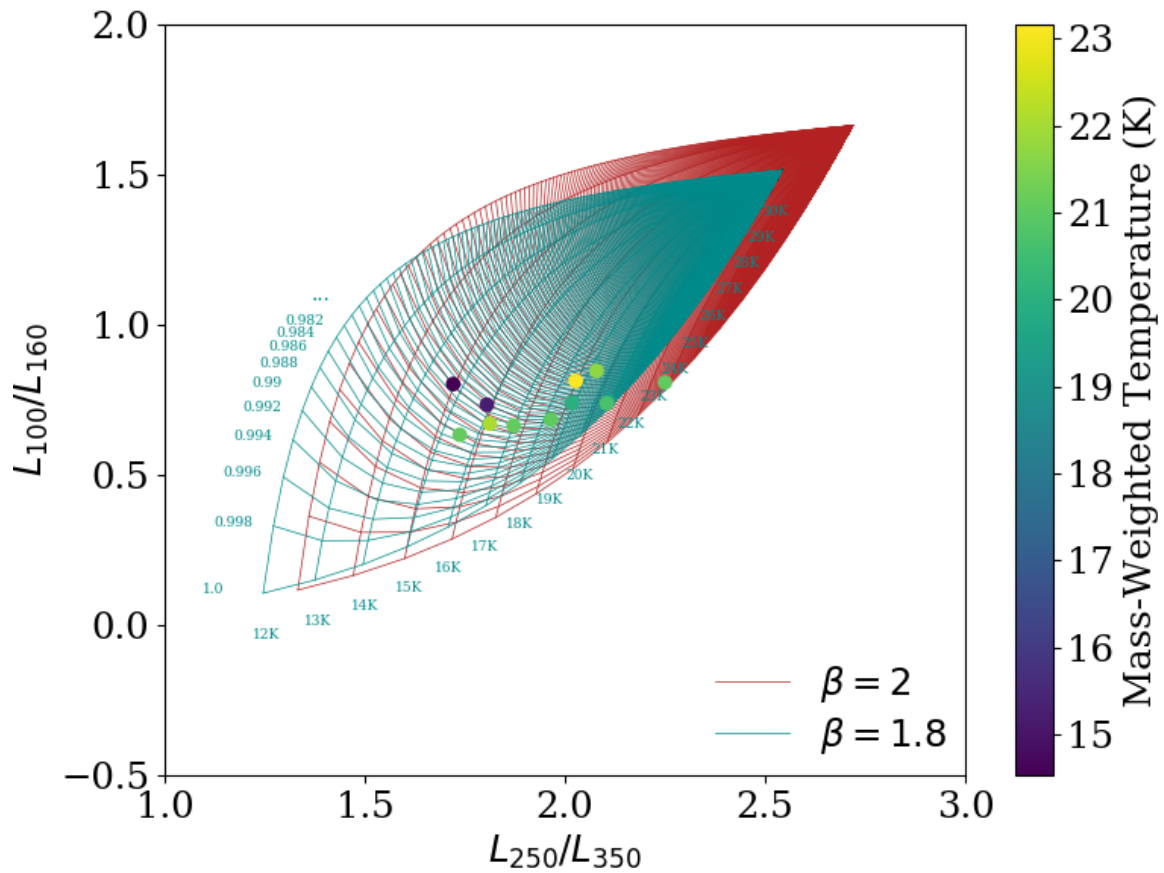


FIGURE 5.7 The observed $100\ \mu\text{m}/160\ \mu\text{m}$ colours for the *H*-ATLAS sample stacked SEDs in the $L - z$ bins described in Section 5.2.2.1 against their observed $250\ \mu\text{m}/350\ \mu\text{m}$ colours. The stacked SED datapoints are coloured by their best-fitting mass-weighted temperatures. We show grids of evenly increasing cold temperature and cold/warm component mass ratio with a constant warm temperature of 40 K for β values of 1.8 (cyan), and 2 (red) as though observed at $z = 0.5$.

individual galaxies.

When deriving dust masses for the stacked bins, we use the [James et al. \(2002\)](#) $\kappa_{850\ \mu\text{m}} = 0.077\text{m}^2\ \text{kg}^{-1}$ in line with that used in B18 and D11. The resulting stacked SEDs and the best-fitting one and two component MBB functions for the lowest z slice are shown in Figure 5.9, and for the remaining redshift slices in Figure 5.10. The best-fitting SED parameters for all $L - z$ bins are listed in Table 5.1.

The one component MBB temperature is essentially luminosity-weighted, since it accounts for the majority of the luminosity unlike the mass-weighted temperature which accounts for most of the mass. We believe that the mass-weighted temperature from the two component MBB fit gives a better idea of the dust mass of the stacked SED for each bin than the luminosity-weighted temperature from the one component MBB. Since k -correcting an SED with one component is much

TABLE 5.1 The best-fitting SED parameters derived for the stacked galaxies in each of our $L - z$ bins.

| Δz | $\Delta \log L_{250}$ (WHz^{-1}) | N | one component MBB | | | | two component MBB | | | | | | |
|-------------|--|------|-------------------|-----------------------------|---------------|----------|-------------------|-----------------|------------------|--------------------------------------|--------------------|--------------------|----------|
| | | | T_d (K) | $\log M_d$ (M_\odot) | β | χ^2 | T_{dC} (K) | T_{dW} (K) | T_{dMW} (K) | $\log M_{d,\text{tot}}$ M_\odot | M_c M_\odot | M_w M_\odot | χ^2 |
| 0.002 - 0.1 | 21.6 - 22.2 | 27 | 23.2 \pm 0.3 | 5.32 \pm 0.02 | 1.5 \pm 0.0 | 0.84 | 27.5 \pm 8.2 | 15.2 \pm 0.6 | 16.3 \pm 0.5 | 4.44 \pm 0.04 | 5.45 \pm 0.02 | 5.49 \pm 0.04 | 1.29 |
| 0.002 - 0.1 | 22.2 - 22.9 | 167 | 22.4 \pm 0.2 | 6.38 \pm 0.01 | 1.5 \pm 0.0 | 1.64 | 25.2 \pm 2.4 | 15.1 \pm 0.2 | 16.2 \pm 0.2 | 5.56 \pm 0.02 | 6.48 \pm 0.01 | 6.53 \pm 0.01 | 2.92 |
| 0.002 - 0.1 | 22.9 - 23.6 | 1147 | 24.1 \pm 0.4 | 7.05 \pm 0.01 | 1.5 \pm 0.0 | 0.18 | 25.1 \pm 3.5 | 16.0 \pm 0.6 | 17.7 \pm 0.4 | 6.44 \pm 0.03 | 7.09 \pm 0.01 | 7.18 \pm 0.03 | 1.18 |
| 0.002 - 0.1 | 23.6 - 24.3 | 2201 | 23.3 \pm 0.4 | 7.43 \pm 0.01 | 1.8 \pm 0.0 | 0.17 | 25.4 \pm 4.2 | 19.0 \pm 1.0 | 20.5 \pm 0.5 | 6.83 \pm 0.06 | 7.36 \pm 0.05 | 7.48 \pm 0.02 | 0.58 |
| 0.002 - 0.1 | 24.3 - 25.0 | 199 | 24.0 \pm 0.4 | 7.88 \pm 0.01 | 1.9 \pm 0.1 | 0.42 | 25.6 \pm 4.7 | 21.9 \pm 1.6 | 22.9 \pm 0.5 | 7.34 \pm 0.14 | 7.75 \pm 0.14 | 7.89 \pm 0.02 | 0.57 |
| 0.1 - 0.2 | 23.7 - 25.3 | 7739 | 24.0 \pm 0.4 | 7.91 \pm 0.01 | 1.8 \pm 0.0 | 0.81 | 29.7 \pm 19.4 | 19.9 \pm 1.6 | 20.7 \pm 0.5 | 6.88 \pm 0.08 | 7.93 \pm 0.07 | 7.97 \pm 0.02 | 0.18 |
| 0.2 - 0.3 | 24.2 - 25.4 | 6365 | 25.7 \pm 0.4 | 8.42 \pm 0.01 | 1.6 \pm 0.0 | 2.46 | 49.0 \pm 77.2 | 20.9 \pm 0.4 | 21.1 \pm 0.3 | 6.29 \pm 0.02 | 8.49 \pm 0.0 | 8.49 \pm 0.02 | 0.26 |
| 0.3 - 0.4 | 24.5 - 26.1 | 5861 | 27.2 \pm 0.2 | 8.76 \pm 0.01 | 1.5 \pm 0.0 | 5.66 | 57.1 \pm 75.2 | 21.1 \pm 0.2 | 21.3 \pm 0.2 | 6.46 \pm 0.01 | 8.86 \pm 0.0 | 8.86 \pm 0.01 | 0.77 |
| 0.4 - 0.5 | 24.7 - 25.8 | 5529 | 27.7 \pm 0.1 | 9.06 \pm 0.01 | 1.5 \pm 0.0 | 9.24 | 58.1 \pm 73.7 | 21.3 \pm 0.2 | 21.5 \pm 0.2 | 6.74 \pm 0.01 | 9.18 \pm 0.0 | 9.18 \pm 0.01 | 0.65 |

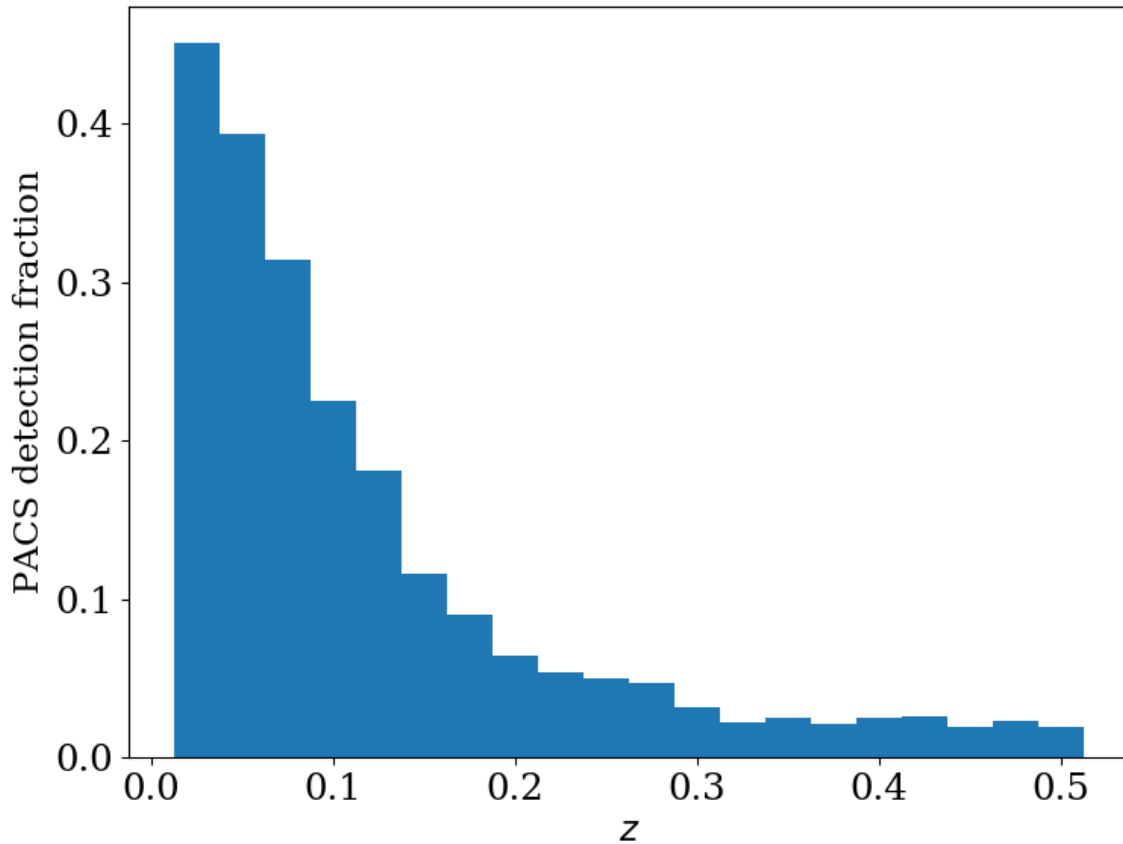


FIGURE 5.8 The fraction of sources with at least one PACS detection as a function of redshift.

simpler than k -correcting with two components, we choose to calculate the rest-frame L_{250} of each galaxy using the k -corrections based on the one component MBB of its $L - z$ bin. The one component MBB gives a good representation of the shape of the stacked SEDs and so using this luminosity-weighted estimate of the temperature will reproduce the shape of the SED much more reliably than the mass-weighted temperature. In order to calculate dust masses for each galaxy, we use its rest-frame $250\ \mu\text{m}$ luminosity and the mass-weighted temperature of its $L - z$ bin along with Equation 5.8, we call this mass estimate the "2C stacked dust mass".

5.2.2.3 COMPARING THE ONE AND TWO COMPONENT GREYBODY FITS

Figure 5.11 (top) demonstrates that the dust temperatures derived from the one component MBB can be vastly different to the mass-weighted temperatures derived from the two component MBB fits to the stacked luminosities for each $L - z$ bin. The largest offsets are seen with SEDs with the lowest mass-weighted

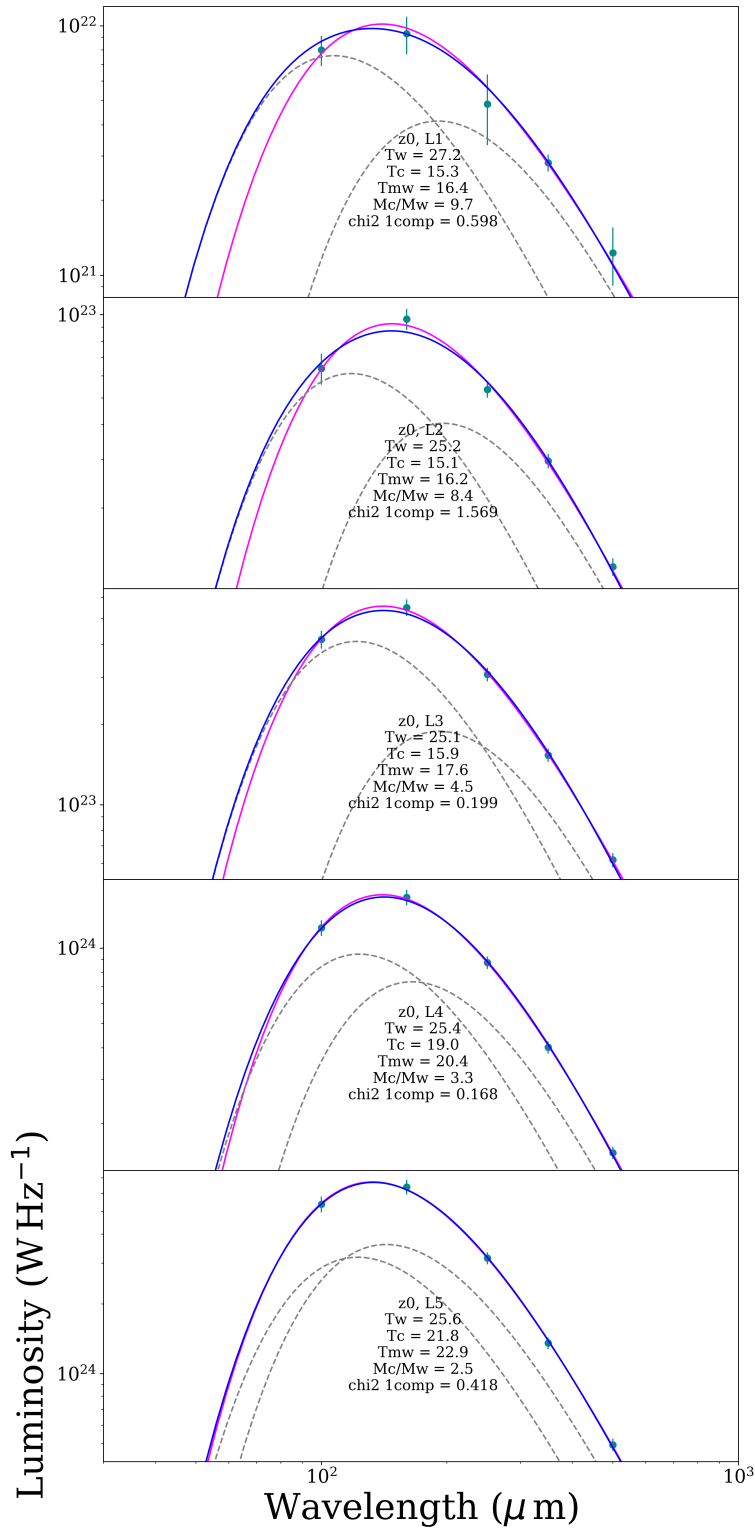


FIGURE 5.9 The stacked luminosity SEDs for the $L - z$ bins in the lowest redshift slice, and their best-fitting one and two component greybody fits arranged with increasing redshift from top to bottom.

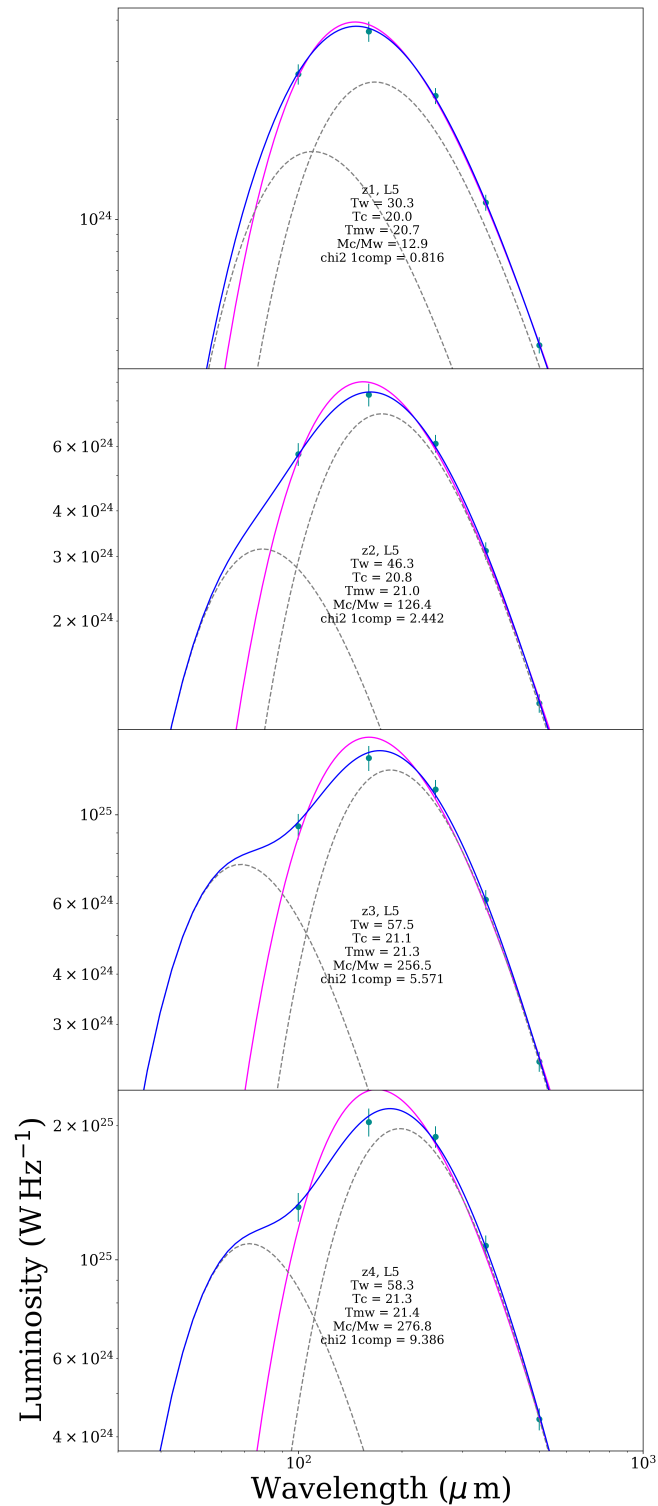


FIGURE 5.10 The stacked luminosity SEDs for the higher redshift slices, and their best-fitting one and two component greybody fits arranged with increasing redshift from top to bottom.

dust temperatures (these $L - z$ bins are the three lowest luminosity bins in the lowest redshift slice), where there is evidence for dust temperatures at < 20 K. These stacked SEDs are similar to those dust-rich (in comparison to their stellar mass) sources with dust temperatures 13–20 K found in the 250 μm selected blind survey of [Clark et al. \(2015\)](#). We are likely only sensitive to these sources in the lowest redshift slice since the galaxies contained in these $L - z$ bins drop out of our survey due to having low absolute dust masses ($< 10^6 M_{\odot}$) and cold dust temperatures (therefore lower 250 μm luminosities). This discrepancy in T_{d} (one component MBB fit) and $T_{\text{d,MW}}$ (two component MBB fit) for these low dust temperatures results in an offset of ~ 0.16 dex in dust mass as shown in [Figure 5.11](#).

5.2.3 EVOLUTION OF DUST PROPERTIES

In [Figure 5.12](#) we present the evolution of both mass-weighted and luminosity-weighted temperature with L_{250} (top panel), and M_{d} (bottom panel). The mass-weighted temperatures in the lowest redshift slice are a strong function of L_{250} and M_{d} . This is unsurprising since dust becomes increasingly bright per unit mass with increasing temperature, and where there is more dust we will naturally expect more emission. We see a shallow and steady increase in mass-weighted temperature for each subsequent redshift slice, but since we also see an increase in L_{250} in these bins we cannot disentangle whether redshift or luminosity is the most important factor in this increase. In [Figure 5.13](#) we show L_{250} as a function of redshift for our full sample in order to illustrate the difficulty of choosing a luminosity range over which to test the evolution of dust properties with redshift. We cannot choose a luminosity slice which is well-populated across all redshifts, and this prevents us from determining whether mass-weighted temperature evolves with redshift. The luminosity-weighted temperature has a shallow evolution with luminosity in the lowest redshift slice but shows a rapid increase with both luminosity and dust mass in subsequent redshift slices. In the case of both luminosity- and mass-weighted temperature we expect decreased sensitivity to cold dust with redshift since the effective range of rest-frame frequencies will be higher, but it is unlikely that this effect could account for all of the evolution we see. Once again it is not possible to distinguish whether this evolution is driven by increasing redshift or luminosity.

Both [Dunne et al. \(2000\)](#) and [Dale et al. \(2001\)](#) reported that the dust temperatures of nearby galaxies ($z < 0.1$) seem to have a strong correlation to their IR luminosity. This trend was not observed at higher redshifts (see e.g. [Coppin et al.](#)

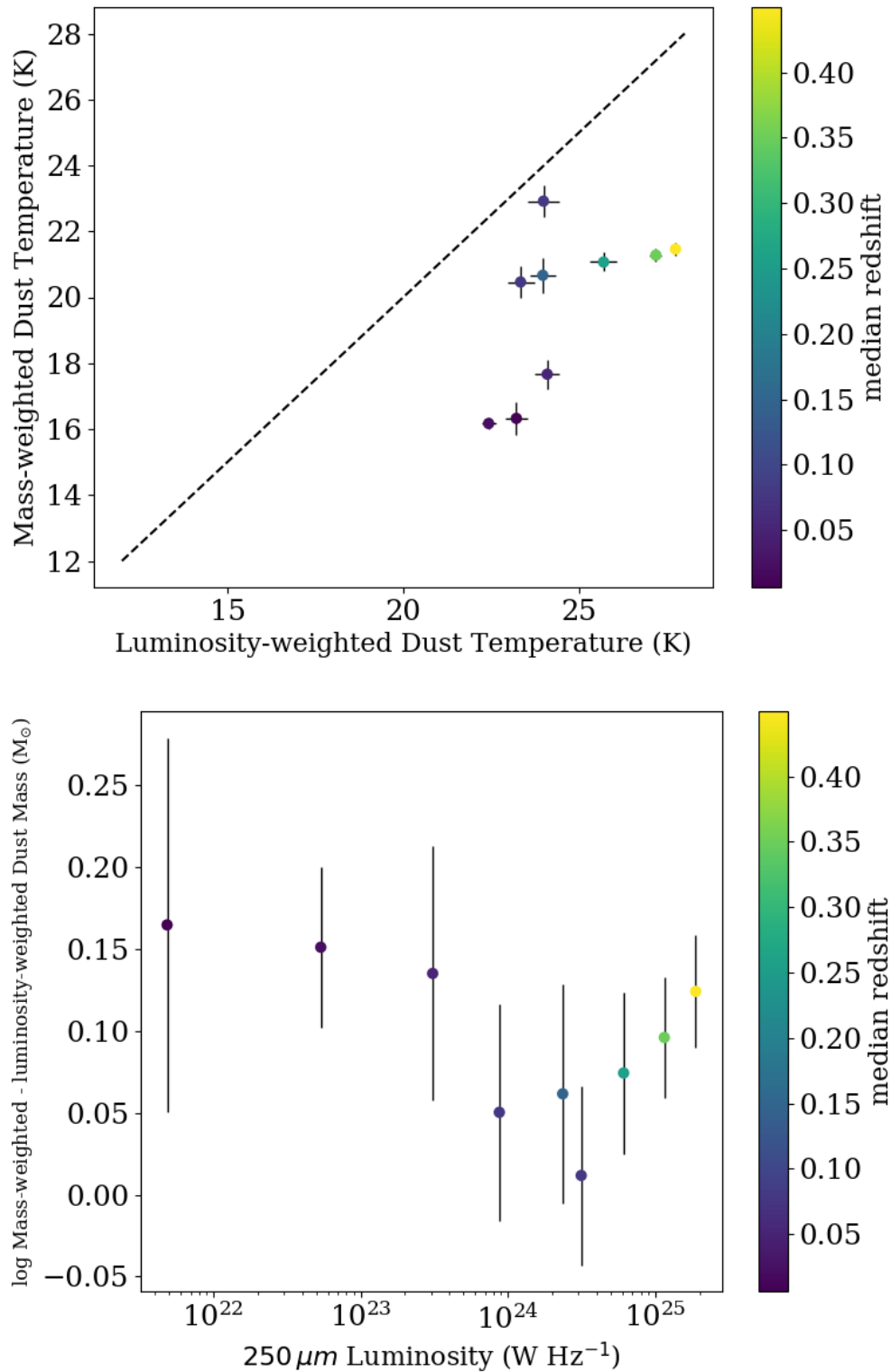


FIGURE 5.11 *Top:* A comparison of the one component temperature and two component mass-weighted temperature with data points coloured by redshift for the stacked SEDs. *Bottom:* The difference between the logarithm of the best-fitting mass from the two component MBB fit to the stacked SEDs and the logarithm of the best-fitting one component MBB fit to the stacked SEDs with data points coloured by redshift for the stacked SEDs.

2008; Symeonidis et al. 2009; Amblard et al. 2010; Rex et al. 2010; Seymour et al. 2010), and Symeonidis et al. (2011) attributed this to colder galaxies evolving more rapidly at earlier times. D11 found no evidence of dust temperature evolution with either redshift or luminosity for the SDP *H*-ATLAS galaxies. The difference in the trend we see for dust temperature to evolve with luminosity to that of D11 is likely due to the much larger sample size used in this work since we see some evidence of evolution with redshift even when repeating the same method used in D11 (using the $L - M_d$ relationship from MAGPHYS, see discussion in the following Section).

The stacking analysis of Bourne et al. (2012) mostly focused on the evolution of dust properties with optical or stellar properties. When selecting sources based not on their dust but rather their stellar component (M_r is highly correlated with stellar mass), the majority of sources will have no strong detection in any Herschel band. Stacking is therefore necessary in this case to draw meaningful conclusions about dust property trends. Bourne et al. (2012) split their galaxies into "red sequence", "green valley", and "blue cloud" galaxies (hereafter red, green, and blue galaxies, respectively) using their optical rest-frame colours and r -band magnitude. The dust temperature of blue galaxies was found to be strongly correlated with stellar mass up to a peak at around $6 \times 10^{10} M_\odot$ where at larger masses, the temperature decreased. The correlation in the green bin was far noisier making conclusions speculative, and the red bin was noisier still and no trend between dust temperature and stellar mass could be discerned for red galaxies. Throughout the investigation no trend with redshift was observed.

Bourne et al. (2012) found that the temperatures of red galaxies, generally agreed to be passive, are lower than green or blue galaxies. This was puzzling, Bourne et al. (2012) concluded that the results may have been biased by lensed galaxies. Interestingly though, Smith et al. (2012c), find that the ETGs (including passive red and dead ellipticals) in the HRS actually have warmer dust temperatures than their late-type counterparts. This comparison is not exact though, since while early types are generally much redder than late types, they were classified morphologically into Hubble types in Smith et al. (2012c), and not into red, green, and blue based on their optical colours.

5.3 COMPARING THE DUST MASS ESTIMATES

In this section we compare the dust mass estimates from the different methods described in previous sections as well as the dust temperatures derived using

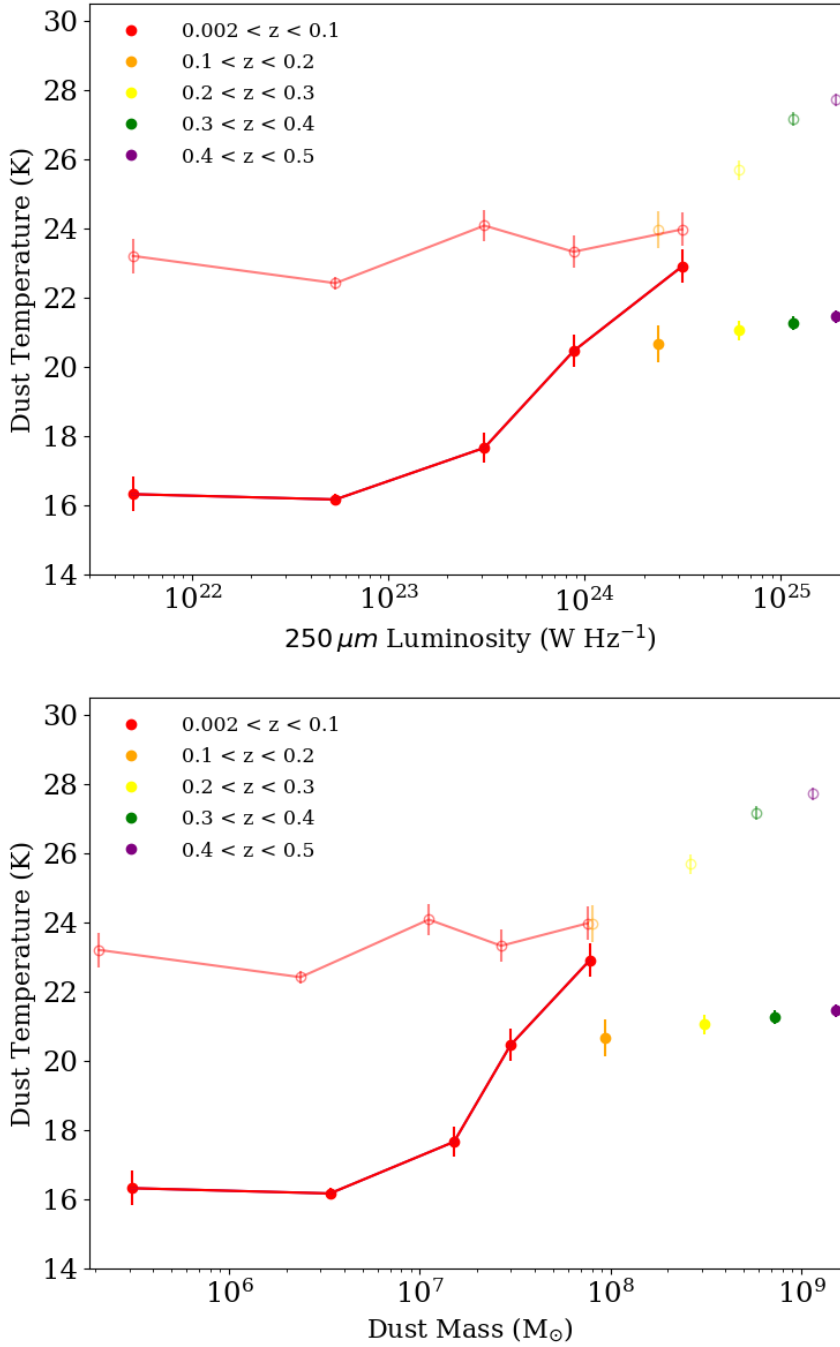


FIGURE 5.12 The mass-weighted temperature from the best-fitting SEDs as a function of (*Top:*) 250 μm luminosity for the stacked SEDs and (*Bottom:*) The best-fitting dust mass to the stacked SED. In each figure the temperature value comes from the median of the probability distribution calculated by the `lmfit` implementation of `emcee` for each $L - z$ bin, and the uncertainties come from the 16th and 84th percentile values from these probability distributions. The solid translucent points represent the mass-weighted temperatures, and the empty transparent points represent the luminosity-weighted temperature. For the first redshift slice (where more than one $L - z$ bin is used), we link the points with a straight line to emphasize the evolution of temperature in this slice.

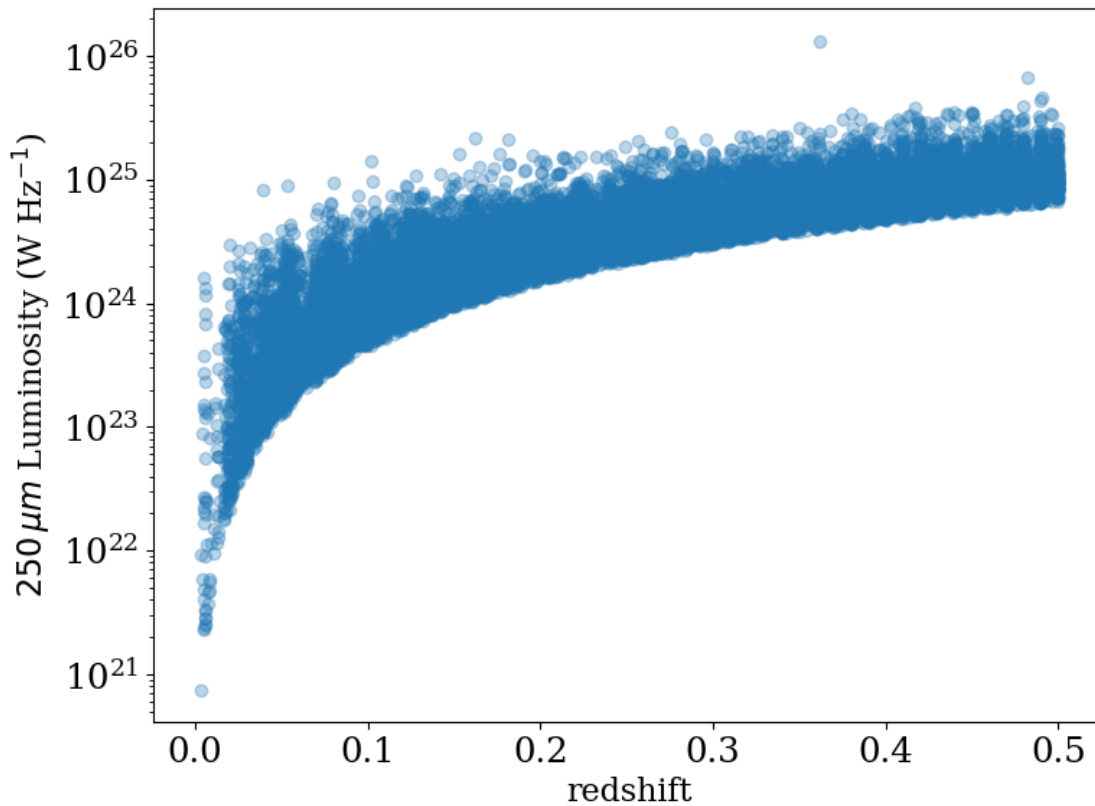


FIGURE 5.13 The 250 μm luminosities for the *H*-ATLAS sample as a function of redshift.

the one and two component MBB fits. Generally the dust masses derived by using the SED parameters from the stacking analysis are fairly similar to those from MAGPHYS for the low-redshift ($z < 0.1$) slice (see Figure 5.14) with a median offset of only ~ 0.01 dex, but with a significant scatter around 1 dex. There is a tendency for MAGPHYS to assign lower masses at low luminosities and higher masses at high luminosities than the 2C stacked dust masses. As seen in Figure 5.15, at higher redshifts the MAGPHYS estimates of dust mass are generally higher than the 2C stacked masses. This may point to a bias within either the MAGPHYS fitting routine, or with the stacking analysis, or even both. In Chapter 2 we discussed the potential flaws of MAGPHYS, namely its propensity to simply return the priors in the absence of a very strong signal. It is probably this effect of returning the median of the prior for the cold temperature (20 K) that causes the difference, since the mass-weighted temperatures in the higher redshift slices are all above this value. As discussed previously, there is a reduction in sensitivity at higher redshift to cold temperatures caused both by colder dust shining much less brightly than warmer dust and the range of rest-frame frequencies probed at different redshifts.

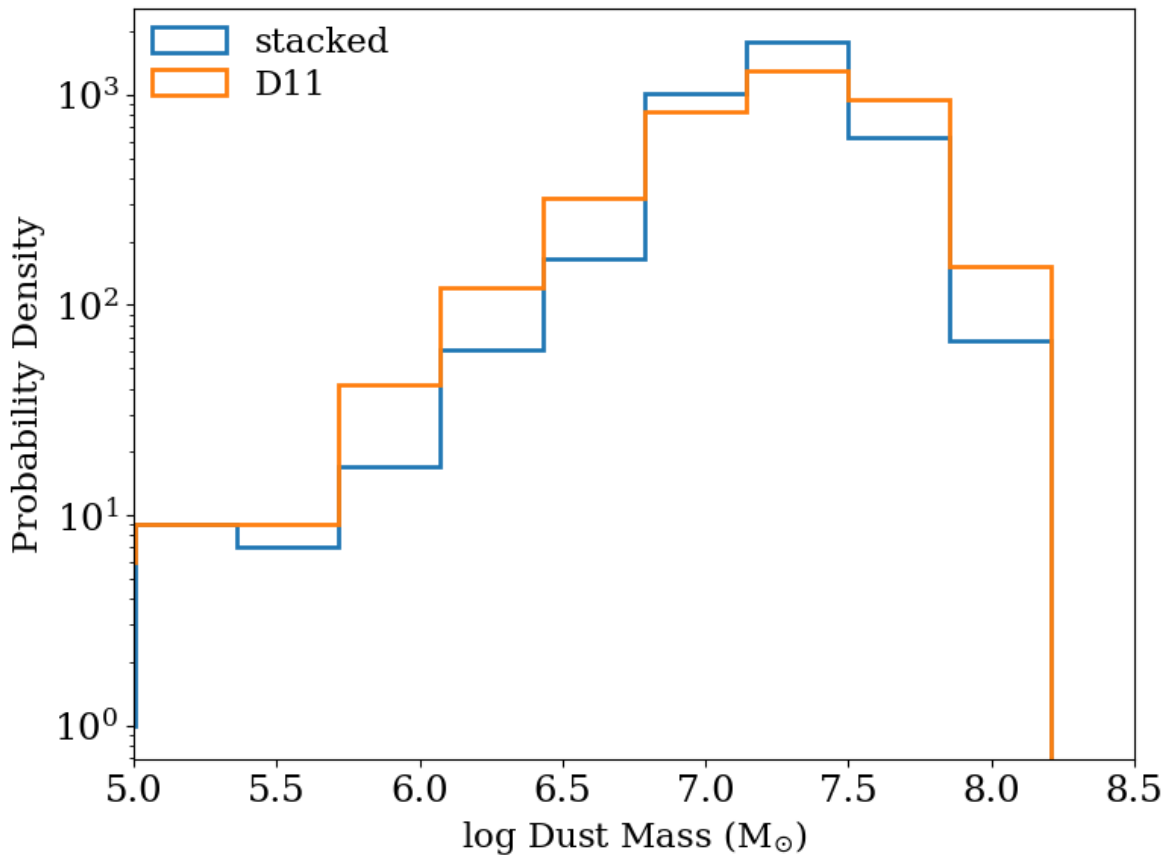


FIGURE 5.14 The distribution of MAGPHYS based dust masses and 2C stacked dust masses at $z < 0.1$.

This means that the fits to the higher redshift stacked SEDs will be more sensitive to warm dust and less sensitive to cold dust. There are many caveats to the dust masses found through stacking, which we will discuss next.

5.3.1 CAVEATS

Whilst stacking may be a helpful tool in divining general trends between properties for a large number of galaxies, we note that the global properties of the stacked SED may not in fact be representative of all of the galaxies in the sample. Also, a single mass-weighted temperature could arise from very different SED shapes, and so we are assuming that the stacked SED is a good representation of the underlying dataset in terms of the cold and warm temperatures as well as the fraction of the total luminosity assigned to each component. As mentioned earlier, the sensitivity to cold dust is hampered at higher redshifts because of the intrinsic range of rest-frame frequencies probed. We could therefore be missing a whole

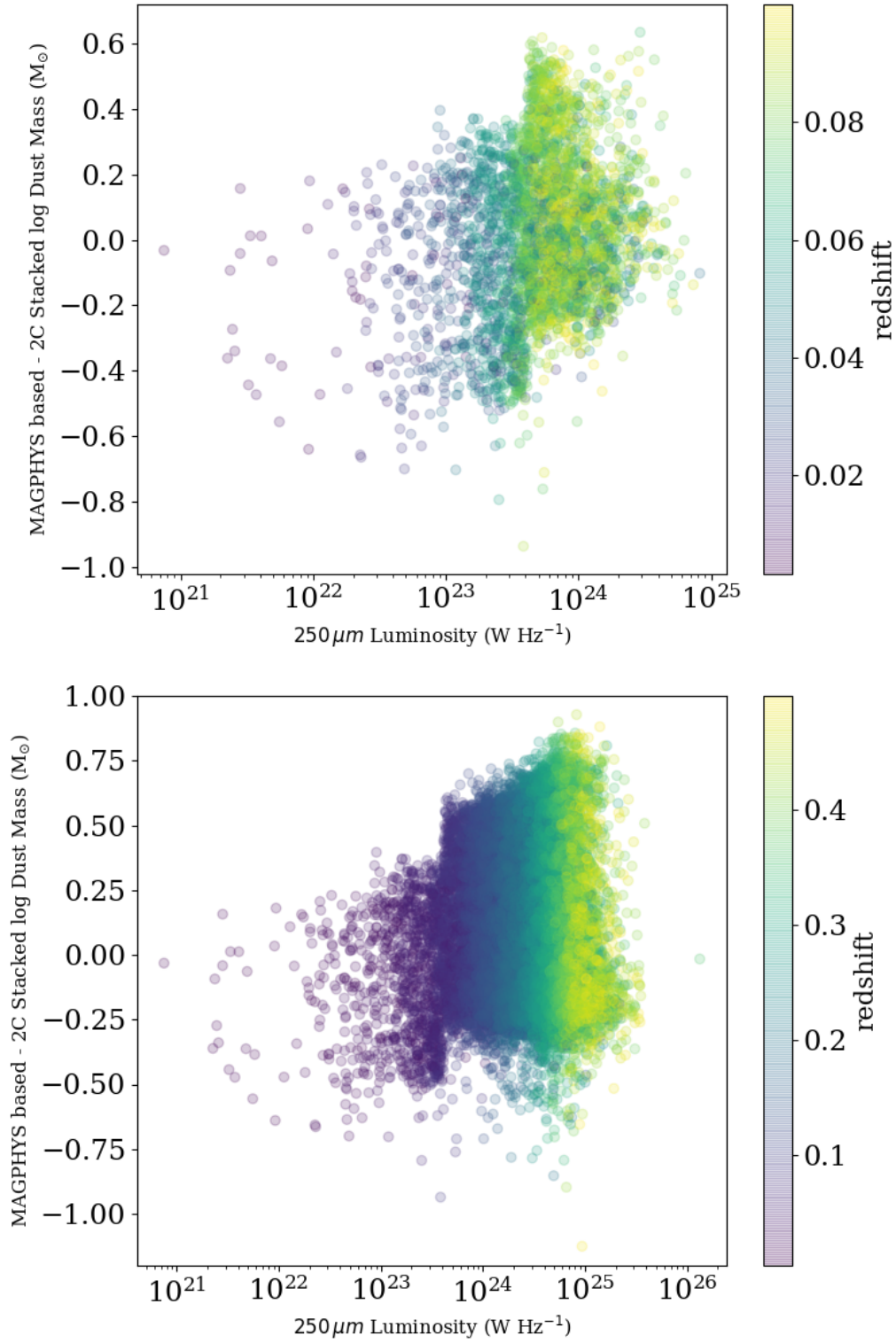


FIGURE 5.15 The difference between the MAGPHYS based dust masses and the 2C stacked dust masses as a function of $250\ \mu\text{m}$ luminosity for $z < 0.1$ (top) and $z < 0.5$ (bottom).

class of galaxies from our analysis, either because they are simply too faint to be detected, or because only their warm dust is observable with our survey constraints.

Stacking galaxies with very different SED shapes could introduce significant bias into our results. Galaxy SEDs with the same mass-weighted temperature can look very different, and can arise from wide ranges of other SED properties. In simulations we have found that even when stacking galaxy SEDs with the same mass-weighted temperature, the scatter in the resulting mass-weighted temperatures from a two component MBB fit can be around 3 K. Further work into these simulations must be undertaken to ascertain how viable stacking is as a means of recovering individual galaxy properties.

Contamination of flux measurements from high redshift sources could have a significant effect on the flux measurements of the *H-ATLAS* sources. This contamination could arise from confusion, whereby the flux an undetected background source is erroneously attributed to a source within the catalogue. Contamination can also arise because of galaxy lensing (e.g. [Negrello et al. 2017](#)), whereby the light from a higher redshift source can be deflected by an intermediate redshift one towards the observer. A typical dust SED with temperatures around 20 K will peak at around 120 μm in the observed frame at $z = 0.1$, but the same source at $z = 0.5$ would peak at 180 μm in the observed frame. This means that contamination from high redshift sources gets stronger with longer wavelengths. The *Herschel* beam sizes also increase with longer wavelengths, meaning that contamination is much more likely in these bands. Recent work by Dunne et al., (*in prep.*) has shown that this effect could represent up to 13, 26, and 44% of the flux contribution of the measured flux at 250, 350, and 500 μm respectively for $z \sim 0.35$. This could evolve with redshift, since the probability that a galaxy will be a lens is not constant with redshift, the probability peaks around $z \sim 0.3 - 0.4$, and at low redshift galaxies are unlikely to be affected by lensing (e.g. [Ofek et al. 2003](#)). This means that our higher redshift bins may be biased to lower temperatures, due to the artificial increase at longer wavelengths where the cold component peaks. There is a strong evolution towards bluer colours in the ratio of the 100 and 160 μm rest-frame luminosities with redshift (see the top panel of [Figure 5.16](#)), but the same is not true for the 250 to 500 μm ratio (see the bottom panel of [Figure 5.16](#)). Since the warm component is not strongly affected by this, we feel confident in saying that the increase across our higher redshift slices in both mass-weighted and luminosity-weighted temperature seen in this work are real, and could be underestimated by this analysis.

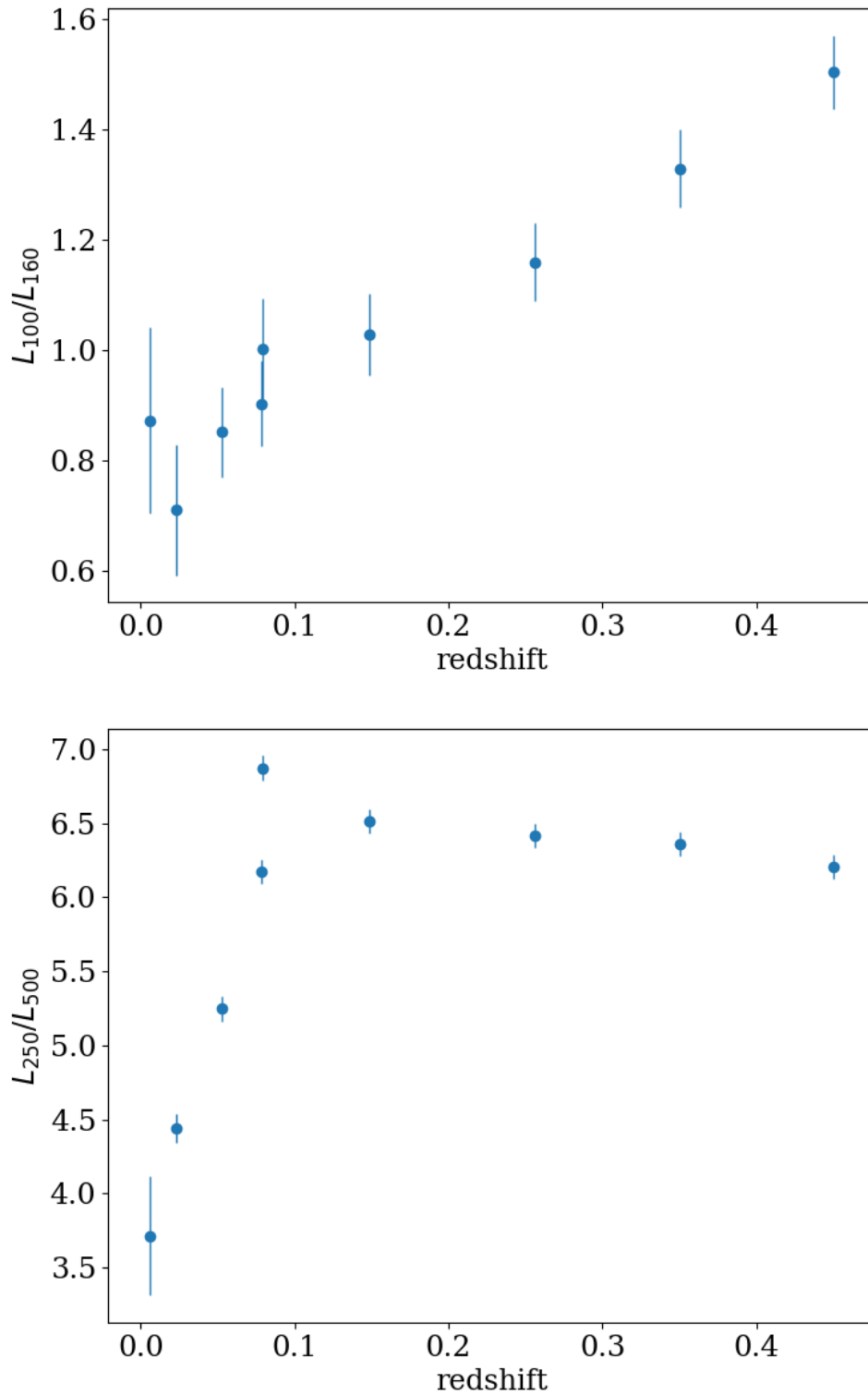


FIGURE 5.16 The ratio of (*top*) 100 and 160 μm luminosity, and (*bottom*) 250 and 500 μm luminosity as a function of redshift for the stacked SEDs for our $L - z$ bins.

5.4 CONCLUSIONS

We find dust properties for 29 235 galaxies below a redshift of 0.5 in the *H-ATLAS* sample using two different methods. The main conclusions we draw from our analyses of the dust properties in our sample are:

- Mass-weighted dust temperature appears to evolve with luminosity at low redshifts when we use the stacked luminosities to derive two-component mass-weighted temperatures for our bins. There is some less significant evolution of luminosity-weighted temperature with luminosity for the lowest redshift slice.
- There is a strong evolution of luminosity-weighted temperature in the higher redshift slices, which is also observed in the mass-weighted temperature but less strongly. We were unable to discern whether this evolution was driven by increasing redshift, or the increase in luminosity with redshift that we observe.
- At low luminosity there is an average offset of around 0.01 dex in dust mass when comparing the stacked results to the ones found by pinning dust masses to a simple linear relationship as in D11, with the MAGPHYS masses being slightly higher. There is a tendency for MAGPHYS to assign lower masses to low luminosity galaxies and higher masses to high luminosity galaxies compared to the 2C stacked masses.
- We confirm the relationship between $\log(M_d)$ and $\log(L_{250})$ found by D11 with a sample size ~ 19 times larger than theirs, and spanning a range of luminosities two orders of magnitude wider. We do not find any evidence that this relationship evolves with redshift. The relationship can be well-approximated by using a one component MBB with temperature ~ 20 K to calculate dust mass from luminosity.

CHAPTER 6

EVOLUTION IN THE DUST MASS FUNCTION TO $z = 0.5$

*‘Once you can accept the Universe as matter
expanding into nothing that is something,
wearing stripes with plaid comes easy.’*

EINSTEIN

In this Chapter, we derive 250 μm luminosity functions (LFs), and dust mass functions (DMFs) in five redshift slices out to $z = 0.5$ for the FIR selected galaxies introduced in Chapter 5. In Chapter 2 we derived a low-redshift DMF for the largest sample of galaxies to date using the optically selected GAMA catalogue over 150 sq. deg of sky for $z \leq 0.1$. In this Chapter we will use both the MAGPHYS based dust mass estimates and dust masses derived through stacking from Chapter 5 to estimate DMFs for five redshift slices out to $z = 0.5$ in steps of 0.1 for the FIR selected *Herschel* Astrophysical Terahertz Large Area Survey (*H-ATLAS*) sample. Using these DMFs we will investigate (i) whether selecting galaxies to be dusty rather than for their stellar population introduces systematic differences compared to the optically selected DMF, and (ii) the evolution of the DMF over the past ~ 5 Gyr. We use data from the *H-ATLAS* to calculate the luminosity function (LF) and dust mass function (DMF) for a range of redshift slices. In this way we can compare our lowest-redshift slice to the literature of DMFs of the nearby Universe, as well as probing the evolution of the dust content of the Universe over cosmic time. We use two methods to calculate the LF and DMF, firstly the traditional V_{max} method, and secondly the [Page & Carrera \(2000\)](#) method.

6.1 INTRODUCTION

Previous studies have shown that the dust luminosity of galaxies appears to evolve rapidly with redshift (e.g. [Huynh et al. 2007](#); [Dye et al. 2010](#); [Marchetti et al. 2012](#); [Patel et al. 2013](#); [Gruppioni et al. 2013](#)). For example using the *H*-ATLAS SDP, [Dye et al. \(2010\)](#) found that the evolution of the 250 μm density is proportional to $(1+z)^{7.1}$ out to a redshift of ~ 0.2 . [Dunne et al. \(2011\)](#), hereafter D11, saw significant evolution of the 250 μm LF out to $z = 0.5$ using the same sample. Since star formation rate (SFR) density is also seen to evolve across cosmic time, the dust evolution is generally believed to be tied to this. The driving force behind dust luminosity evolution in this paradigm is therefore assumed to be due to increased heating of the dust due to the higher SFRs in the past. However, the gas content of the Universe has been observed to decrease over time, and typically a galaxy's gas mass is strongly linked to its dust content (e.g. [Eales et al. 2012](#); [Genzel et al. 2015](#); [Scoville et al. 2016, 2017](#); [Tacconi et al. 2018](#)). Interestingly, there is contention in the literature as to the cause of the evolution of the dust luminosity.

From a sample of 1867 galaxies in the *H*-ATLAS SDP field, D11 derived dust properties for 1120 galaxies using MAGPHYS. They did not see any strong evidence within these results for evolution of dust temperature with either redshift or luminosity. They instead found that the evolution of the FIR LF was driven by an evolution in the dust content of the Universe, which evolved dramatically with redshift out to $z = 0.5$. Similarly, using the Balloon-borne Large Aperture Submillimeter Telescope (BLAST), [Eales et al. \(2009\)](#) found that the DMF evolved significantly between $z = 0$ and $z = 1$. Conversely, [Driver et al. \(2018\)](#), who used an optically-selected sample, found no strong evolution of dust density out to $z = 0.5$, necessitating a strong temperature evolution in order to explain the evolution in the dust luminosity.

[Driver et al. \(2018\)](#) see a decline in star formation rate (SFR) density over the past few Gyr, but not in either stellar mass or dust mass. They find that the dust mass density (Ω_d) peaked at $z \sim 1$. This happens to coincide roughly with the peak in SFR density they measure, suggesting that the dust and star formation are linked (see also [Cucciati et al. 2012](#); [Burgarella et al. 2013](#)). They argue that while all dust production mechanisms are relevant, this close relationship with star formation could point toward supernovae being the dominant method by which dust forms in galaxies. Supernovae have been observed to produce significant amounts of dust (e.g. [Dunne et al. 2003a](#); [Gomez et al. 2012](#); [De Looze et al. 2017, 2019](#); [Matsuura et al. 2011](#); [Rho et al. 2009, 2018](#); [Chawner et al. 2019](#); [Cigan et al. \(submitted\)](#)),

but it is unclear how much of this dust is able to survive the resulting supernovae shocks. Grain growth instead depends on the ISM, and while dust from asymptotic giant branch stars is related to SFR, they have much longer lifetimes than massive stars which result in supernovae. [Driver et al. \(2018\)](#) do see a decline in Ω_d between $0.5 < z < 1$.

As discussed Chapter 1, space-based telescopes have revolutionised the study of dust allowing more reliable estimates of the DMF down to much lower masses. Using the sample described in Chapter 5 consisting of 29 235 galaxies across ~ 160 square degrees of sky from the *H*-ATLAS DR1 sample, we can compare the evolution of dust properties out to $z = 0.5$ in a larger sample than D11. We can also compare the low redshift dust content of the Universe when using optical and FIR selections. [Clark et al. \(2015\)](#) found that FIR selected surveys tend to pick up dust-rich galaxies with colder dust temperatures than those selected at optical or near IR wavelengths.

In the next section we will describe the ways in which our catalogue is incomplete, and how we correct for this.

6.2 COMPLETENESS CORRECTIONS

To derive the DMF for our FIR selected sample we first need to consider the completeness of our survey, which is determined by three main factors. In this study we correct the number counts of sources using estimates of completeness for the submm and optical catalogues, as well as incompleteness introduced by source ID matching.

6.2.0.1 SUBMILLIMETRE CATALOGUE COMPLETENESS

The submm catalogue completeness correction (c_s) is decided by both the flux limit of the survey and the source extraction process used to compile the *H*-ATLAS catalogue, these completeness estimates come from ([Valiante et al., 2016](#)). [Valiante et al. \(2016\)](#) produced a catalogue of simulated sources and added them to the real *H*-ATLAS maps, they then perform the same source extraction technique to determine the likelihood that sources are lost to noise. The values for the submm catalogue completeness corrections as a function of $250\ \mu\text{m}$ flux (S_{250}) are listed in Table 6.1.

| $S_{250\mu\text{m}}(Jy)$ | c_s | N | % |
|--------------------------|-------|------|------|
| 20.6 - 25.4 | 1.357 | 383 | 1.3 |
| 25.4 - 31.2 | 1.151 | 4461 | 15.3 |
| 31.2 - 38.3 | 1.073 | 8536 | 29.2 |
| 38.3 - 47.0 | 1.029 | 5776 | 19.8 |
| 47.0 - 57.8 | 1.012 | 3819 | 13.1 |
| 57.8 - 71.0 | 1.009 | 2324 | 7.9 |
| 71.0 - 87.2 | 1.006 | 1408 | 4.8 |

TABLE 6.1 The submm catalogue completeness correction (c_s) for different $250\mu\text{m}$ flux ranges, as well as the number of sources in each flux bin in our sample and the percentage of the total sample that corresponds to courtesy of [Valiante et al. \(2016\)](#).

| M_r (mag) | c_r | N | % |
|-------------|-------|-----|------|
| 21.5 - 21.6 | 1.10 | 131 | 0.45 |
| 21.6 - 21.7 | 1.14 | 123 | 0.42 |
| 21.7 - 21.8 | 1.21 | 118 | 0.4 |
| 21.8 - 21.9 | 1.29 | 100 | 0.34 |
| 21.9 - 22.0 | 1.42 | 110 | 0.38 |
| 22.0 - 22.1 | 1.62 | 82 | 0.28 |
| 22.1 - 22.2 | 1.9 | 96 | 0.33 |
| 22.2 - 22.3 | 2.33 | 76 | 0.26 |
| 22.3 - 22.4 | 5.88 | 72 | 0.25 |

TABLE 6.2 The optical catalogue completeness correction (c_r) for different M_r ranges, as well as the number of sources in each magnitude bin and the percentage of the total sample that corresponds to, courtesy of D11.

6.2.0.2 OPTICAL CATALOGUE COMPLETENESS

Optical data for the galaxies in our sample is taken from the SDSS catalogue, which has a magnitude limit of 22.4 in the r -band, as this limit is approached the SDSS completeness suffers. D11 assumed that the catalogue was complete between r -band magnitudes of 19 – 21.5 mag and fit a linear slope to the logarithm of the number counts of sources in bins between these magnitudes. This fit was extrapolated to fainter magnitudes and compared to observed number counts in order to find the completeness c_r of the optical catalogue. This method is valid since the SDSS catalogue is very close to 100% completeness up to $M_r = 21.5$ mag. We use the same corrections calculated in D11 here, and the corrections as a function of absolute r -band magnitude (M_r) are listed in [Table 6.2](#).

| z | c_z | N | % |
|-----------|-------|------|------|
| 0 - 0.1 | 1.095 | 3741 | 12.8 |
| 0.1 - 0.2 | 1.140 | 7739 | 26.5 |
| 0.2 - 0.3 | 1.244 | 6365 | 21.8 |
| 0.3 - 0.4 | 1.385 | 5861 | 20.0 |
| 0.4 - 0.5 | 1.451 | 5529 | 18.9 |

TABLE 6.3 The optical ID completeness correction (c_z) for different redshift ranges, as well as the number of sources in each redshift bin and the percentage of the total sample that corresponds to, courtesy of [Bourne et al. \(2016\)](#).

6.2.0.3 ID COMPLETENESS

[Bourne et al. \(2016\)](#) find optical IDs for the H -ATLAS sources using a likelihood ratio technique as described in Section 5.1.2. They also calculate an estimate of the completeness c_z of the catalogue using the number of reliable IDs and the number of sources they estimate will have counterparts which will be visible both in the optical and submm catalogues. The completeness corrections as a function of redshift are listed in Table 6.3.

6.3 METHODS OF ESTIMATING THE FIR LUMINOSITY FUNCTION

We use two methods to calculate the luminosity and mass functions. Firstly, the traditional V_{\max} method ([Schmidt, 1968](#)) similar to the method of Chapters 2 - 4, and secondly the method proposed by [Page & Carrera \(2000\)](#) (hereafter the PC00 method).

6.3.1 RECAP OF THE V_{\max} METHOD

Unlike the B18 analysis, we use the traditional V_{\max} method here without the additional density corrections described in Chapter 2. We choose not to include these since corrections were only available out to $z = 0.1$, and tracing structures at higher redshifts becomes very difficult and so could introduce bias at higher redshifts. This is because there is no way of recovering the number or location of galaxies that fall below the detection limit, and so estimates of the required density correction become unreliable. We therefore use the traditional V_{\max} estimator but with the important addition of multiplicative corrections for the sources of incompleteness described in Section 6.2. This gives:

$$\phi(L_i) = \sum_{n=1}^{N_i} \frac{c_r c_s c_z}{V_{\max}}, \quad (6.1)$$

where ϕ is the number volume density in units of $\text{Mpc}^{-3} \text{dex}^{-1}$, the sum extends over N_i galaxies - the number of galaxies in the i^{th} bin, V_{\max} is the accessible volume and c_r , c_s , and c_z are the completeness corrections (Section 6.2). We calculate the volume accessible to each galaxy using its SED shape, luminosity, and limiting signal-to-noise ratio (SNR). We find the maximum redshift available to each galaxy numerically by minimising the following:

$$\left| \frac{L_\nu(1+z)}{4\pi D_L^2 K} - S_{\nu,\text{lim}} \right| \quad (6.2)$$

where L_ν is the luminosity of the galaxy at frequency ν , z is the redshift, D_L is the luminosity distance, K is the K -correction of the source based on the SED shape of the $L - z$ bin of the galaxy as described in Chapter 5, and $S_{\nu,\text{lim}}$ is the limiting flux for which the source would be visible based on the properties of the *H-ATLAS* survey. The *H-ATLAS* catalogue consists of sources with a $\text{SNR} > 4$, in theory in any of the *Herschel* bands, but in practice at $250 \mu\text{m}$, and so we use four times the uncertainty on the $250 \mu\text{m}$ flux as our $S_{\nu,\text{lim}}$. The SED shape properties T_d and β were taken from the one-component modified blackbody fits to the stacked SED of the containing $L - z$ bin for each galaxy described in Chapter 5.

6.3.2 THE PAGE AND CARRERA METHOD

We also calculate the LF and DMF using a modified version of the PC00 method. Once again we include corrections for the various forms of incompleteness affecting the catalogue addressed in Section 6.2. The V_{\max} method assumes that the accessible volume is constant across the range of luminosities available in each luminosity bin of a given redshift slice. The PC00 method has the advantage that the shape of the limiting volume curve across the luminosity bin is allowed to vary for each bin. An illustration of the effect that this assumption has is shown in Figure 6.1, taken from PC00. This effect is strongest in the lowest brightness bin in any given redshift slice since it will have proportionally more galaxies close to the detection limit than any other bin, which the V_{\max} method tends to overestimate.

The PC00 method takes the form:

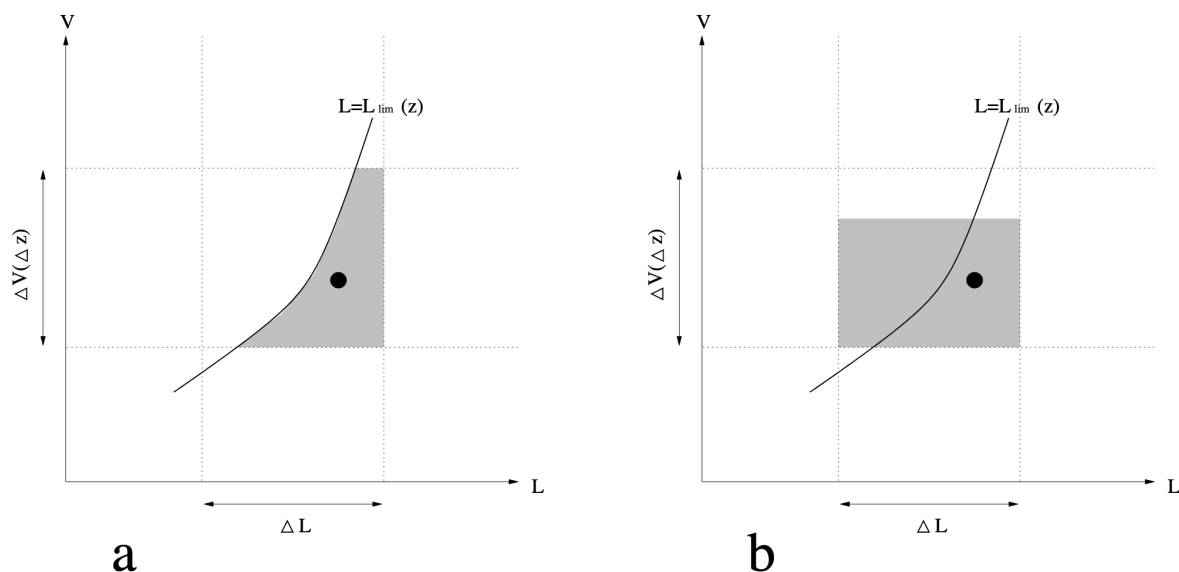


FIGURE 6.1 Figure taken from PC00 showing the volume-luminosity space ‘available’ to an object (the black dot) in (a) the PC00 method, and (b) the traditional V_{\max} method. The black line $L = L_{\text{lim}}(z)$ denotes the minimum detectable luminosity of an object at redshift z , and is determined by the flux limit of the survey.

$$\phi(L_i) = \frac{\sum_{n=1}^{N_i} c_s c_z c_r}{\int_{L_{\min}}^{L_{\max}} \int_{z_{\min}}^{z_{\max}(L)} \frac{dV}{dz} dz dL} \quad (6.3)$$

where N is the number of galaxies in the bin, c_s , c_z , c_r are the completeness corrections for each galaxy as described in Section 6.2. The quantity $\frac{dV}{dz}$ refers to the path the galaxies in the bin take through luminosity-volume space with redshift, as seen in Figure 6.1. L_{\min} and L_{\max} are the minimum and maximum luminosities of the bin, z_{\min} and $z_{\max}(L)$ are the minimum redshift of the slice, and the maximum redshift to which a source with luminosity L could be detected within the flux limit with a given K -correction, but is not allowed to exceed the maximum redshift of the slice. In essence here the volume is taken from the integral under the curve a source with given intrinsic properties would take through the $L-z$ plane, rather than just using the single value corresponding to the exact redshift at which the source happens to lie.

PC00 initially just presented a version of this estimator where all galaxies in a bin would follow the same $L-z$ relationship. D11 modified this to allow each galaxy to trace a unique path across the $L-z$ plane. This is more realistic since the SED properties of each galaxy can be different, as well as the complication that the H -ATLAS selection is based on the signal-to-noise ratio (SNR) of a source rather than a single limiting flux across the catalogue, so a different limiting flux can also

be employed. This modified PC00 method takes the form:

$$\phi(L_i) = \sum_{n=1}^{N_i} \frac{c_s c_z c_r}{\int_{L_{\min}}^{L_{\max}} \int_{z_{\min}}^{z_{\max,i}} \frac{dV}{dz} dz dL} \quad (6.4)$$

where $z_{\max,i}$ is the maximum redshift across the luminosity bin for galaxy i , as a function of luminosity, limiting flux, and the temperature assumed for the grey-body SED.

Allowing the accessible volume to evolve across the luminosity bin is most effective when considering those galaxies which lie close to the boundary at which they would fall out of the survey. In Figure 6.2 we show the difference between the two methods to illustrate the bias seen in the V_{\max} method compared to the PC00. For the V_{\max} LFs there is a clear downturn in the lower luminosity bins, which is combated by the PC00 method. The V_{\max} method is exactly the same for both the LF and DMF, but in order to use the PC00 method for a DMF we need to make an adjustment whereby we calculate for each galaxy a new set of L bin edges. The new bin edges are calculated using the dust mass bin edges, the assigned dust temperature for that galaxy, along with Equation 5.8. For the remainder of our analysis we will show the PC00 estimates of the LF and DMF unless otherwise stated.

For both estimators, we bootstrap the LF by resampling with replacement 1000 times and recalculating the LF in order to quantify the uncertainty on the data points. We then fit a Schechter function (SF, see Chapter 2) to each LF bootstrap realisation to quantify the statistical uncertainty on the best-fitting parameters. In $\log L$ space, the SF takes the form:

$$S(L; \alpha, L^*, \phi^*) = \phi^* e^{-10^{\log L - \log L^*}} \times \left(10^{\log L - \log L^*}\right)^{\alpha+1} d \log L, \quad (6.5)$$

where we have explicitly included the factor $\ln 10$ in the definition of ϕ^* , such that ϕ^* is in units of $\text{Mpc}^{-3} \text{dex}^{-1}$. We use the individual best-fitting SF fits to find uncertainty estimates for each SF parameter, we quote the median of these values for our best-fitting SF fit parameters.

We estimate that the error introduced by cosmic variance is 14.2%, 8.5%,

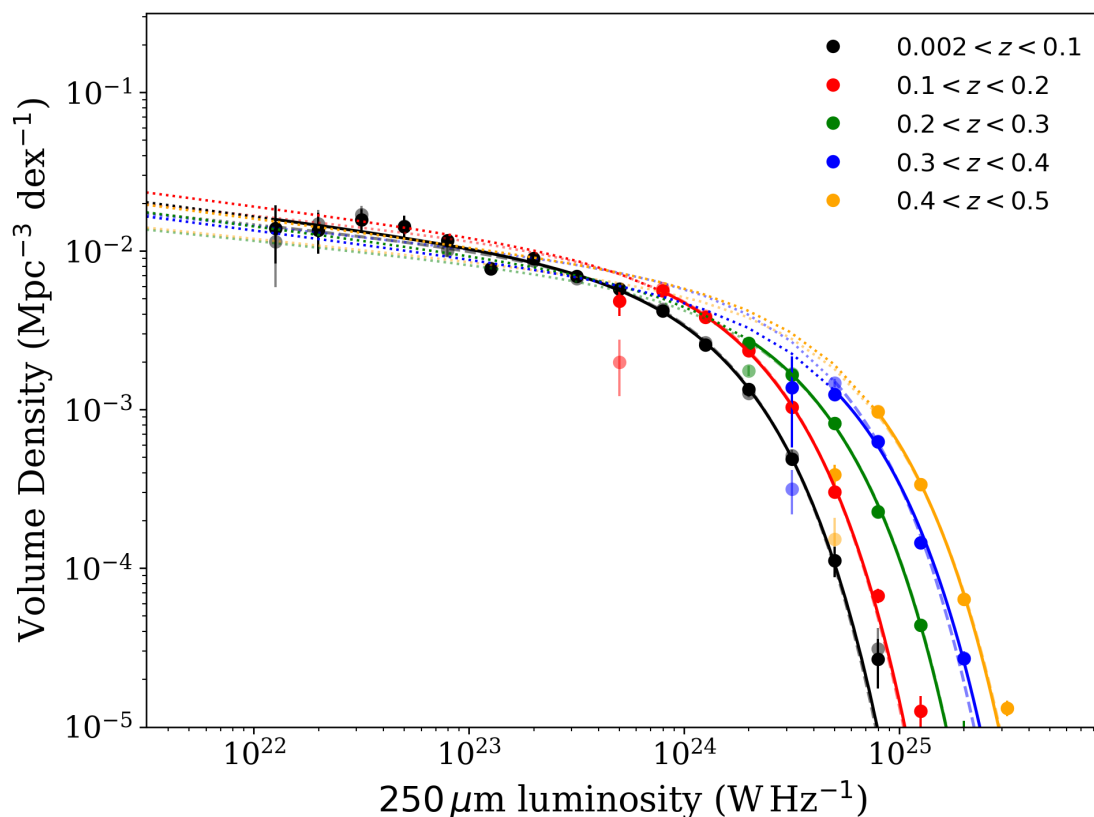


FIGURE 6.2 The $250\ \mu\text{m}$ LF from the masses derived by stacking produced using the V_{max} (transparent points), and PC00 (opaque points) estimators for 5 redshift slices ($0 < z < 0.1$, $0.1 < z < 0.2$, $0.2 < z < 0.3$, $0.3 < z < 0.4$, and $0.4 < z < 0.5$ in black red, green, blue, and yellow respectively). SF fits to the PC00 and V_{max} LFs for each redshift slice are shown as solid and dashed curves respectively. Error bars are derived from a bootstrap analysis whereby 1000 realisations of the LF are fitted and the variance determines the uncertainty on each datapoint.

6.5%, 5.5%, 4.9% for each redshift slice respectively using the cosmic variance estimator from [Driver & Robotham \(2010\)](#)¹ for the full survey volume as described in Chapter 2. Naturally this uncertainty will vary across the different LF and DMF bins due to the different maximum volumes available to the galaxies in each bin. We choose therefore not to present the cosmic variance uncertainty across the LFs and DMFs, and quote it separately from the statistical uncertainty for the cosmic dust density. We use the field-by-field density corrections for G09, G12, and G15 given by [Wright et al. \(2017\)](#), which are 1.36, 0.98, and 1.22 respectively.

¹ cosmocalc.icrar.org

6.3.3 THE EVOLUTION OF THE LUMINOSITY FUNCTION

The evolution of the LF with redshift derived using both the V_{\max} and PC00 methods is shown in Figure 6.6 and the best-fitting SF parameters are listed in Table 6.4. The bias in the low luminosity bins using the V_{\max} method is clearly being addressed, but not necessarily fully, by the PC00 method. The evolution seen in the LF can either be driven by the properties of the dust present at different cosmic times, or by the dust content of the Universe at different epochs. If the evolution of the LF was due to an increase in temperature due to increased star formation activity (star formation is known to peak around a redshift of 2), then we would expect either the stacking analysis or the MAGPHYS results to display a tendency for temperature to increase rapidly with redshift. We do not see any evidence for an increase in temperature with redshift for the MAGPHYS-based sample, and while we do see a steady increase in mass-weighted temperature for each successive redshift slice, it is only an increase of around 1 K in total over $0 < z < 0.5$. In a later section we will test whether the dust content of the Universe appears to evolve with redshift, providing an explanation for the evolution of the luminosity function seen in the *H*-ATLAS fields. In Figure 6.3 we show the luminosity densities ρ_L of the five redshift slices as a function of redshift. We fit a function of the form:

$$\rho_L \propto (1 + z)^X \quad (6.6)$$

where we find $X = 6.35 \pm 0.78$ using the V_{\max} points, and $X = 6.24 \pm 0.58$ using the PC00 derived LF datapoints, which are both similar to the $X = 7.1$ found by Dye et al. (2010) for the smaller SDP *H*-ATLAS field.

6.4 THE DUST MASS FUNCTION

As for the LF, the DMF is calculated by the V_{\max} and PC00 methods, the results of which we will describe here. The dust masses used to derive the DMFs in this Chapter come from the two methods described in Chapter 5. Briefly, the first mass estimate is based on MAGPHYS fits from Eales et al. (2018) for most of the galaxies in our sample. We used the available MAGPHYS fits to establish a simple relationship between $250 \mu\text{m}$ luminosity (L_{250}) and dust mass. We then collated dust mass estimates from MAGPHYS where available, and from using the

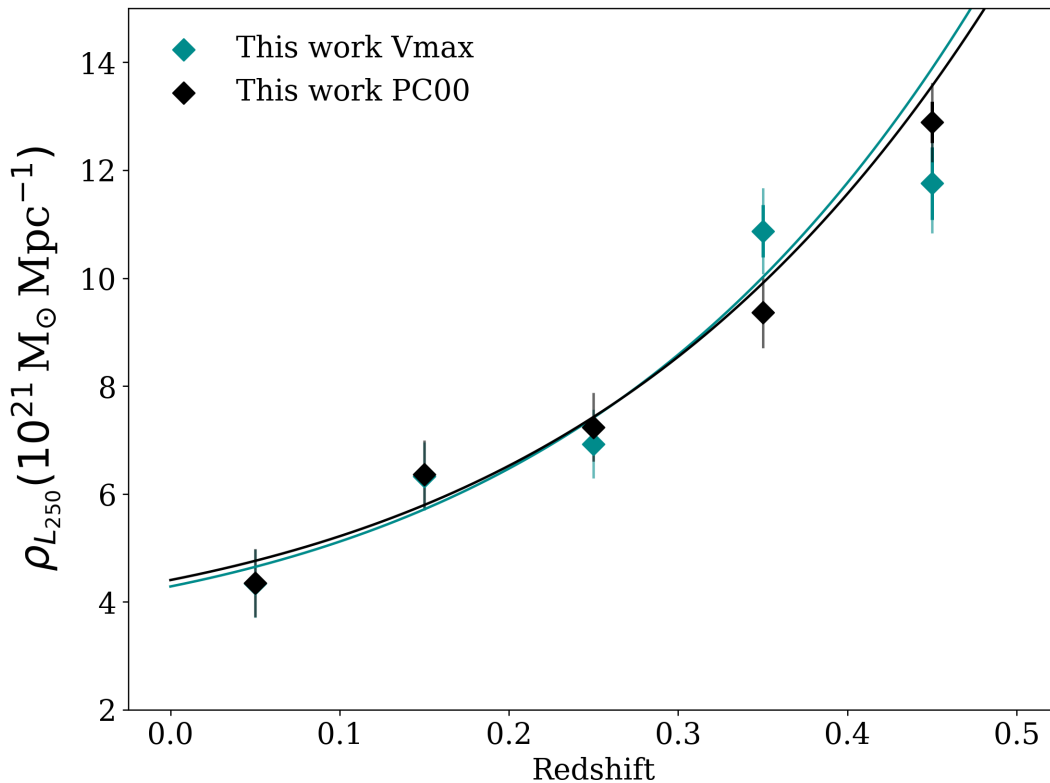


FIGURE 6.3 The $250\ \mu\text{m}$ luminosity density derived by integrating the SF fits to the LF for the five redshift slices for the V_{max} (green) and PC00 (black) methods. Solid error bars represent the statistical uncertainty on the luminosity density, and transparent error bars represent the statistical uncertainty and cosmic variance added in quadrature. The best fitting function of Equation 6.6 is shown as a solid line.

$250\ \mu\text{m}$ luminosity and the L_{250} -dust mass relationship to infer dust mass estimates, we refer to these masses as the MAGPHYS-based masses. The second set of dust masses came from a stacking analysis, whereby we split galaxies in two dimensions, L_{250} and redshift ($L - z$ bins), and stacked the luminosities of the galaxies in that bin. The masses we will use here (the 2C stacked masses) came from fitting a two component modified blackbody to the stacked SEDs in each bin and using the SED shape of each $L - z$ bin, and the L_{250} for the galaxies in the bin to estimate dust masses for our sample.

| method | z | L^* ($h_{70}^2 \text{ W Hz}^{-1}$) | α | ϕ^* ($10^{-3} h_{70}^3 \text{ Mpc}^{-3} \text{ dex}^{-1}$) | ρ_L ($10^{21} \text{ W Hz}^{-1} \text{ Mpc}^{-3}$) |
|------------------|-----------|---|------------------|--|--|
| V_{max} | 0 – 0.1 | $24.09 \pm_{0.02}^{0.02}$ | -1.14 ± 0.03 | 4.37 ± 0.26 | 4.43 ± 0.06 |
| | 0.1 – 0.2 | $24.21 \pm_{0.01}^{0.01}$ | -1.14 | 1.97 ± 0.05 | 6.44 ± 0.06 |
| | 0.2 – 0.3 | $24.44 \pm_{0.01}^{0.01}$ | -1.14 | 1.27 ± 0.05 | 7.02 ± 0.11 |
| | 0.3 – 0.4 | $24.56 \pm_{0.01}^{0.01}$ | -1.14 | 1.54 ± 0.12 | 11.0 ± 0.49 |
| | 0.4 – 0.5 | $24.69 \pm_{0.01}^{0.01}$ | -1.14 | 1.20 ± 0.10 | 11.87 ± 0.68 |
| PC00 | 0 – 0.1 | $24.11 \pm_{0.02}^{0.02}$ | -1.19 ± 0.03 | 1.42 ± 0.10 | 3.88 ± 0.04 |
| | 0.1 – 0.2 | $24.1 \pm_{0.02}^{0.02}$ | -1.19 | 4.10 ± 0.20 | 4.45 ± 0.05 |
| | 0.2 – 0.3 | $24.45 \pm_{0.01}^{0.01}$ | -1.19 | 1.27 ± 0.05 | 7.44 ± 0.11 |
| | 0.3 – 0.4 | $24.61 \pm_{0.01}^{0.01}$ | -1.19 | 1.13 ± 0.05 | 9.6 ± 0.18 |
| | 0.4 – 0.5 | $24.69 \pm_{0.01}^{0.01}$ | -1.19 | 1.30 ± 0.07 | 13.22 ± 0.4 |

TABLE 6.4 Best-fitting Schechter function values for luminosity functions derived in five redshift bins for our sample. Uncertainty estimates are derived from a bootstrap analysis whereby 1000 realisations of the LF are fitted and the variance determines the uncertainty on each SF parameter.

6.4.1 THE LOW-REDSHIFT DUST MASS FUNCTION

Most of the literature around the DMF concerns the local Universe since until the launch of *Herschel*, it was very difficult to observe large areas of sky to a sufficient depth to measure any kind of evolution. Here we compare the lowest redshift slice DMF to the literature of observations. For a full description of the literature in terms of observed DMFs, please see the Introduction and Chapter 2. These DMFs cover the same redshift range as B18 and D11, and represent the largest estimation of their kind for a FIR-selected sample, with 3741 sources. The DMF for both mass estimates is well described by a SF, and the best-fitting SF and those from previous studies is shown in Figure 2.10, and the parameters are listed in Table 6.5 along with literature values. The integrated dust mass density parameter (Ω_d) is calculated by using the incomplete gamma function to integrate the dust mass density ρ_d down to $M_d = 10^4 M_\odot$, in line with B18. This value is then divided by the critical density at $z = 0$ where $\rho_{c,0} = 1.36 \times 10^{11} M_\odot \text{ Mpc}^{-3}$. Figure 6.5 and Table 6.5 compares Ω_d for this work and the literature. We see that there is no significant offset between the different estimators/surveys in the total integrated dust mass, aside from the Driver et al. (2007) and Clark et al. (2015)

| Survey | M^* ($10^7 h_{70}^2 M_\odot$) | α | ϕ^* ($10^{-3} h_{70}^3 \text{Mpc}^{-3} \text{dex}^{-1}$) | Ω_d (10^{-6}) |
|--------------------------------|--------------------------------------|-------------------------|--|-----------------------------|
| C13 | 5.27 ± 1.56 | -1.34 ± 0.4 | 4.78 ± 1.81 | 1.1 ± 0.22 |
| D11 | $3.9^{+0.74}_{-0.63}$ | $-1.01^{+0.17}_{-0.14}$ | $8.09^{+1.9}_{-1.72}$ | 1.01 ± 0.15 |
| V05 | $6.0^{+0.45}_{-0.55}$ | $-1.39^{+0.03}_{-0.02}$ | $3.33^{+0.74}_{-0.5}$ | 0.94 ± 0.44 |
| B18 pV_{max} | 4.65 ± 0.18 | -1.22 ± 0.01 | 6.26 ± 0.28 | 1.11 ± 0.02 |
| B18 BBD | 4.67 ± 0.15 | -1.27 ± 0.01 | 5.65 ± 0.23 | 1.11 ± 0.02 |
| V_{max} 2C stacked | 2.71 ± 0.10 | -1.11 ± 0.01 | 2.42 ± 0.07 | 0.93 ± 0.01 |
| PC00 2C stacked | 2.55 ± 0.09 | -1.11 ± 0.04 | 11.58 ± 0.53 | 1.01 ± 0.02 |
| V_{max} MAGPHYS-based | 3.84 ± 0.20 | -1.12 ± 0.04 | 1.68 ± 0.12 | 0.92 ± 0.01 |
| PC00 MAGPHYS-based | 3.82 ± 0.20 | -1.12 ± 0.04 | 8.18 ± 0.56 | 1.08 ± 0.01 |

TABLE 6.5 Schechter function values for dust mass functions in the literature and this work $z < 0.1$. The other literature studies include: C13 - [Clemens et al., 2013](#), D11 - [Dunne et al., 2011](#), V05 - [Vlahakis et al., 2005](#). All have been scaled to the same dust mass absorption coefficient and cosmology used here. The [Dunne et al. \(2011\)](#) DMF includes a correction of 1.42 for the density of the GAMA09 field ([Driver et al., 2011](#)), B18 includes the running density-weighted corrections from W17, and this work includes the field-by-field density corrections from W17.

studies which have larger uncertainties.

The shape of the MAGPHYS-based DMF is very similar to the literature, agreeing very well with B18 at the high-mass end, but with a shallower low-mass slope. The 2C stacked mass DMF shows more of a departure from the literature, with a higher ϕ^* and lower M^* than seen elsewhere in the literature. We note that the last high mass end of the 2C stacked mass DMF appears to be slightly underestimated by our SF fit. It is possible that the dust properties derived through stacking for each $L - z$ bin may be a useful probe of general trends, but when applied to individual galaxies to find physical properties this method may not be valid. It is also possible that the evolution we observe in mass-weighted temperature could be underestimated compared to if we were to properly account for the effect of confusion on the flux measurements in the *H-ATLAS* catalogue ([Dunne et al., in prep.](#)). It is certainly possible that using MAGPHYS to derive dust properties for individual galaxies with noisy SEDs is biased by the tendency of MAGPHYS to simply return the prior of the temperature distribution without strong FIR constraints. This bias would act to enhance the evolution in Ω_d since it effectively flattens any trend in dust temperature with redshift.

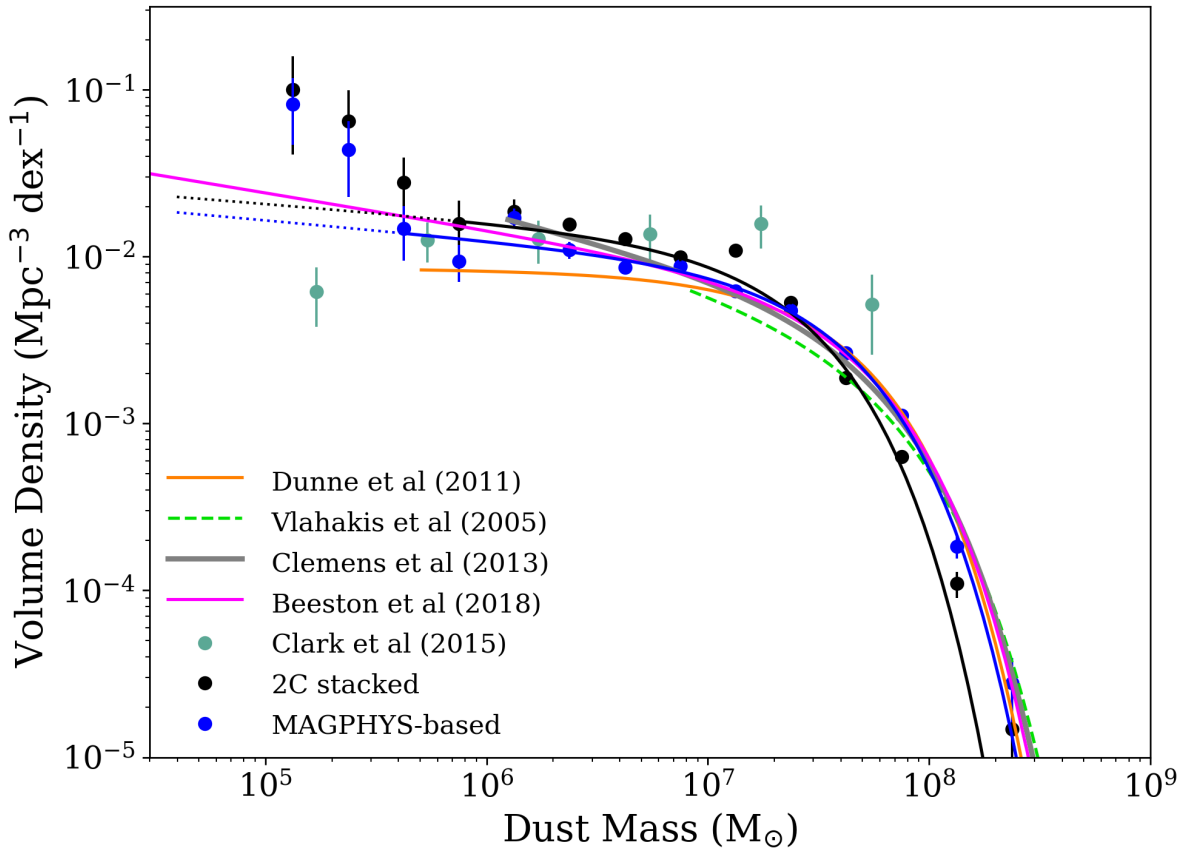


FIGURE 6.4 Comparison of the DMFs from this work from both the D11 method mass estimation (blue) along with the masses derived from a stacking analysis (black) with those from the literature. We compare with (i) the blind, local $z < 0.01$ galaxy sample from [Clark et al. \(2015\)](#) (ii) the all-sky local star-forming galaxies from the bright *Planck* catalogue from [Clemens et al. \(2013\)](#) (iii) the ground-based submm measurements of local optical galaxies from [Vlahakis et al. \(2005\)](#) (iv) the 222 galaxies out to $z < 0.1$ from the *H-ATLAS* survey ([Dunne et al., 2011](#)) and (v) the pV_{\max} DMF from the optically selected DMF from the GAMA/*H-ATLAS* overlap from B18. Schechter fit parameters are listed in Table 2.1.

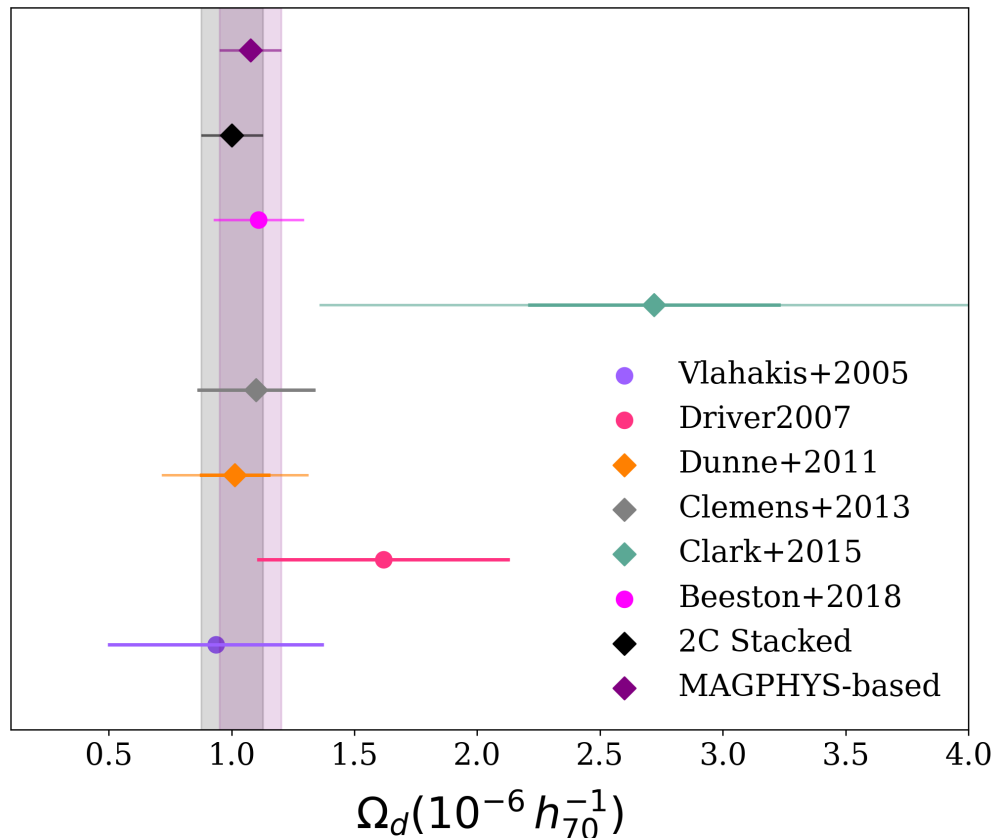


FIGURE 6.5 Comparison of the dust mass densities Ω_d from this work with those from the literature. We compare with (i) the blind, local $z < 0.01$ galaxy sample from [Clark et al. \(2015\)](#) (ii) the all-sky local star-forming galaxies from the bright *Planck* catalogue from [Clemens et al. \(2013\)](#) (iii) the ground-based submm measurements of local optical galaxies from [Vlahakis et al. \(2005\)](#) (iv) the 222 galaxies out to $z < 0.1$ from the *H*-ATLAS survey ([Dunne et al., 2011](#)) and (v) the pV_{\max} DMF from the optically selected DMF from the GAMA/*H*-ATLAS overlap from B18. Schechter fit parameters are listed in Table 2.1. The dust density parameter (Ω_d) measurements are scaled to the same cosmology, with diamonds representing dust-selected measurements, and circles representing optically-selected samples. The solid error bars on Ω_d indicate the published uncertainty derived from the error in the fit whilst the transparent error bars indicate the total uncertainty derived by combining the published uncertainty and the cosmic variance uncertainty estimate for that sample (where known). The [Dunne et al. \(2011\)](#) DMF includes the correction factor of 1.42 for the density of the GAMA09 field ([Driver et al., 2011](#)) and the B18 data points have been weighted by running density correction factors from [Wright et al. \(2017\)](#), in this work we weight using the field-by-field density corrections from [Wright et al. \(2017\)](#). The shaded region emphasises the range of Ω_d derived from our observed SF fits to the DMFs with width showing the error from the combination of cosmic variance and statistical uncertainty.

6.5 EVOLUTION OF THE DUST MASS FUNCTION

The PC00 DMFs for our FIR selected sample of 29 235 galaxies are shown in Figure 6.6. Here we will attempt to ascertain whether the evolution of the dust content of the Universe over cosmic time observed by D11 is also present in this larger survey. The DMFs for the 5 redshift slices used here are shown with their corresponding SF fits in Figure 6.7. The best-fitting SF parameters for each redshift bin are also listed in Table 6.6. Since there is not enough data below the knee to determine the low mass slope for the higher redshift slices, we choose to keep the α constant after $z < 0.1$. We use the same value for α as derived for the low redshift slice. We make no corrections for density in the lowest redshift slice here in order to ensure homogeneous treatment across our full sample.

It is clear from Figure 6.6 that our DMFs are evolving over cosmic time, with the characteristic masses by up to 0.7 dex depending on the masses and estimators used to derive the DMF. While the increase in M^* with redshift is very apparent, it is also clear that there is also a trend for ϕ^* to decrease with redshift. In order to trace the evolution of dust with redshift more faithfully, we examine the evolution of the dust density with redshift in Figure 6.7. The integrated dust mass density (ρ_d) is calculated by using the incomplete gamma function to integrate the dust mass density ρ_d down to $M_d = 10^4 M_\odot$, in line with B18 (Chapter 2).

Evidence for evolution with redshift is present in the dust density derived from the DMFs using both mass estimates, though the evolution appears to be stronger in the MAGPHYS-based DMFs. Like D11 we use the relation:

$$\rho_d \propto (1+z)^X \quad (6.7)$$

to describe the evolution of the dust density with redshift. We find best-fitting $X = 2.08 \pm 0.25$ and $X = 2.65 \pm 0.24$ for the stacked method and MAGPHYS-based method of mass calculation respectively. We attribute the difference in these two values to the lack of evolution seen in the temperatures used to calculate dust masses in the MAGPHYS-based method compared to the 2C stacked method. Using the relationship $M_d \propto T^{-2.4}$ (D11), we can calculate the change in temperature required in order for the evolution of ρ_d to be flat across our z bins (i.e. equal to the low-redshift slice). For the 2C stacked masses, the mass-weighted temperature at each of the higher redshift slices in turn would have to be 23.2 K, 24.7 K, 26.7 K, and 29.8 K. For the MAGPHYS-based masses we assume that all redshift slices have a mass-weighted temperature of 20 K since this is the value we found by fitting

the $\log L_{250}$ - $\log M_d$ to the data in Chapter 5. The MAGPHYS-based masses would therefore require mass-weighted temperatures 23.0 K, 24.8 K, 26.9 K, and 26.1 K in order to have the same Ω_d as the lowest redshift slice. For both sets of masses, this is a much stronger evolution with temperature than we observe in our data.

6.5.1 LITERATURE COMPARISONS

There have been few observational measurements of the evolution of the DMF because of the technical challenges involved. D11 found that M^* increased rapidly with increasing redshift; however, M^* and ϕ^* are correlated, and over the same redshift range ϕ^* appears to decrease. For this reason, the overall dust density and its evolution with redshift is a more robust measure of the evolution of the dust properties of the Universe. Indeed, D11 find that $X = 4$ is a good representation of all but their final data point using Equation 6.7, this value for X is significantly higher than we find using either the 2C stacked masses or the MAGPHYS-based dust masses, which is the same method D11 use to derive their DMFs. There is an apparent drop in Ω_d in their final redshift bin, which they attribute to incompleteness that is not completely dealt with even with the PC00 method. They believe this incompleteness may be related to the decreasing fraction of spectroscopic redshifts available for $z > 0.35$. We see a similar dip in our highest redshift bin using the MAGPHYS-based dust masses, but not for our 2C stacked masses. In the three lowest redshift bins we see relatively good agreement between this work and D11 for the 2C stacked mass ρ_d and the MAGPHYS-based mass ρ_d values are in good agreement with D11 for the highest three redshift slices. We have been able to push the measurements of the dust density for a FIR selected survey past $z = 0.4$ more reliably than ever before using an order of magnitude more galaxies than D11, and 12 times larger sky area than used in their analysis. We note that as seen in Chapter 5, we also see the same trend for the fraction of galaxies with a spectroscopic redshift to decrease with redshift, which could impact the trend we see here.

In Figure 6.8 we compare our dust densities as a function of redshift with work carried out by Driver et al. (2018), D11, B18, and Dunne et al. (2003a). Over the redshift range of the D11 analysis, the relationship Driver et al. (2018) find is relatively flat, but they note that the majority of the points agree within error with the D11 data; however, this is only because D11s final redshift bin appears to suffer from incompleteness, otherwise the two trends are very divergent. It is possible that Driver et al. (2018) do not sufficiently account for incompleteness across their

| method | z | M^* ($h_{70}^2 M_{\odot}$) | α | ϕ^* ($10^{-2} h_{70}^3 \text{Mpc}^{-3} \text{dex}^{-1}$) | ρ_d ($10^5 M_{\odot} \text{Mpc}^{-3}$) |
|--------------------------------|-----------|-----------------------------------|------------------|--|--|
| V_{max} 2C stacked | 0 – 0.1 | $7.43 \pm_{0.01}^{0.01}$ | -1.11 ± 0.01 | 2.42 ± 0.07 | 1.03 ± 0.02 |
| | 0.1 – 0.2 | $7.64 \pm_{0.01}^{0.01}$ | -1.11 | 1.97 ± 0.05 | 1.66 ± 0.02 |
| | 0.2 – 0.3 | $7.83 \pm_{0.16}^{0.11}$ | -1.11 | 1.34 ± 0.41 | 1.78 ± 0.54 |
| | 0.3 – 0.4 | $8.00 \pm_{0.02}^{0.02}$ | -1.11 | 1.10 ± 0.12 | 2.13 ± 0.13 |
| | 0.4 – 0.5 | $8.06 \pm_{0.01}^{0.01}$ | -1.11 | 1.37 ± 0.05 | 3.04 ± 0.07 |
| PC00 2C stacked | 0 – 0.1 | $7.35 \pm_{0.01}^{0.01}$ | -1.11 ± 0.04 | 11.58 ± 0.53 | 1.37 ± 0.03 |
| | 0.1 – 0.2 | $7.61 \pm_{0.01}^{0.01}$ | -1.11 | 2.28 ± 0.07 | 1.82 ± 0.02 |
| | 0.2 – 0.3 | $7.8 \pm_{0.01}^{0.01}$ | -1.11 | 1.63 ± 0.05 | 2.01 ± 0.03 |
| | 0.3 – 0.4 | $7.95 \pm_{0.02}^{0.02}$ | -1.11 | 1.37 ± 0.14 | 2.38 ± 0.17 |
| | 0.4 – 0.5 | $8.07 \pm_{0.01}^{0.01}$ | -1.11 | 1.32 ± 0.10 | 3.03 ± 0.13 |
| V_{max} MAGPHYS-based | 0 – 0.1 | $7.58 \pm_{0.02}^{0.02}$ | -1.12 ± 0.04 | 1.68 ± 0.12 | 1.26 ± 0.02 |
| | 0.1 – 0.2 | $7.73 \pm_{0.01}^{0.01}$ | -1.12 | 1.92 ± 0.05 | 2.03 ± 0.02 |
| | 0.2 – 0.3 | $7.92 \pm_{0.01}^{0.01}$ | -1.12 | 1.42 ± 0.05 | 2.32 ± 0.05 |
| | 0.3 – 0.4 | $8.09 \pm_{0.01}^{0.01}$ | -1.12 | 1.20 ± 0.07 | 2.84 ± 0.09 |
| | 0.4 – 0.5 | $8.23 \pm_{0.01}^{0.01}$ | -1.12 | 0.86 ± 0.05 | 2.83 ± 0.13 |
| PC00 MAGPHYS-based | 0 – 0.1 | $7.59 \pm_{0.01}^{0.01}$ | -1.12 ± 0.04 | 8.18 ± 0.56 | 1.47 ± 0.02 |
| | 0.1 – 0.2 | $7.58 \pm_{0.02}^{0.02}$ | -1.12 | 4.70 ± 0.32 | 2.04 ± 0.03 |
| | 0.2 – 0.3 | $7.91 \pm_{0.01}^{0.01}$ | -1.15 | 2.46 ± 0.04 | 1.47 ± 0.02 |
| | 0.3 – 0.4 | $8.09 \pm_{0.01}^{0.01}$ | -1.15 | 1.20 ± 0.05 | 2.97 ± 0.07 |
| | 0.4 – 0.5 | $8.25 \pm_{0.02}^{0.02}$ | -1.15 | 0.77 ± 0.10 | 2.76 ± 0.18 |

TABLE 6.6 Best-fitting Schechter function values for DMFs derived in five redshift bins for our sample. Uncertainty estimates are derived from a bootstrap analysis whereby 1000 realisations of the DMF are fitted and the variance determines the uncertainty on each SF parameter.

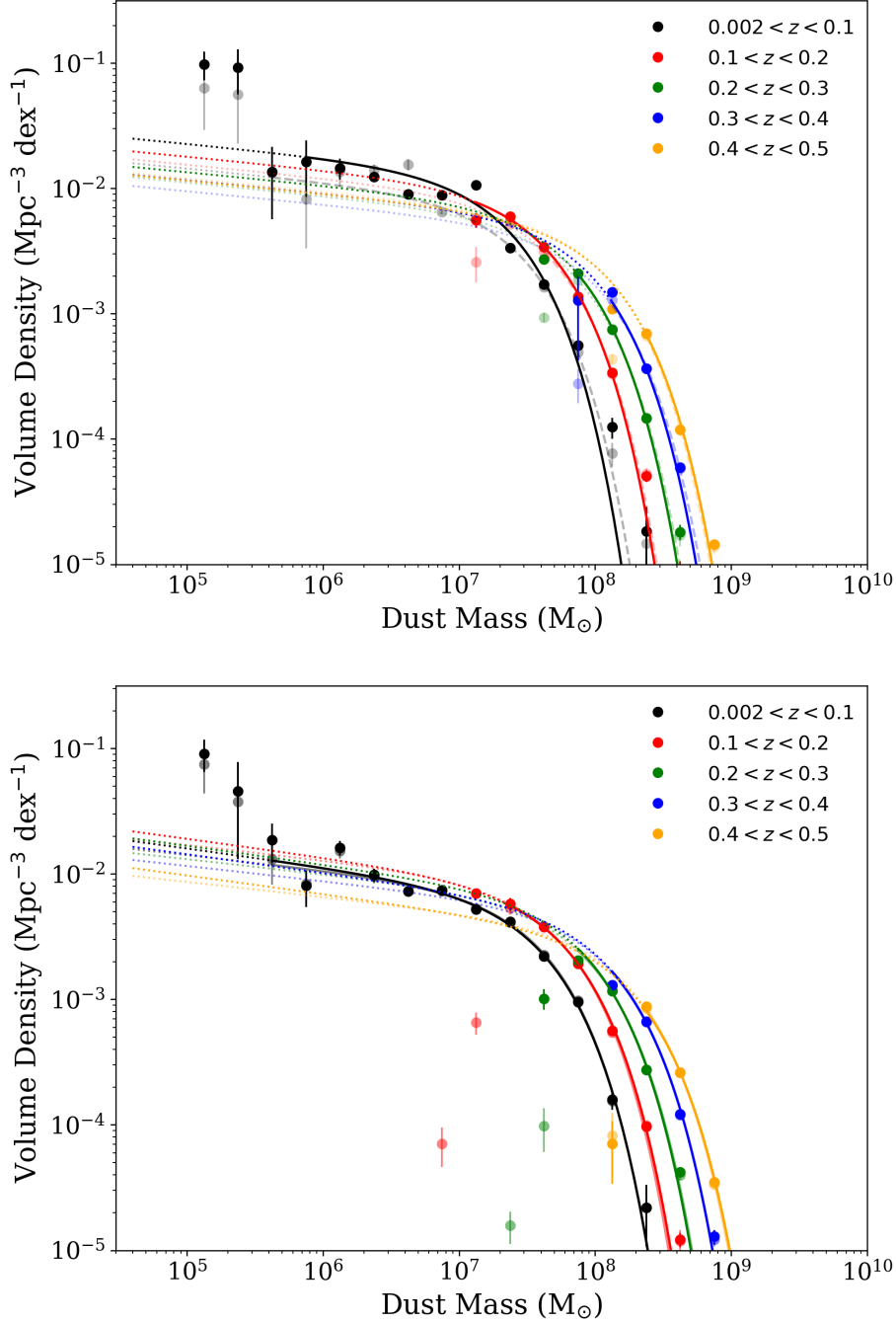


FIGURE 6.6 The DMF from (*top:*) the masses derived by the 2C stacking method, and (*bottom:*) the MAGPHYS-based dust masses produced using the V_{\max} (transparent points), and PC00 (opaque points) estimators for 5 redshift slices ($0 < z < 0.1$, $0.1 < z < 0.2$, $0.2 < z < 0.3$, $0.3 < z < 0.4$, and $0.4 < z < 0.5$ in black red, green, blue, and yellow respectively). SF fits to the PC00 and V_{\max} LFs for each redshift slice are shown as solid and dashed curves respectively. Error bars are derived from a bootstrap analysis whereby 1000 realisations of the LF are fitted and the variance determines the uncertainty on each datapoint.

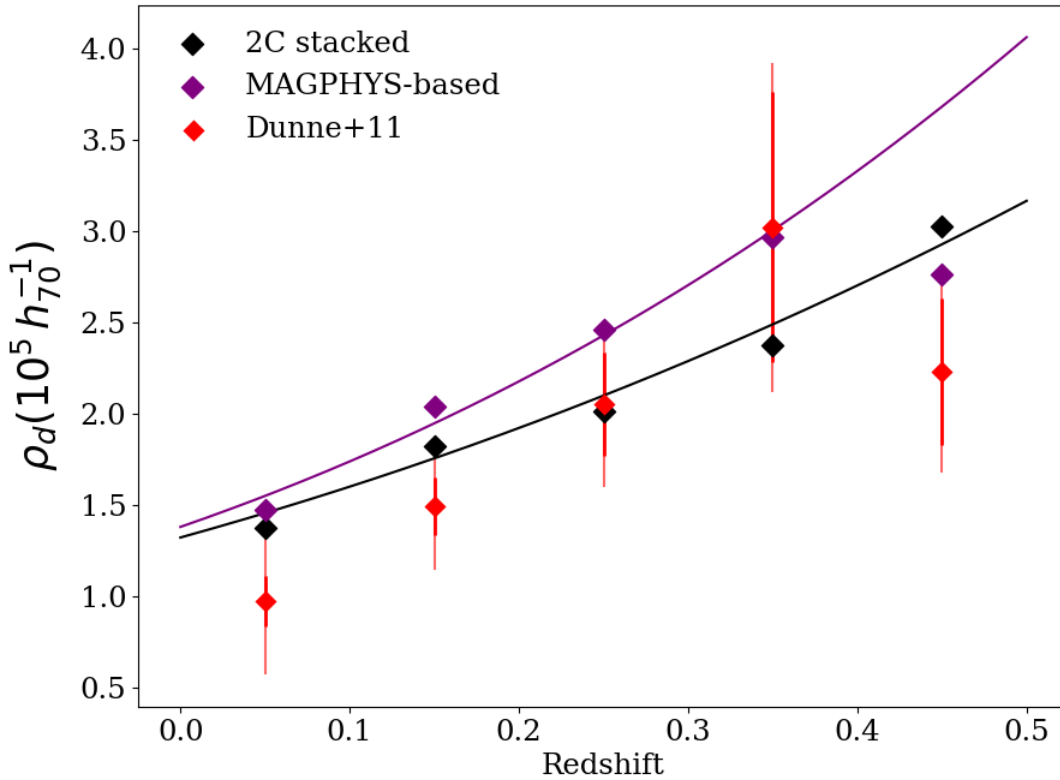


FIGURE 6.7 The dust mass densities ρ_d from this work as a function of redshift as well as those found in D11. The solid error bars on ρ_d indicate the statistical uncertainty derived from the error in the fit whilst the transparent error bars indicate the total uncertainty derived by combining the statistical uncertainty and the cosmic variance uncertainty estimate.

DMF. Their method of addressing the bias, that is targeted specifically by the PC00 method in this work and in D11, is to compare their DMF at all points to a deeper survey. If the deeper surveys also suffer from this bias (albeit less so), then some incompleteness will remain. [Driver et al. \(2018\)](#) do not fit any SF to their observed data, but rather integrate under spline fits to find overall dust mass densities. Since they also used dust masses derived from MAGPHYS it is puzzling as to how such large differences in the values that we find using the MAGPHYS-based masses can occur.

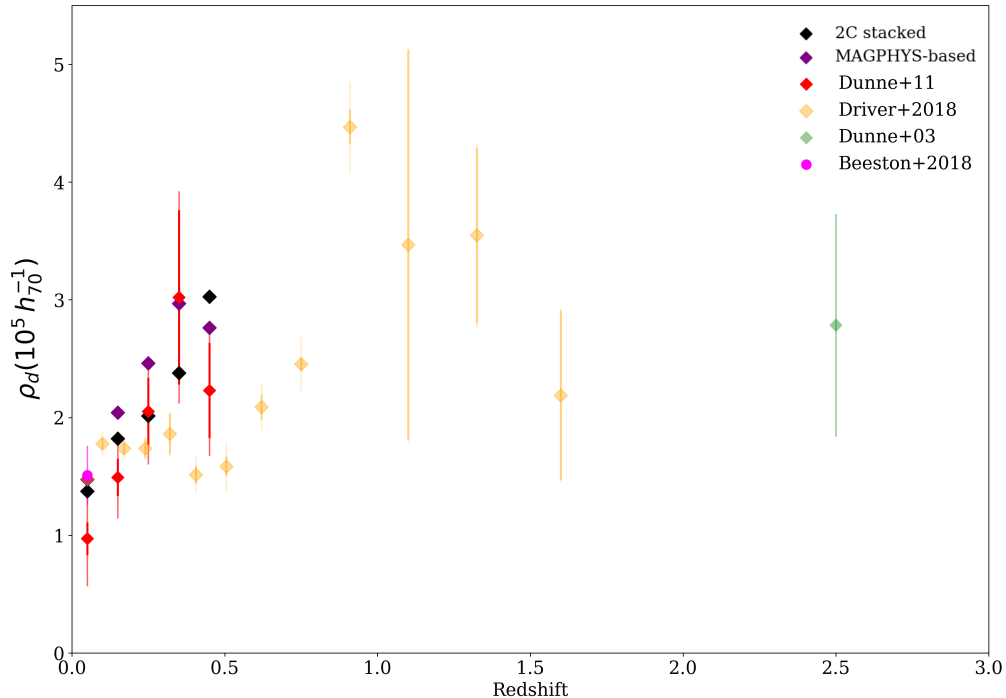


FIGURE 6.8 Comparison of the dust mass densities ρ_d as a function of redshift from this work with those from the literature. The solid error bars on ρ_d indicate the statistical uncertainty derived from the error in the fit whilst the transparent error bars indicate the total uncertainty derived by combining the statistical uncertainty and the cosmic variance uncertainty estimate. Blue are the pinned MAGPHYS dust masses, black are the dust masses from stacked SEDs, and purple are the D11 values.

6.6 CONCLUSIONS

We measure the LF and DMF in five redshift slices across our sample out to $z = 0.5$ for 29 235 sources. We use both the traditional V_{\max} method, and the PC00 method for two different estimates of the dust mass based on the method of D11, and a stacking analysis based on that employed in [Bourne et al. \(2012\)](#). This work represents the largest FIR selected study of its kind. Our main conclusions are:

- The LF and DMF are both seen to evolve with redshift. Since the dust temperature does not appear to evolve with redshift, and the dust density of the Universe does appear to evolve with redshift, we conclude that a decrease in the dust content of the Universe over cosmic time is what drives the evolution of the LF and DMF with redshift.

- We find reasonable agreement in the evolution with redshift of the luminosity with [Dye et al. \(2010\)](#) who performed a very similar analysis using the *H*-ATLAS SDP field. We find that the evolution of the luminosity density in our sample can be estimated by $\rho_L \propto (1+z)^{6.24 \pm 0.58}$.
- The stacking analysis seems to produce a DMF which has a different shape the rest of the literature with more low mass galaxies and fewer high mass galaxies. Despite this the dust density parameter is consistent with literature values, excepting that of [Clark et al. \(2015\)](#). The DMF derived using the MAGPHYS-based masses has much more conventional SF parameters, and the dust density is very similar to B18. We see no statistically significant offset between the optically selected and FIR selected samples, contrary to [Clark et al. \(2015\)](#) who find that in the nearby Universe ($z < 0.01$) FIR selected surveys are much more sensitive to colder, dust-rich galaxies.
- We find that using either the MAGPHYS-based masses or the 2C stacked masses, there is significant evolution of the dust density parameter out to $z = 0.5$, but the evolution is stronger using the MAGPHYS-based masses, the method used in D11. The evolution of the dust density in our sample can be estimated by $\rho_d \propto (1+z)^{2.08 \pm 0.25}$ and $\rho_d \propto (1+z)^{2.65 \pm 0.24}$ for the 2C stacked masses and MAGPHYS-based masses respectively.

CHAPTER 7

CONCLUSION

‘Every day you seem to know less and less about more and more.’

P.G. WODEHOUSE

IN this Thesis, we have used two samples of galaxies to investigate the dust content of the local ($z < 0.1$) Universe. The first sample was taken from the Galaxy and Mass Assembly (GAMA, [Driver et al. 2007](#)) catalogue, which is selected based on the r -band magnitude of galaxies, and has aperture matched photometry across 21 wavebands including *Herschel* measurements thanks to its overlap with the *Herschel* Astrophysical Terahertz Large Area Survey (*H-ATLAS*). From this sample we were able to derive the DMF of the largest sample of galaxies to date with over 15 000 galaxies through MAGPHYS fits from [Driver et al. \(2018\)](#). The second sample was taken from the *H-ATLAS* DR1 catalogue ([Valiante et al., 2016](#); [Bourne et al., 2016](#)), which is selected based on FIR flux. By stacking the luminosities of galaxies in bins of luminosity and redshift ($L - z$) bins, and fitting modified blackbodies (MBBs) to the stacked SEDs, we were able to investigate how dust properties evolve with both redshift and luminosity. The dust masses for the galaxies in our sample were then estimated using the dust properties assigned to the $L - z$ bin the galaxy resides in. From these measurements we were able to derive the DMF for the largest sample of local FIR selected galaxies to date. We were also able to trace the evolution of the dust content of the Universe using this sample in redshift slices of width 0.1 out to $z = 0.5$.

7.1 KEY FINDINGS FROM THE OPTICALLY SELECTED GAMA-H-ATLAS SAMPLE

Using the MAGPHYS fits to the GAMA galaxies from [Driver et al. \(2018\)](#) and two kinds of estimators we were able to derive the two estimates of the DMF for the largest sample of galaxies to date. The first of the DMF estimators, the density corrected maximum volume (pV_{max}), was performed using density corrected maximum volumes from [Wright et al. \(2017\)](#). The best fitting Schechter function (SF) for the local DMF using this method has $\alpha = -1.22 \pm 0.01$, $M^* = (4.65 \pm 0.18) \times 10^7 h_{70}^2 M_{\odot}$, $\phi_* = (6.26 \pm 0.28) \times 10^{-3} h_{70}^3 \text{Mpc}^{-3} \text{dex}^{-1}$, and $\Omega_{\text{d}} = (1.11 \pm 0.02) \times 10^{-6}$.

The second method of calculating the DMF used a bivariate brightness distribution (BBD), i.e. binning galaxies in two dimensions corresponding to the two properties thought to have the largest effect on their visibility in the survey. In each bin it is then assumed that the galaxies all have a similar maximum accessible volume and that galaxies within that bin are evenly distributed in space. Provided these assumptions hold true then a good estimate of the maximum volume available to galaxies in a given bin is to use twice the median volume, which is more robust than simply using the maximum observed volume in a bin. We tested this method using two different BBDs, the first with surface brightness and stellar mass as the two axes in order to follow the method of [Wright et al. \(2017\)](#), and secondly using surface brightness and r -band as the two axes, since the GAMA sample is selected on r -band magnitude rather than stellar mass. The best fitting single Schechter function parameters for the local DMF are $\alpha = -1.27 \pm 0.01$, $M^* = (4.67 \pm 0.15) \times 10^7 h_{70}^2 M_{\odot}$, $\phi_* = (5.65 \pm 0.23) \times 10^{-3} h_{70}^3 \text{Mpc}^{-3} \text{dex}^{-1}$, and $\Omega_{\text{d}} = (1.11 \pm 0.02) \times 10^{-6}$.

All the DMFs derived for the GAMA sample in this work agreed very well with each other. At the high mass end our DMFs also agreed very well with the literature of observed DMFs, and most SF parameters derived in other studies also agreed within error with our best fitting parameters. The dust density of the Universe derived from integrating the incomplete gamma function was also in good agreement with previous observed DMFs. We find that the theoretical models that we compare this DMF to were very discrepant. The DMFs of [Popping et al. \(2017\)](#) were very offset at the high mass end, we believe this is due to their choice of relationship between stellar and dust mass which does not reflect observations of dust in nearby galaxies. The work of [McKinnon et al. \(2017\)](#) using cosmological

hydrodynamical simulations to derive a DMF under-predicts the high mass end compared to our observations, potentially because of their very limited volume.

We investigated the potential bias that could affect our optically selected DMF and found that bias due to poor FIR constraints on the dust properties was small. We found evidence that the fitting range used in finding the SF parameters could have an effect on the resulting best fit parameters. Using a smaller fitting range would move the SF parameters closer to the DMF of [Dunne et al. \(2011\)](#), which are already in agreement, but further away from the rest of the literature. In order to test the effect of Eddington bias in our DMF we fitted a deconvolved SF fit and found that the effect on the resulting SF parameters were likely to be very small. This is because the uncertainties on the dust mass at the high mass end of the DMF tend to be low, and so the likelihood that they would jump from one DMF bin to the next is small.

We estimated DMFs for galaxies of different morphological types, and found that there is around 10 times more dust in late type galaxies (LTGs) than early type galaxies (ETGs). The LTG DMF was well described by a SF, unlike the ETG DMF. The dust density parameters were $\Omega_d = (0.88 \pm 0.03) \times 10^{-6}$ and $\Omega_d = (0.060 \pm 0.005) \times 10^{-6}$ for the LTGs and ETGs respectively. We compared our DMF to the galaxy stellar mass functions (GSMFs) from [Wright et al. \(2017\)](#) and [Moffett et al. \(2016a,b\)](#). We found that we can find an adequate representation of the DMF by scaling the LTG galaxy stellar mass function (GSMF) to the LTG DMF using a ratio of $\rho_d/\rho_s = (8.07 \pm 0.35) \times 10^{-4}$. We also found agreement between the the disk GSMF multiplied by the ratio $\rho_d/\rho_s = (10.21 \pm 0.45) \times 10^{-4}$ and our LTG DMF.

7.2 KEY FINDINGS FROM THE FIR SELECTED H-ATLAS SAMPLE

Through performing a stacking analysis on galaxies out to $z = 0.5$ in the *H*-ATLAS catalogue, we were able to fit one and two component modified blackbodies (MBBs) to stacked spectral energy distributions (SEDs) in two dimensional luminosity-redshift bins ($L - z$ bins). Using the best-fitting SEDs, we were able to trace trends in both mass-weighted and luminosity-weighted temperatures with $250 \mu\text{m}$ luminosity (L_{250}), dust mass, and redshift. At low redshifts we find that mass-weighted temperature is a strong function of luminosity. Within the lowest redshift slice ($z < 0.1$) we see an increase of nearly 7 K in luminosity-weighted

temperature. The evolution of luminosity-weighted temperature in this redshift slice is much less strong; however, with each successive redshift slice we do see a much larger increase in luminosity-weighted temperature than mass-weighted temperature. We cannot distinguish whether increase of the luminosity- and mass-weighted temperature in each redshift slice is driven by the increase of redshift or luminosity, since we cannot populate a luminosity range well enough across all redshifts to disentangle the two effects. We use the two component MBB SED shape of each $L - z$ bin to find individual dust masses for the galaxies within the bins, which we refer to as the 2C stacked masses.

We use MAGPHYS fits for a subsample of the *H-ATLAS* galaxies from [Eales et al. \(2018\)](#) to find a relationship between $250 \mu\text{m}$ luminosity and dust mass, which is in very good agreement with a similar analysis done for a smaller sample using the *H-ATLAS* Science Demonstration Phase by [Dunne et al. \(2011\)](#). The relationship we derive is essentially the same as using a one component MBB with temperature 20 K to calculate dust mass. We do not find any evidence that this relationship evolves with redshift. We collate the dust masses from MAGPHYS where available with masses derived using this relationship to find estimates of the dust mass for all the galaxies in our sample, which we call the MAGPHYS-based masses. The MAGPHYS-based masses tend to be lower than the masses from the stacking analysis at low L_{250} and higher than the 2C stacked mass estimates at high L_{250} .

We measure the $250 \mu\text{m}$ LF and the DMF for the largest FIR sample of galaxies to-date with 29 235 sources out to $z = 0.5$. We find that the LF evolves very strongly out to $z = 0.5$, with the resulting luminosity densities ρ_L evolving as $\rho_L \propto (1 + z)^{6.24 \pm 0.58}$. We derive DMFs using the 2C stacked masses and MAGPHYS-based masses from Chapter 5. The low-redshift DMF for this FIR selected sample yields dust density parameters which are similar to the Ω_d of the optically selected DMF with $\Omega_d = (1.01 \pm 0.02) \times 10^{-6}$, and $(1.07 \pm 0.01) \times 10^{-6}$ for the 2C stacked masses and MAGPHYS-based dust masses respectively. We find using either the 2C stacked masses or the MAGPHYS-based masses, the dust density of the Universe evolves strongly out to a redshift of $z = 0.5$. The evolution of the DMF is stronger for the MAGPHYS-based estimates, which we believe is due to the bias that MAGPHYS has towards returning the prior where there are not strong FIR constraints. Since the majority of our sample (74%) has only one detection in any *Herschel* band this could have a significant effect on the overall dust properties of our sample. We find that the evolution of the dust density evolves as $\rho_d \propto (1 + z)^{2.08 \pm 0.25}$ and $\rho_d \propto (1 + z)^{2.65 \pm 0.24}$ for the 2C stacked masses and MAGPHYS-based masses respectively. While we find significantly less evolution with redshift than [Dunne](#)

[et al. \(2011\)](#), we do not agree with the flat relationship with redshift derived for the optically selected sample from the GAMA/*H*-ATLAS overlap. Using a sample containing an order of magnitude more galaxies than [Dunne et al. \(2011\)](#), we find that the dust content of the Universe has evolved significantly over the last 5 billion years.

7.3 FUTURE WORK

There are many directions in which this project could progress, one of which would be to try to perform more realistic simulations to explore the efficacy of stacking as a means of recovering dust properties that are a good representation of the underlying distribution of “true” galaxy properties. We have tested a few methods of generating simulated SEDs to populate our $L - z$ bins, none of which appear to reproduce our observations sufficiently well. One such method was to sample 1000 $250\ \mu\text{m}$ luminosities in each $L - z$ bin to populate our simulated $L - z$ bins. To find simulated SEDs, we generate 1000 SED shapes and assign each to one of the randomly selected observed $250\ \mu\text{m}$ luminosities. We then scaled the SED shape to the L_{250} point and extracted the values at each *Herschel* waveband. For each $L - z$ bin we would have 8 realisations, each of which would be assigned a different mass-weighted temperature, chosen evenly between 15 K and 30 K. In each of these realisations (and $L - z$ bins therein) we generated cold temperatures between 12 K, and the mass-weighted temperature of the bin, and warm temperatures between the mass-weighted temperature of the bin and 60 K, we then used these values along with the mass-weighted temperature of the bin to find the ratio of cold to warm mass. The SED shape was then scaled to have the same $250\ \mu\text{m}$ luminosity as the simulated source it was assigned to, and the galaxies in each bin were stacked in exactly the same way as for observed galaxies and fitted with a two component MBB. The mass-weighted temperatures were consistent with the input values, but the scatter was very large (around 3 K in the worst cases) with large uncertainty estimates. Since we do not see such large uncertainties on the mass-weighted temperatures of our observed galaxies it is clear that the range of SED shapes populating each bin is too wide compared to reality. We also note that the stacked observed colour ratios were significantly offset from the simulated colour ratios. Without knowing the exact distribution of SED shapes that describes our observations it is not possible to accurately recreate our observations and determine how much bias to each galaxy’s dust properties is introduced through stacking.

Another avenue of exploration could be to either perform the stacking analysis on the optically selected sample to test whether the trends we see for the FIR sample also apply to those galaxies. We could also try to more faithfully recreate the [Bourne et al. \(2012\)](#) analysis, and split the galaxies into the “red sequence”, “green valley”, and “blue cloud” to see whether the trends they find using the optically selected sample from GAMA hold for FIR selected galaxies.

BIBLIOGRAPHY

- Abazajian K. N., et al., 2009, *ApJS*, 182, 543
- Agius N. K., et al., 2013, *MNRAS*, 431, 1929
- Agius N. K., et al., 2015, *MNRAS*, 451, 3815
- Ahn C. P., et al. 2013, *VizieR Online Data Catalog*, p. V/139
- Amblard A., et al., 2010, *A&A*, 518, L9
- Amblard A., Riguccini L., Temi P., Im S., Fanelli M., Serra P., 2014, *ApJ*, 783, 135
- Asano R. S., Takeuchi T. T., Hirashita H., Inoue A. K., 2013a, *Earth, Planets, and Space*, 65, 213
- Asano R. S., Takeuchi T. T., Hirashita H., Nozawa T., 2013b, *MNRAS*, 432, 637
- Baldry I. K., et al., 2010, *MNRAS*, 404, 86
- Baldry I. K., et al., 2012, *MNRAS*, 421, 621
- Baldry I. K., et al., 2014, *MNRAS*, 441, 2440
- Baldry I. K., et al., 2018, *MNRAS*, 474, 3875
- Bamford S. P., et al., 2009, *MNRAS*, 393, 1324
- Barnard E. E., 1907, *ApJ*, 25, 218
- Barnard E. E., 1910, *ApJ*, 31, 8
- Beeston R. A., et al., 2018, *MNRAS*, 479, 1077
- Bekki K., 2013, *MNRAS*, 432, 2298
- Bekki K., Couch W. J., 2011, *MNRAS*, 415, 1783

- Bendo G. J., et al., 2010, *A&A*, 518, L65
- Bendo G. J., et al., 2015, *MNRAS*, 448, 135
- Berta S., et al., 2013, *A&A*, 551, A100
- Bianchi L., GALEX Team 1999, Mem. Soc. Astron. Italiana, 70
- Bianchi S., Schneider R., 2007, *MNRAS*, 378, 973
- Bilicki M., et al., 2018, *A&A*, 616, A69
- Blain A. W., 2004, Galaxy Formation and Evolution in the Cold Universe. p. 1, [doi:10.1007/3-540-31636-1_1](https://doi.org/10.1007/3-540-31636-1_1)
- Blanton M. R., Roweis S., 2007, *AJ*, 133, 734
- Boselli A., et al., 2010, *PASP*, 122, 261
- Bourne N., et al., 2012, *MNRAS*, 421, 3027
- Bourne N., et al., 2016, *MNRAS*, 462, 1714
- Bregman J. N., Snider B. A., Grego L., Cox C. V., 1998, *ApJ*, 499, 670
- Bruzual G., Charlot S., 2003, *MNRAS*, 344, 1000
- Burgarella D., et al., 2013, *A&A*, 554, A70
- Butcher H., Oemler A. J., 1984, *ApJ*, 285, 426
- Calzetti D., et al., 2007, *ApJ*, 666, 870
- Cannon R., et al., 2006, *MNRAS*, 372, 425
- Cappellari M., et al., 2011, Monthly Notices of the Royal Astronomical Society, 413, 813
- Carroll B. W., Ostlie D. A., 1996, An Introduction to Modern Astrophysics
- Casey C. M., Narayanan D., Cooray A., 2014, *Phys. Rep.*, 541, 45
- Catinella B., Cortese L., 2015, *MNRAS*, 446, 3526
- Chabrier G., 2005, in Corbelli E., Palla F., Zinnecker H., eds, Astrophysics and Space Science Library Vol. 327, The Initial Mass Function 50 Years Later. p. 41 ([arXiv:astro-ph/0409465](https://arxiv.org/abs/astro-ph/0409465)), [doi:10.1007/978-1-4020-3407-7_5](https://doi.org/10.1007/978-1-4020-3407-7_5)

- Charlot S., Fall S. M., 2000, *ApJ*, **539**, 718
- Chawner H., et al., 2019, *MNRAS*, **483**, 70
- Ciesla L., et al., 2012, *A&A*, **543**, A161
- Clark C. J. R., et al., 2015, *MNRAS*, **452**, 397
- Clark C. J. R., Schofield S. P., Gomez H. L., Davies J. I., 2016, *MNRAS*, **459**, 1646
- Clark C. J. R., et al., 2019, *MNRAS*, p. 2174
- Clemens M. S., et al., 2010, *A&A*, **518**, L50
- Clemens M. S., et al., 2013, *MNRAS*, **433**, 695
- Cole S., 2011, *MNRAS*, **416**, 739
- Colless M., et al., 2001, *MNRAS*, **328**, 1039
- Collister A. A., Lahav O., 2004, *PASP*, **116**, 345
- Combes F., 2018, *A&A Rev.*, **26**, 5
- Coppin K., et al., 2008, *MNRAS*, **384**, 1597
- Cortese L., et al., 2012a, *Astronomy & Astrophysics*, **540**, A52
- Cortese L., et al., 2012b, *Astronomy & Astrophysics*, **544**, A101
- Croom S., et al., 2004, in Mújica R., Maiolino R., eds, *Multiwavelength AGN Surveys*. pp 57–62, [doi:10.1142/9789812702432_0015](https://doi.org/10.1142/9789812702432_0015)
- Croom S. M., et al., 2009, *MNRAS*, **399**, 1755
- Cucciati O., et al., 2012, *A&A*, **539**, A31
- Daddi E., et al., 2007, *ApJ*, **670**, 156
- Dale D. A., Helou G., Contursi A., Silbermann N. A., Kolhatkar S., 2001, *ApJ*, **549**, 215
- De Looze I., Barlow M. J., Swinyard B. M., Rho J., Gomez H. L., Matsuura M., Wesson R., 2017, *MNRAS*, **465**, 3309
- De Looze I., et al., 2019, *MNRAS*, **488**, 164

- De Vis P., et al., 2017a, *MNRAS*, 464, 4680
- De Vis P., et al., 2017b, *MNRAS*, 471, 1743
- Dole H., et al., 2006, *A&A*, 451, 417
- Draine B. T., 2003, *ARA&A*, 41, 241
- Draine B. T., 2009, in Henning T., Grün E., Steinacker J., eds, *Astronomical Society of the Pacific Conference Series Vol. 414, Cosmic Dust - Near and Far*. p. 453 ([arXiv:0903.1658](https://arxiv.org/abs/0903.1658))
- Draine B. T., Li A., 2007, *ApJ*, 657, 810
- Drinkwater M. J., et al., 2010, *MNRAS*, 401, 1429
- Driver S. P., Robotham A. S. G., 2010, *MNRAS*, 407, 2131
- Driver S. P., Liske J., Cross N. J. G., De Propriis R., Allen P. D., 2005, *MNRAS*, 360, 81
- Driver S. P., Popescu C. C., Tuffs R. J., Liske J., Graham A. W., Allen P. D., de Propriis R., 2007, *MNRAS*, 379, 1022
- Driver S. P., et al., 2009, *Astronomy and Geophysics*, 50, 5.12
- Driver S. P., et al., 2011, *MNRAS*, 413, 971
- Driver S. P., et al., 2012, *MNRAS*, 427, 3244
- Driver S. P., et al., 2016, *MNRAS*, 455, 3911
- Driver S. P., et al., 2018, *MNRAS*, 475, 2891
- Duley W. W., Seahra S., 1998, *ApJ*, 507, 874
- Dunne L., Eales S. A., 2001, *MNRAS*, 327, 697
- Dunne L., Eales S., Edmunds M., Ivison R., Alexander P., Clements D. L., 2000, *MNRAS*, 315, 115
- Dunne L., Eales S. A., Edmunds M. G., 2003a, *MNRAS*, 341, 589
- Dunne L., Eales S., Ivison R., Morgan H., Edmunds M., 2003b, *Nature*, 424, 285
- Dunne L., et al., 2009, *MNRAS*, 394, 1307

- Dunne L., et al., 2011, *MNRAS*, 417, 1510
- Dunne L., et al., 2018, *MNRAS*, 479, 1221
- Dwek E., 1998, *ApJ*, 501, 643
- Dwek E., Cherchneff I., 2011, *ApJ*, 727, 63
- Dwek E., Galliano F., Jones A. P., 2007, *Nuovo Cimento B Serie*, 122, 959
- Dye S., et al., 2010, *A&A*, 518, L10
- Eales S., et al., 2009, *ApJ*, 707, 1779
- Eales S., et al., 2010, *PASP*, 122, 499
- Eales S., et al., 2012, *ApJ*, 761, 168
- Eales S., et al., 2018, *MNRAS*, 473, 3507
- Eddington A. S., 1913, *MNRAS*, 73, 359
- Edmunds M. G., 2001, *MNRAS*, 328, 223
- Falco E. E., et al., 1999, *PASP*, 111, 438
- Feldmann R., 2015, *MNRAS*, 449, 3274
- Ferrarotti A. S., Gail H. P., 2006, *A&A*, 447, 553
- Fixsen D. J., Dwek E., Mather J. C., Bennett C. L., Shafer R. A., 1998, *ApJ*, 508, 123
- Foreman-Mackey D., 2016, *The Journal of Open Source Software*, 24
- Foreman-Mackey D., Hogg D. W., Lang D., Goodman J., 2013, *PASP*, 125, 306
- Gall C., Hjorth J., Andersen A. C., 2011, *A&A Rev.*, 19, 43
- Genzel R., et al., 2015, *ApJ*, 800, 20
- Gilra D. P., 1972, *Collective Excitations and Dust Particles in Space*. p. 295
- Gomez H., et al., 2010, *Astronomy & Astrophysics*, 518, L45
- Gomez H. L., et al., 2012, *ApJ*, 760, 96
- Gordon K. D., Clayton G. C., Misselt K. A., Landolt A. U., Wolff M. J., 2003, *ApJ*, 594, 279

- Goto T., Yamauchi C., Fujita Y., Okamura S., Sekiguchi M., Smail I., Bernardi M., Gomez P. L., 2003, *MNRAS*, 346, 601
- Gott III J. R., Jurić M., Schlegel D., Hoyle F., Vogeley M., Tegmark M., Bahcall N., Brinkmann J., 2005, *The Astrophysical Journal*, 624, 463
- Gott J. Richard I., Vogeley M. S., Podariu S., Ratra B., 2001, *ApJ*, 549, 1
- Griffin M. J., et al., 2010, *A&A*, 518, L3
- Griffin M. J., et al., 2013, *MNRAS*, 434, 992
- Gruppioni C., et al., 2013, *MNRAS*, 432, 23
- Hartung J., Knapp G., Sinha B. K., 2011, *Statistical meta-analysis with applications*. Vol. 738, John Wiley & Sons
- Heckman T. M., 2003, in Avila-Reese V., Firmani C., Frenk C. S., Allen C., eds, *Revista Mexicana de Astronomia y Astrofisica Conference Series Vol. 17*, *Revista Mexicana de Astronomia y Astrofisica Conference Series*. pp 47–55
- Herschel W., 1811, *Philosophical Transactions of the Royal Society of London Series I*, 101, 269
- Holland W. S., et al., 1999, *MNRAS*, 303, 659
- Holland W. S., et al., 2013, *MNRAS*, 430, 2513
- Hopkins A. M., 2004, *ApJ*, 615, 209
- Hopkins A. M., Beacom J. F., 2006, *ApJ*, 651, 142
- Hopkins A. M., et al., 2013, *MNRAS*, 430, 2047
- Hubble E. P., 1926, *The Astrophysical Journal*, 64, 321
- Hunter J. D., 2007, *Computing in Science & Engineering*, 9, 90
- Huynh M. T., Frayer D. T., Mobasher B., Dickinson M., Chary R.-R., Morrison G., 2007, *ApJ*, 667, L9
- Hwang H. S., et al., 2010, *MNRAS*, 409, 75
- Issa M. R., MacLaren I., Wolfendale A. W., 1990, *A&A*, 236, 237
- James A., Dunne L., Eales S., Edmunds M. G., 2002, *MNRAS*, 335, 753

- Jones A. P., Nuth J. A., 2011, *A&A*, 530, A44
- Jones D. H., et al., 2009, *MNRAS*, 399, 683
- Kapteyn J. C., 1909, *ApJ*, 29, 46
- Karim A., et al., 2011, *ApJ*, 730, 61
- Kelvin L. S., et al., 2014a, *MNRAS*, 439, 1245
- Kelvin L. S., et al., 2014b, *MNRAS*, 444, 1647
- Kennicutt Jr. R. C., 1998, *ApJ*, 498, 541
- Kim S. H., Martin P. G., 1994a, *JRASC*, 88, 263
- Kim S.-H., Martin P. G., 1994b, *ApJ*, 431, 783
- Kirchhoff G., 1860, *Annalen der Physik*, 185, 275
- Kozasa T., Nozawa T., Tominaga N., Umeda H., Maeda K., Nomoto K., 2009, in Henning T., Grün E., Steinacker J., eds, *Astronomical Society of the Pacific Conference Series Vol. 414, Cosmic Dust - Near and Far*. p. 43 ([arXiv:0903.0217](https://arxiv.org/abs/0903.0217))
- Larson R. B., Tinsley B. M., Caldwell C. N., 1980, *ApJ*, 237, 692
- Lee S.-K., Ferguson H. C., Somerville R. S., Wiklind T., Giavalisco M., 2010, *ApJ*, 725, 1644
- Lianou S., Xilouris E., Madden S. C., Barmby P., 2016, *MNRAS*, 461, 2856
- Liske J., et al., 2015, *MNRAS*, 452, 2087
- Loveday J., Peterson B. A., Efstathiou G., Maddox S. J., 1992, *ApJ*, 390, 338
- Loveday J., et al., 2012, *MNRAS*, 420, 1239
- Loveday J., et al., 2015, *MNRAS*, 451, 1540
- Madau P., Dickinson M., 2014, *Annual Review of Astronomy and Astrophysics*, 52, 415
- Madau P., Pozzetti L., Dickinson M., 1998, *ApJ*, 498, 106
- Madden S. C., et al., 2013, *PASP*, 125, 600
- Magdis G. E., et al., 2012, *ApJ*, 760, 6

- Marchetti L., Vaccari M., Franceschini A., Rodighiero G., Bock J., Oliver S., 2012, in Science from the Next Generation Imaging and Spectroscopic Surveys. p. 8
- Marchetti L., et al., 2016, [MNRAS](#), **456**, 1999
- Matsuura M., et al., 2011, [Science](#), **333**, 1258
- Matsuura M., Indebetouw R., Kamenetzky J., McCray R., Zanardo G., Barlow M. J., Dwek E., 2015, in Iono D., Tatematsu K., Wootten A., Testi L., eds, Astronomical Society of the Pacific Conference Series Vol. 499, Revolution in Astronomy with ALMA: The Third Year. p. 323
- McKinnon R., Torrey P., Vogelsberger M., 2016, [MNRAS](#), **457**, 3775
- McKinnon R., Torrey P., Vogelsberger M., Hayward C. C., Marinacci F., 2017, [MNRAS](#), **468**, 1505
- Michałowski M. J., Murphy E. J., Hjorth J., Watson D., Gall C., Dunlop J. S., 2010a, [A&A](#), **522**, A15
- Michałowski M. J., Watson D., Hjorth J., 2010b, [ApJ](#), **712**, 942
- Michałowski M. J., Watson D., Hjorth J., 2010c, [ApJ](#), **712**, 942
- Moffett A. J., et al., 2016a, [MNRAS](#), **457**, 1308
- Moffett A. J., et al., 2016b, [MNRAS](#), **462**, 4336
- Morgan H. L., Edmunds M. G., 2003, [MNRAS](#), **343**, 427
- Navarro J. F., Frenk C. S., White S. D. M., 1995, [MNRAS](#), **275**, 56
- Negrello M., et al., 2013, [MNRAS](#), **429**, 1309
- Negrello M., et al., 2017, [MNRAS](#), **465**, 3558
- Neugebauer G., et al., 1984, [ApJ](#), **278**, L1
- Newville M., Stensitzki T., Allen D. B., Rawlik M., Ingargiola A., Nelson A., 2016, Lmfit: Non-Linear Least-Square Minimization and Curve-Fitting for Python (ascl:1606.014)
- Ofek E. O., Rix H.-W., Maoz D., 2003, [MNRAS](#), **343**, 639
- Oliphant T. E., 2006, A guide to NumPy. Vol. 1, Trelgol Publishing USA

- Oliver S. J., et al., 2012, *MNRAS*, 424, 1614
- Ormel C. W., Min M., Tielens A. G. G. M., Dominik C., Paszun D., 2011, *A&A*, 532, A43
- Page M. J., Carrera F. J., 2000, *MNRAS*, 311, 433
- Patel H., Clements D. L., Vaccari M., Mortlock D. J., Rowan-Robinson M., Pérez-Fournon I., Afonso-Luis A., 2013, *MNRAS*, 428, 291
- Pilbratt G. L., et al., 2010, *A&A*, 518, L1
- Pimblet K. A., Smail I., Kodama T., Couch W. J., Edge A. C., Zabludoff A. I., O'Hely E., 2002, *MNRAS*, 331, 333
- Planck Collaboration XIII 2016, *A&A*, 594, A13
- Planck Collaboration XXIX 2016, *A&A*, 586, A132
- Poglitsch A., et al., 2010, *A&A*, 518, L2
- Popping G., Somerville R. S., Trager S. C., 2014, *MNRAS*, 442, 2398
- Popping G., Somerville R. S., Galametz M., 2017, *MNRAS*, 471, 3152
- Puget J.-L., Abergel A., Bernard J.-P., Boulanger F., Burton W. B., Desert F.-X., Hartmann D., 1996, *A&A*, 308, L5
- Quenouille M. H., 1949, in *Mathematical Proceedings of the Cambridge Philosophical Society*. pp 483–484
- R Core Team 2016, *R: A Language and Environment for Statistical Computing*. R Foundation for Statistical Computing, Vienna, Austria, <https://www.R-project.org/>
- Rémy-Ruyer A., et al., 2013, *A&A*, 557, A95
- Rex M., et al., 2010, *A&A*, 518, L13
- Rho J., Reach W. T., Tappe A., Hwang U., Slavin J. D., Kozasa T., Dunne L., 2009, *ApJ*, 700, 579
- Rho J., et al., 2018, *MNRAS*, 479, 5101
- Robotham A., et al., 2010, *PASA*, 27, 76

- Roth N., Kasen D., Hopkins P. F., Quataert E., 2012, *The Astrophysical Journal*, 759, 36
- Rowan-Robinson M., 2012, in Tuffs R. J., Popescu C. C., eds, IAU Symposium Vol. 284, The Spectral Energy Distribution of Galaxies - SED 2011. pp 446–455 ([arXiv:1201.1559](https://arxiv.org/abs/1201.1559)), [doi:10.1017/S174392131200960X](https://doi.org/10.1017/S174392131200960X)
- Rowlands K., et al., 2012, *MNRAS*, 419, 2545
- Rowlands K., Gomez H. L., Dunne L., Aragón-Salamanca A., Dye S., Maddox S., da Cunha E., Werf P. v. d., 2014, *MNRAS*, 441, 1040
- Sadeh I., Abdalla F. B., Lahav O., 2016, *PASP*, 128, 104502
- Salpeter E. E., 1974, *ApJ*, 193, 579
- Santini P., et al., 2010, *A&A*, 518, L154
- Santini P., et al., 2014, *A&A*, 562, A30
- Sargent B. A., et al., 2010, *ApJ*, 716, 878
- Schechter P., 1976, *ApJ*, 203, 297
- Schmidt M., 1968, *ApJ*, 151, 393
- Schneider N., Urban J., Baron P., 2009, *Planet. Space Sci.*, 57, 1419
- Scoville N., et al., 2014, *ApJ*, 783, 84
- Scoville N., et al., 2016, *ApJ*, 820, 83
- Scoville N., et al., 2017, *ApJ*, 837, 150
- Seymour N., Symeonidis M., Page M. J., Huynh M., Dwelly T., McHardy I. M., Rieke G., 2010, *MNRAS*, 402, 2666
- Shull J. M., Smith B. D., Danforth C. W., 2012, *ApJ*, 759, 23
- Skibba R. A., et al., 2011, *ApJ*, 738, 89
- Smith D. J. B., et al., 2011, *MNRAS*, 416, 857
- Smith D. J. B., et al., 2012a, *MNRAS*, 427, 703
- Smith D., et al., 2012b, *Monthly Notices of the Royal Astronomical Society*, 427, 703

- Smith M. W. L., et al., 2012c, *ApJ*, 748, 123
- Somerville R. S., Popping G., Trager S. C., 2015, *MNRAS*, 453, 4337
- Stecher T. P., Donn B., 1965, *ApJ*, 142, 1681
- Struve F. G. W., 1847, *Etudes d'Astronomie Stellaire: Sur la voie lactee et sur la distance des etoiles fixes*
- Sugerman B. E. K., et al., 2006, *Science*, 313, 196
- Sutherland W., et al., 2015, *A&A*, 575, A25
- Symeonidis M., Page M. J., Seymour N., Dwelly T., Coppin K., McHardy I., Rieke G. H., Huynh M., 2009, *MNRAS*, 397, 1728
- Symeonidis M., Page M. J., Seymour N., 2011, *MNRAS*, 411, 983
- Symeonidis M., et al., 2013, *MNRAS*, 431, 2317
- Tacconi L. J., et al., 2013, *ApJ*, 768, 74
- Tacconi L. J., et al., 2018, *ApJ*, 853, 179
- Takeuchi T. T., Buat V., Burgarella D., 2005, *A&A*, 440, L17
- Taylor M. B., 2005, in Shopbell P., Britton M., Ebert R., eds, *Astronomical Society of the Pacific Conference Series Vol. 347, Astronomical Data Analysis Software and Systems XIV*. p. 29
- Taylor E. N., et al., 2011, *MNRAS*, 418, 1587
- Temim T., Sonneborn G., Dwek E., Arendt R. G., Gehrz R. D., Slane P., Roellig T. L., 2012, *ApJ*, 753, 72
- Tielens A. G. G. M., Allamandola L. J., 1987, in Morfill G. E., Scholer M., eds, *NATO ASIC Proc. 210: Physical Processes in Interstellar Clouds*. pp 333–376
- Tonry J. L., Blakeslee J. P., Ajhar E. A., Dressler A., 2000, *ApJ*, 530, 625
- Trumpler R. J., 1930, *Lick Observatory Bulletin*, 420, 154
- Tukey J., 1958, *Ann. Math. Statist.*, 29, 614
- Valiante R., Schneider R., Bianchi S., Andersen A. C., 2009, *MNRAS*, 397, 1661

- Valiante R., Schneider R., Salvadori S., Bianchi S., 2011, *MNRAS*, 416, 1916
- Valiante E., et al., 2016, *MNRAS*, 462, 3146
- Viaene S., et al., 2014, *A&A*, 567, A71
- Vlahakis C., Dunne L., Eales S., 2005, *MNRAS*, 364, 1253
- Walter F., et al., 2014, *ApJ*, 782, 79
- Werner M. W., et al., 2004, *ApJS*, 154, 1
- White S. D. M., Rees M. J., 1978, *MNRAS*, 183, 341
- Wilkins S. M., Trentham N., Hopkins A. M., 2008, *MNRAS*, 385, 687
- Wright E. L., 2006, *PASP*, 118, 1711
- Wright E. L., et al., 2010, *AJ*, 140, 1868
- Wright A. H., et al., 2016, *MNRAS*, 460, 765
- Wright A. H., et al., 2017, *MNRAS*, 470, 283
- Yin J., Hou J. L., Prantzos N., Boissier S., Chang R. X., Shen S. Y., Zhang B., 2009, *A&A*, 505, 497
- York D. G., et al., 2000, *AJ*, 120, 1579
- Zafar T., Watson D., 2013, *A&A*, 560, A26
- Zhukovska S., Henning T., 2014, arXiv e-prints, p. [arXiv:1407.8489](https://arxiv.org/abs/1407.8489)
- da Cunha E., Charlot S., Elbaz D., 2008, *MNRAS*, 388, 1595
- de Graauw T., et al., 2010, *A&A*, 518, L6
- de Jong J. T. A., et al., 2013, *The Messenger*, 154, 44
- de Jong J. T. A., et al., 2017, *A&A*, 604, A134